PERIDYNAMIC-BASED MULTISCALE FRAMEWORKS FOR CONTINUOUS AND DISCONTINUOUS MATERIAL RESPONSE

PhD Thesis

By

Yakubu Kasimu Galadima

Peridynamic Research Centre

Department of Naval Architecture, Ocean, and Marine Engineering

University of Strathclyde, Glasgow

United Kingdom

July 2023

Author statement

This thesis is the result of the author's original research. It has been composed by the author and has not been previously submitted for examination which has led to the award of a degree.

Signed: Date:

Abstract

This PhD thesis aimed to develop two broad classes of multiscale frameworks for peridynamic theory to address two pressing needs: first is increased computational efficiency and the second is characterisation of heterogeneous media. To achieve these goals, two multiscale frameworks were proposed: model order reduction methodologies and homogenization frameworks. The model order reduction schemes were designed to improve computational efficiency, while the homogenization methodology aimed to provide frameworks for characterisation of heterogeneous materials within the peridynamic theory. Two specific model order reduction schemes were proposed, including a coarsening methodology and a model order reduction method based on static condensation. These schemes were applied to benchmark problems and shown to be effective in reducing the computational requirement of peridynamic models without compromising the fidelity of the simulation results. Additionally, a first-order nonlocal computational homogenization framework was proposed to characterise heterogeneous systems in the framework of peridynamics. This framework was utilised to characterise the behaviour of elastic and viscoelastic materials and materials with evolving microstructures. The results from these studies agreed with published results. The thesis achieved the goal of contributing to the development of efficient and accurate multiscale frameworks for peridynamic theory, which have potential applications in a wide range of fields, including materials science and engineering.

Acknowledgements

I would like to express my gratitude to:

- My first supervisor Prof. Erkan Oterkus for his guidance and support
- My second supervisor Prof. Selda Oterkus for her guidance and support
- Administrative staff of NAOME for their support
- My sponsors, the Petroleum Technology Development Fund (PTDF) for awarding me the scholarship.
- My employer, Ahmadu Bello University Zaria for granting me the fellowship to undertake this research.
- My friends and colleagues in NAOME and especially within the Peridynamic Research centre for their support and friendship.
- My family for the love and support.
- And finally, and most importantly, to Allah SWT for the gift of life, guidance, and health.

Dedication

"Truly, my prayer and my service of sacrifice, my life and my death are (all) for Allah, the Cherisher of the worlds."

Al-Qur'an 6:162

Table of Contents

Author statement ii

Abstract iii

Acknowledgements iv

Dedication v

Table of Contents vi

Table of Figures xi

List of Tables xvi

Nomenclature xvii

Chapter 1 1

1.0 Introduction 1

1.1 Motivations 2

1.2 Research objectives 3

1.3 Research workflow 4

1.4 Research contributions 5

1.4.1 Methodologies of the first category 5

1.4.2 Methodologies of the second category 7

1.4.3 Research output 8

1.5 Thesis structure 10

Chapter 2 11

2.0 Literature Review and Theoretical Foundations 11

2.1 State-of-the-art in Peridynamic multiscale modelling 11

2.2 Nonlocal vector calculus primer 14

2.2.1 Nonlocal divergence and gradient operators and their adjoint 16

2.2.2 Interaction kernels and domains 17

2.2.3 Nonlocal interaction operators 18

2.2.4 Nonlocal integral theorem 18

2.2.5 Nonlocal weighted operators 20

2.2.6 Nonlocal differential operators for peridynamic application 21
2.3 Peridynamic theory 22
2.3.1 Important concepts 22
2.3.2 Governing equation of motion in Peridynamics 23
2.3.3 Bond-based peridynamic model 25
2.3.4 State-based peridynamic model 30
2.4 Discretization of the Peridynamic model 37
Chapter 3 39
3.0 Coarsening Method for Linear Peridynamic Theory 39
3.1 Peridynamic coarsening formulation. 39
3.2 Discretization of the coarsening method 42
3.3 Coarsening the Micromodulus Function 43
3.3.1 Coarsening of one-dimensional micromodulus functions 43
3.3.2 Coarsening of two-dimensional micromodulus function 45
3.4 Numerical Results 47
3.4.1 One-dimensional homogeneous bar under tension loading 47
3.4.2 One-dimensional composite bar under tension loading 48
3.4.3 One-dimensional homogeneous bar with a defect 49
3.4.4 Two-dimensional homogeneous plate under tension loading 51
3.4.5 Two-dimensional composite plate under tension loading 53
3.5 Computational cost 55
3.6 Conclusions 56
Chapter 4 57
4.0 Static condensation for linear peridynamics 57
4.1 Introduction to MOR using Static condensation 57
4.2 Reduced static PD models. 58
4.3 Reduced dynamic models 59
4.4 Reduced eigenvalue models 60

4.5 Condensation of the micromodulus function 61
4.6 Numerical results 63
4.6.1 Reduction of static problems 63
4.6.2 Reduced Eigenproblems 66
4.6.3 Reduction of dynamic problems 68
4.7 Conclusion 73
Chapter 5 74
5.0 Static condensation of peridynamic heat transport model 74
5.1 The nonlocal peridynamic heat transport model 74
5.2 Relationship between micro-conductivity and thermal conductivity 79
5.2.1 One-dimensional micro-conductivity 80
5.2.2 Two-dimensional micro conductivity function 82
5.3 The discrete heat conduction equation 82
5.4 Static condensation of the peridynamic head conduction model 83
5.4.1 Handling boundary conditions 84
5.4.2 Condensation of parameters of peridynamic heat conduction model 85
5.5 Numerical verification 86
5.5.1 A homogenous bar with constant temperature applied at both ends. 86
5.5.2 Numerical study of heat conduction in plate with a pre-existing crack 88
5.5.3 Example 1. Case I: Dirichlet boundary condition 90
5.5.4 Example 2. Case II: Neumann boundary condition 91
5.5.5 Example 3. Neumann boundary condition with retained nodes selected randomly. 93
5.5.6 Example 3. Nonuniform condensation 94
5.6 Conclusion 96
Chapter 6 97
6.0 Introduction 97
6.1 A Computational Homogenization Framework for Peridynamics 97

6.1.1 Effective material constants 97
6.1.2 Micro-macro scale transition 99
6.1.3 RVE boundary volume constraints 102
6.1.4 Bounds for effective properties. 106
6.1.5 Computational implementation of the PDCHT 107
6.2 Validation of the homogenization scheme 109
6.2.1 Comparing the PDCHT results with bounding theorems and other established methods. 111
6.2.2 Comparing the PDCHT results with results from published works 114
6.2.3 Effective properties of RVE with elliptical fibre inclusion 115
6.3 Conclusion 118
Chapter 7 120
7.0 Homogenization of Materials with Evolving Microstructure and Damage 120
7.1 Introduction 120
7.2 Summary of implementation strategy for PDCHT 120
7.3 Numerical implementation of the first order homogenization 121
7.3.1 Material softening due to crack propagation. 122
7.3.2 Damage evolution due to randomly distributed microcracks 124
7.4 Conclusion 127
Chapter 8 129
8.0 Computational homogenization of viscoelastic composites 129
8.1 Introduction 129
8.2 Linear viscoelastic constitutive model 130
8.3 Dynamic properties 133
8.4 Computational homogenization 134
8.4.1 Definition of scales and homogenization rule 135
8.4.2 Localization and solution of the microscale RVE problem 136
8.4.3 RVE volume constraint problem 137

8.5 Implementation strategy 138
8.6 Numerical examples 139
8.6.1 Two-phase composite with elastic inclusion and viscoelastic matrix 140
8.6.2 Two-phase composite with viscoelastic inclusion and matrix phases. 143
8.6.3 Effect of nonlocality on the effective mechanical properties of composites 145
8.7 Conclusion 149
Chapter 9 151
9.0 Conclusion and future work 151
9.1 Summary of contributions 151
9.1.1 Model order reduction methodologies 151
9.1.2 Computational homogenization framework 152
9.2 Future work 153
9.2.1 Future research direction in the model reduction schemes 153
9.2.2 Future research direction in computational homogenization 154
References 155

Table of Figures

Figure 2-1: Interaction Domain 18
Figure 3-1. A Peridynamic body showing model levels 0, 1 and 2. 39
Figure 3-2. Schematic representation of the one-dimensional coarsening process 44
Figure 3-3. Micromodulus function associated with a uniform bond constant. 44
Figure 3-4. Micromodulus function associated with a bond constant function having triangular profile. 45
Figure 3-5. Micromodulus function associated with a bond constant function having inverted triangular profile. 45
Figure 3-6. Detailed level 0 and coarsened level 1 bodies for coarsening of two-dimensional micromodulus function 46
Figure 3-7. Coarsening of two-dimensional micromodulus function: (a) $\boldsymbol{x}-\boldsymbol{x}$ interaction (b) $\boldsymbol{x}-\boldsymbol{y}$ interaction (c) $\boldsymbol{y}-\boldsymbol{x}$ interaction, and (d) $\boldsymbol{y}-\boldsymbol{y}$ interaction. 46
Figure 3-8. Displacement fields for a one-dimensional homogeneous bar under tension loading 48
Figure 3-9. Displacement fields for levels 0, 1, and 2 for a one-dimensional composite bar under tension loading 49
Figure 3-10. One-dimensional homogeneous bar with a defect 50
Figure 3-11. Schematic representation of the coarsening process for example 3.4.3. 50
Figure 3-12. Coarsened displacement fields in a one-dimensional homogeneous bar with a defect 51
Figure 3-13. Discretisation and coarsening of the two-dimensional homogeneous plate. 51
Figure 3-14. Profile of $\boldsymbol{x}$ −axis displacement field: (a) Detailed (Level 0) model and (b) Coarsened (Level 1) model. 52
Figure 3-15. Profile of y−axis displacement field: (a) Detailed (Level 0) model and (b) Coarsened (Level 1) model. 52
Figure 3-16: Profile of displacement field along a grid line of points in the $\boldsymbol{y}$ −direction 53
Figure 3-17: Profile of displacement field along a grid line of points in the x-direction 53
Figure 3-18: Discretisation and coarsening of the two-dimensional composite plate. 54
Figure 3-19: Displacement fields for levels 0, 1, and 2 for a two-dimensional plate under tension loading. 54
Figure 4-1: Schematic representation of 1D reduction process 62
Figure 4-2: Coarsening of 1D Micromodulus function. 62

Figure 4-3: A schematic representation of the composite bar showing hard and soft material strips. 63
Figure 4-4: Displacement fields for detailed and reduced models..... 64
Figure 4-5: Schematic representation of the PD model of plate for static response analysis..... 65
Figure 4-6: Displacement profile in x-direction (a) Detail model (b) Condensed mode..... 65
Figure 4-7: Displacement profile in y-direction (a) Detail model (b) Condensed model..... 65
Figure 4-8: A bar with one end fixed and one end free. 66
Figure 4-9: Comparison of eigenvalues from the full PD model and reduced model..... 67
Figure 4-10: Discretization and condensation of the full PD model. 68
Figure 4-11: Time-history response of material points located at (a) $x = 0.0995$, and (b) $x = 0.4995$, for both full and reduced models. 69
Figure 4-12: Displacement values at all nodes at (a) 5000th time step, (b) 10000th time step, (c) 20000th time step, and (d) 26000th time step. 69
Figure 4-13: Time-history response of material points located at (a) $x = 0.0995$ (b) $x = 0.2995$ (c) $x = 0.4995$ and (d) $x = 0.7995$ for both the Full PD model and Condensed model..... 70
Figure 4-14: Displacement values at all nodes at (a) 5000th time step, (b) 10000th time step, (c) 20000th time step, and (d) 26000th time step. 71
Figure 4-15: Time-history response of material points located at $x = 0.0995$, 0.2995, 0.4995 and 0.7995 for both the Full PD model and Condensed model. 72
Figure 4-16: Displacement values at all nodes at (a) 10000th time step, (b) 20000th time step, (c) 50000th time step, and (d) 86000th time step 72
Figure 5-1 : Comparison of micro-conductivity functions. 82
Figure 5-2 : A discretized bar to illustrate condensation of the micro-conductivity functions..... 85
Figure 5-3 : Static condensation of micro-conductivity functions of a homogeneous bar: (a) Constant micro-conductivity, (b) Linear micro-conductivity and (c) Quadratic micro-conductivity 85
Figure 5-4 : Static condensation of micro-diffusivity functions of a homogeneous bar: (a) corresponding to constant micro-conductivity, (b) corresponding to linear micro-conductivity and (c) corresponding to quadratic micro-conductivity..... 86
Figure 5-5 : A homogeneous bar subjected to constant temperature at both ends. 87
Figure 5-6 : Temperature distribution in a homogeneous bar subjected to constant temperature at both ends corresponding to retaining every 2nd node of the full model and response function (a) $f1$ (b) $f2$ and (c) $f3$..... 87

Figure 5-7: Temperature distribution in a homogeneous bar subjected to constant temperature at both ends corresponding to retaining every 5th node of the full model and response function (a) $f1$ (b) $f2$ and (c) $f3$ 87
Figure 5-8: Temperature distribution in a homogeneous bar subjected to constant temperature at both ends corresponding to retaining every 10th node of the full model and response function (a) $f1$ (b) $f2$ and (c) $f3$ 88
Figure 5-9 : Example 2 problem setup: A plate with pre-existing crack 89
Figure 5-10 : Schematic representation of static condensation 89
Figure 5-11 : Dirichlet boundary condition: Temperature distribution across the plate: (a) Full model corresponding to $t = 7\times10 - 5$ s (b) Full model corresponding to $t = 7\times10 - 4$ s (c) Full model corresponding to $t = 7\times10 - 3$ s (d) Reduced model corresponding to $t = 7 \times 10 - 5$ s (e) Reduced model corresponding to $t = 7\times10 - 4$ s , (f) Reduced model corresponding to $t = 7\times10- 3$ s 90
Figure 5-12 : Temperature profile along the grid at $x = -5.5\times10 - 5\ m$ parallel to the y −axis of the plate with Dirichlet boundary condition. 91
Figure 5-13 : Neumann boundary condition: Temperature distribution across the plate: (a) Full model corresponding to $t = 7\times10 - 5$ s (b) Full model corresponding to $t = 7\times10 - 4$ s (c) Full model corresponding to $t = 7\times10 - 3$ s (d) Reduced model corresponding to $t = 7\times10 - 5$ s (e) Reduced model corresponding to $t = 7\times10 - 4$ s, (f) Reduced model corresponding to $t = 7\times10 - 3$ s 92
Figure 5-14 : Temperature profile along the grid at $x = -5.5\times10 - 5$ m parallel to the y −axis of the plate with Neumann boundary condition. 92
Figure 5-15: Neumann boundary condition: Temperature distribution across the plate: (a) Full model corresponding to $t = 7\times10$-5 s, (b) Full model corresponding to $t = 7\times10$-4 s (c) Full model corresponding to $t = 7\times10$-3 s (d) Reduced model corresponding. 93
Figure 5-16: Temperature profile along a grid of the plate with Neumann boundary condition and condensation achieved through random selection of nodes. 94
Figure 5-17 : Adaptive condensation: Temperature distribution across the plate: (a) Full model corresponding to $t = 10$ s (b) Full model corresponding to $t = 20$ s, (c) Full model corresponding to $t = 30$ s, (d) Reduced model corresponding to $t = 10$ s, (e) Reduced model corresponding to $t = 20$ s, (f) Reduced model corresponding to $t = 30$ s, ... 95
Figure 5-18 : Adaptive condensation. Temperature profile along a grid of the plate with Neumann boundary condition 95

Figure 6-1: Schematic Representation of Homogenization Process: Defining Representative Volume Element (RVE) in a Heterogeneous Material..... 98
Figure 6-2: Example square RVE showing corresponding boundary regions..... 104
Figure 6-3: RVE geometry showing various configuration. 110
Figure 6-4: Evolution of the effective stiffness tensor of glass in epoxy-matrix composite – LDBVC (a) $C11 *= C22 *$ (b) $C22 *$ (c) $C33 *$ and (d) $C12 *$ 111
Figure 6-5: Evolution of the effective elastic constants – LDBVC (a) Effective bulk modulus, (b) Effective shear modulus and (c) Effective Elastic modulus..... 112
Figure 6-6: Evolution of the effective stiffness tensor of glass in epoxy-matrix composite – PBVC (a) $C11 *= C22 *$ (b) $C22 *$ (c) $C33 *$ and (d) $C12 *$ 112
Figure 6-7: Evolution of the effective elastic constants – PBVC (a) Effective bulk modulus, (b) Effective shear modulus and (c) Effective Elastic modulus..... 112
Figure 6-8: Evolution of effective elastic constant obtained using the LDBVC and PBVC..... 113
Figure 6-9: Evolution of effective stiffness ratio under LDBVC (a) $\varphi = 1.07$ (b) $\varphi = 3.44$ 115
Figure 7-1: RVEs with (a) Single subscale crack (b) Two interacting subscale cracks 122
Figure 7-2: Evolution of the component $C22$ of the effective stiffness tensor (a) RVE with a single propagating crack, (b) RVE with two coalescing cracks..... 123
Figure 7-3: Elastic anisotropy index for the single crack and coalescing cracks 124
Figure 7-4: Arrangement of randomly distributed microcracks (a) Horizontally aligned (b) Randomly aligned..... 125
Figure 7-5: Evolution of damage due to random cracks (a) Horizontally aligned, (b) Randomly aligned..... 125
Figure 7-6: Elastic anisotropy index for cracks aligned horizontally and randomly. 126
Figure 8-1: Micro computational domain showing solution and boundary domains..... 136
Figure 8-2: RVE showing microstructure topology of composites..... 140
Figure 8-3: Effective stress relaxation stiffness tensor. Graph showing the $C11$ component.... 142
Figure 8-4: Effective relaxation modulus obtained from the effective stress relaxation stiffness tensor. 142
Figure 8-5: Effective loss tangent in frequency domain 143
Figure 8-6: Component $C11$ of the effective stiffness tensor of a two-phase matrix-inclusion composite system with both matrix and inclusion made of viscoelastic materials. 144
Figure 8-7: Effective relaxation modulus of the composite system obtained from the effective stiffness tensor..... 144

Figure 8-8: Effective loss tangent of a two-phase matrix-inclusion composite system made of viscoelastic inclusion and matrix. 145
Figure 8-9: Effect of nonlocality on the effective relaxation modulus of a two-phase matrix-inclusion composite system 146
Figure 8-10: Effect of nonlocality on the effective loss modulus of a two-phase matrix-inclusion composite system 147
Figure 8-11: Effect of nonlocality on the effective storage modulus of a two-phase matrix-inclusion composite system 147
Figure 8-12: Creep strain during stress relaxation in a bar for effective relaxation moduli obtained from different degree of nonlocality. 149

List of Tables

Table 2-1: Micromodulus functions with their corresponding bond force constants 30
Table 4-1: Natural frequencies of the first five modes computed using the full PD model, reduced PD model and FE analysis. 67
Table 6-1: Material properties of the constituents of RVEs 110
Table 6-2: Effective material properties for boron/aluminium composite ($c1 = 0.47$) 114
Table 6-3: Evolution of the elastic modulus in directions 1 and 2 (Glass in aluminium: circular inclusion) 116
Table 6-4: Evolution of the elastic modulus in directions 1 and 2 (Graphite in aluminium: circular inclusion) 116
Table 6-5: Evolution of the elastic modulus in directions 1 and 2 (Glass in aluminium: elliptical inclusion) 116
Table 6-6: Evolution of the elastic modulus in directions 1 and 2 (Graphite in aluminium: elliptical inclusion) 117
Table 8-1: Prony coefficients for effective relaxation modulus data 141
Table 8-2: Coefficients of Prony series representation of effective relaxation modulus 143

Nomenclature

Acronyms

ADR	Adaptive Dynamic Relaxation
BBPD	Bond-based Peridynamics
CCM	Classical Continuum Mechanics
FE	Finite Element
FEM	Finite Element Method
HMM	Heterogenous Multiscale Method
IVCP	Initial Volume Constraint Problem
LDBVC	Linear Displacement Boundary Volume Constraint
LTEHOT	Linear Thermoelastic Higher-Order Theory
NOSBPD	Non-ordinary State-based Peridynamics
OSBPD	Ordinary State-based Peridynamics
OSBPDHT	Ordinary State-based Peridynamic Homogenization Theory
PBVC	Periodic Boundary Volume Constraint
PD	Peridynamic, Peridynamics
PDCHT	Peridynamic Computational Homogenization Theory
PMB	Prototype Microelastic Brittle
RVE	Representative Volume Element
SBPD	State-based Peridynamics
UC	Unit Cell
VAMUCH	Variational Asymptotic Method for Unit Cell Homogenization
VCP	Volume Constraint Problem

Symbols and Notations

$(\cdot)^s$	Symmetric tensor operator
$(\cdot)_\omega$	Weighted operator
$\mathcal{H}_x$	Family of point x
$\widehat{\mathbf{T}}$	Material constitutive model
$\underline{\mathbf{T}}$	Force state
$\underline{\mathbf{X}}$	Reference position vector state
$\underline{\mathbf{Y}}$	Deformation state
s_0	Critical bond stretch
$\mathbf{E}$	Nonlocal Green-Lagrange strain tensor
$\mathbf{F}$	Deformation tensor
$\mathbf{K}$	Shape tensor
$\mathbf{M}$	Deformed bond direction vector
$\mathbf{f}$	Force density
$\mathbf{t}$	Force density functions
E	Young's modulus
H	Heaviside step function
W	Total strain energy
c	Bond elastic constant
s	Bond stretch
w	Micropotential

$\boldsymbol{C}$	Micromodulus function
$\boldsymbol{u}$	Displacement vector
$\mathcal{D}$	Nonlocal divergence operator
$\mathcal{G}$	Nonlocal gradient operator
$\mathcal{N}$	Nonlocal point interaction operator
$\mathcal{S}$	Point interaction operator
δ	Horizon
μ	Time-dependent damage criteria
ξ	Bond length
ω	Weight function
$\boldsymbol{\varepsilon}$	Infinitesimal strain tensor
$\boldsymbol{\eta}$	Relative displacement vector

Chapter 1

1.0 Introduction

Understanding how materials behave through theoretical and applied mechanics has contributed immensely to the advancement recorded in many fields of human endeavours including oil and gas exploration and exploitation, civil infrastructures, automobile, and the aerospace as well as biomedical industries [1]. To adequately characterise materials for any meaningful application requires a good understanding of their mechanical properties. Mathematical modelling is increasingly gaining acceptance as a tool to characterise the behaviour of material and structures [2]. This is because of the many advantages that mathematical modelling offers. An important advantage offered by mathematical modelling over physical experimentation is that it allows for the prediction of the behaviour of materials and structures under a range of conditions, some of which can be difficult or impossible to achieve through physical experimentation. This is particularly important in the design and optimization of materials and structures, as it allows for the exploration of a larger space of input parameters to identify key factors that govern the behaviour of the system.

Classical continuum theory has long been the dominant mathematical framework for the study of materials and structures by scientists and engineers. Despite its success in modelling a wide range of physical processes, the classical continuum theory has been shown to be deficient in its ability to model an increasing number of phenomena accurately and/or efficiently. This limitation can be attributed primarily to the mathematical structure of the classical theory.

The classical theory relies on partial differential equations to relate the properties of a material to its state. The use of derivatives inherently presupposes the principle of local action [3] which implies that the state of a material at a point depends solely on the value of the field variable at that point. This description of material effectively makes the classical theory a local theory, and the locality is manifested by the absence of an internal length parameter, a characteristic of the classical theory that has been identified as responsible for the unphysical solutions in the modelling of materials exhibiting size effects and strain softening behaviour [4, 5], for example.

Furthermore, the use of derivatives in the classical continuum theory also implies that the material behaviour is smooth and continuous at least in the solution variables, which is not always the case. Many materials exhibit discontinuous behaviour, such as cracking and fragmentation, and since these derivatives are not defined in the presence of such discontinuities, the equation of motion of the classical theory becomes undefined. This limitation makes the computational simulation of

discontinuous material response based on the classical continuum framework an unresolved problem [6]. These deficiencies of the classical continuum theory have led to the development of nonlocal continuum theories and modelling frameworks with extended capabilities in modelling the behaviour of materials and structures. See [7-9] for review of nonlocal theories.

One of the alternative continuum theories developed to overcome the deficiencies of the classical theory is the Peridynamic theory [10] which is a continuum but nonlocal reformulation of the classical theory using integral rather than differential operator. The use of integral operator introduces the notion of nonlocal action in the peridynamic theory which allows the state fields at a point in a material to be influenced by the state field at points located at a finite distance away. This mathematical structure endows the peridynamic theory with two desirable characteristics.

The first is that the use of integral operators eliminate the smoothness and continuity requirements. This allows the fundamental governing equation of motion of peridynamics to be valid in both continuous and discontinuous material response. Secondly, the nonlocality that emerges from the integral formulation endows peridynamics with an internal length parameter called horizon which is the parameter that controls the degree of nonlocality in the peridynamic framework. The presence of the internal length parameter gave the peridynamic theory the capability to model processes and phenomenon such as size dependent behaviour [11] and strain softening phenomenon [12]. These extended capabilities have motivated the use of peridynamic theory to study a wide range of engineering problems [13-29].

1.1 Motivations

To fully leverage the capabilities of peridynamics as a simulation tool, it is imperative to develop multiscale frameworks. This endeavour is motivated by physics as well as computational considerations. The physics-based consideration stems from the fact that many observable behaviour of materials are influenced by phenomena and processes occurring over multiple length scales [30, 31]. To accurately model the behaviour of materials will therefore require a computational framework that will couple the multiple scales in a consistent manner that will allow the exchange of information between the scales.

The numerical motivation for a multiscale framework for peridynamic theory is driven by the requirement for increased efficiency in computation. As a nonlocal model, peridynamics is not as computationally efficient as the local classical continuum theory [32, 33]. thus, is because the nonlocal interactions allowed in peridynamics result in larger degrees of freedom in the system and

thus a larger number of equations to be solved compared to the classical continuum theory. This translates to a requirement for additional computational resources.

Efforts have already been expended in the development of multiscale frameworks for PD, aiming to overcome these challenges and broaden the applicability of PD to a wide range of problems. In section 2.1 of this thesis, a comprehensive state-of-the-art review will be presented, assessing the existing multiscale methodologies developed for PD, and highlighting potential research gaps that need to be addressed.

1.2 Research objectives

Considering the foregoing motivations for the development of multiscale methods within the framework of peridynamics, this thesis proposes two broad categories of multiscale frameworks for the peridynamic theory. Through the implementation of these frameworks, this thesis aims to expand the scope and capabilities of peridynamic theory as a tool for numerical characterisation of materials.

The first category are termed *model order reduction* (MOR) methodologies and are motivated by the requirement for increased computational efficiency to alleviate the inherent computational deficiency of peridynamic model due to nonlocal interactions. The goal in developing these frameworks is to reduce the number of degrees of freedom in a system while still capturing its essential behaviour. This is achieved by eliminating the internal (or subscale) degrees of freedom and replacing them with a set of reduced order equations that can adequately describe the behaviour of the system. A major advantage to be derived from utilizing these frameworks is reduction in computational cost. Another advantage is that reducing the degrees of freedom of the system will allow peridynamics to be utilised in solving large-scale problems that would otherwise be impossible due to computational resource constraints.

The second category of multiscale frameworks developed are called *computational homogenization* methodologies. The goal in developing these frameworks is to derive effective macroscopic properties of a material or structure from the properties of its microstructure. This is achieved by averaging the properties of the microstructure over a representative volume element (RVE) and deriving effective properties that can be used to model the behaviour of the material or structure at the macroscopic scale. By providing a means to accurately extract the effective behaviour of materials using information from the microstructure, the proposed homogenization framework provides a pathway of gaining a deeper understanding of the relationship between microstructure and material properties. In particular, the nonlocal homogenization framework proposed in this

thesis provide the unique advantage of leveraging on the extended capabilities of peridynamic theory to study the effects of nonlocal driven phenomena and processes, such as size effect and strain softening, as well as discontinuous responses, such as cracks occurring at the subscale on the effective behaviour of materials at the macroscale.

1.3 Research workflow

To achieve the objectives of this thesis, a comprehensive work plan was designed, encompassing literature review, mathematical framework conceptualization, computational scheme development, numerical validation, and dissemination of the research findings.

Workflow:

1. Literature Review: The initial phase in the research involved conducting an extensive literature review to explore existing research on multiscale frameworks for peridynamics. Various published papers, journal articles, and conference proceedings were analysed to understand the state-of-the-art and identify potential research gaps and opportunities for meaningful contributions. The limitations and weaknesses of existing approaches were critically evaluated to guide the subsequent research.

2. Conceptualization and Mathematical Frameworks: Based on the insights gained from the literature review, the mathematical frameworks for the proposed multiscale frameworks were conceptualized and developed. For the MOR framework, the mathematical framework of the coarsening method is extended from its original one-dimensional form to two-dimension. A new MOR framework based on the static condensation protocol for implementation within the PD modelling framework was also conceptualised and the necessary mathematical equations for the reduction procedure were derived. The theoretical conceptualization of the CH framework involved defining the microscale and macroscale domains, followed by the selection of appropriate scale transition operators that link the microscale and macroscale fields. Subsequently, during the derivation of the mathematical framework, rigorous mathematical analysis was performed to establish the equations and relationships that accurately capture the effective properties and behaviour of the heterogeneous material at the macroscale.

3. Development of Computational Scheme: Subsequently, the proposed multiscale frameworks were implemented into computational schemes. To achieve this, custom computer codes were written in MATLAB to numerically solve the developed multiscale frameworks. The implementation involved devising numerical and computational

algorithms to handle the coupling between different scales, perform matrix operations, and address boundary conditions appropriately. Particular attention was given to ensuring computational efficiency and accuracy, as well as overcoming any challenges specific to peridynamic modelling.

4. Numerical Validation and Benchmarking: To validate the developed computational schemes, extensive numerical validation and benchmarking were carried out. Numerous test cases and benchmark problems, including material characterization of elastic/viscoelastic materials and evolving microstructures, were simulated to assess the performance and accuracy of the proposed multiscale frameworks. The results were thoroughly compared with high-fidelity models (in the case of MOR frameworks) and results from literature (in the case of CH theory) to verify their accuracy and efficiency.

5. Thesis Writing and Dissemination: Throughout the research, efforts were made to continuously document all steps, methodologies, and results in a clear and coherent manner. Regular presentations and discussions with supervisors and peers provided valuable feedback and insights. As the research progressed, the findings were disseminated through conference presentations, journal publications, and a book chapter to contribute to the advancement of the state-of-the-art in the field of computational characterizations of materials using PD.

In summary, the comprehensive research work plan implemented in this study proved highly effective in achieving its objectives. By conducting an extensive literature review, conceptualizing robust mathematical frameworks, developing efficient computational schemes, performing thorough numerical validations, and disseminating the findings, this thesis successfully expanded the scope of applicability of PD and made significant strides in advancing the field of multiscale modelling for PD theory.

1.4 Research contributions

This thesis presents a significant contribution to the field of multiscale modelling within the peridynamic computational framework. The research aims to achieve increased computational efficiency and the ability to characterise the effective properties of heterogeneous materials through the development of the two categories of multiscale methodologies.

1.4.1 Methodologies of the first category

These are the so-called MOR methods. The goal of developing these methodologies is to increase the computational efficiency of peridynamic theory. Generally, methodologies belonging to this

category seek to reduce the computational requirement of solving high-fidelity model by replacing it with a reduced-order model having fewer degrees of freedom, while still maintaining a high level of accuracy and reliability in the results. This is usually achieved using techniques such as the *coarsening method* [34, 35], *static condensation* [36], *proper orthogonal decomposition* [37, 38], and *reduced basis method* [39-41] among others.

The first technique explored to develop a model order reduction framework for the peridynamic theory is the coarsening method. The contribution made in this thesis in this regard is to generalise the coarsening method to two-dimension which was originally proposed and implemented for 1D problems in [34]. Beyond expanding to higher dimensions, another contribution of this thesis is the implementation of various micromodulus functions within the coarsening framework. Results of numerical investigation conducted demonstrated the robustness of the technique in reducing the order of the peridynamic model for a range of problems, without compromising on predictive capability.

Addressing real-world engineering challenges and achieving increased accuracy are the key motivations for extending the coarsening method from one dimension to higher dimensions. Many engineering problems, such as structural analysis, material characterization, and fluid-structure interaction for example, inherently involve phenomena occurring in higher-dimensional space. Extending the coarsening method to higher dimension will therefore expand its scope of application to these problems. Furthermore, the extension of the coarsening method to higher dimensions offers significant advantages in terms of increased accuracy of simulations. By enabling the representation of large and complex systems with fewer degrees of freedom, this method preserves essential features of simulation results that would otherwise only be attainable with high-resolution models.

Despite its proven effectiveness, the coarsening algorithm is limited by the requirement that boundary regions with applied forces or prescribed non-zero displacements must be retained in the coarse model, thus limiting the flexibility in choosing which degrees of freedom to eliminate or retain. Additionally, the algorithm is not suitable for solving dynamic equilibrium problems. To address these limitations, a novel MOR technique was proposed employing the static condensation method. This marks the first-ever utilization of the static condensation protocol to reduce the order of peridynamic models, paving the way for unprecedented flexibility in selecting degrees of freedom. A series of numerical simulations were conducted to demonstrate the efficiency and effectiveness of this proposed framework. The results showed that the proposed method was able to reduce the order of both static and dynamic problems without compromising the accuracy of

the results. Furthermore, the static condensation framework was extended to reduce the order of peridynamic heat models, with numerical investigations demonstrating its effectiveness and efficiency in this regard.

While this thesis has successfully implemented the static condensation MOR framework to some benchmark mechanical and heat transport models, potential applications such as test-analysis-model (TAM) development and reanalysis remain promising avenues for future research, providing valuable tools for test/analysis correlation, system identification, and re-solving of structural models with modified conditions.

1.4.2 Methodologies of the second category

As mentioned in 1.2, methodologies belonging to this category are generally called CH frameworks and are motivated by the requirement to have a framework that allows the determination of effective properties of microscopically heterogeneous materials. In this regard, a peridynamic computational homogenization theory (PDCHT) was proposed. To ensure consistency with the nonlocal nature of the peridynamic theory, the development of this theory is anchored on the framework of a newly proposed nonlocal vector calculus [42, 43]. The theory is validated through numerical solution of Representative Volume Elements (RVE) from composite materials and comparison with established methodologies demonstrated the effectiveness of the proposed homogenization theory.

The PDCHT is then utilised to characterise the effective behaviour of materials with evolving microstructure. In this contribution, the proposed PDCHT was utilized to study the evolution of effective material response of damaged media. In particular, the framework is applied to model and study the effect of stationary and propagating micro cracks and their interactions on the effective properties of materials.

Subsequently, a peridynamic computational framework for homogenization of viscoelastic composite was proposed. The time dependent behaviour of viscoelastic materials as represented by the Boltzmann integral constitutive model introduces an additional layer of nonlocality to the peridynamic homogenization framework. This temporal nonlocality is taken onboard by incorporating the Boltzmann integral constitutive model into the PDCHT framework, which allows for the capture of time-dependent response. This proposed framework was then validated by conducting numerical simulations on RVE of viscoelastic composite materials and comparing the results with those obtained using established methodologies. The results demonstrate the

effectiveness and efficiency of the proposed framework in capturing the time-dependent behaviour of viscoelastic composite materials and determining their effective properties.

1.4.3 Research output

This section presents the research output of this thesis in the form of journal articles, conference papers, and book chapter. The works presented here is a culmination of the research conducted over the course of this study, which aimed to develop two classes of multiscale modelling frameworks for peridynamics. These frameworks were developed to address the need for increased computational efficiency and provide a method for characterizing the effective properties of materials with complex microstructure or those exhibiting nonlocal behaviour. The following is the lists of research output:

A. **Journal articles**:

1. Galadima, Y. K., Oterkus, S., Oterkus, E., Amin, I., El-Aassar, A.-H., & Shawky, H. (2023). Effect of phase contrast and inclusion shape on the effective response of viscoelastic composites using peridynamic computational homogenization theory. *Mechanics of Advanced Materials and Structures*, 1-9. https://doi.org/https://doi.org/10.1080/15376494.2023.2218364
2. Galadima, Y. K., Oterkus, S., Oterkus, E., Amin, I., El-Aassar, A.-H., & Shawky, H. (2023). A nonlocal method to compute effective properties of viscoelastic composite materials based on peridynamic computational homogenization theory. Composite Structures, 319, 117147. https://doi.org/https://doi.org/10.1016/j.compstruct.2023.117147
3. Galadima, Y. K., Oterkus, S., Oterkus, E., Amin, I., El-Aassar, A.-H., & Shawky, H. (2023). Modelling of viscoelastic materials using non-ordinary state-based peridynamics. *Engineering with Computers*. https://doi.org/10.1007/s00366-023-01808-9
4. Galadima, Y. K., Xia, W., Oterkus, E., & Oterkus, S. (2023). A computational homogenization framework for non-ordinary state-based peridynamics. Engineering with Computers, 39(1), 461-487. https://doi.org/10.1007/s00366-021-01582-6
5. Galadima, Y. K., Xia, W., Oterkus, E., & Oterkus, S. (2022). Peridynamic computational homogenization theory for materials with evolving microstructure and damage. Engineering with Computers. https://doi.org/10.1007/s00366-022-01696-5

6. Galadima, Y. K., Oterkus, E., & Oterkus, S. (2022). Static condensation of peridynamic heat conduction model. *Mathematics and Mechanics of Solids*, *0*(0), 10812865221081160. https://doi.org/10.1177/10812865221081160

7. Galadima, Y. K., Oterkus, E., & Oterkus, S. (2021). Model order reduction of linear peridynamic systems using static condensation. *Mathematics and Mechanics of Solids*, *26*(4), 552-569. https://doi.org/10.1177/1081286520937045

8. Galadima, Y. K., Oterkus, E., & Oterkus, S. (2020). Investigation of the effect of shape of inclusions on homogenized properties by using peridynamics. *Procedia Structural Integrity*, *28*, 1094-1105. https://doi.org/10.1016/j.prostr.2020.11.124

9. Galadima, Y., Oterkus, E., & Oterkus, S. (2019). Two-dimensional implementation of the coarsening method for linear peridynamics. *AIMS Material Science*, *6*(2), 252-275. https://doi.org/http://dx.doi.org/10.3934/matersci.2019.2.252

B. **Conference Presentations**

1. Galadima, Y. K., Oterkus, E., & Oterkus, S. (2023). A Non-Ordinary State-Based Viscoelastic Peridynamic Computational Homogenisation Model to Calculate the Effective Properties of Viscoelastic Composite Materials ASME 2023 International Mechanical Engineering Congress and Exposition (IMECE2023), Boston, Massachusetts, USA.

2. Galadima, Y. K., Oterkus, E., & Oterkus, S. (2023). Modelling the Mechanical response of Single Crystal S2 Ice using Non-Ordinary State-Based Peridynamics. 27th International Conference on Port and Ocean Engineering under Arctic Conditions, Glasgow, United Kingdom.

3. Galadima, Y. K., Oterkus, E., Oterkus, S., Amin, I., El-Aassar, A., & Shawky, H. (2023). Effect of Phase Contrast on the Effective Instantaneous and Equilibrium Response of Viscoelastic Composites using Peridynamic Computational Homogenization Theory International Conference on Advanced Topics in Mechanics of Materials, Structures and Construction (AToMech1), Al Khobar, Saudi Arabia.

4. Galadima, Y. K., Xia, W., Oterkus, E., & Oterkus, S. (2022). A Non-Ordinary State-Based Peridynamic Computational Homogenisation Model by Considering Damage. ASME 2022 International Mechanical Engineering Congress & Exposition, Columbus, OH, USA.

5. Galadima, Y. K., Oterkus, E., & Oterkus, S. (2020). Homogenization of Peridynamic Models: Effect of Inclusion Shape on Effective Properties. First Virtual European Conference on Fracture (VECF1), Online.

6. Galadima, Y. K., Oterkus, E., & Oterkus, S. (2018). A Two-Dimensional Implementation of the Coarsening Method for Linear Peridynamics. ASME 2018 International Mechanical Engineering Congress & Exposition, Pittsburgh, PA, USA.

C. **Book chapter**

1. Galadima, Y. K., Xia, W., Oterkus, E., & Oterkus, S. (2021). Chapter 17 - Multiscale modeling with peridynamics. In E. Oterkus, S. Oterkus, & E. Madenci (Eds.), Peridynamic Modeling, Numerical Techniques, and Applications (pp. 371-386). Elsevier. https://doi.org/https://doi.org/10.1016/B978-0-12-820069-8.00018-4

1.5 Thesis structure

The remainder of this thesis is structured as follows: Chapter 2 provides a state-of-the-art literature survey and the introduction of the mathematical and theoretical basis of the frameworks proposed in this thesis. This includes a primer on nonlocal vector calculus, which is essential for the construction of important concepts in the multiscale frameworks proposed as well as the fundamental theory of peridynamics, covering the bond-based and state-based variants of the theory. Chapter 3 presents the development of the coarsening method, its generalization to 2D, and numerical examples to validate the methodology. Chapter 4 introduces the peridynamic static condensation multiscale framework, along with numerical studies to validate the framework. The static condensation framework is extended in chapter 5 to reduce the order of peridynamic heat transport model. Chapter 6 presents the development of the PDCHT and numerical studies that utilize the proposed theory to characterize the effective elastic properties of heterogeneous materials. Chapter 7 focuses on the use of the PDCHT in characterizing materials with evolving microstructure. Chapter 8 presents an extension of the PDCHT to homogenize viscoelastic composites. Finally, Chapter 9 provides concluding remarks and recommendations for future work.

Chapter 2

2.0 Literature Review and Theoretical Foundations

This chapter begins with a comprehensive state-of-the-art literature survey, exploring relevant background information and studies pertinent to the research presented in this thesis. subsequently, the chapter presents a brief introduction to vector calculus, laying the mathematical foundation for various aspects of the research. Lastly, the fundamental theory of peridynamics is thoroughly reviewed, encompassing both the bond-based and state-based formulations.

2.1 State-of-the-art in Peridynamic multiscale modelling

This section will provide a review of the state-of-the-art in multiscale modelling within the peridynamic framework. Multiscale modelling aims to capture the behaviour of a system at multiple scales of length and time, and the peridynamic framework offers a unique platform to address this challenge. To strike a balance between acceptable model fidelity and computational cost, increasing amount of research effort is being expended to develop a range of multiscale enrichment protocols for the peridynamic theory. The objective of these protocols is to enhance the capability of peridynamics in capturing and utilizing information across spatial scales at an acceptable computational cost. To achieve this objective, researchers have adopted one of two approaches. The first approach involves developing a framework that allows for the coupling of various resolutions of peridynamic model or coupling of peridynamic model with models based on other theories of mechanics to leverage the strengths of the coupled theories. This approach falls under the purview of *concurrent multiscale* modelling. The second approach involves frameworks that permit coupling of models at different length scales in the same part of a computational domain. These are categorized as *hierarchical multiscale* modelling frameworks.

A variety of concurrent multiscale modelling frameworks for peridynamics have been proposed. These approaches can broadly be categorised into *monomodel* and *multimodel* approaches. In the monomodel approach, peridynamics is used to model the entire computational domain. Multiscale capability is achieved by refining the grid appropriately to resolve details at different length scales. Development in this respect include the adaptive grid refinement method proposed in [44-46]. Refinement of the grid requires changing the grid density and the horizon which in turn induces a change in the micromodulus function of the peridynamic model. This change is done relying on a scaling algorithm. A variable horizon method was proposed in [47] to solve the problem of ghost forces that is a consequence of using variable horizon by introducing the concept of *partial stress* and a *splice technique*. To resolve the problem of ghost forces without recourse to the partial stress

and splice technique of [47], a dual horizon method [48] was proposed with extended capability of covering both bond-based peridynamics and state-based peridynamics. The dual horizon method was extended as Voronoi-based peridynamics in [49] for non-uniform discretization based on Voronoi diagrams.

The multimodel concurrent approaches are hybridization frameworks that focus primarily on developing coupling methodologies that allow peridynamics to be used concurrently with other modelling frameworks such as the classical continuum or atomistic modelling theories. The goal is to leverage on the advantages offered by each of the coupled models. These methods can broadly be classified as kinematic-based, force-based or energy-based coupling methods. In the kinematic-based methods [28, 50-52], coupling is achieved by implementing a contact algorithm over the interface region that requires the satisfaction of a series of kinematical constraints. The force-based approaches [53-59] rely on the balance of force in the interface region to achieve coupling of the models. In some cases, nonlocal weight functions are used to account for the contributions from the models in the balance of force. In the energy-based approach, coupling relies on the principle of energy conservation in the interface region. Two notable subclasses of the energy-based approach have been proposed such as the morphing methods [60-65] and the Arlequin coupling method [66].

In the hierarchical multiscale subclass, several researchers have dedicated their efforts to developing various hierarchical frameworks for the PD theory. These frameworks can be broadly classified into two categories: MOR frameworks and homogenization frameworks. One specific methodology within the MOR category, known as the coarsening method, was proposed in [34] for the linear PD one-dimensional model. The primary aim of the coarsening method is to capture the behaviour of high-fidelity models using a reduced number of degrees of freedom. This reduction in model order is achieved by substituting the original high-fidelity model with a surrogate model that contains fewer degrees of freedom.

The limitation of the coarsening method to one-dimensional applications is a significant research problem that motivates further investigation and development. The extension of the coarsening framework to higher dimensions presents several compelling reasons and research motivations. Firstly, higher-dimensional problems are prevalent in various scientific and engineering disciplines, and being able to model these systems efficiently and accurately is of utmost importance. Secondly, the reduced computational cost associated with the coarsening method allows for the analysis of larger and more complex systems, leading to advancements in understanding and design. Lastly, by extending the coarsening method to higher dimensions, we can bridge the gap between the

theoretical framework and its practical implementation, enabling PD to have a more significant impact in engineering applications.

Addressing the research gap of extending the coarsening framework to higher dimensions is a fundamental research problem that drives a significant portion of this thesis. By developing and validating an extended coarsening methodology for higher-dimensional problems, this thesis aims to overcome the current limitations and open new possibilities for efficient and accurate multiscale modelling in the peridynamic theory. The successful extension of the coarsening framework to higher dimensions will contribute to advancing the field of peridynamics and provide valuable insights for a wide range of applications, such as material science, structural analysis, and computational mechanics.

With respect to the second category of the hierarchical frameworks the earliest attempt at developing a homogenization framework for peridynamics appeared in [67, 68] in which a two-scale solution expansion of the peridynamic equation for a heterogeneous medium was proposed based on the concept of two-scale convergence. The framework is a three-step solution strategy of computing an average displacement field as a solution of a peridynamic macroscopic equation and computing micro-level displacement field from solution of a microscopic equation. The displacement field of the heterogeneous medium is found by superimposition of the micro displacement field unto the macro field in a final step. Although the mathematical framework was developed, numerical validation for the method is yet to be done.

A class of mean-field homogenization methods that can be categorised as a generalization of the self-consistent methods of the classical theory to peridynamics were proposed in [69-71] by extending the effective field hypothesis of the classical elasticity of composites to the nonlocal peridynamic framework. The effective elastic properties of a heterogeneous medium are determined through the introduction of a stress polarization tensor.

Among the homogenization methodologies exist a class designated as full field (computational) homogenization techniques which achieve a much higher resolution of the microscopic fields than the mean-field methods. A BBPD unit cell approach to predict the effective thermoelastic material properties of heterogeneous microstructures was proposed in [72]. Deriving from the strength of PD, this framework allows the determination of effective properties in the presences of discontinuities such as debonds, voids and microcracks which enables the determination of a damage tensor for progressive failure analysis. Another BBPD homogenization framework that seek to generalise a computational homogenization approach from the locally elastic case to the peristatic case for composite materials with a periodic structure was proposed in [73].

However, it is worth noting that all the homogenization frameworks discussed above were developed specifically for the BBPD. A systematic survey of the literature reveals a significant research gap: the absence of a homogenization framework for the SBPD. The state-based theory is a more generalized theory compared to the BBPD theory, as it alleviates some of the restrictions and limitations of the BBPD theory, allowing for the modelling of more generalized materials. This research gap motivates the development of a homogenization framework specifically tailored for the SBPD model.

Developing a homogenization framework for the SBPD model is crucial for advancing the state-of-the-art in the field of PD simulations and expanding its applicability to a wider range of materials and structures. It will allow for the characterization of heterogeneous materials with discontinuous response and nonlocal behaviour, providing insights into their effective properties and failure mechanisms. By filling this research gap, this thesis aims to contribute to the development of a comprehensive multiscale framework for peridynamics, facilitating its broader adoption in various fields, including material science, structural analysis, and computational mechanics.

In summary, the literature review has highlighted the existing MOR and homogenization frameworks for PD. MOR frameworks, such as the coarsening method, aim to increase computational efficiency by capturing the behaviour of high-fidelity models using fewer degrees of freedom. However, a research gap exists as the original proposal of the coarsening method was limited to one dimension, calling for its extension to higher dimensions. In addition to addressing this gap, this thesis aims to explore the development of other MOR methods with extended capabilities. Furthermore, the absence of a homogenization framework specifically designed for the SBPD theory poses a limitation in characterizing more generalized materials. This thesis also aims to fill this research gap by developing a comprehensive homogenization framework for the SBPD model. Through these contributions, this research enhances the scope of application of PD as a computational tool in material science and structural analysis, thereby advancing the field of multiscale modelling within the PD framework.

2.2 Nonlocal vector calculus primer

In this section, the mathematical framework that underlies the development of the multiscale frameworks in this thesis will be presented. This framework is built upon a nonlocal vector calculus, which provides a robust mathematical foundation that is consistent with the nonlocal nature of the PD theory. Nonlocal vector calculus [42, 43] is a mathematical framework that extends classical vector calculus to incorporate nonlocal, or long-range, interactions between points in a system. In classical vector calculus, the behaviour of a point in space is influenced only

by its immediate neighbours, whereas in nonlocal vector calculus, the behaviour of a point can be influenced by all other points in the system. This framework is particularly useful for modelling phenomena that exhibit nonlocal interactions, such as wave propagation [74], diffusion [75, 76], and image processing [77]. The presentation of the nonlocal calculus in this section will rely on the work presented in [42].

In developing the nonlocal vector calculus, two types of functions and operators are defined. Let k, m and n be positive integers and let $\boldsymbol{x}$ and $\boldsymbol{x}'$ be points in $\mathbb{R}^n$. For a given domain $\Omega \subseteq \mathbb{R}^n$, functions or operators that maps Ω into $\mathbb{R}^{m\times n}$ or $\mathbb{R}^n$ or $\mathbb{R}$ are called point functions or operators, respectively. On the other hand, functions, or operators from $\Omega \times \Omega$ into $\mathbb{R}^{m\times n}$ or $\mathbb{R}^n$ or $\mathbb{R}$ are called two-point functions or operators, respectively. Point functions and two-point functions could be scalar, vector or tensor valued functions.

A very important concept to start with in this review is the nonlocal flux. Given a tensor two-point function $\boldsymbol{\psi} : \mathbb{R}^n \times \mathbb{R}^n \longrightarrow \mathbb{R}^k$, then the definition

$$\mathcal{F}(\Omega_1, \Omega_2; \boldsymbol{q}) \coloneqq \int_{\Omega_1}\int_{\Omega_2} \boldsymbol{\psi}(\boldsymbol{x}, \boldsymbol{x}')\, d\boldsymbol{x}' d\boldsymbol{x} \tag{2-1}$$

is the nonlocal flux of $\boldsymbol{q}$ from Ω_1 into Ω_2 where $\int_{\Omega_2} \boldsymbol{\psi}(\boldsymbol{x}, \boldsymbol{x}')\, d\boldsymbol{x}'$ is identified as the nonlocal flux density into the region Ω_2 from point $\boldsymbol{x} \in \Omega_1$. It can be deduced from (2-1) that the nonlocal flux is not necessarily zero even if the intersection of the closures of Ω_1 and Ω_2 is an empty set. This is in stark contrast with the local flux which is zero if $\overline{\Omega}_1 \cap \overline{\Omega}_2 = \emptyset$. The nonlocal flux density is related to the intensive quantity $\boldsymbol{q}$ through a constitutive relation. If $\boldsymbol{\psi}(\boldsymbol{x}, \boldsymbol{x}')$ is assumed to be antisymmetric, then the following statements are true:

1. There is no self-interaction, *i.e.*,

$$\int_{\Omega}\int_{\Omega} \boldsymbol{\psi}(\boldsymbol{x}, \boldsymbol{x}')\, d\boldsymbol{y} d\boldsymbol{x} = \boldsymbol{0} \tag{2-2}$$

2. The nonlocal action-reaction principle holds for $\Omega_1, \Omega_2 \subset \Omega$

$$\int_{\Omega_1}\int_{\Omega_2} \boldsymbol{\psi}(\boldsymbol{x}, \boldsymbol{x}')\, d\boldsymbol{x}' d\boldsymbol{x} + \int_{\Omega_2}\int_{\Omega_1} \boldsymbol{\psi}(\boldsymbol{x}, \boldsymbol{x}')\, d\boldsymbol{x}' d\boldsymbol{x} = \boldsymbol{0} \tag{2-3}$$

The action-reaction principle given by (2-3) simply states that the flux from Ω_1 into Ω_2 is equal to the flux that exits Ω_2 into Ω_1.

2.2.1 Nonlocal divergence and gradient operators and their adjoint

Given the two-point function $\boldsymbol{v} : \mathbb{R}^n \times \mathbb{R}^n \longrightarrow \mathbb{R}^k$ and the scalar two-point function $u : \mathbb{R}^n \longrightarrow \mathbb{R}$. Let $\boldsymbol{\alpha}(\boldsymbol{x}, \boldsymbol{x}'): \mathbb{R}^n \times \mathbb{R}^n \longrightarrow \mathbb{R}^m$ be an antisymmetric vector two-point function. The action of nonlocal divergence operator $\mathcal{D}$ and its adjoint $\mathcal{D}^*$ on $\boldsymbol{v}$ and u respectively are defined as

$$\mathcal{D}(\boldsymbol{v})(\boldsymbol{x}) \coloneqq \int_{\mathbb{R}^n} \big(\boldsymbol{v}(\boldsymbol{x}, \boldsymbol{x}') + \boldsymbol{v}(\boldsymbol{x}', \boldsymbol{x}) \cdot \boldsymbol{\alpha}(\boldsymbol{x}, \boldsymbol{x}')\big)\, d\boldsymbol{x}' \quad \forall\, \boldsymbol{x} \in \mathbb{R}^n \tag{2-4}$$

and

$$\mathcal{D}^*(u)(\boldsymbol{x}, \boldsymbol{x}') \coloneqq -\big(u(\boldsymbol{x}') - u(\boldsymbol{x})\big) \otimes \boldsymbol{\alpha}(\boldsymbol{x}, \boldsymbol{x}') \quad \forall\, \boldsymbol{x} \in \mathbb{R}^n \tag{2-5}$$

Where $\mathcal{D}(\boldsymbol{v})(\boldsymbol{x}) : \mathbb{R}^n \times \mathbb{R}^n \longrightarrow \mathbb{R}^k$ and $\mathcal{D}^*(u)(\boldsymbol{x}, \boldsymbol{x}') : \mathbb{R}^n \longrightarrow \mathbb{R}^m \times \mathbb{R}^k$

Given the scalar two-point function $\eta : \mathbb{R}^n \times \mathbb{R}^n \longrightarrow \mathbb{R}$ and the vector point function $\boldsymbol{u} : \mathbb{R}^n \longrightarrow \mathbb{R}^k$. For a given antisymmetric vector two-point function $\boldsymbol{\beta}(\boldsymbol{x}, \boldsymbol{x}'): \mathbb{R}^n \times \mathbb{R}^n \longrightarrow \mathbb{R}^m$, the action of the nonlocal gradient operator $\mathcal{G}$ and its adjoint $\mathcal{G}^*$ on η and $\boldsymbol{u}$ respectively are defined as

$$\mathcal{G}(\eta)(\boldsymbol{x}) \coloneqq \int_{\mathbb{R}^n} (\eta(\boldsymbol{x}, \boldsymbol{x}') + \eta(\boldsymbol{x}', \boldsymbol{x})\, \boldsymbol{\beta}(\boldsymbol{x}, \boldsymbol{x}') d\boldsymbol{y} \quad \forall\, \boldsymbol{x} \in \mathbb{R}^n \tag{2-6}$$

and

$$\mathcal{G}^*(\boldsymbol{u})(\boldsymbol{x}, \boldsymbol{x}') \coloneqq -\big(\boldsymbol{u}(\boldsymbol{x}') - \boldsymbol{u}(\boldsymbol{x})\big) \cdot \boldsymbol{\beta}(\boldsymbol{x}, \boldsymbol{x}') \quad \forall\, \boldsymbol{x} \in \mathbb{R}^n \tag{2-7}$$

where $\mathcal{G}(\eta)(\boldsymbol{x}) : \mathbb{R}^n \times \mathbb{R}^n \longrightarrow \mathbb{R}^k$ and $\mathcal{G}^*(\boldsymbol{u})(\boldsymbol{x}, \boldsymbol{x}') : \mathbb{R}^n \longrightarrow \mathbb{R}$.

Observe that, unlike in local calculus which deals with point functions only, nonlocal calculus involves two kinds of functions: point and two-point functions. This therefore necessitates the definition of alternative forms of the nonlocal operators defined in (2-8)-(2-7). The alternative forms of the nonlocal divergence and gradient operators were given in [42] to be the pairs $\mathcal{D}, -\mathcal{G}^*$ and $\mathcal{G}, -\mathcal{D}^*$. For example, in the alternative pair $\mathcal{D}, -\mathcal{G}^*$, while $\mathcal{D}$ operates on tensor two-point functions, $-\mathcal{G}^*$ operates on tensor point functions. Similarly, for the pair $\mathcal{G}, -\mathcal{D}^*$, $\mathcal{G}$ operates on vector two-point functions while $-\mathcal{D}^*$ operate on vector point functions.

It is possible to apply the nonlocal divergence operator on a tensor function and the nonlocal gradient operator on a vector function. Let $\boldsymbol{\alpha}(\boldsymbol{x}, \boldsymbol{x}'): \mathbb{R}^n \times \mathbb{R}^n \longrightarrow \mathbb{R}^m$ be an antisymmetric vector two-point function. Given the tensor two-point function $\boldsymbol{\Psi}: \mathbb{R}^n \times \mathbb{R}^n \longrightarrow \mathbb{R}^{m \times k}$and the vector two-point function $\boldsymbol{v}: \mathbb{R}^n \times \mathbb{R}^n \longrightarrow \mathbb{R}^k$. The nonlocal divergence is defined by its action on $\boldsymbol{\Psi}$ as

$$\mathcal{D}(\boldsymbol{\Psi})(\boldsymbol{x}) \coloneqq \int_{\mathbb{R}^n} \big(\boldsymbol{\Psi}(\boldsymbol{x},\boldsymbol{x}') + \boldsymbol{\Psi}(\boldsymbol{x}',\boldsymbol{x}) \cdot \boldsymbol{\alpha}(\boldsymbol{x},\boldsymbol{x}')\big) d\boldsymbol{x}' \quad \forall\, \boldsymbol{x} \in \mathbb{R}^n \tag{2-8}$$

where $\mathcal{D}(\boldsymbol{\Psi})(\boldsymbol{x}) : \mathbb{R}^n \times \mathbb{R}^n \longrightarrow \mathbb{R}^{m\times k}$. The action of the nonlocal adjoint operator $\mathcal{D}^*$ on $\boldsymbol{v}$ is given by:

$$\mathcal{D}^*(\boldsymbol{v})(\boldsymbol{x},\boldsymbol{x}') \coloneqq -\big(\boldsymbol{v}(\boldsymbol{x}') - \boldsymbol{v}(\boldsymbol{x})\big) \otimes \boldsymbol{\alpha}(\boldsymbol{x},\boldsymbol{x}') \quad \forall\, \boldsymbol{x} \in \mathbb{R}^n \tag{2-9}$$

where $\mathcal{D}^*(\boldsymbol{v})(\boldsymbol{x},\boldsymbol{x}') : \mathbb{R}^n \longrightarrow \mathbb{R}^m \times \mathbb{R}^k$. The nonlocal gradient of $\boldsymbol{v}$ is given by:

$$\mathcal{G}(\boldsymbol{v})(\boldsymbol{x}) = \int_{\mathbb{R}^n} (\boldsymbol{v}(\boldsymbol{x},\boldsymbol{x}') + \boldsymbol{v}(\boldsymbol{x}',\boldsymbol{x}) \otimes \boldsymbol{\beta}(\boldsymbol{x},\boldsymbol{x}') d\boldsymbol{x}' \quad \forall\, \boldsymbol{x} \in \mathbb{R}^n \tag{2-10}$$

where $\mathcal{G}(\boldsymbol{v})(\boldsymbol{x}): \mathbb{R}^n \times \mathbb{R}^n \longrightarrow \mathbb{R}^{m\times k}$. The action of the nonlocal adjoint operator $\mathcal{G}^*$ on $\boldsymbol{\Psi}$ is given by:

$$\mathcal{D}^*(\boldsymbol{v})(\boldsymbol{x},\boldsymbol{y}) = -\big(\boldsymbol{\Psi}(\boldsymbol{x}') - \boldsymbol{\Psi}(\boldsymbol{x})\big) \cdot \boldsymbol{\alpha}(\boldsymbol{x},\boldsymbol{x}') \quad \forall\, \boldsymbol{x} \in \mathbb{R}^n \tag{2-11}$$

2.2.2 Interaction kernels and domains

In (2-8)-(2-7), the two-point vector functions $\boldsymbol{\alpha}(\boldsymbol{x},\boldsymbol{x}')$ and $\boldsymbol{\beta}(\boldsymbol{x},\boldsymbol{x}')$are also known as the interaction kernels. In the context of Peridynamics, these kernels are assumed to have a finite domain that does not map to zero. Given two points $\boldsymbol{x},\boldsymbol{x}' \in \mathbb{R}^n$, and $\delta \in \mathbb{R}^+$. Let $\mathcal{B}_\delta(\boldsymbol{x})$ be a ball or radius δ centered at $\boldsymbol{x}$, then for example, the interaction kernel $\boldsymbol{\alpha}(\boldsymbol{x},\boldsymbol{x}')$ is nonzero only if $\boldsymbol{x}' \in \mathcal{B}_\delta(\boldsymbol{x})$, *i.e.*

$$\boldsymbol{\alpha}(\boldsymbol{x},\boldsymbol{x}') \begin{cases} \neq 0 & \forall\, y \in \mathcal{B}_\delta(\boldsymbol{x}) \\ = 0 & \forall\, y \notin \mathcal{B}_\delta(\boldsymbol{x}) \end{cases} \tag{2-12}$$

where δ is the interaction radius also known as the horizon in the context of PD. Interaction kernels that satisfy (2-12) are called truncated kernels [78] or localized kernels [79]. Another key concept that is connected to the notion of truncated kernels is the interaction domain. Let $\Omega \subset \mathbb{R}^n$ be a bounded open set. The interaction domain Ω_I consist of points outside of Ω that interact with points in Ω. Given the truncated interaction kernel $\boldsymbol{\alpha}(\boldsymbol{x},\boldsymbol{x}')$, an interaction domain Ω_I is defined as

$$\Omega_I = \{\boldsymbol{y} \in \mathbb{R}^n \backslash \Omega : \exists\, \boldsymbol{x} \in \Omega :\ \boldsymbol{\alpha}(\boldsymbol{x},\boldsymbol{x}') \neq 0\} \tag{2-13}$$

The interaction subdomain contains all the points $\boldsymbol{x'}$ in the complement domain $\mathbb{R}^n \backslash \Omega$ that interact with points $\boldsymbol{x}$ in Ω. Many geometrical relationships exist between Ω and Ω_I [42]. A typical such relationship is shown in Figure 2-1.

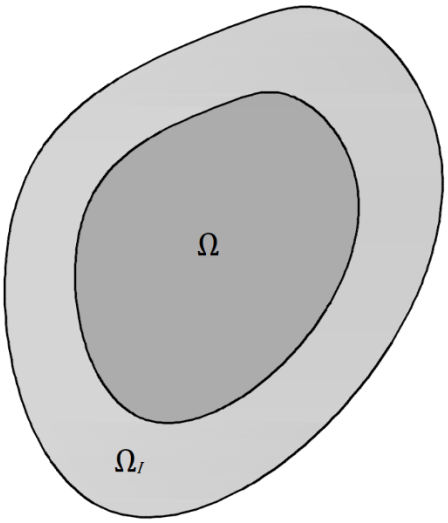

Figure 2-1: Interaction Domain

2.2.3 Nonlocal interaction operators

Given a domain Ω, let Ω_I be the interaction domain associated with Ω as defined in 2.2.2. Corresponding to the nonlocal divergence operator $\mathcal{D}(\boldsymbol{v})(\boldsymbol{x})$, a point interaction operator $\mathcal{N}(\boldsymbol{v})$: $\mathbb{R}^n \times \mathbb{R}^n \longrightarrow \mathbb{R}$ is defined as

$$\mathcal{N}(\boldsymbol{v})(\boldsymbol{x}) \coloneqq -\int_{\Omega \cup \Omega_I} (\boldsymbol{v}(\boldsymbol{x}, \boldsymbol{x'}) + \boldsymbol{v}(\boldsymbol{x'}, \boldsymbol{x}) \cdot \boldsymbol{\alpha}(\boldsymbol{x}, \boldsymbol{x'}) d\boldsymbol{x'} \quad \forall\, \boldsymbol{x} \in \Omega_I \tag{2-14}$$

Corresponding to the nonlocal gradient operator $\mathcal{G}(\eta)(\boldsymbol{x})$, a point interaction operator $\mathcal{S}(\eta)(\boldsymbol{x})$: $\mathbb{R}^n \times \mathbb{R}^n \longrightarrow \mathbb{R}^{m \times k}$ is defined as

$$\mathcal{S}(\eta)(\boldsymbol{x}) \coloneqq -\int_{\Omega \cup \Omega_I} (\eta(\boldsymbol{x}, \boldsymbol{x'}) + \eta(\boldsymbol{x'}, \boldsymbol{x}) \otimes \boldsymbol{\beta}(\boldsymbol{x}, \boldsymbol{x'}) d\boldsymbol{x'} \quad \forall\, \boldsymbol{x} \in \Omega_I \tag{2-15}$$

2.2.4 Nonlocal integral theorem

A very important outcome of the nonlocal operators developed in the proceeding subsections is statement of the nonlocal Gauss theorem. Recall from (2-2) that:

$$\int_{\Omega \cup \Omega_I} \int_{\Omega \cup \Omega_I} (\boldsymbol{v}(\boldsymbol{x}, \boldsymbol{x'}) + \boldsymbol{v}(\boldsymbol{x'}, \boldsymbol{x}) \cdot \boldsymbol{\alpha}(\boldsymbol{x}, \boldsymbol{x'}) d\boldsymbol{x'} d\boldsymbol{x} = \boldsymbol{0}$$

$$\int_{\Omega}\int_{\Omega\cup\Omega_I}\int_{\Omega\cup\Omega_I}(\boldsymbol{v}(\boldsymbol{x},\boldsymbol{x}')+\boldsymbol{v}(\boldsymbol{x}',\boldsymbol{x})\cdot\boldsymbol{\alpha}(\boldsymbol{x},\boldsymbol{x}')d\boldsymbol{x}'d\boldsymbol{x}$$

$$+\int_{\Omega_I}\int_{\Omega\cup\Omega_I}\int_{\Omega\cup\Omega_I}(\boldsymbol{v}(\boldsymbol{x},\boldsymbol{x}')+\boldsymbol{v}(\boldsymbol{x}',\boldsymbol{x})\cdot\boldsymbol{\alpha}(\boldsymbol{x},\boldsymbol{x}')d\boldsymbol{x}'d\boldsymbol{x}\ =\mathbf{0}$$

$$\int_{\Omega}\int_{\mathbb{R}^n}\int_{\Omega\cup\Omega_I}(\boldsymbol{v}(\boldsymbol{x},\boldsymbol{x}')+\boldsymbol{v}(\boldsymbol{x}',\boldsymbol{x})\cdot\boldsymbol{\alpha}(\boldsymbol{x},\boldsymbol{x}')d\boldsymbol{x}'d\boldsymbol{x}$$

$$+\int_{\Omega_I}\int_{\Omega\cup\Omega_I}\int_{\Omega\cup\Omega_I}(\boldsymbol{v}(\boldsymbol{x},\boldsymbol{x}')+\boldsymbol{v}(\boldsymbol{x}',\boldsymbol{x})\cdot\boldsymbol{\alpha}(\boldsymbol{x},\boldsymbol{x}')d\boldsymbol{x}'d\boldsymbol{x}\ =\mathbf{0}$$

$$\int_{\Omega}\mathcal{D}(\boldsymbol{v})(\boldsymbol{x})d\boldsymbol{x}=-\int_{\Omega_I}\int_{\Omega\cup\Omega_I}\int_{\Omega\cup\Omega_I}(\boldsymbol{v}(\boldsymbol{x},\boldsymbol{x}')+\boldsymbol{v}(\boldsymbol{x}',\boldsymbol{x})\cdot\boldsymbol{\alpha}(\boldsymbol{x},\boldsymbol{x}')d\boldsymbol{x}'d\boldsymbol{x} \tag{2-16}$$

$$\int_{\Omega}\mathcal{D}(\boldsymbol{v})(\boldsymbol{x})d\boldsymbol{x}=\int_{\Omega_I}\mathcal{N}(\boldsymbol{v})(\boldsymbol{x})\,d\boldsymbol{x} \tag{2-17}$$

Consider the right-hand side of (2-16). If the kernel function $\boldsymbol{\alpha}(\boldsymbol{x},\boldsymbol{x}')$ is antisymmetric and (2-2) holds, then:

$$-\int_{\Omega_I}\int_{\Omega\cup\Omega_I}(\boldsymbol{v}(\boldsymbol{x},\boldsymbol{x}')+\boldsymbol{v}(\boldsymbol{x}',\boldsymbol{x})\cdot\boldsymbol{\alpha}(\boldsymbol{x},\boldsymbol{x}')d\boldsymbol{x}'\,d\boldsymbol{x}$$

$$=-\int_{\Omega_I}\int_{\Omega}(\boldsymbol{v}(\boldsymbol{x},\boldsymbol{x}')+\boldsymbol{v}(\boldsymbol{x}',\boldsymbol{x})\cdot\boldsymbol{\alpha}(\boldsymbol{x},\boldsymbol{x}')d\boldsymbol{x}'\,d\boldsymbol{x}$$

$$=\int_{\Omega}\int_{\Omega_I}(\boldsymbol{v}(\boldsymbol{x},\boldsymbol{x}')+\boldsymbol{v}(\boldsymbol{x}',\boldsymbol{x})\cdot\boldsymbol{\alpha}(\boldsymbol{x},\boldsymbol{x}')d\boldsymbol{x}'\,d\boldsymbol{x} \tag{2-18}$$

From (2-18) and considering (2-3), it can be deduced that $\int_{\Omega_I}\mathcal{N}(\boldsymbol{v})(\boldsymbol{x})\,d\boldsymbol{x}$ in (2-17) represents the flux from Ω into Ω_I. Thus (2-17) is the mathematical statement of the nonlocal Gauss theorem which postulate that the integral of the nonlocal divergence of $\boldsymbol{v}$ over Ω is equal to the total flux exiting Ω into Ω_I.

We next consider the nonlocal analogue of integration by parts expressions involving the nonlocal divergence and gradient operators. Given the point functions $u(\boldsymbol{x})\colon\mathbb{R}^n\longrightarrow\mathbb{R}$ and $\boldsymbol{v}(\boldsymbol{x})\colon\mathbb{R}^n\longrightarrow\mathbb{R}^m$

$$\int_{\Omega} u\mathcal{D}(\boldsymbol{v})d\boldsymbol{x} - \int_{\Omega\cup\Omega_I}\int_{\Omega\cup\Omega_I} \mathcal{D}^*(u)\cdot \boldsymbol{v}d\boldsymbol{x}'\,d\boldsymbol{x} = \int_{\Omega_I} u\mathcal{N}(\boldsymbol{v})\,d\boldsymbol{x} \tag{2-19}$$

$$\int_{\Omega} \boldsymbol{v}\cdot \mathcal{G}(u)d\boldsymbol{x} - \int_{\Omega\cup\Omega_I}\int_{\Omega\cup\Omega_I} \mathcal{G}^*(\boldsymbol{v})ud\boldsymbol{x}'\,d\boldsymbol{x} = \int_{\Omega_I} \boldsymbol{v}\cdot \mathcal{S}(u)d\boldsymbol{x} \tag{2-20}$$

2.2.5 Nonlocal weighted operators

Because the classical continuum theory is a local theory, the functions utilised are point functions. This is not the case with peridynamics which is a nonlocal theory, hence some of the function utilised are point functions while some are two-point functions. The differential operators defined in 2.2.1 are operators that act on two-point functions. To complete the definition of the nonlocal operators, another class of operators that act on point functions need to be defined.

Given the point function $\boldsymbol{u}:\mathbb{R}^n \longrightarrow \mathbb{R}^k$ and the point function $v:\mathbb{R}^n \longrightarrow \mathbb{R}$. Let $\omega(\boldsymbol{x},\boldsymbol{x}')\colon \mathbb{R}^n\times\mathbb{R}^n \longrightarrow \mathbb{R}^+$ and let the operators $\mathcal{D}$ and $\mathcal{G}$ be as defined in 2.2.1, then the weighted nonlocal divergence operator acting on $\boldsymbol{u}$ is defined as

$$\mathcal{D}_{\omega}(\boldsymbol{u})(\boldsymbol{x}) \coloneqq \mathcal{D}\big(\omega(\boldsymbol{x},\boldsymbol{x}')\boldsymbol{u}(\boldsymbol{x})\big) \qquad \forall \boldsymbol{x}\in\mathbb{R}^n \tag{2-21}$$

The weighted nonlocal gradient operator acting on v is defined as:

$$\mathcal{G}_{\omega}(v)(\boldsymbol{x}) \coloneqq \mathcal{G}\big(\omega(\boldsymbol{x},\boldsymbol{x}')v(\boldsymbol{x})\big) \qquad \forall \boldsymbol{x}\in\mathbb{R}^n \tag{2-22}$$

The extended application of the weighted nonlocal divergence and gradient operators on tensor and vector fields respectively follows as in (2-8) and (2-10). Also, as is with the unweighted nonlocal operators, adjoint operators can also be defined for the weighted nonlocal operators. Let $\mathcal{D}^*$ and $\mathcal{G}^*$ be as defined in 2.2.1 and $\omega\colon \mathbb{R}^n\times\mathbb{R}^n \longrightarrow \mathbb{R}$ be a non-negative symmetric function known as the weight function, then the action of the adjoint operator $\mathcal{D}^*_{\omega}$ corresponding to the nonlocal weighted divergence operator on v is defined as

$$\mathcal{D}^*_{\omega}(v)(\boldsymbol{x}) \coloneqq \int_{\mathbb{R}} \mathcal{D}^*(v)(\boldsymbol{x},\boldsymbol{y})\omega(\boldsymbol{x},\boldsymbol{y})d\boldsymbol{x}' \qquad \forall \boldsymbol{x}\in\mathbb{R}^n \tag{2-23}$$

The action of the adjoint operator $\mathcal{G}^*$ corresponding to the nonlocal weighted gradient operator $\mathcal{G}^*_{\omega}$ on $\boldsymbol{v}$ is defined as

$$\mathcal{G}_{\omega}^{*}(\boldsymbol{v})(\boldsymbol{x}) \coloneqq \int_{\mathbb{R}} \mathcal{G}^{*}\boldsymbol{v}(\boldsymbol{x},\boldsymbol{x}')\omega(\boldsymbol{x},\boldsymbol{y})d\boldsymbol{x}' \qquad \forall \boldsymbol{x} \in \mathbb{R}^{n} \tag{2-24}$$

The relationship established between $\mathcal{D}$ and $-\mathcal{G}^{*}$ and between $\mathcal{G}$ and $-\mathcal{D}^{*}$ allows us to respectively write (2-21) and (2-22) as

$$\mathcal{D}_{\omega}(\boldsymbol{u})(\boldsymbol{x}) = -\mathcal{G}_{\omega}^{*}\big(\boldsymbol{u}(\boldsymbol{x})\big) \qquad \forall \boldsymbol{x} \in \mathbb{R}^{n} \tag{2-25}$$

and

$$\mathcal{G}_{\omega}(v)(\boldsymbol{x}) = -\mathcal{D}_{\omega}^{*}\big(v(\boldsymbol{x})\big) \qquad \forall \boldsymbol{x} \in \mathbb{R}^{n} \tag{2-26}$$

Equations (2-25) and (2-26) serves to define two forms to each of the weighted nonlocal divergence and gradient operators, respectively and have been shown to be equal [42]. For example, from (2-25), the first form of the weighted nonlocal divergence is given by:

$$\mathcal{D}_{\omega}(\boldsymbol{u})(\boldsymbol{x}) = \int_{\mathbb{R}^{n}} \omega(\boldsymbol{x},\boldsymbol{y})\big(\boldsymbol{u}(\boldsymbol{x}') - \boldsymbol{u}(\boldsymbol{x})\big) \cdot \boldsymbol{\alpha}(\boldsymbol{x},\boldsymbol{x}') \qquad \forall \boldsymbol{x} \in \mathbb{R}^{n} \tag{2-27}$$

and the second form is given by:

$$\mathcal{D}_{\omega}(\boldsymbol{u})(\boldsymbol{x}) = \int_{\mathbb{R}^{n}} \omega(\boldsymbol{x},\boldsymbol{y})\big(\boldsymbol{u}(\boldsymbol{x}) + \boldsymbol{u}(\boldsymbol{x}')\big) \cdot \boldsymbol{\alpha}(\boldsymbol{x},\boldsymbol{x}')d\boldsymbol{x}' \qquad \forall \boldsymbol{x} \in \mathbb{R}^{n} \tag{2-28}$$

2.2.6 Nonlocal differential operators for peridynamic application

Often, the governing equations in the classical continuum theory are expression of physical balance laws that are composed of partial differential operators. Although the peridynamic theory as a nonlocal model, replaces the spatial derivatives with integral operators, it can be shown to have retained the structure of the balance law in the classical theory. This is achieved by introducing nonlocal analogues of the differential operators used in the local theory. The nonlocal operators presented in section 2.2 will be used to derive application specific nonlocal differential operators and the generalised notion of nonlocal derivative for application in peridynamics. Let $\omega\colon \mathbb{R}^{n} \times \mathbb{R}^{n} \longrightarrow \mathbb{R}$ be a non-negative weight function of compact support in $\mathcal{B}_{\delta}(\boldsymbol{x}) \subset \mathbb{R}^{n}$ where $\mathcal{B}_{\delta}(\boldsymbol{x})$ is a ball of radius $\delta > 0$ centered at $\boldsymbol{x}$. Let a shape tensor [80] $\mathbf{K}\colon \mathbb{R}^{n} \times \mathbb{R}^{n} \longrightarrow \mathbb{R}^{n\times n}$ be defined as

$$\mathbf{K} = \int_{\mathcal{B}_{\delta}(\boldsymbol{x})} \omega(|\boldsymbol{\xi}_{\boldsymbol{x}\boldsymbol{x}'}|)\boldsymbol{\xi}_{\boldsymbol{x}\boldsymbol{x}'} \otimes \boldsymbol{\xi}_{\boldsymbol{x}\boldsymbol{x}'} dV_{\boldsymbol{x}'} \tag{2-29}$$

Where $\boldsymbol{\xi_{xx'} = x' - x}$ and $\boldsymbol{x' \in \mathcal{H}_x = \{y \in \mathbb{R}^n : |x' - x| \leq \delta\}}$. Let $\boldsymbol{\alpha(x, x') = \beta(x, x') = \xi_{xx'} \mathbf{K}^{-1}}$, then the nonlocal unweighted and weighted divergence and gradient operators from (2-4), (2-6), (2-25)and (2-26) are respectively given as

$$\mathcal{D}(\boldsymbol{v})(\boldsymbol{x}) \coloneqq \left[\int_{\mathbb{R}^n} \left(\big(\boldsymbol{v}(\boldsymbol{x}, \boldsymbol{x}') + \boldsymbol{v}(\boldsymbol{x}', \boldsymbol{x})\big) \cdot \boldsymbol{\xi}_{xx'}\right) d\boldsymbol{x}'\right] \mathbf{K}^{-1} \quad \forall\, \boldsymbol{x} \in \mathbb{R}^n \tag{2-30}$$

$$\mathcal{G}(\eta)(\boldsymbol{x}) \coloneqq \left[\int_{\mathbb{R}^n} \big(\eta(\boldsymbol{x}, \boldsymbol{x}') + \eta(\boldsymbol{x}', \boldsymbol{x})\big)\boldsymbol{\xi}_{xx'} d\boldsymbol{x}'\right] \mathbf{K}^{-1} \quad \forall\, \boldsymbol{x} \in \mathbb{R}^n \tag{2-31}$$

$$\mathcal{D}_\omega(\boldsymbol{u})(\boldsymbol{x}) = \left[\int_{\mathbb{R}^n} \omega(\boldsymbol{x}, \boldsymbol{x}')\big(\boldsymbol{u}(\boldsymbol{x}') - \boldsymbol{u}(\boldsymbol{x})\big) \cdot \boldsymbol{\xi}_{xx'} d\boldsymbol{x}'\right] \mathbf{K}^{-1} \quad \forall \boldsymbol{x} \in \mathbb{R}^n \tag{2-32}$$

$$\mathcal{G}_\omega(v)(\boldsymbol{x}) = \left[\int_{\mathbb{R}^n} \omega(\boldsymbol{x}, \boldsymbol{x}')\big(v(\boldsymbol{x}') - v(\boldsymbol{x})\big)\boldsymbol{\xi}_{xx'} d\boldsymbol{x}'\right] \mathbf{K}^{-1} \quad \forall \boldsymbol{x} \in \mathbb{R}^n \tag{2-33}$$

Where (2-32) and (2-33) appeared in [81] defined as the notions of nonlocal material divergence and gradient operators respectively. From (2-28), the second form of the weighted nonlocal divergence operator is:

$$\mathcal{D}_\omega(\boldsymbol{u})(\boldsymbol{x}) = \left[\int_{\mathbb{R}^n} \omega(\boldsymbol{x}, \boldsymbol{x}')\big(\boldsymbol{u}(\boldsymbol{x}') + \boldsymbol{u}(\boldsymbol{x})\big) \cdot \boldsymbol{\xi}_{xx'} d\boldsymbol{x}'\right] \mathbf{K}^{-1} \quad \forall \boldsymbol{x} \in \mathbb{R}^n \tag{2-34}$$

2.3 Peridynamic theory

Before proceeding to develop the governing equation of the peridynamic theory, some important concepts in peridynamic theory would be presented.

2.3.1 Important concepts

Given a bounded open domain $\Omega \in \mathbb{R}^n$, in Peridynamics, a continuum point $\boldsymbol{x} \in \Omega$ interacts with infinitely many other points located within its domain of influence. If this domain of influence is assumed to be a ball $\mathcal{B}_\delta(\boldsymbol{x})$ of radius $\delta > 0$ centered at $\boldsymbol{x}$, then δ is called the horizon of $\boldsymbol{x}$, such that:

$$\mathcal{B}_\delta(\boldsymbol{x}) = \{\boldsymbol{x}' \in \mathcal{R}: |\boldsymbol{x}' - \boldsymbol{x}| < \delta\} \tag{2-35}$$

Where $\mathcal{B}_\delta(\boldsymbol{x})$ is called the family of $\boldsymbol{x}$. Interaction between two points $\boldsymbol{x}$ and $\boldsymbol{x}'$ is called a *bond* and the distance $\boldsymbol{\xi} = \boldsymbol{x}' - \boldsymbol{x}$ in the undeformed reference configuration is called the *bond length*. The relative displacement vector $\boldsymbol{\eta}$ in the deformed configuration is given by:

$$\boldsymbol{\eta} = \boldsymbol{u}(\boldsymbol{x}', t) - \boldsymbol{u}(\boldsymbol{x}, t) \tag{2-36}$$

where $\boldsymbol{u}(\boldsymbol{x}', t)$ and $\boldsymbol{u}(\boldsymbol{x}, t)$ are respectively, the displacement vectors of points $\boldsymbol{x}$ and $\boldsymbol{x}'$, and the magnitude $\eta = |\boldsymbol{\eta}|$ is designated as the *bond elongation*. A scalar-valued function s designated as *bond-stretch* is defined as:

$$s = \frac{|\boldsymbol{\xi} + \boldsymbol{\eta}| - |\boldsymbol{\xi}|}{|\boldsymbol{\xi}|} \tag{2-37}$$

which in more explicit form can be written as

$$s = \frac{\left((\boldsymbol{\xi} + \boldsymbol{\eta}) \cdot (\boldsymbol{\xi} + \boldsymbol{\eta})\right)^{1/2} - (\boldsymbol{\xi} \cdot \boldsymbol{\xi})^{1/2}}{(\boldsymbol{\xi} \cdot \boldsymbol{\xi})^{1/2}} \tag{2-38}$$

A *deformed bond direction vector* $\mathbf{M}$ is a vector-valued function that is defined through the relationship:

$$\mathbf{M}(\boldsymbol{\xi}, t) = \frac{\boldsymbol{y}(\boldsymbol{x}', t) - \boldsymbol{y}(\boldsymbol{x}, t)}{|\boldsymbol{y}(\boldsymbol{x}', t) - \boldsymbol{y}(\boldsymbol{x}, t)|} \tag{2-39}$$

$\mathbf{M}(\boldsymbol{\xi}, t)$ is a unit vector that point from the position of $\boldsymbol{x}$ towards the position of $\boldsymbol{x}'$ in the deformed configuration.

2.3.2 Governing equation of motion in Peridynamics

Computational simulation in the peridynamic framework is governed by a statement of nonlocal balance law which postulates the dependence of the rate of change in the content of an extensive quantity over a given domain on the rate at which the quantity is produced within the domain and a flux through the boundary of the domain. Consider a deformable body $\mathcal{B}$ occupying the open domain $\Omega \subseteq \mathbb{R}^n$. Let $\widetilde{\Omega} \subseteq \Omega$ be an open subregion, then a quantitative statement of a balance law for Ω can be stated as

$$\mathcal{A}(\widetilde{\Omega}, \boldsymbol{q}) = \mathcal{P}(\widetilde{\Omega}) - \mathcal{F}(\widetilde{\Omega}, \mathbb{R}^n \backslash \widetilde{\Omega}; \boldsymbol{q}) \tag{2-40}$$

Where (2-40) postulate that $\mathcal{A}(\widetilde{\Omega}, \boldsymbol{q})$ (the time rate of change of the intensive quantity $\boldsymbol{q}$) is equal to $\mathcal{P}(\widetilde{\Omega})$ (the rate at which the quantity is produced within the subdomain by sources, minus $\mathcal{F}(\widetilde{\Omega}, \mathbb{R}^n \backslash \widetilde{\Omega}; \boldsymbol{q})$ (the rate at which the intensive quantity exit the subdomain). Let the quantity $(\boldsymbol{q})$

to be balanced be the momentum density so that $\boldsymbol{q} = \rho\dot{\boldsymbol{u}}$ where $\dot{\boldsymbol{u}}$ is the velocity of a point in $\widetilde{\Omega}$ and ρ is the density of the material. Let $\boldsymbol{b}$ denote the rate of production of $\boldsymbol{q}$ in $\widetilde{\Omega}$, then:

$$\mathcal{A}(\widetilde{\Omega}, \boldsymbol{q}) = \frac{\partial}{\partial t}\int_{\widetilde{\Omega}} \boldsymbol{q}(\boldsymbol{x}, t)\, d\boldsymbol{x} = \rho \int_{\widetilde{\Omega}} \frac{\partial^2 \boldsymbol{u}}{\partial t^2} d\boldsymbol{x} \quad \text{and} \quad \mathcal{P}(\widetilde{\Omega}) = \int_{\widetilde{\Omega}} \boldsymbol{b}(\boldsymbol{x}, t) d\boldsymbol{x} \tag{2-41}$$

To obtain an expression for the rate at which the flux of $\boldsymbol{q}$ exits the subdomain $\widetilde{\Omega}$, let $\widetilde{\Omega}_I \subset \Omega$ be the domain interacting with $\widetilde{\Omega}$ as defined in (2-13), then:

$$\mathcal{F}(\widetilde{\Omega}, \widetilde{\Omega}_I; \boldsymbol{q}) = \int_{\Omega_I} \mathcal{N}_\omega(\boldsymbol{\Psi})(\boldsymbol{x})\, d\boldsymbol{x} \tag{2-42}$$

Applying the nonlocal Gauss theorem (2-17), then (2-42) can be written as

$$\mathcal{F}(\widetilde{\Omega}, \widetilde{\Omega}_I; \boldsymbol{q}) = \int_{\Omega} \mathcal{D}_\omega(\boldsymbol{\Psi})(\boldsymbol{x}) d\boldsymbol{x} \tag{2-43}$$

Thus (2-40) becomes:

$$\rho \int_{\widetilde{\Omega}} \frac{\partial^2 \boldsymbol{u}}{\partial t^2} d\boldsymbol{x} = -\int_{\Omega} \mathcal{D}_\omega(\boldsymbol{\Psi})(\boldsymbol{x}) d\boldsymbol{x} + \int_{\widetilde{\Omega}} \boldsymbol{b}(\boldsymbol{x}, t) d\boldsymbol{x} \tag{2-44}$$

which owing to the arbitrariness of $\tilde{\Omega}$, (2-44) localizes to the field equation:

$$\rho \frac{\partial^2 \boldsymbol{u}}{\partial t^2} = -\mathcal{D}_\omega(\boldsymbol{\Psi})(\boldsymbol{x}) + \boldsymbol{b}(\boldsymbol{x}, t) \tag{2-45}$$

From (2-34), (2-45) can be written as

$$\begin{aligned} \rho \frac{\partial^2 \boldsymbol{u}}{\partial t^2} &= -\left[\int_{\mathbb{R}^n} \omega(\boldsymbol{x}, \boldsymbol{y})(\boldsymbol{\Psi}(\boldsymbol{x}') + \boldsymbol{\Psi}(\boldsymbol{x}) \cdot \boldsymbol{\xi}_{\boldsymbol{x}\boldsymbol{x}'}) d\boldsymbol{x}'\right] \mathbf{K}^{-1} + \boldsymbol{b}(\boldsymbol{x}, t) \\ &= \int_{\boldsymbol{\Omega}_\mathbf{s} \cup \boldsymbol{\Omega}_I} \omega(\boldsymbol{x}, \boldsymbol{y})(\boldsymbol{\Psi}(\boldsymbol{x}')\mathbf{K}^{-1} \cdot \boldsymbol{\xi}_{\boldsymbol{x}'\boldsymbol{x}} - \boldsymbol{\Psi}(\boldsymbol{x})\mathbf{K}^{-1} \cdot \boldsymbol{\xi}_{\boldsymbol{x}\boldsymbol{x}'})\, d\boldsymbol{x}' + \boldsymbol{b}(\boldsymbol{x}, t) \end{aligned} \tag{2-46}$$

Where (2-46) follows from the antisymmetric property of $\boldsymbol{\xi}$. By writing

$$\mathbf{t} = \omega(\boldsymbol{x}, \boldsymbol{y})\boldsymbol{\Psi}\mathbf{K}^{-1}\boldsymbol{\xi} \tag{2-47}$$

and since $\boldsymbol{\alpha}(\boldsymbol{x}, \boldsymbol{x}') = 0$ whenever $\boldsymbol{x}' \notin \mathcal{B}_\delta(\boldsymbol{x})$, then (2-46) can be written as

$$\rho \frac{\partial^2 \boldsymbol{u}}{\partial t^2} = \int_{\mathcal{B}_\delta(\boldsymbol{x})} \big(\mathbf{t}(\boldsymbol{x}' - \boldsymbol{x}) - \mathbf{t}(\boldsymbol{x} - \boldsymbol{x}')\big)\, d\boldsymbol{x}' + \boldsymbol{b}(\boldsymbol{x}, t) \tag{2-48}$$

Equation (2-48) is the general statement of peridynamic equation of motion, where $\mathbf{t}(\boldsymbol{x}' - \boldsymbol{x})$ and $\mathbf{t}(\boldsymbol{x} - \boldsymbol{x}')$ are the force density functions at $\boldsymbol{x}$ and $\boldsymbol{x}'$ respectively. Sometimes (2-48) is written in a more simplified way as:

$$\rho\ddot{\boldsymbol{u}}(\boldsymbol{x}, t) = \int_{\mathcal{B}_\delta(\boldsymbol{x})} \mathbf{f}(\boldsymbol{x}, \boldsymbol{x}', t)\, d\boldsymbol{x}' + \boldsymbol{b}(\boldsymbol{x}, t) \qquad \forall \boldsymbol{x} \in \mathcal{B} \tag{2-49}$$

Such that

$$\mathbf{f}(\boldsymbol{x}, \boldsymbol{x}', t) = \mathbf{t}(\boldsymbol{x}' - \boldsymbol{x}) - \mathbf{t}(\boldsymbol{x} - \boldsymbol{x}') \tag{2-50}$$

is a vector valued pairwise force density function that represents the force density that the material located at $\boldsymbol{x}'$ exerts on $\boldsymbol{x}$. The determination of the pairwise force density $\mathbf{f}(\boldsymbol{x}, \boldsymbol{x}', t)$ will require a material constitutive model $\widehat{\mathbf{T}}$ which is typically an expression showing the dependence of the force density at a point on relevant physical quantities at the point such as the deformation $\boldsymbol{y}$, the rate of deformation $\dot{\boldsymbol{y}}$, temperature T and damage $\mathcal{D}$ amongst others. The general form is given by:

$$\mathbf{t} = \widehat{\mathbf{T}}(\boldsymbol{y}, \dot{\boldsymbol{y}}, T, \mathcal{D}, \dots) \tag{2-51}$$

The specific arguments that go into (2-51) depends on the material response anticipated such as elastic, thermoelastic, viscoelastic, and plastic response. On the other hand, the functional form of (2-51) depends on the assumption made about the mechanism of bond deformation. This gives rise to two broad categories of peridynamic models; bond-based [10] and state-based [80] models.

2.3.3 Bond-based peridynamic model

The bond-based peridynamic (BBPD) model assumes that each bond in a material has its own constitutive relationship, which is independent of other bonds, and is defined such that.:

$$\mathbf{t} = \widehat{\mathbf{T}}(\boldsymbol{y}, \boldsymbol{\xi}) \tag{2-52}$$

2.3.3.1 Linear microelastic model

The *linear microelastic model* is the simplest model in BBPD. This model approximates the behaviour of a material by modelling it as a network of an infinite number of springs which respond to change in the state of the material in a linear manner. The linear microelastic material model is developed by selecting the tensor quantity $\boldsymbol{\Psi}$ in (2-47) such that the pairwise force function in (2-50) takes the form [82, 83]:

$$\mathbf{f} = \mathrm{f}(s)\mathbf{M}(\boldsymbol{\xi}, t), \tag{2-53}$$

where $\mathbf{f}$ is a scalar-valued function called the *scalar bond force* [50] and is given by

$$\mathrm{f}(s) = c(\boldsymbol{\xi})s(\boldsymbol{\xi}, t) \tag{2-54}$$

In (2-54), $c(\boldsymbol{\xi})$ is a function that is characteristic of the material and is called the *bond elastic stiffness constant* or *bond constant* for short. Notice that the pairwise force function $\mathbf{f}(\boldsymbol{x}, \boldsymbol{x}', t)$ in (2-53) is defined only by the reference and deformed positions of the interacting particles $\boldsymbol{x}$ and $\boldsymbol{x}'$ and is aligned with the deformed bond between them, with the force density $\mathbf{t}(\boldsymbol{x}' - \boldsymbol{x})$ at $\boldsymbol{x}$ being equal but opposite to the force density $\mathbf{t}(\boldsymbol{x} - \boldsymbol{x}')$ at $\boldsymbol{x}'$. For a microelastic (the PD equivalent of an elastic material in CCM), the pairwise force function $\mathbf{f}(\boldsymbol{x}, \boldsymbol{x}', t)$ between any two particles $\boldsymbol{x}$ and $\boldsymbol{x}'$ is conservative, *i.e.*, there exist a scalar-valued microelastic potential w defined such that the scalar bond force $f(s)$ is expressed as:

$$f(s) = \frac{\partial w}{\partial \eta}(s) = \frac{1}{\xi}\frac{\partial w}{\partial s}(s) \qquad \forall \xi, \eta \tag{2-55}$$

The micropotential (w) is the energy in a single bond and represents a local strain energy density [82] which from (2-55), considering (2-54), is given as:

$$w(\boldsymbol{\xi}, t) = \frac{c(\boldsymbol{\xi})s^2\xi}{2} \tag{2-56}$$

The total strain energy at a point $\boldsymbol{x}$ is therefore the sum of the microelastic potential contribution from all bonds in $\mathcal{H}_{\boldsymbol{x}}$ and is expressed as

$$W(\boldsymbol{x}, t) = \frac{1}{2}\int_{\mathcal{H}_{\boldsymbol{x}}} w(\boldsymbol{\xi}, t)d\boldsymbol{\xi} \tag{2-57}$$

Since the strain energy in both Peridynamic (PD) and Classical Continuum Mechanics (CCM) is the work done by external forces on the material, equation (2-57) in PD represents the same quantity as in CCM and offers a straightforward way of calibrating the function $c(\boldsymbol{\xi})$. By equating (2-57) with the strain energy expression from CCM, the expression for the bond constant for microelastic materials can be determined.

2.3.3.1.1 Bond constant in one-dimension

Let δ be the horizon that is characteristic of the material, then using (2-56) in (2-57) and assuming a one-dimensional problem:

$$W = \frac{A}{4}\int_{-\delta}^{\delta} c(|\xi|)s^2|\xi|d\xi \tag{2-58}$$

If we assume $c(|\xi|)$ to be independent of bond length i.e.,

$$c(\boldsymbol{\xi}) = c_0 \tag{2-59}$$

then (2-58) becomes.

$$W = \frac{A}{4}\int_{-\delta}^{\delta} c_0 s^2 |\xi| d\xi = \frac{A c_0 s^2 \delta^2}{4} \tag{2-60}$$

the strain energy density (W) from classical continuum theory is:

$$W = \frac{E s^2}{2} \tag{2-61}$$

Equating (2-60) and (2-61) yields

$$c_0 = \frac{2E}{A\delta^2} \tag{2-62}$$

In the case where $c(|\xi|)$ is dependent on the bond length and assumed to have a triangular profile, i.e.,

$$c(\boldsymbol{\xi}) = c_1\left(1 - \frac{\xi}{\delta}\right) \tag{2-63}$$

Then (2-58) becomes:

$$W = \frac{1}{4}\int_{-\delta}^{\delta} c_1\left(1 - \frac{|\xi|}{\delta}\right) s^2 |\xi| d\xi = \frac{A c_1 s^2 \delta^2}{12} \tag{2-64}$$

Equating (2-64) with (2-61) gives:

$$c_1 = \frac{6E}{A\delta^2} \tag{2-65}$$

In the case where the dependency of $c(|\xi|)$ result in an inverted triangular profile [84], in which case, bonds closer to the principal point are softer than bonds further away from it, such that,

$$c(\boldsymbol{\xi}) = c_2\left(\frac{\xi}{\delta}\right) \tag{2-66}$$

for bonds within the horizon. In this case, (2-58) becomes:

$$W = \frac{A}{4}\int_{-\delta}^{\delta} c_2\left(\frac{|\xi|}{\delta}\right) s^2 |\xi| d\xi = \frac{A c_2 s^2 \delta^2}{6} \tag{2-67}$$

Also, equating (2-67) with (2-61) gives:

$$c_2 = \frac{3E}{A\delta^2} \tag{2-68}$$

2.3.3.1.2 Bond constant in two-dimension

In the two-dimensional case, let δ be the radius of sphere $\mathcal{H}$ describing the horizon. Then the two-dimensional equivalence of the bond constants (2-62), (2-65), and (2-68) are respectively given as

$$c_0 = \frac{9E}{\pi\delta^3 h}, \quad c_1 = \frac{36E}{\pi\delta^3 h}\left(1 - \frac{\xi}{\delta}\right), \quad c_2 = \frac{8E}{\pi\delta^4 h}\xi \tag{2-69}$$

where δ is the horizon, h is the out of plane thickness, E is the elastic modulus, and A is the cross-sectional area.

2.3.3.2 Prototype microelastic brittle material

If the microelastic material model described by (2-52)-(2-54) considering $c(\boldsymbol{\xi}) = c_0$ is modified to include a time-dependent damage criteria $\mu(\boldsymbol{\xi}, t)$ such that

$$\mathbf{f}(\boldsymbol{x}, \boldsymbol{x}', t) = f(s)\,\underline{\mathbf{M}}\langle\boldsymbol{\xi}\rangle\mu(\boldsymbol{\xi}, t) \tag{2-70}$$

then the linear microelastic material is designated as the *prototype microelastic brittle* (PMB) material. The function $\mu(\boldsymbol{\xi}, t)$ takes values between 0 and 1, with 1 representing the pristine undamaged state and 0 representing the completely damaged state. As the material undergoes loading, the function $\mu(\boldsymbol{\xi}, t)$ changes from 1 to 0 according to a prescribed damage law, indicating the progression of damage or failure in the material. A simple damage law that has been used extensively in the PD research community is the one that prescribes a critical bond stretch threshold s_0 beyond which a bond is deemed to have been broken. The functional form of $\mu(\boldsymbol{\xi}, t)$ then takes the form:

$$\mu(\boldsymbol{\xi}, t) = 1 - H(t - t_{break}) \tag{2-71}$$

where H is the Heaviside step function and t_{break} is the time at which $s(\xi, t) \geq s_0$. The critical bond stretch s_0 is a material property and can be calibrated to ensure that the energy released during fracture or damage matches the known critical energy release rate for the material [82, 83, 85].

2.3.3.3 Linearized Bond-Based Peridynamic Model

With the definition of s in (2-38), the pairwise force function $\mathbf{f}(\boldsymbol{\eta}, \boldsymbol{\xi})$ in (2-53) or (2-70) is a nonlinear function of $\boldsymbol{\eta}$. To linearize $\mathbf{f}(\boldsymbol{\eta}, \boldsymbol{\xi})$ in $\boldsymbol{\eta}$, the small perturbation hypothesis is invoked

which has as one of its implications that $\eta \ll 1$. A first order Taylor series expansion of $\mathbf{f}(\boldsymbol{\eta}, \boldsymbol{\xi})$ say in (2-53) around $\boldsymbol{\eta} = \mathbf{0}$ yields:

$$\mathbf{f}(\boldsymbol{\eta}, \boldsymbol{\xi}) = \mathbf{f}(\mathbf{0}, \boldsymbol{\xi}) + \nabla_{\boldsymbol{\eta}} \mathbf{f}(\mathbf{0}, \boldsymbol{\xi}) \cdot \boldsymbol{\eta} \tag{2-72}$$

where $\nabla_{\boldsymbol{\eta}}$ denotes the gradient operator with respect to $\boldsymbol{\eta}$. If the internal force in the bond in the undeformed configuration is assumed to be zero, then the first term in (2-72) vanishes, and (2-72) reduces to:

$$\mathbf{f}(\boldsymbol{\eta}, \boldsymbol{\xi}) = \nabla_{\boldsymbol{\eta}} \mathbf{f}(\mathbf{0}, \boldsymbol{\xi}) \cdot \boldsymbol{\eta} \tag{2-73}$$

Introducing (2-53) into (2-73) and noting the explicit expressions for s and $\mathbf{M}$ in (2-37) and (2-39) respectively yields

$$\mathbf{f}(\boldsymbol{\eta}, \boldsymbol{\xi}) = \nabla_{\boldsymbol{\eta}} \left(c(\boldsymbol{\xi}) \left(\frac{|\boldsymbol{\xi} + \boldsymbol{\eta}| - |\boldsymbol{\xi}|}{|\boldsymbol{\xi}|} \right) \left(\frac{\boldsymbol{\xi} + \boldsymbol{\eta}}{|\boldsymbol{\xi} + \boldsymbol{\eta}|} \right) \right) \Bigg|_{\boldsymbol{\eta}=\mathbf{0}} \boldsymbol{\eta}$$

$$= c(\boldsymbol{\xi}) \nabla_{\boldsymbol{\eta}} \left(\left(\frac{1}{|\boldsymbol{\xi}|} - \frac{1}{|\boldsymbol{\xi} + \boldsymbol{\eta}|} \right) (\boldsymbol{\xi} + \boldsymbol{\eta}) \right) \Bigg|_{\boldsymbol{\eta}=\mathbf{0}} \boldsymbol{\eta}$$

$$= c(\boldsymbol{\xi}) \left(\nabla_{\boldsymbol{\eta}} \left(\frac{1}{|\boldsymbol{\xi}|} - \frac{1}{|\boldsymbol{\xi} + \boldsymbol{\eta}|} \right) \otimes (\boldsymbol{\xi} + \boldsymbol{\eta}) + \left(\left(\frac{1}{|\boldsymbol{\xi}|} - \frac{1}{|\boldsymbol{\xi} + \boldsymbol{\eta}|} \right) \nabla_{\boldsymbol{\eta}} (\boldsymbol{\xi} + \boldsymbol{\eta}) \right) \right) \Bigg|_{\boldsymbol{\eta}=\mathbf{0}} \boldsymbol{\eta}$$

$$= c(\boldsymbol{\xi}) \frac{(\boldsymbol{\xi} \otimes \boldsymbol{\xi})}{|\boldsymbol{\xi}|^3} \boldsymbol{\eta} \qquad \forall \boldsymbol{\xi}, \boldsymbol{\eta} \tag{2-74}$$

Equation (2-74) can be written as

$$\mathbf{f}(\boldsymbol{\eta}, \boldsymbol{\xi}) = \boldsymbol{C}(\boldsymbol{\xi}) \boldsymbol{\eta} \qquad \forall \boldsymbol{\xi}, \boldsymbol{\eta} \tag{2-75}$$

where

$$\boldsymbol{C}(\boldsymbol{\xi}) \boldsymbol{\eta} = c(\boldsymbol{\xi}) \frac{(\boldsymbol{\xi} \otimes \boldsymbol{\xi})}{|\boldsymbol{\xi}|^3} \qquad \forall \boldsymbol{\xi} \tag{2-76}$$

is a tensor valued function called the *micromodulus*. Notice that the pairwise function in (2-75) is now a linear function of the relative displacement. The micromodulus functions corresponding to the bond constants derived above for 1D and 2D are provided in Table 2-1. Substituting (2-75) into (2-49), yields:

$$\rho(\boldsymbol{x}) \ddot{\boldsymbol{u}}(\boldsymbol{x}, t) = \int_{\mathcal{H}_{\boldsymbol{x}}} \boldsymbol{C}(\boldsymbol{x}' - \boldsymbol{x}) \big(\boldsymbol{u}(\boldsymbol{x}', t) - \boldsymbol{u}(\boldsymbol{x}, t) \big) dV_{\boldsymbol{x}'} + b(\boldsymbol{x}, t) \tag{2-77}$$

Equation (2-77) is the linearized bond-based peridynamic equation of motion.

Table 2-1: Micromodulus functions with their corresponding bond force constants

	Bond Constant $c(\boldsymbol{\xi})$	Micromodulus function $\boldsymbol{C}(\boldsymbol{\xi})$
1D	$\frac{2E}{A\delta^2}$	$\frac{2E}{A\delta^2\lvert\xi\rvert}$
	$\frac{6E}{A\delta^2}$	$\frac{6E}{A\delta^2\lvert\xi\rvert}\left(1-\frac{\lvert\xi\rvert}{\delta}\right)$
	$\frac{3E}{A\delta^2}$	$\frac{3E}{A\delta^3}$
2D	$\frac{9E}{\pi\delta^3 h}$	$\frac{9E}{\pi\delta^3 h\lvert\xi\rvert^3}\begin{bmatrix}\xi_x^2 & \xi_x\xi_y\\ \xi_x\xi_y & \xi_y^2\end{bmatrix}$
	$\frac{36E}{\pi\delta^3 h}\left(1-\frac{\xi}{\delta}\right)$	$\frac{36E}{\pi\delta^3 h\lvert\xi\rvert^3}\left(1-\frac{\lvert\xi\rvert}{\delta}\right)\begin{bmatrix}\xi_x^2 & \xi_x\xi_y\\ \xi_x\xi_y & \xi_y^2\end{bmatrix}$
	$\frac{8E}{\pi\delta^4 h}\xi$	$\frac{8E}{\pi\delta^4 h\lvert\xi\rvert^2}\begin{bmatrix}\xi_x^2 & \xi_x\xi_y\\ \xi_x\xi_y & \xi_y^2\end{bmatrix}$

2.3.4 State-based peridynamic model

The material model represented by the linear microelastic material (2-53), the prototype microelastic brittle material (2-70) or other material models within the bond-based framework assume that individual bond connected to a primary point x responds independently of all other bonds within the family of x. Additionally, the pairwise force generated in a bond due to deformation is collinear with the bond in the deformed configuration. As a result of these assumptions, it was shown that the elastic response of a bond-based material model always results in a Poisson's ratio of 1/3 for 2D and 1/4 for 3D isotropic solids. The constraint on the Poisson's ratio within bond-based models restricts the range of material behaviours that can be reproduced. To overcome this, and other limitations of bond-based models, a *state-based peridynamic* (SBPD) framework was proposed [80].

The state-based model, in contrast to the bond-based approach, considers the deformation of all bonds within a family when determining the response of a given bond. This eliminates the restriction on the Poisson's ratio and extends the capability of the SBPD model to model materials with Poisson's ratio spanning the entire permissible range. This extended capability of the SBPD framework is made possible by the introduction of mathematical objects known as states, which

are non-local operators that map bonds to scalar or vector quantities. To define the domain $\mathcal{H}$ of the state, let $\delta > 0$ be the horizon of a point $\boldsymbol{x}$ in a body $\mathfrak{B}$. Then:

$$\mathcal{H} = \{\boldsymbol{\xi} \in (\mathbb{R}\backslash\mathbf{0}) | (\boldsymbol{\xi} + \boldsymbol{x}) \in (\mathcal{B}_\delta(\boldsymbol{x}) \cap \mathfrak{B})\} \tag{2-78}$$

is the family of bonds for the point $\boldsymbol{x}$. Equation (2-78) allows for a more precise definition of a state. Let $\mathcal{L}_m$ be the set of all tensors of order m, then a state of order m associated with the point $\boldsymbol{x}$ is a function $\underline{\mathbf{A}}\langle\cdot\rangle : \mathcal{H} \longrightarrow \mathcal{L}_m$. Angle brackets are used to indicate the bond acted upon by the state. A state that maps vectors in $\mathcal{H}$ to a scalar is called a scalar state. Similarly, a state that maps vectors in $\mathcal{H}$ to vectors is called a vector state. The set of all states of order m is denoted by A_m, thus if the set of all scalar states is denoted $\mathcal{S}$, then $\mathcal{S} = A_1$ and similarly if the set of all vector states is denoted $\mathcal{V}$, then $\mathcal{V} = A_2$. Let $\underline{\omega}\langle\boldsymbol{\xi}\rangle$ be an influence function obtained when the scalar state $\underline{\omega} \in \mathcal{S}$ acts on $\boldsymbol{\xi}$, then the tensor product of two vector states $\underline{\mathbf{A}} \in \mathcal{V}$ and $\underline{\mathbf{B}} \in \mathcal{V}$ is defined as

$$\underline{\mathbf{A}} * \underline{\mathbf{B}} = \int_{\mathcal{H}} \underline{\omega}\langle\boldsymbol{\xi}\rangle\, \underline{\mathbf{A}}\langle\boldsymbol{\xi}\rangle \otimes \underline{\mathbf{B}}\langle\boldsymbol{\xi}\rangle dV_\xi \tag{2-79}$$

Perhaps the most important state in the peridynamic formulation is the vector state and there are three important vector states that are worth mentioning here: the reference position vector state, deformation state $\underline{\mathbf{Y}}$ and the force vector state $\underline{\mathbf{T}}$.

The reference position vector state $\underline{\mathbf{X}}$ is a function whose value is the bond it acts on. It is defined as

$$\underline{\mathbf{X}}[\boldsymbol{x}]\langle\boldsymbol{x}' - \boldsymbol{x}\,\rangle = \boldsymbol{x}' - \boldsymbol{x} = \boldsymbol{\xi}, \qquad \xi = |\boldsymbol{\xi}| \tag{2-80}$$

The reference position vector state can be thought of as an identity vector state since it simply output the value of its argument. The deformation state $\underline{\mathbf{Y}}$ is a function operating on each bond length $\boldsymbol{\xi} = \boldsymbol{x}' - \boldsymbol{x}$ in the family of point $\boldsymbol{x}$, whose value is the image of the bond in the deformed configuration:

$$\underline{\mathbf{Y}}[\boldsymbol{x}, t]\langle\boldsymbol{x}' - \boldsymbol{x}\,\rangle = \boldsymbol{y}'(\boldsymbol{x}', t) - \boldsymbol{y}(\boldsymbol{x}, t) \tag{2-81}$$

where $\boldsymbol{y}'(\boldsymbol{x}', t)$ and $\boldsymbol{y}(\boldsymbol{x}, t)$ are respectively the coordinates of the points $\boldsymbol{x}'$ and $\boldsymbol{x}$ in the deformed configuration at time t. The force state $\underline{\mathbf{T}}$ is a function that associate each bond in the family of point $\boldsymbol{x}$ with some force density vector such that:

$$\underline{\mathbf{T}}[\boldsymbol{x},t]\langle \boldsymbol{x}'-\boldsymbol{x}\rangle = \mathbf{t}(\boldsymbol{x}',\boldsymbol{x},t) \tag{2-82}$$

A very import tensor (already introduced in section 2.2.6) in the formulation of nonlocal differential operators is the shape tensor $\mathbf{K}$. This tensor can also be defined using the notion of states. Following from (2-79), the shape tensor $\mathbf{K}$ is defined as

$$\mathbf{K} = \underline{\mathbf{X}} * \underline{\mathbf{X}} \tag{2-83}$$

Where $\underline{\mathbf{X}}$ is as defined in (2-80). Although vector state and second order tensors both map vectors to vectors, they are essentially different. For example, a state is in general nonlinear in its argument and is infinite dimensional. In contrast, a second order tensor is linear function of its argument and has dimension 9. It was however demonstrated in [80] that given a second order tensor $\boldsymbol{\Phi}$, it is possible to obtain a vector state through an expansion operation defined as

$$\underline{\mathcal{E}}(\boldsymbol{\Phi})\langle\boldsymbol{\xi}\rangle = \boldsymbol{\Phi}\boldsymbol{\xi} \qquad \forall \boldsymbol{\xi} \tag{2-84}$$

Where $\underline{\mathcal{E}}(\boldsymbol{\Phi})\langle\boldsymbol{\xi}\rangle$ is the vector state expanded from $\boldsymbol{\Phi}$. Conversely, given a vector state $\underline{\mathbf{A}} \in \mathcal{V}$, a second order tensor can be obtained by a reduction operation defined as

$$\underline{\mathcal{R}}(\underline{\mathbf{A}}) = (\underline{\mathbf{A}} * \underline{\mathbf{X}})\mathbf{K}^{-1} \tag{2-85}$$

To incorporate the notion of state into the peridynamic equation of motion, the force density function in (2-47) is expressed as a function of the force state $\underline{\mathbf{T}}$. Recalling the definition of the force state in (2-82), (2-47) can be written as:

$$\underline{\mathbf{T}}[\boldsymbol{x},t]\langle \boldsymbol{x}'-\boldsymbol{x}\rangle = \omega(\boldsymbol{x},\boldsymbol{y})\boldsymbol{\Psi}\mathbf{K}^{-1}\boldsymbol{\xi} \tag{2-86}$$

Compared to (2-84), the right-hand side of (2-86) can be understood to be a vector obtained when a vector state $\underline{\mathcal{E}}\left(\underline{\omega}\langle\boldsymbol{\xi}\rangle\boldsymbol{\Psi}\mathbf{K}^{-1}\right)$ is expanded from a second order tensor $\underline{\omega}\langle\boldsymbol{\xi}\rangle\boldsymbol{\Psi}\mathbf{K}^{-1}$ acting upon the bond $\boldsymbol{\xi}_{\boldsymbol{x}\boldsymbol{x}'}$ or $\boldsymbol{\xi}_{\boldsymbol{x}'\boldsymbol{x}}$ as the case maybe, so that

$$\underline{\mathbf{T}}[\boldsymbol{x},t] = \underline{\omega}\langle\boldsymbol{\xi}\rangle\underline{\mathcal{E}}(\boldsymbol{\Psi}\mathbf{K}^{-1}) \tag{2-87}$$

then (2-48) can be written as

$$\rho\frac{\partial^2\boldsymbol{u}}{\partial t^2} = \int_{\mathcal{B}_\delta(\boldsymbol{x})}\left(\underline{\mathbf{T}}[\boldsymbol{x},t]\langle\boldsymbol{x}'-\boldsymbol{x}\rangle - \underline{\mathbf{T}}[\boldsymbol{x}',t]\langle\boldsymbol{x}-\boldsymbol{x}'\rangle\right)d\boldsymbol{x}' + \boldsymbol{b}(\boldsymbol{x},t) \tag{2-88}$$

Equation (2-48) is the state-based peridynamic equation of motion. $\underline{\mathbf{T}}[\boldsymbol{x},t]$ and $\underline{\mathbf{T}}[\boldsymbol{x}',t]$ are the force states at $\boldsymbol{x}$ and $\boldsymbol{x}'$ respectively. When these states act upon the bonds $\boldsymbol{\xi}_{\boldsymbol{x}\boldsymbol{x}'}$ and $\boldsymbol{\xi}_{\boldsymbol{x}'\boldsymbol{x}}$ respectively, the results are bond force density vectors acting at points $\boldsymbol{x}$ and $\boldsymbol{x}'$ respectively. To

complete the development of the SBPD framework, a constitutive material model $\underline{\widehat{\mathbf{T}}}$ is required that will relate the force vector state $\underline{\mathbf{T}}$ with the appropriate physical quantities such as the deformation vector state $\underline{\mathbf{Y}}$, the rate of deformation $\underline{\dot{\mathbf{Y}}}$, temperature T, damage $\mathcal{D}$, e.t.c. The general form is given by:

$$\underline{\mathbf{T}}[\mathbf{x}, t] = \underline{\widehat{\mathbf{T}}}\left[\underline{\mathbf{Y}}, \underline{\dot{\mathbf{Y}}}, T, \mathcal{D}, \dots\right] \tag{2-89}$$

Two class of material model arises from (2-89). When $\underline{\widehat{\mathbf{T}}}$ is such that $\underline{\mathbf{T}}$ and $\underline{\mathbf{Y}}$ are colinear, then $\underline{\widehat{\mathbf{T}}}$ is said to be an ordinary state-based peridynamic (OSBPD) material model, otherwise $\underline{\widehat{\mathbf{T}}}$ is said to be non-ordinary state-based peridynamic (NOSBPD) material model [80]. In this thesis, only the NOSBPD framework based on the *constitutive correspondence model* will receive further consideration. The motivation for this choice stem from the fact that the correspondence constitutive model provides a framework for modelling more general materials and can admit constitutive models from classical continuum mechanics. This enables taking advantage of decades of development and calibration as well as state-of-the-art in the well-established classical theory. Consequently, it allows for the use of familiar quantities such as strain and stress within the peridynamic framework.

2.3.4.1 Nonlocal kinematic quantities

In this section, the nonlocal differential operators in section 2.2.6 will be used to derive the expression of relevant kinematic objects that are nonlocal analogue of their counterparts in the local theory. These quantities are important in the development of the SBPD.

2.3.4.1.1 Gradient of the displacement and deformation vector fields

An important quantity in the formulation of continuum mechanics is the gradient of the displacement vector. Let $\boldsymbol{u}(\boldsymbol{x}, t)$ be the displacement of a point $\boldsymbol{x}$ at time t. Then from (2-33), the gradient of the displacement field at $\boldsymbol{x}$ as a function of the undeformed bond is given as:

$$\mathcal{G}_{\omega_{\boldsymbol{x}}}\big(\boldsymbol{u}(\boldsymbol{x})\big) = \left[\int_{\mathbb{R}^n} \underline{\omega}\langle\boldsymbol{\xi}\rangle\big(\boldsymbol{u}(\boldsymbol{x}', t) - \boldsymbol{u}(\boldsymbol{x}, t)\big)\otimes\boldsymbol{\xi}_{\boldsymbol{x},\boldsymbol{x}'}\, d\boldsymbol{x}'\right]\mathbf{K}^{-1} \tag{2-90}$$

Another key kinematic quantity that plays an important role in the development of the state-based peridynamic theory is the concept of the deformation tensor. In the nonlocal peridynamic setting, the deformation tensor, denoted $\mathbf{F}$ is the finite dimensional equivalent of the deformation state. Let $\mathcal{L}^+$ be the set of all second order tensors with positive determinants. Let Ω_0 and Ω_t be the reference and deformed configuration of a body $\mathfrak{B}$ undergoing deformation. Let $\boldsymbol{x}$ be the position of a material point in Ω_0 and $\boldsymbol{y}$ be its position in Ω_t. Let $\mathbf{F} \in \mathcal{L}^+$ exist such that the deformed image of the bond $\boldsymbol{\xi}_{\boldsymbol{x}\boldsymbol{x}'}$ is given by:

$$\underline{\mathbf{Y}}[\boldsymbol{x},t]\langle\boldsymbol{\xi}_{\boldsymbol{x},\boldsymbol{x}'}\rangle = \mathbf{F}\boldsymbol{\xi}_{\boldsymbol{x},\boldsymbol{x}'} = \mathbf{F}(\boldsymbol{x}'-\boldsymbol{x}) = \boldsymbol{y}(\boldsymbol{x}',t) - \boldsymbol{y}(\boldsymbol{x},t) \tag{2-91}$$

Using (2-33), the nonlocal material gradient of the deformation as a function of the undeformed bond is evaluated as

$$\mathcal{G}_{\omega_{\boldsymbol{x}}}(\boldsymbol{y}) = \mathbf{F}(\boldsymbol{x}) = \left[\int_{\mathbb{R}^n} \underline{\omega}\langle\boldsymbol{\xi}\rangle\big(\boldsymbol{y}(\boldsymbol{x}',t) - \boldsymbol{y}(\boldsymbol{x},t)\big)\otimes\boldsymbol{\xi}_{\boldsymbol{x},\boldsymbol{x}'}d\boldsymbol{x}'\right]\mathbf{K}^{-1} \tag{2-92}$$

Equation (2-92) is the definition of the nonlocal deformation gradient given in [80]. We can further write (2-92) as

$$\begin{aligned}\mathbf{F} &= \left[\int_{\mathbb{R}^n} \underline{\omega}\langle\boldsymbol{\xi}\rangle(\boldsymbol{u}(\boldsymbol{x}',t) + \boldsymbol{x}' - \boldsymbol{u}(\boldsymbol{x},t) - \boldsymbol{x})\otimes\boldsymbol{\xi}_{\boldsymbol{x},\boldsymbol{x}'}d\boldsymbol{x}'\right]\mathbf{K}^{-1}\\ &= \left[\int_{\mathbb{R}^n} \underline{\omega}\langle\boldsymbol{\xi}\rangle\big(\boldsymbol{u}(\boldsymbol{x}',t) - \boldsymbol{u}(\boldsymbol{x},t)\big)\otimes\boldsymbol{\xi}_{\boldsymbol{x},\boldsymbol{x}'}d\boldsymbol{x}'\right]\mathbf{K}^{-1}\\ &\quad + \left[\int_{\mathbb{R}^n} \omega(|\boldsymbol{\xi}|)(\boldsymbol{x}'-\boldsymbol{x})\otimes\boldsymbol{\xi}_{\boldsymbol{x},\boldsymbol{x}'}d\boldsymbol{x}'\right]\mathbf{K}^{-1}\\ \mathbf{F} &= \mathcal{G}_{\omega_{\boldsymbol{x}}}\big(\boldsymbol{u}(\boldsymbol{x})\big) + \mathbf{I}\end{aligned} \tag{2-93}$$

Where the second equality follows from the linearity of the integral operator. Notice that the nonlocal deformation gradient is devoid of any notion of the local derivative operator which would have required that the deformation field be continuously differentiable (at least in a weak sense for the case of Finite Element Method). In its present form, the deformation gradient is still defined in the presence of singularities such as cracks.

2.3.4.1.2 Nonlocal strain tensor

We can define the notion of strain by comparing the length of a bond before and after deformation. Let $\boldsymbol{\xi} = \boldsymbol{x}' - \boldsymbol{x}$ and $\boldsymbol{\lambda} = \boldsymbol{y}(\boldsymbol{x}') - \boldsymbol{y}(\boldsymbol{x})$, then from (2-80) and (2-91), we have:

$$\lambda^2 - \xi^2 = \boldsymbol{\lambda}\cdot\boldsymbol{\lambda} - \boldsymbol{\xi}\cdot\boldsymbol{\xi} = \boldsymbol{\xi}^T\mathbf{F}^T\mathbf{F}\boldsymbol{\xi} - \boldsymbol{\xi}^T\boldsymbol{\xi} = \boldsymbol{\xi}^T(\mathbf{F}^T\mathbf{F} - \mathbf{I})\boldsymbol{\xi} \tag{2-94}$$

If we define a deformation or strain matrix $\mathbf{E}$ as:

$$\mathbf{E} = \frac{1}{2}(\mathbf{F}^T\mathbf{F} - \mathbf{I}) \tag{2-95}$$

Then (2-94) can be written as

$$\lambda^2 - \xi^2 = 2\boldsymbol{\xi}^T\mathbf{E}\boldsymbol{\xi} \tag{2-96}$$

where $\mathbf{E}$ is the nonlocal analogue of the Green-Lagrange strain tensor and $\mathbf{F}$ is the nonlocal deformation gradient defined in (2-92). Considering (2-93), (2-95) can be written as

$$\mathbf{E} = \frac{1}{2}\left(\left(\mathcal{G}_{\omega_{\boldsymbol{x}}}(\boldsymbol{u}(\boldsymbol{x}))\right) + \left(\mathcal{G}_{\omega_{\boldsymbol{x}}}(\boldsymbol{u}(\boldsymbol{x}))\right)^T + \left(\mathcal{G}_{\omega_{\boldsymbol{x}}}(\boldsymbol{u}(\boldsymbol{x}))\right)^T \left(\mathcal{G}_{\omega_{\boldsymbol{x}}}(\boldsymbol{u}(\boldsymbol{x}))\right)\right) \tag{2-97}$$

Following from the assumption of infinitesimal deformation where the displacement gradient is small, that is $\left|\mathcal{G}_{\omega_{\boldsymbol{x}}}(\boldsymbol{u}(\boldsymbol{x}))\right| \ll 1$, we may neglect the nonlinear term in the definition of the Green-Lagrange strain tensor $\mathbf{E}$ so that (2-97) reduces to

$$\mathbf{E} \approx \boldsymbol{\varepsilon} = \mathcal{G}^s_{\omega_{\boldsymbol{x}}}(\boldsymbol{u}(\boldsymbol{x})) = \frac{1}{2}\left(\left(\mathcal{G}_{\omega_{\boldsymbol{x}}}(\boldsymbol{u}(\boldsymbol{x}))\right) + \left(\mathcal{G}_{\omega_{\boldsymbol{x}}}(\boldsymbol{u}(\boldsymbol{x}))\right)^T\right) = \frac{1}{2}(\mathbf{F} + \mathbf{F}^T) - \mathbf{I} \tag{2-98}$$

where $\boldsymbol{\varepsilon}$ is the infinitesimal strain tensor and $\mathcal{G}^s$ denotes a symmetric tensor operator

2.3.4.2 constitutive model

Let $W(\underline{\mathbf{Y}}) : \mathcal{V} \longrightarrow \mathbb{R}$ be the peridynamic strain energy density, then generally, for an elastic material, the force density state can be expressed [80] as

$$\underline{\mathbf{T}} = \nabla W(\underline{\mathbf{Y}}) \tag{2-99}$$

Where $\nabla W(\underline{\mathbf{Y}})$ is the Fréchet derivative of $W(\underline{\mathbf{Y}})$ with respect to $\underline{\mathbf{Y}}$. In the correspondence model, $W(\underline{\mathbf{Y}})$ is assumed to be equal to the strain energy density $\Omega(\mathbf{F}) : \mathcal{L}_2 \longrightarrow \mathbb{R}$ from the classical theory where the deformation gradient $\mathbf{F}$ from the local theory is approximated by its nonlocal counterpart given by (2-92). So that (2-99) becomes:

$$\underline{\mathbf{T}} = \nabla \Omega(\mathbf{F}) \tag{2-100}$$

Evaluating the Fréchet derivative in (2-100) is shown [80] to result in the expression

$$\underline{\mathbf{T}}\langle \boldsymbol{\xi}_{\boldsymbol{x},\boldsymbol{x}'} \rangle = \underline{\omega}\langle \boldsymbol{\xi} \rangle \mathbf{P}\mathbf{K}^{-1} \boldsymbol{\xi}_{\boldsymbol{x},\boldsymbol{x}'} \tag{2-101}$$

where $\mathbf{P}$ is the first Piola stress tensor. Comparing (2-101) to (2-84), it can be deduced that:

$$\boldsymbol{\Psi} = \mathbf{P} \tag{2-102}$$

and

$$\underline{\mathbf{T}} = \underline{\omega}\langle \boldsymbol{\xi} \rangle \underline{\mathcal{E}}(\mathbf{P}\mathbf{K}^{-1}) \tag{2-103}$$

Thus, in compact notation, the state-based peridynamic balance of linear momentum can be written as

$$\rho\ddot{\boldsymbol{u}} = -\mathcal{D}_{\omega}(\mathbf{P})(\boldsymbol{x}) + \boldsymbol{b}(\boldsymbol{x}, t) \tag{2-104}$$

To complete the definition of the nonlocal problem, appropriate constraints need to be applied to certain regions of the problem domain. To this end, let the interaction domain $\Omega_I = \Omega_c$ be the constrained volume. Let Ω_c split into two disjoint subdomains Ω_{cd} and Ω_{cn} such that $\Omega_{cd} \cap \Omega_{cn} = \emptyset$ and either of Ω_{cd} and Ω_{cn} could be an empty set. Ω_{cd} is the subdomain where Dirichlet boundary condition is applied and Ω_{cn} is the subdomain where Neumann boundary condition is applied. Analogous to the boundary value problem of the classical local theory, constraint on the solution $\boldsymbol{u}$ of (2-45) over Ω is applied as follows: a given function value $\boldsymbol{g}_d$ is prescribed on the solution over Ω_{cd} such that:

$$\boldsymbol{u}(\boldsymbol{x}) = \boldsymbol{g}_d \qquad \forall \boldsymbol{x} \in \Omega_{cd} \tag{2-105}$$

To prescribe the Neumann type constraint, recall that in the classical boundary value problem, this involves prescribing a traction or flux density $\boldsymbol{\sigma} \cdot \boldsymbol{n}$ over the traction boundary. From (2-18) and the discussion that follows, the nonlocal flux density over Ω_{In} is given by $\int_{\Omega_I} \mathcal{N}_{\omega}(\mathbf{P})(\boldsymbol{x})\, d\boldsymbol{x}$. Let $\boldsymbol{g}_n$ be a given function value of the flux density over Ω_{cn}. The Neumann constraint can be stated as

$$\int_{\Omega_{cn}} \mathcal{N}_{\omega}(\mathbf{P})(\boldsymbol{x})\, d\boldsymbol{x} = \boldsymbol{g}_{\boldsymbol{n}} \qquad \forall \boldsymbol{x} \in \Omega_{cn} \tag{2-106}$$

The presence of the second order time derivative of the solution $\boldsymbol{u}$ in (2-104) means in addition to the boundary constraints (2-105), (2-106), initial conditions also need to be specified. The initial condition involves prescribing the initial values of the solution and its first derivative. Let $\boldsymbol{u}_I$ and $\dot{\boldsymbol{u}}_I$ be the initial values of $\boldsymbol{u}(\boldsymbol{x})$ and $\dot{\boldsymbol{u}}(\boldsymbol{x})$ respectively, then

$$\boldsymbol{u}(\boldsymbol{x}, 0) = \boldsymbol{u}_I \quad \forall \boldsymbol{x} \in \Omega, \text{for } t = 0 \tag{2-107}$$

and

$$\dot{\boldsymbol{u}}(\boldsymbol{x}, 0) = \dot{\boldsymbol{u}}_I \quad \forall \boldsymbol{x} \in \Omega, \text{for } t = 0 \tag{2-108}$$

are the initial conditions. So that (2-104)-(2-108) gives the complete definition of the nonlocal problem:

$$\begin{cases} \rho\ddot{\boldsymbol{u}} = -\mathcal{D}_{\omega}(\mathbf{P})(\boldsymbol{x}) + \boldsymbol{b}(\boldsymbol{x},t) & \forall \boldsymbol{x} \in \Omega_s \\ \boldsymbol{u}(\boldsymbol{x}) = \boldsymbol{g}_d & \forall \boldsymbol{x} \in \Omega_{cd} \\ \int_{\Omega_{cn}} \mathcal{N}_{\omega}(\mathbf{P})(\boldsymbol{x})\, d\boldsymbol{x} = \boldsymbol{g_n} & \forall \boldsymbol{x} \in \Omega_{cd} \\ \boldsymbol{u}(\boldsymbol{x},0) = \boldsymbol{u}_I & \forall \boldsymbol{x} \in \Omega, \text{for } t = 0 \\ \dot{\boldsymbol{u}}(\boldsymbol{x},0) = \dot{\boldsymbol{u}}_I & \forall \boldsymbol{x} \in \Omega, \text{for } t = 0 \end{cases} \tag{2-109}$$

Notice that the constraints (2-105) and (2-106) are prescribed over domains Ω_{cd} and Ω_{cn} that have positive volume in $\mathbb{R}^n$. This contrasts with the classical local theory where constraints are applied on domains that have zero volume. For this reason, (2-109) is referred to as *initial volume constraint problem.*

2.4 Discretization of the Peridynamic model

As can be seen from (2-48), the governing equation of motion in Peridynamics give rise to a continuum model. In order to be amenable to computer implementation, different numerical approximation schemes have been proposed such as the meshfree method [82, 86], the collocation methods [87, 88] and methods based on finite elements mesh [89, 90]. Due to its simple implementation algorithm and relatively low computational cost, the meshfree method suggested in [82] is the most widely used [91] and is the preferred method in this work for these same reasons. In this approximation method, the discrete form of (2-48) is:

$$\rho_i \ddot{\boldsymbol{u}}_{\boldsymbol{i}} = \sum_{j=1}^{N} \left[\underline{\mathbf{T}}[\boldsymbol{x},t]\langle \boldsymbol{x}_j - \boldsymbol{x}_i \rangle - \underline{\mathbf{T}}[\boldsymbol{x}',t]\langle \boldsymbol{x}_i - \boldsymbol{x}_j \rangle \right] V_j + \boldsymbol{b}_{\boldsymbol{i}} \tag{2-110}$$

where $\rho_i \coloneqq \rho(\boldsymbol{x}_i)$, $\ddot{\boldsymbol{u}}_{\boldsymbol{i}} = \frac{\partial \boldsymbol{u}_i}{\partial t}$ with $\boldsymbol{u}_i \coloneqq \ddot{\boldsymbol{u}}(\boldsymbol{x}_i)$ and N is the number of nodes in the neighbourhood of node $\boldsymbol{i}$. The discretised form of equation (2-77) is

$$\rho \ddot{\boldsymbol{u}}_i^n = \sum_{j}^{N_i} \boldsymbol{C}\big(x_j - x_i\big)\big(u_j - u_i\big)V_j + \boldsymbol{b}_i^n \tag{2-111}$$

The assembled PD equations of equilibrium for the body in matrix notation takes the form:

$$[M]\{\ddot{\boldsymbol{u}}\} + [\boldsymbol{C}]\{\boldsymbol{u}\} = \{\boldsymbol{b}\} \tag{2-112}$$

Where $\{u\}$ is a vector of all displacement DoFs, $\{b\}$ is a vector that collect all applied body forces. $[M]$ is a diagonal matrix of mass density, $[C]$ is the micromodulus matrix which is analogous to the stiffness matrix in the FE method.

Chapter 3

3.0 Coarsening Method for Linear Peridynamic Theory

The goal of the coarsening method is to provide a multiscale framework based on peridynamic theory that will predict macroscale response of medium based on the underlying evolving microstructure, without necessarily resolving all microstructural details. This is achieved by a process of successive elimination of points from the medium called coarsening. Each successive coarsening results in a medium with reduced material points as well as reduced level of geometrical details. However, the property of the coarsened medium is determined such that the effect of the excluded material points is implicitly included in the coarsened level simulation. The coarsening formulation presented here is adapted from [14] for the completeness of presentation.

3.1 Peridynamic coarsening formulation.

To coarsen a detailed model, let $\mathcal{B}^0$ be a linear elastic peridynamic body as shown in Figure 3-1. Let $\mathcal{A}^0$ be the set of linear admissible displacement field on $\mathcal{B}^0$, and let $\boldsymbol{C^0}: \mathcal{B}^0 \times \mathcal{B}^0 \to \ell$ be the micromodulus tensor associated with the material of the body where $\mathcal{L}$ is the set of all second order tensors. Assume r^0 is a positive number that represents the maximum interaction distance for all points in $\mathcal{B}^0$, such that if:

$$|\boldsymbol{q} - \boldsymbol{x}| > r^0 \quad \Longrightarrow \quad C^0(\boldsymbol{x}, \boldsymbol{q}) = 0 \quad \forall \boldsymbol{x}, \boldsymbol{q} \in \mathcal{B}^0 \tag{3-1}$$

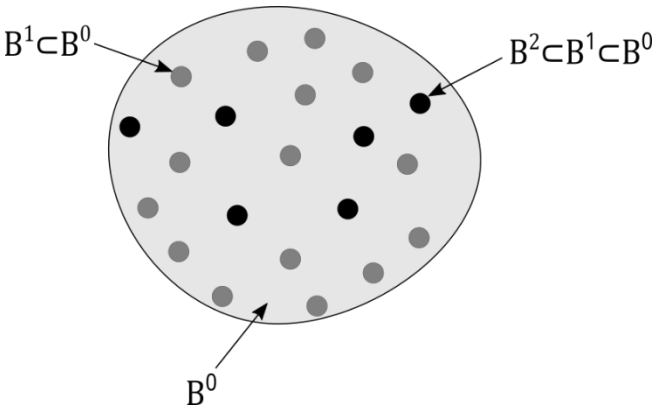

Figure 3-1. A Peridynamic body showing model levels 0, 1 and 2.

Let $\mathcal{B}^1 \subset \mathcal{B}^0$, and let $\mathcal{A}^1$ represent the set of admissible displacement field on $\mathcal{B}^1$. $\mathcal{B}^0$ and $\mathcal{B}^1$ are called level 0 and level 1 body, respectively. The objective of this coarsening process is to express the internal forces acting on $\mathcal{B}^1$ in terms of its own displacements only while implicitly accounting for forces that points in $\mathcal{B}^0 - \mathcal{B}^1$ exerts on $\mathcal{B}^1$. To achieve this objective, let $\mathbf{x}$ be an arbitrary

point in $\mathcal{B}^1$ and let δ^1 be a positive number. Let $\mathcal{H}_{\mathbf{x}}^1$ be the closed neighbourhood of $\mathbf{x}$ in $\mathcal{B}^0$ with radius r^1

$$\mathcal{H}_{\mathbf{x}}^1 = \left\{\mathbf{q} \in \mathcal{B}^0 \middle| |\mathbf{q} - \mathbf{x}| \leq r^1\right\}$$

Let $\mathcal{R}_{\mathbf{x}}^1 = \mathcal{H}_{\mathbf{x}}^1 \cap \mathcal{B}^1$. Suppose $\boldsymbol{u}^1 \in \mathcal{A}^1$ is given and let $\boldsymbol{u}^0 \in \mathcal{A}^0$ satisfy the compatibility condition:

$$\boldsymbol{u}^0(\mathbf{p}) = \boldsymbol{u}^1(\mathbf{p}) \qquad \forall \mathbf{p} \in \mathcal{R}_{\mathbf{x}}^1 \tag{3-2}$$

Outside of $\mathcal{R}_{\boldsymbol{x}}^1$, assume that $\boldsymbol{u}^0$ satisfies the equilibrium condition, neglecting interactions between $\mathcal{H}_{\boldsymbol{x}}^1$ and its exterior:

$$\boldsymbol{\mathcal{L}}^0(\mathbf{z}) + b(\mathbf{z}) = 0 \qquad \forall \mathbf{z} \in \mathcal{H}_{\mathbf{x}}^1 - \mathcal{R}_{\mathbf{x}}^1 \tag{3-3}$$

where:

$$\boldsymbol{\mathcal{L}}^0(\mathbf{z}) = \int_{\mathcal{H}_{\mathbf{x}}^1} \boldsymbol{C}^0(\mathbf{z}, \mathbf{p})\big(\boldsymbol{u}^0(\mathbf{p}) - \boldsymbol{u}^0(\mathbf{z})\big) dV_{\mathrm{p}} \qquad \forall \mathbf{z} \in \mathcal{H}_{\mathbf{x}}^1 \tag{3-4}$$

Also, assume that there is no body force density applied outside $\mathcal{R}_{\mathbf{x}}^1$

$$b(\mathbf{z}) = 0 \qquad \forall \mathbf{z} \in \mathcal{H}_{\mathbf{x}}^1 - \mathcal{R}_{\mathbf{x}}^1 \tag{3-5}$$

Further assume that for a given displacement field $\boldsymbol{u}^1$ (3-2) and (3-3) have a unique solution $\boldsymbol{u}^0$ on $\mathcal{H}_{\mathbf{x}}^1$, and let $\boldsymbol{S}_x^{0,1}$ be the resolvent kernel that generates this solution:

$$\boldsymbol{u}^0(\mathbf{p}) = \int_{\mathcal{R}_{\mathbf{x}}^1} \boldsymbol{S}_x^{0,1}(\mathbf{p}, \mathbf{q})\big(\boldsymbol{u}^1(\boldsymbol{q})\big) dV_{\mathrm{q}} \qquad \forall \mathbf{p} \in \mathcal{H}_{\mathbf{x}}^1 \tag{3-6}$$

From (3-2) and (3-6), we can infer that:

$$\boldsymbol{S}_x^{0,1}(\mathbf{p}, \mathbf{q}) = \mathbb{I}\Delta(\mathbf{p} - \mathbf{q}) \qquad \forall \mathbf{p} \in \mathcal{R}_{\mathbf{x}}^1, \forall \mathbf{q} \in \mathcal{H}_{\mathbf{x}}^1 \tag{3-7}$$

where $\mathbb{I}$ is the isotropic tensor and Δ is the three-dimensional Dirac delta function. For the special case where $\boldsymbol{u}^0$ represents a linear rigid translation of points in $\mathcal{R}_{\mathbf{x}}^1$ through an arbitrary displacement $\overline{\boldsymbol{u}}$, then all points in $\mathcal{H}_{\mathbf{x}}^1 - \mathcal{R}_{\mathbf{x}}^1$ will also translate by $\overline{\boldsymbol{u}}$. Therefore, from (3-6), we see that:

$$\overline{\boldsymbol{u}} = \left[\int_{\mathcal{R}_{\mathbf{x}}^1} \boldsymbol{S}_x^{0,1}(\mathbf{p}, \mathbf{q}) dV_{\mathrm{q}}\right] \overline{\boldsymbol{u}} \qquad \forall \mathbf{p} \in \mathcal{H}_{\mathbf{x}}^1$$

from which we can obtain the following identity

$$\int_{\mathcal{R}_{\mathbf{x}}^1} \boldsymbol{S}_x^{0,1}(\mathbf{p},\mathbf{q}) dV_{\mathrm{q}} = 1 \qquad \forall \mathbf{p} \in \mathcal{H}_{\mathbf{x}}^1 \tag{3-8}$$

Subtracting $\boldsymbol{u}^0(\mathbf{z})$ from both sides of (3-6) and using the identity given in (3-8), yields:

$$\boldsymbol{u}^0(\mathbf{p}) - \boldsymbol{u}^0(\mathbf{z}) = \int_{\mathcal{R}_{\mathbf{x}}^1} \boldsymbol{S}_x^{0,1}(\mathbf{p},\mathbf{q})\big(\boldsymbol{u}^1(\boldsymbol{q}) - \boldsymbol{u}^1(\boldsymbol{z})\big) dV_{\mathrm{q}} \qquad \forall \mathbf{p},\mathbf{z} \in \mathcal{H}_{\mathbf{x}}^1 \tag{3-9}$$

Substituting this result in (3-4) yields

$$\boldsymbol{\mathcal{L}}^0(\mathbf{z}) = \int_{\mathcal{H}_{\mathbf{x}}^1} \mathbf{C}^0(\mathbf{z},\mathbf{p}) \left[\int_{\mathcal{R}_{\mathbf{x}}^1} \boldsymbol{S}_x^{0,1}(\mathbf{p},\mathbf{q})\big(\boldsymbol{u}^1(\boldsymbol{q}) - \boldsymbol{u}^1(\boldsymbol{z})\big) dV_{\mathrm{q}} \right] dV_{\mathrm{p}} \qquad \forall \mathbf{z} \in \mathcal{H}_{\mathbf{x}}^1 \tag{3-10}$$

Reversing the order of integration and rearranging gives

$$\boldsymbol{\mathcal{L}}^0(\mathbf{z}) = \int_{\mathcal{R}_{\mathbf{x}}^1} \left[\int_{\mathcal{H}_{\mathbf{x}}^1} \mathbf{C}^0(\mathbf{z},\mathbf{p}) \boldsymbol{S}_x^{0,1}(\mathbf{p},\mathbf{q}) dV_{\mathrm{p}} \right] \big(\boldsymbol{u}^1(\boldsymbol{q}) - \boldsymbol{u}^1(\boldsymbol{z})\big) dV_{\mathrm{q}} \qquad \forall \mathbf{z} \in \mathcal{H}_{\mathbf{x}}^1 \tag{3-11}$$

Recalling that $\mathbf{x}$ is an arbitrary point in $\mathcal{B}^1$, if we denote the force density in any such choice of $\mathbf{x}$ by

$$\boldsymbol{\mathcal{L}}^0(\mathbf{x}) = \boldsymbol{\mathcal{L}}^1(\mathbf{x}) \qquad \forall \mathbf{x} \in \mathcal{B}^1 \tag{3-12}$$

Then, from (3-9) and (3-10) we can obtain:

$$\boldsymbol{\mathcal{L}}^1(\mathbf{x}) = \int_{\mathcal{R}_{\mathbf{x}}^1} \mathbf{C}^1(\mathbf{x},\mathbf{q}) \Big(\boldsymbol{u}^1(\mathbf{q}) - \boldsymbol{u}^1(\mathbf{x})\Big) dV_{\mathrm{q}} \qquad \forall \mathbf{x} \in \mathcal{B}^1 \tag{3-13}$$

where the coarsened micromodulus in level 1 $\mathbf{C}^1 : \mathcal{B}^1 \times \mathcal{B}^1$ is defined by

$$\mathbf{C}^1(\mathbf{z},\mathbf{q}) = \int_{\mathcal{H}_{\mathbf{x}}^1} \mathbf{C}^0(\mathbf{x},\mathbf{p}) \boldsymbol{S}_x^{0,1}(\mathbf{p},\mathbf{q}) dV_{\mathrm{p}} \qquad \forall \mathbf{x},\mathbf{q} \in \mathcal{B}^1 \tag{3-14}$$

Similarly, for any level m in the coarsening process, the force density can be obtained from

$$\boldsymbol{\mathcal{L}}^m(\mathbf{x}) = \int_{\mathcal{R}_{\mathbf{x}}^m} \mathbf{C}^m(\mathbf{x},\mathbf{q})\big(\boldsymbol{u}^m(\mathbf{q}) - \boldsymbol{u}^m(\mathbf{x})\big) dV_{\mathrm{q}} \qquad \forall \mathbf{x} \in \mathcal{B}^m \tag{3-15}$$

where the coarsened micromodulus in level m, $\boldsymbol{C}^m : \mathcal{B}^m \times \mathcal{B}^m$ is defined by

$$\mathbf{C}^m(\mathbf{z},\mathbf{q}) = \int_{\mathcal{H}_{\mathbf{x}}^m} \mathbf{C}^{m-1}(\mathbf{x},\mathbf{p}) \boldsymbol{S}_x^{m-1,m}(\mathbf{p},\mathbf{q}) dV_{\mathrm{p}} \qquad \forall \mathbf{x},\mathbf{q} \in \mathcal{B}^m \tag{3-16}$$

3.2 Discretization of the coarsening method

To carry out the numerical implementation of the coarsening method described in the preceding section, $\mathcal{B}^0$ is discretised into nodes, which for simplicity are taken to have equal volume v. Let $\mathbf{x_i}$ be the position of node i in level m_i. For any nodes i and j, let

$$\mathbf{C}_{i,j}^{\mathbf{0}} = v\mathbf{C}^{\mathbf{0}}(\mathbf{x}_i, \mathbf{x}_j) \tag{3-17}$$

The coarsened micromodulus $\mathbf{C}_{i,j}^{\mathbf{1}}$ is obtained by discretizing (3-14) as

$$\mathbf{C}_{i,j}^{\mathbf{1}} = v\sum_{k=1}^{N} \mathbf{C}_{i,k}^{\mathbf{0}}\mathbf{S}_{k,j}^{\mathbf{0,1}} \tag{3-18}$$

To evaluate (3-18), the resolvent kernel $\mathbf{S}_{k,j}^{\mathbf{0,1}}$ need to be determined. A convenient means of obtaining the kernel function was proposed in [34]. Successive coarsening to higher levels can be achieved by following the same procedure as above, so that for any $m \geq 1$,

$$\mathbf{C}_{i,j}^{\boldsymbol{m}} = v\sum_{k=1}^{N^m} \mathbf{C}_{i,k}^{\boldsymbol{m-1}}\mathbf{S}_{k,j}^{\boldsymbol{m-1,m}} \tag{3-19}$$

To compute the coarsened micromodulus at level m for node i, the resolvent kernel $\mathbf{S}_{k,j}^{\boldsymbol{m-1,m}}$ must be determined. A method was suggested in [34] for determining the resolvent kernel. This method proceeds by creating and merging two sub-systems of equations into a global system of equations. To create such a system, two vectors $\{u^0\}$ representing displacement field in level 0 body and $\{u^1\}$ representing displacement field in level 1 body are defined. The relationship between these two displacements fields is formulated as follows:

The displacement fields $\mathbf{u}_i^{\mathbf{0}}$ and $\mathbf{u}_i^{\mathbf{1}}$ for nodes in level 1 body are constrained to satisfy Eq. (3-2):

$$\mathbf{u}_i^0 = \mathbf{u}_i^1 \qquad \forall\, i \in \mathcal{B}^1 \tag{3-20}$$

The second system of equations are obtained by ensuring that the nodes complementary to nodes in level 1 body $(\mathcal{H}_x^1 - \mathcal{R}_x^1)$ satisfy (3-3), (3-4) and (3-5). Concatenation of these two systems of equations results in a global system of equations that has the following form in one dimension:

$$\begin{bmatrix} \mathbf{1} & 0 & 0 & 0 & \dots & & \\ \vdots & & & & & & \\ \dots & 0 & \mathbf{1} & 0 & 0 \dots & & \\ \vdots & & & & & & \\ \dots & & \mathbf{C_{i,i-1}^0} & \mathbf{-P_i} & \mathbf{C_{i,i+1}^0} & \dots & \\ \vdots & & & & & & \\ & & & \dots & & \mathbf{C_{N,N-1}^0} & \mathbf{-P_N} \end{bmatrix} \begin{Bmatrix} \mathbf{u_1^0} \\ \vdots \\ \mathbf{u_R^0} \\ \vdots \\ \mathbf{u_i^0} \\ \vdots \\ \mathbf{u_N^0} \end{Bmatrix} = \begin{Bmatrix} \mathbf{u_1^1} \\ \vdots \\ \mathbf{u_R^1} \\ \vdots \\ \mathbf{0} \\ \vdots \\ \mathbf{0} \end{Bmatrix} \tag{3-21}$$

where R is the number of nodes in $\mathcal{R}_x^1$, N is the number of nodes in $\mathcal{H}_x^1$ and the diagonal elements $\mathbf{P}_i$ are given by:

$$\mathbf{P}_i = \sum_{j \neq i} \mathbf{C_{i,j}^0}$$

In shorthand notation, Eq. (3-21) can be written as:

$$[A]\{u^0\} = \{b\} \tag{3-22}$$

where $[A]$ is $N \times N$ square matrix in one-dimension and $2N \times 2N$ in two-dimension. Let $[A]^{-1}$ be the inverse of $[A]$, $[S^{0,1}]$ in one-dimension will be the leftmost R columns of $[A]^{-1}$. In two-dimension, $[S^{0,1}]$ is the leftmost $2R$ columns of $[A]^{-1}$.

3.3 Coarsening the Micromodulus Function

In this section, the coarsened form of various micromodulus functions will be presented. One-dimensional cases will be followed by a two-dimensional case.

3.3.1 Coarsening of one-dimensional micromodulus functions

The one-dimensional problem is a homogeneous bar with a length of 1 m. The elastic modulus of the material is assumed to be 200 GPa. Three scenarios will be investigated by considering the following micromodulus functions:

$$\mathbf{C}(\xi) = \begin{cases} \dfrac{2\mathrm{E}}{A\delta^2|\xi|}, & \text{if } |\xi| \leq \delta \\ 0, & \text{if } |\xi| > \delta \end{cases} \tag{3-23}$$

$$\mathbf{C}(\xi) = \begin{cases} \dfrac{6\mathrm{E}}{A\delta^2|\xi|}\left(1 - \dfrac{|\xi|}{\delta}\right), & \text{if } |\xi| \le \delta \\ 0, & \text{if } |\xi| > \delta \end{cases} \tag{3-24}$$

$$\mathbf{C}(\xi) = \begin{cases} \dfrac{3\mathrm{E}}{A\delta^3}, & \text{if } |\xi| \le \delta \\ 0, & \text{if } |\xi| > \delta \end{cases} \tag{3-25}$$

The level 0 horizon is specified as $\delta_0 = 25$ mm. The bar is discretized into 400 nodes with spacing Δx=2.5 mm. Coarsening of the detailed model to level 1 body is carried out by retaining every fourth node of level 0 body. Similarly, coarsening of level 1 body to level 2 body proceeds by retaining every second node in level 1 body. Figure 3-2 shows a schematic representation of the coarsening process. The micromodulus of the detailed model (level 0) $\mathbf{C^0}$ as well as the coarsened micromodulus $\mathbf{C^1}$ and $\mathbf{C^2}$ for the three scenarios are shown in Figure 3-3, Figure 3-4, and Figure 3-5 These curves are characterized by sharp peaks consistent with the fact that the coarsened micromodulus functions are defined only at their respective coarsened regions.

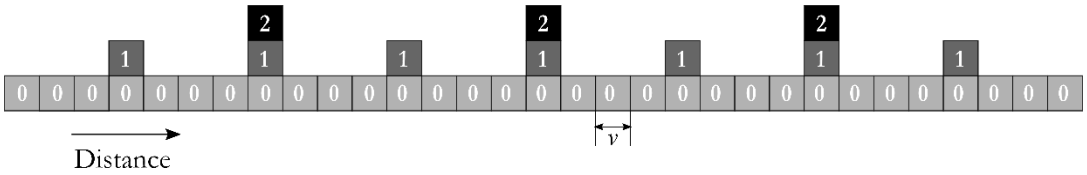

Figure 3-2. Schematic representation of the one-dimensional coarsening process

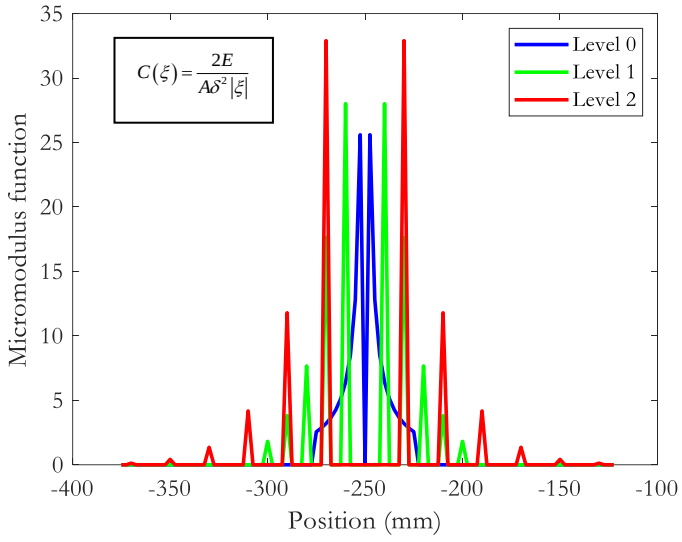

Figure 3-3. Micromodulus function associated with a uniform bond constant.

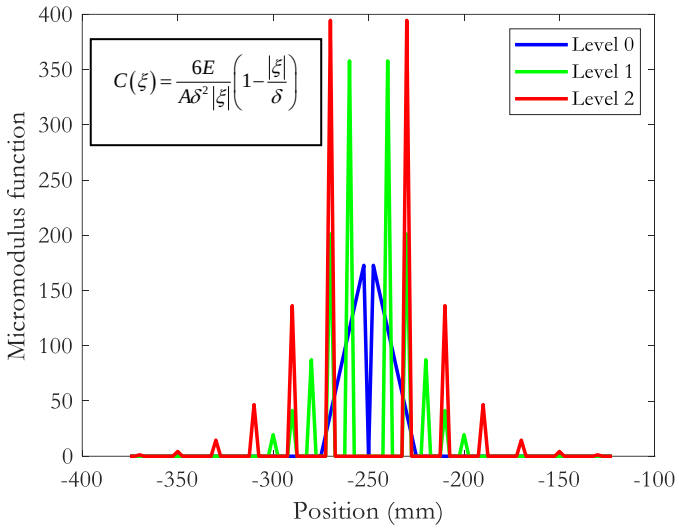

Figure 3-4. Micromodulus function associated with a bond constant function having triangular profile.

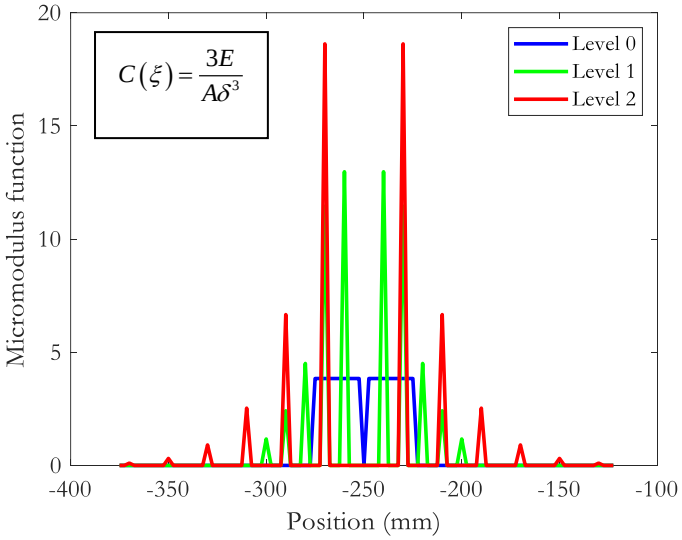

Figure 3-5. Micromodulus function associated with a bond constant function having inverted triangular profile.

3.3.2 Coarsening of two-dimensional micromodulus function

The two-dimensional problem is a 500 mm×500 mm square plate with a thickness of 50 mm. Let the elastic modulus of the plate be 200 GPa and its micromodulus function be given by

$$\mathbf{C}(\xi)=\begin{cases}\dfrac{36E}{\pi\delta^3 h|\xi|^3}\left(1-\dfrac{|\xi|}{\delta}\right)\begin{bmatrix}\xi_x^2 & \xi_x\xi_y\\ \xi_x\xi_y & \xi_y^2\end{bmatrix}, & \text{if } |\boldsymbol{q}-\boldsymbol{x}|\le\delta\\ 0, & \text{if } |\boldsymbol{q}-\boldsymbol{x}|>\delta\end{cases} \tag{3-26}$$

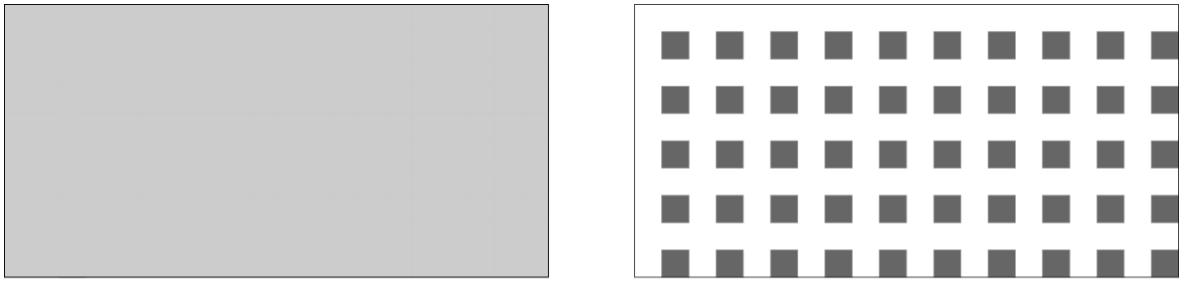

Figure 3-6. Detailed level 0 and coarsened level 1 bodies for coarsening of two-dimensional micromodulus function

Coarsening is carried out as shown schematically in Figure 3-6. Every second nodes in every second row of the level 0 model is retained in the coarsened level 1 model. Figure 3-7 shows the micromodulus function $\mathbf{C^0}$ of level $\mathbf{0}$ model as well as the coarsened micromodulus $\mathbf{C^1}$ of level 1 model. It is noticed that the coarsened micromodulus $\mathbf{C^1}$ is characterised by sharp peaks which reflects the fact that it is only defined at the coarsened region. Figure 3-7(a) shows the response of the $i-th$ material point in the $x-$direction for a displacement of the $j-th$ point in the $x-$direction. Figure 3-7(b) shows the response of the $i-th$ material point in $x-$direction if the $j-th$ point is displaced in the $y-$direction. Figure 3-7(c) shows the response in $y-$direction of the $i-th$ point when the $j-th$ point displaces in the $x-$direction, and finally, Figure 3-7(d) shows the response of the $i-th$ point in the $y-$direction when the $j-th$ point is displaced in the $y-$direction.

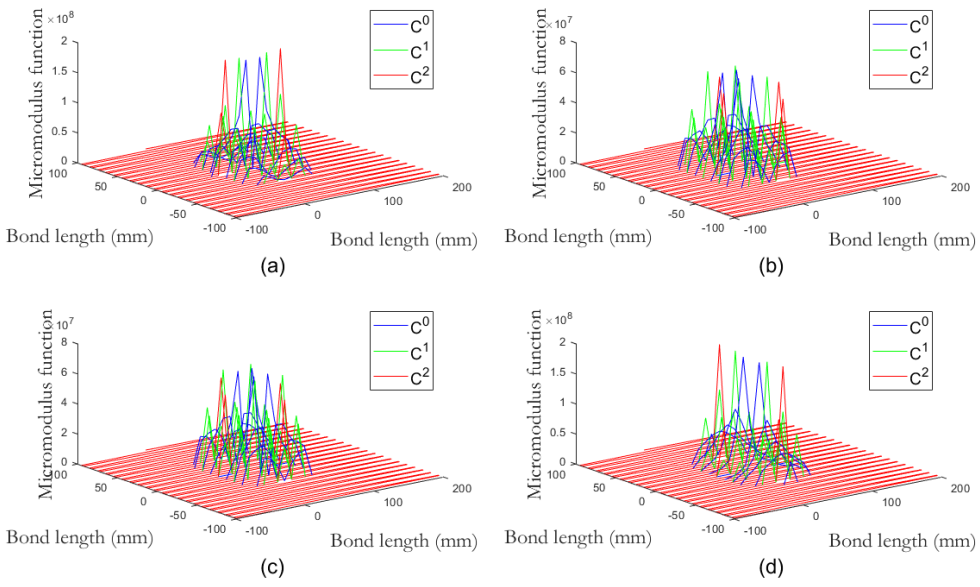

Figure 3-7. Coarsening of two-dimensional micromodulus function: (a) $\boldsymbol{x-x}$ interaction (b) $\boldsymbol{x-y}$ interaction (c) $\boldsymbol{y-x}$ interaction, and (d) $\boldsymbol{y-y}$ interaction.

3.4 Numerical Results

This section comprises five numerical experiments to illustrate the application of the coarsening method in solving solid mechanics problems. The systems are assumed to be in a state of static equilibrium and thus an implicit static solution scheme has been utilized. The first three examples focus on one-dimensional bar under tension loading for cases of homogeneous and composite materials with and/or without defect. The last two examples demonstrate the capability of the coarsening approach for two-dimensional plate problems for isotropic and composite materials.

3.4.1 One-dimensional homogeneous bar under tension loading

This example is a numerical experiment aimed at illustrating the capability of the coarsening method in capturing the correct bulk response of a system even with reduced degrees of freedom as opposed to if the degrees of freedom were to be reduced without the coarsening process. Consider a bar of length 1 m of material having micromodulus function of the form:

$$\mathbf{C}(\xi) = \begin{cases} \dfrac{6\mathrm{E}}{A\delta^2|\xi|}\left(1 - \dfrac{|\xi|}{\delta}\right), & \text{if } |\boldsymbol{q} - \boldsymbol{x}| \le \delta \\ 0, & \text{if } |\boldsymbol{q} - \boldsymbol{x}| > \delta \end{cases} \tag{3-27}$$

The maximum interaction distance δ=10Δx, where Δx is the length of a material point. The detailed model (level 0) is discretized into 1000 points, so that Δx=1 mm. The elastic modulus of the material is E=200 GPa. Coarsening of the level 0 model to level 1 proceeds by retaining every fourth node in level 0. Level 2 model retains every second node in level 1 model as shown in Figure 3-2. Body force density of b=0.001 N⁄mm^3 is applied to the rightmost level 2 node, while the third leftmost level 2 node is constrained to have zero displacement. The displacement field associated with the level 0 and coarsened levels 1 and 2 are shown in Figure 3-8. It is observed that even with reduced degrees of freedom as the detailed model is coarsened into level 1 and subsequently level 2, the displacements fields obtained from all these models are very similar to each other. This would not have been the case if the reduction in degrees of freedom were not achieved through the coarsening process.

The analytical solution based on the classical theory to the axial bar problem is of the form.

$$u(x) = \left(\frac{F}{EA}\right)x \tag{3-28}$$

Where x is the distance from the support, $u(x)$ is the displacement at point x, E is the elastic modulus, A is the cross-sectional area, and F is the force applied at the free end of the bar. The

result from the analytical model and those from the detail level 0 model as well as the results from coarsened levels 1 and 2 model are almost identical.

To illustrate the need for the coarsening process in achieving model order reduction, the number of nodes was reduced from 1000 to 250 and further to 125 without following the coarsening procedure. As shown in Figure 3-8, although the results from the coarsened models and the results from the models with reduced number of nodes are very close to each other, coarsened model results agree better with the analytical solution.

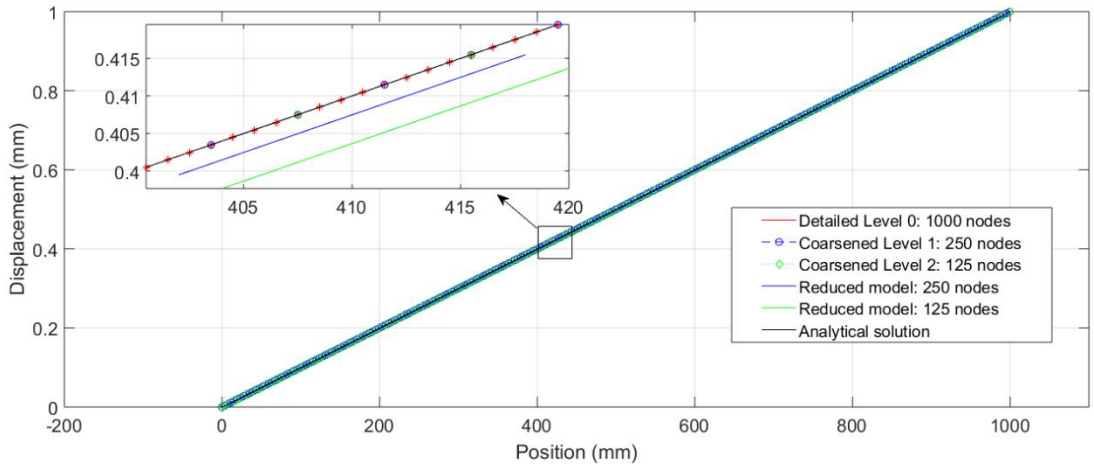

Figure 3-8. Displacement fields for a one-dimensional homogeneous bar under tension loading

3.4.2 One-dimensional composite bar under tension loading

In this example, a one-dimensional composite bar with a length of $1\mathrm{m}$ and a cross-sectional area of 100 mm^2 is considered. The composites bar has a periodic microstructure consisting of alternative strips S_{hard} and S_{soft} of hard and soft materials, respectively. Each strip is 50 mm in length. The horizon for both hard and soft sections is 50 mm. The micromodulus of the composite system has the form:

$$\mathbf{C}(\xi) = \begin{cases} \dfrac{6\mathrm{E}_1}{A\delta^2|\xi|}\left(1-\dfrac{|\xi|}{\delta}\right), & \text{if } |\boldsymbol{q}-\boldsymbol{x}| \le \delta \text{ and } (\boldsymbol{x} \in S_{\mathrm{hard}} \text{ and } \boldsymbol{q} \in S_{\mathrm{hard}}) \\ \dfrac{2\mathrm{E}_2}{A\delta^2|\xi|}, & \text{if } |\boldsymbol{q}-\boldsymbol{x}| \le \delta \text{ and } (\boldsymbol{x} \in S_{\mathrm{soft}} \text{ or } \boldsymbol{q} \in S_{\mathrm{soft}}) \\ 0, & \text{otherwise} \end{cases} \tag{3-29}$$

In other words, bonds with both ends in hard strip have hard properties while bonds with either ends in soft strip have soft properties. The elastic moduli of the hard and soft materials are E_1=200 GPa and E_2=9 GPa, respectively. The level 0 horizon is specified as $\delta^0=10\Delta x$. Coarsening from level 0 to level 1 body is carried out as shown in Figure 3-2 by retaining every fourth node of level

0 body. Similarly, level 1 body is coarsened to level 2 body by retaining every second node in level 1 body.

Body force density of b=0.001 N/mm^3 is applied to the three rightmost level 2 nodes, while the three leftmost level 2 nodes are constrained to have zero displacement. The computed displacements of coarsened level 0, 1, and 2 are shown in Figure 3-9. As expected, computation from level 0 revealed the most detailed microstructural information. As the computational region gets coarsened, these microstructural details get smoothed out. However, both detailed and coarsened models have similar global stretch. This demonstrates the fact that the effective properties produced by the coarsening process accurately reflect the bulk properties of the composite.

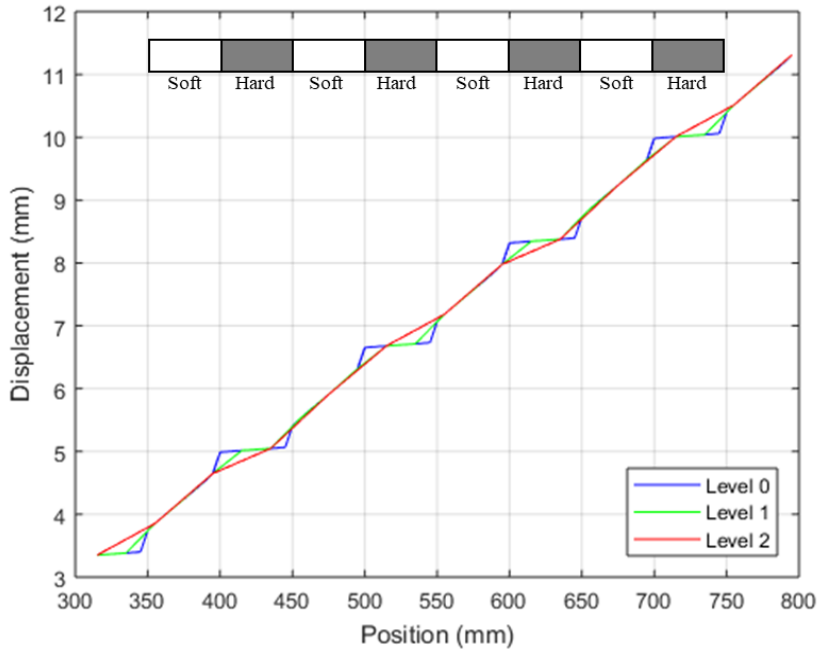

Figure 3-9. Displacement fields for levels 0, 1, and 2 for a one-dimensional composite bar under tension loading

3.4.3 One-dimensional homogeneous bar with a defect

This example considers a homogeneous bar with a defect. The bar has a length of 1 m. The constitutive model of the bar is given by.

$$\mathbf{C}(\xi) = \varphi(\boldsymbol{x},\boldsymbol{q})\begin{cases}\dfrac{2\mathrm{E}}{A\delta^2|\xi|}, & \text{if } |\boldsymbol{q}-\boldsymbol{x}| \le \delta \\ 0, & \text{if } |\boldsymbol{q}-\boldsymbol{x}| > \delta\end{cases} \tag{3-30}$$

where φ is a degrading term given by

$$\varphi = \begin{cases} 0.1, & \text{if } \boldsymbol{x} \le \boldsymbol{x}_d \le \boldsymbol{q} \text{ or } \boldsymbol{q} \le \boldsymbol{x}_d \le \boldsymbol{x} \\ 1.0 & \text{otherwise} \end{cases} \tag{3-31}$$

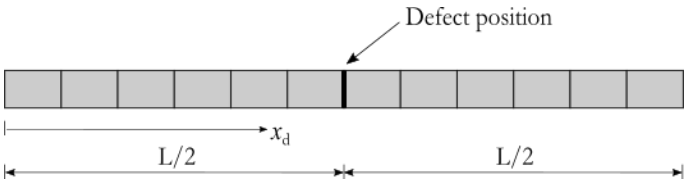

Figure 3-10. One-dimensional homogeneous bar with a defect

The horizon is specified as δ^0=50 mm in level 0 and the bar is discretised into 200 nodes. The defect is located at the center of the bar as shown in Figure 3-10. Level 1 contains every third node in level 0 and similarly, level 2 contains every third node of level 1 as shown in Figure 3-11. Prescribed displacement boundary conditions are applied to the three leftmost and three rightmost level 2 nodes. The values of the prescribed displacements are given by $u_i^0 = u_i^1 = u_i^2 = 0.01x_i$ where x_i is the coordinate of the node.

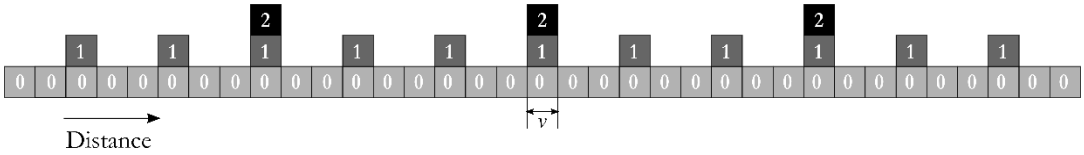

Figure 3-11. Schematic representation of the coarsening process for example 3.4.3.

The displacement fields for the level 0 model as well as the coarsened level 1 and level 2 models near the defect is shown in Figure 3-12. The three levels give identical displacement profile except close to the site of the defect. This reflects the fact that due to fewer nodes in the coarsened models, wider spacing exits between nodes.

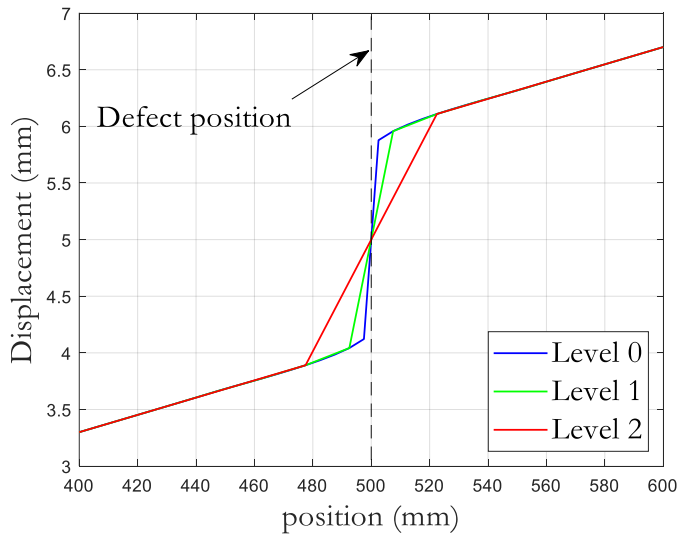

Figure 3-12. Coarsened displacement fields in a one-dimensional homogeneous bar with a defect

3.4.4 Two-dimensional homogeneous plate under tension loading

This example concerns a two-dimensional homogeneous plate under tension loading. The plate is a $500\text{mm} \times 500\text{mm}$ square plate. The micromodulus of the plate is chosen as

$$\mathbf{C}(\xi) = \begin{cases} \dfrac{8\text{E}}{\pi\delta^4 h|\xi|^2}\begin{bmatrix} \xi_x^2 & \xi_x\xi_y \\ \xi_x\xi_y & \xi_y^2 \end{bmatrix}, & \text{if } |\boldsymbol{q}-\boldsymbol{x}| \le \delta \\ 0, & \text{if } |\boldsymbol{q}-\boldsymbol{x}| > \delta \end{cases} \tag{3-32}$$

The horizon for the level 0 body is specified as $\delta^0 = 3.015\Delta x$. The plate is discretized into 200 points in both x and y −directions with every point having $\Delta x = \Delta y = 2.5\ mm$. The thickness of the plate is Δx. Coarsening of the detailed model is achieved by retaining every second point in the second row as shown schematically in Figure 3-13.

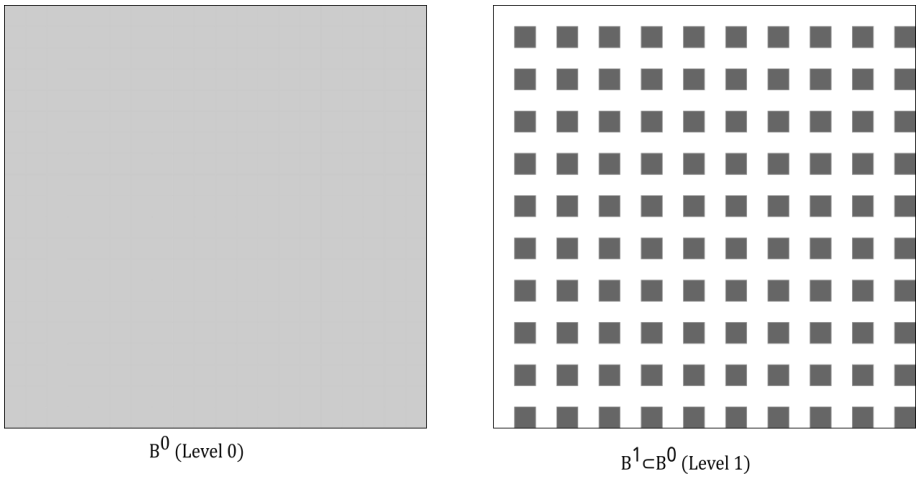

Figure 3-13. Discretisation and coarsening of the two-dimensional homogeneous plate.

Two boundary layers each consisting of one grid of 100 points are created: one along the top edge and the other along the bottom edge. At the top boundary layer, every second point of the detailed model is constrained to have zero displacement. A body force density of 2000 kN/m^3 is applied to every second point in the bottom boundary layer in the detailed model.

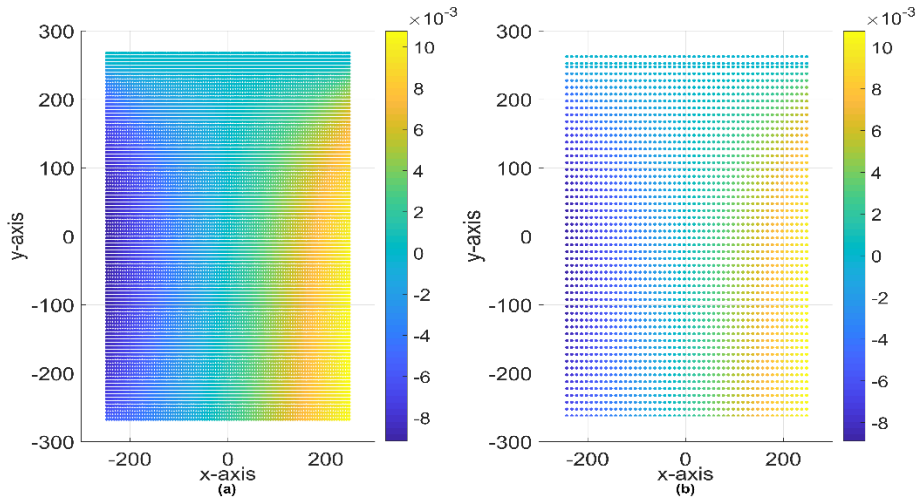

Figure 3-14. Profile of $\boldsymbol{x}$ −axis displacement field: (a) Detailed (Level 0) model and (b) Coarsened (Level 1) model.

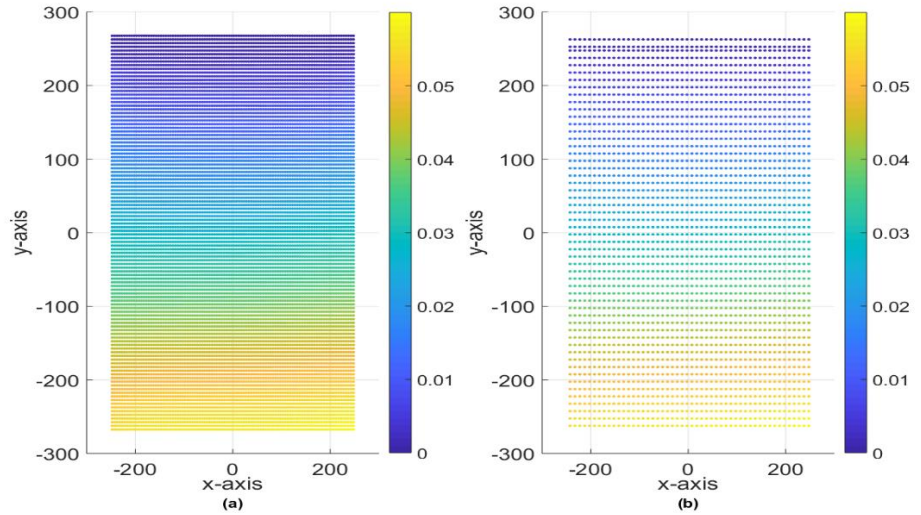

Figure 3-15. Profile of y−axis displacement field: (a) Detailed (Level 0) model and (b) Coarsened (Level 1) model.

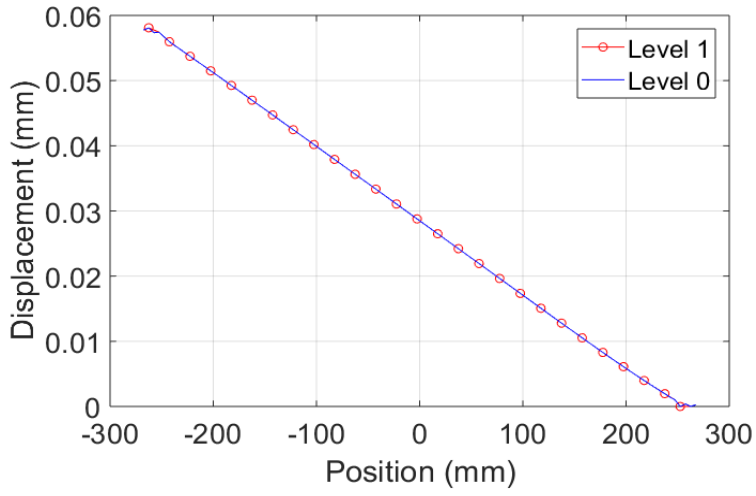

Figure 3-16: Profile of displacement field along a grid line of points in the $\boldsymbol{y}$ −direction

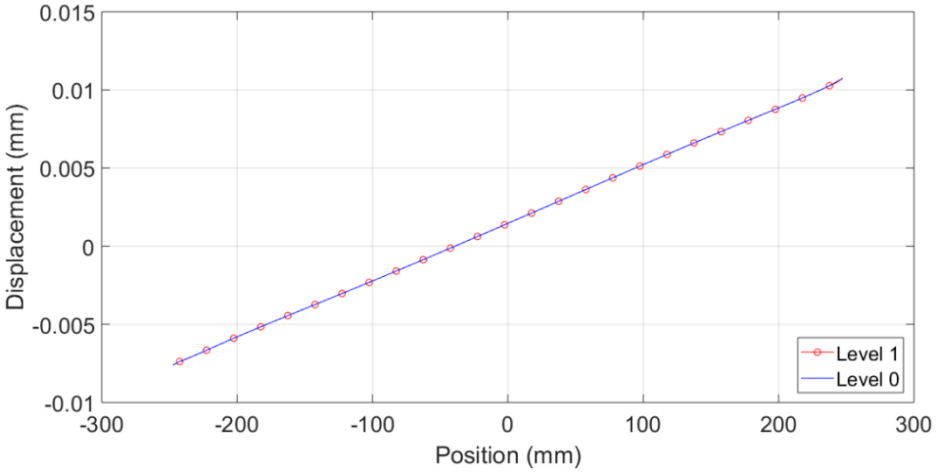

Figure 3-17: Profile of displacement field along a grid line of points in the x-direction

The displacement field obtained from solving both detailed (level 0) and the coarsened model (level 1) are similar as can be seen from Figure 3-14 and Figure 3-15. The displacement profile of a specific grid of points along the y −axis is plotted and shown in Figure 3-16. It is observed that both models result in very similar displacement fields.

3.4.5 Two-dimensional composite plate under tension loading

This example will consider a two-dimensional 500 mm×500 mm square plate with periodic microstructure consisting of alternative strips S_{hard} and S_{soft} of hard and soft materials, respectively as shown in Figure 3-18. Each strip is 50 mm in length. The horizon for both hard and soft sections is 50 mm. The micromodulus of the composite system is given by.

$$\mathbf{C}(\xi) = \begin{cases} \dfrac{36E}{\pi\delta^3 h|\xi|^3}\left(1-\dfrac{|\xi|}{\delta}\right)\begin{bmatrix}\xi_x^2 & \xi_x\xi_y\\ \xi_x\xi_y & \xi_y^2\end{bmatrix}, & \text{if } |\boldsymbol{q}-\boldsymbol{x}| \le \delta \text{ and } (\boldsymbol{x} \in S_{\text{hard}} \text{ and } \boldsymbol{q} \in S_{\text{hard}}) \\ \dfrac{9E}{\pi\delta^3 h|\xi|^3}\begin{bmatrix}\xi_x^2 & \xi_x\xi_y\\ \xi_x\xi_y & \xi_y^2\end{bmatrix}, & \text{if } |\boldsymbol{q}-\boldsymbol{x}| \le \delta \text{ and } (\boldsymbol{x} \in S_{\text{soft}} \text{ or } \boldsymbol{q} \in S_{\text{soft}}) \\ 0, & \text{otherwise} \end{cases} \tag{3-33}$$

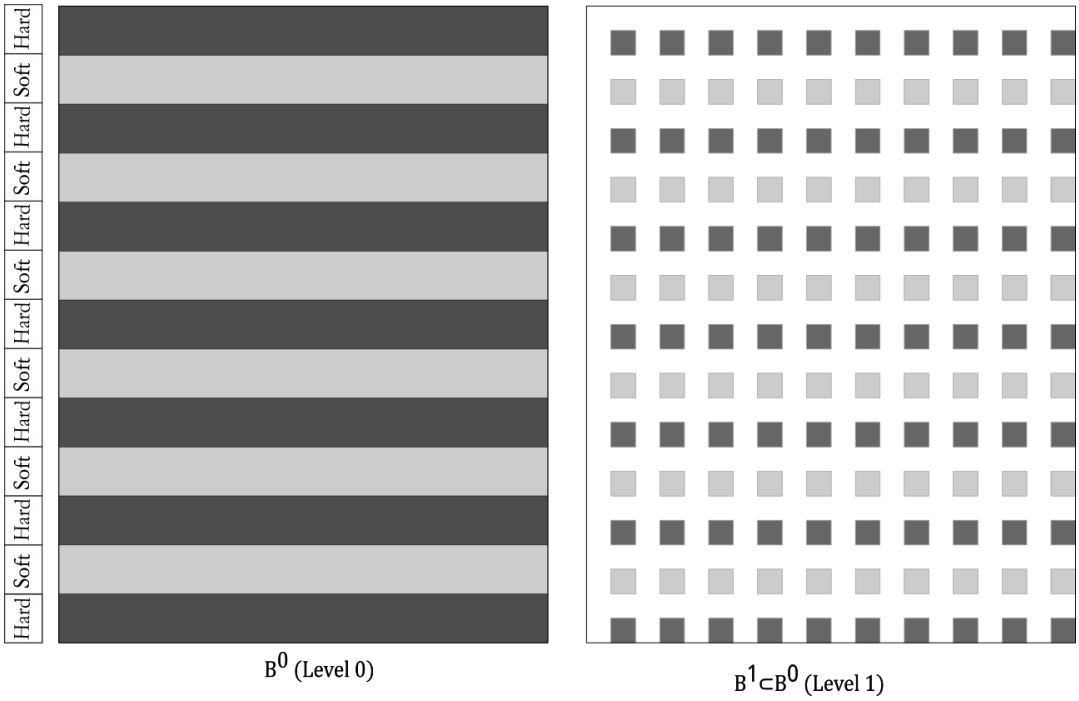

Figure 3-18: Discretisation and coarsening of the two-dimensional composite plate.

The horizon is specified as $\delta^0=3.015\Delta x$. The plate is discretized into 200 points in both x and y −directions with every point having $\Delta x=\Delta y=2.5$ mm. Coarsening of the detailed model and the applied boundary condition is same as that of previous example.

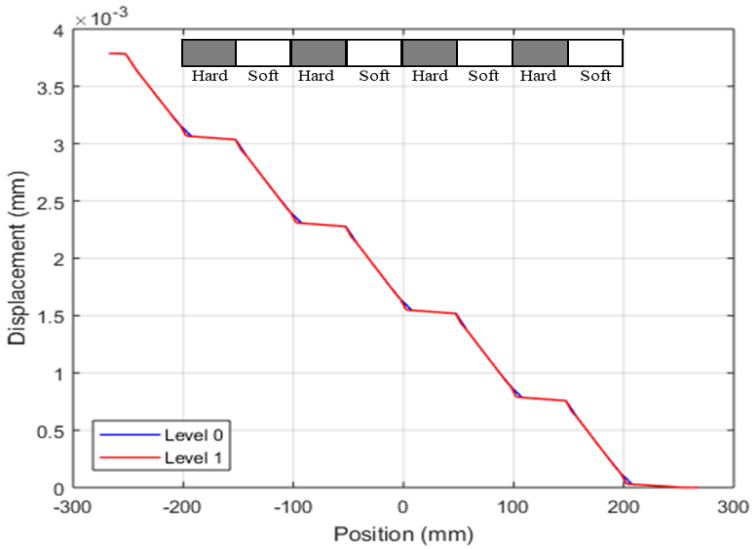

Figure 3-19: Displacement fields for levels 0, 1, and 2 for a two-dimensional plate under tension loading.

The computed displacement profile along the y −direction for the identical boundary condition for the detailed model (level 0) and the coarsened model (level 1) is shown in Figure 3-19. It is observed that because the detailed model included more material points, it has been able to resolve

more microstructural details than the coarsened models. However, both models have the same global stretch thereby demonstrating that the effective properties obtained using this coarsening method are accurate representation of the bulk properties of the composite.

3.5 Computational cost

Determination of computational cost savings arising from coarsening a numerical model will follow from the idea suggested in [1]. Consider a body that is discretized into N_0 nodes in the level 0 model. Let $J=aN_M^n$ be the number of arithmetic operations used by a linear solver to solve the fully coarsened level M model, where a and n are constants (n=3 for Gaussian elimination [1]), and N_M is the total number of nodes in level M model. Suppose each level has $1/\alpha$ as many nodes as the previous level, where α is a constant, such that:

$$N_M = \frac{N_0}{\alpha^{DM}} \tag{3-34}$$

where D is the dimension of the problem (In the example on two-dimensional homogeneous plate, $\alpha = 2$ and $D = 2$). The computational effort in determining material properties at level $m+1$ from level m is proportional to N_m since in doing so, the inverse of the matrix $A_{N_m \times N_m}$ must be computed. Therefore, for some positive constant b, the total arithmetic operations that will be used to coarsen a numerical model and solve the fully coarsened level M model can be written as

$$J = a\left(\frac{N_0}{\alpha^{DM}}\right)^n + \sum_{m=0}^{M-1} \frac{bN_0}{\alpha^{DM}}$$

$$J = a\left(\frac{N_0}{\alpha^{DM}}\right)^n + b\mathrm{N}_0 \frac{1 - 1/\alpha^{DM}}{1 - 1/\alpha}$$

$$J < a\left(\frac{N_0}{\alpha^{DM}}\right)^n + bN_0 \frac{\alpha}{\alpha - 1} \tag{3-35}$$

It can be concluded from (3-35) that the computational effort of coarsening up to level M in a linear solver for a boundary value problem is reduced by a factor of α^{nDM} over the computational effort needed to solve the detailed level 0 model. For a two-dimensional problem such as the example on two-dimensional homogeneous plate, this factor will be $2^{3\times2\times\mathrm{M}} = 2^{6\mathrm{M}}$. The computational price paid to determine the coarsened properties of the model is less than $bN_0\alpha/(\alpha-1)$ which is independent of M. If we are only interested in coarsening up one level only, then $M = 1$, so that the reduction factor becomes $2^6 = 64$ times the number of operations required to solve the complete model.

3.6 Conclusions

The coarsening method developed in [34] extended for two-dimensional application in this thesis has demonstrated its robustness in modelling a range of problems. Moreover, several one-dimensional problems were considered to investigate the effect of different micromodulus functions other than considered in [14]. The examples solved in this work have demonstrated that this method is able to relate the bulk response of materials to the details of their microstructure in two-dimensional problems. This allows us to reduce the order of the problem without losing accuracy in predicting the bulk response of the system. This translates to a reduction in computational time and storage required. Another advantage offered by the coarsening method is that the model retains its attributes such as boundary conditions and applied force density after the coarsening process. This is not the case if the model is reduced without going through the coarsening process. In this case, the boundary conditions and applied force density can no longer be identically applied as in the original model.

It is instructive to mention a few caveats related to this method. This coarsening method is currently valid only for linear and static problems and the boundary conditions applied in the coarsened models must be identical to the boundary conditions of the detailed model.

Chapter 4

4.0 Static condensation for linear peridynamics

This chapter present a MOR framework based on static condensation method [36] that is similar to the coarsening methodology presented in chapter 3.0 in that both methodologies seek to reduce the complexity of a PD model and hence computational effort by reducing the DoFs of the model and yet still able to accurately predict the response of the system. However, the proposed algorithm in this chapter promises to have extended capabilities covering both static and dynamic system response. Numerical investigation will be conducted to demonstrate the robustness of the algorithm in effectively reducing the order of PD models for static, dynamic, and modal response.

4.1 Introduction to MOR using Static condensation

The static condensation scheme is a model order reduction technique widely used in various applications such as structural dynamic optimization, eigenvalue problems, vibration analysis, and fluid-structure interaction. The main objective of model order reduction schemes is to approximate the response of a system with a large number of degrees of freedom using a linear combination of a few selected global approximation vectors. This allows the problem to be reformulated in terms of a smaller set of discrete variables. The transformation equation:

$$\{Z\}_{\boldsymbol{n\times 1}} = [\boldsymbol{T}]_{n\times r}\{\psi\}_{r\times 1} \tag{4-1}$$

is used to map the vector $\{Z\}$ of size n representing the degrees of freedom of the original system, to the reduced vector $\{\psi\}$ of size r, representing the degrees of freedom of the reduced model such that $\{Z\} \gg \{\psi\}$. Model order reduction schemes can be categorized into *physical coordinate reduction*, *generalized coordinate reduction*, and *hybrid coordinate reduction*. In physical coordinate reduction, part of the physical coordinates is eliminated to obtain the reduced model, while in generalized coordinate reduction, the response is described using a set of generalized coordinates that capture the important modes of vibration or deformation. Hybrid coordinate reduction combines physical and generalized coordinates in different regions of the system. In this chapter, the physical coordinate reduction method based on the *static/Guyan condensation* [36]is utilised to develop a reduction framework for the linear PD model.

The subsequent sections will outline the formulation and verification of a MOR framework for linear PD model utilizing the static condensation scheme. In section 4.2, the expression for static condensation of PD static response problem will be derived, to be followed in section 4.3 with the derivation of the expression for the static condensation of PD dynamic response analysis. In

section 4.4, the modal equations of PD theory will be derived, and the proposed condensation algorithm will be applied to obtain the reduced order model for PD eigenproblem. The general form of the reduced micromodulus function is presented in section 4.5. Numerical demonstration of the capabilities of the proposed reduction algorithm in reproducing the static, dynamic, and modal response of PD model using fewer DoFs is presented in section 4.6.

4.2 Reduced static PD models.

Consider a linear PD body $\mathcal{B}$ that is discretised into N number of material points. Considering static response, then (2-112) for a system of N material points is:

$$[C]_{N\times N}\{u\}_N = \{b\}_N \tag{4-2}$$

The objective is to replace this system with a reduced degree of freedom system while maintaining the kinematic characteristics of the original system. Let $\{u_a\} \subset \{u\}_N$ be the primary (active) DoFs to be retained and $\{u_d\} \subset \{u\}_N$ be the secondary DoFs to be condensed out.

To carry out the condensation process, the assembled PD equilibrium equations are partitioned as follows:

$$\begin{bmatrix} [C_{aa}] & [C_{ad}] \\ [C_{da}] & [C_{dd}] \end{bmatrix} \begin{Bmatrix} \{u_a\} \\ \{u_d\} \end{Bmatrix} = \begin{Bmatrix} \{b_a\} \\ \{b_d\} \end{Bmatrix} \tag{4-3}$$

The global vector of DoFs of the system may be written as

$$\{u\}_N = \{u\} = \begin{Bmatrix} \{u_a\} \\ \{u_d\} \end{Bmatrix} \tag{4-4}$$

Multiplying out equation (4-3) we have

$$[C_{aa}]\{u_a\} + [C_{ad}]\{u_d\} = \{b_a\} \tag{4-5}$$

$$[C_{da}]\{u_a\} + [C_{dd}]\{u_d\} = \{b_d\} \tag{4-6}$$

Consider the solution to equation (4-6). If $[C_{dd}]$ is non singular, then we can solve for the DoFs to be condensed out:

$$\{u_d\} = [C_{dd}]^{-1}(\{b_d\} - [C_{ad}]\{u_a\}) \tag{4-7}$$

Substituting equation (4-7) into equation (4-5) yields

$$[C_G]\{u_a\} = \{b_G\} \tag{4-8}$$

Equation (4-8) is the condensed linearized PD equilibrium equation, where:

$$[C_G] = [C_{aa}] - [C_{ad}][C_{dd}]^{-1}[C_{da}], \qquad \{b_G\} = \{b_a\} - [C_{ad}][C_{dd}]^{-1}\{b_d\} \tag{4-9}$$

are the condensed micromodulus matrix and body force vector respectively. If we assume the inertia contribution as well as the external forces acting on the secondary DoFs to be negligible, this will permit a static relationship between the primary DoFs and the secondary DoFs such that equation (4-6) yields:

$$\{u_d\} = [R_G]\{u_a\} \tag{4-10}$$

where $[R_G] \in R^{d\times a}$ represents the Guyan condensation matrix which is defined as

$$[R_G] = -[C_{dd}]^{-1}[C_{da}] \tag{4-11}$$

Introducing equation (4-11) into equation (4-4) gives an expression similar to (4-1):

$$\{u\} = [T_G]\{u_a\} \tag{4-12}$$

In equation (4-12), $[T_G] \in R^{n\times a}$ is a linear transformation matrix that maps DoFs in the reduced model onto DoFs in the full model and is defined as:

$$[T_G] = \begin{bmatrix} [\mathrm{I}] \\ [R_G] \end{bmatrix} \tag{4-13}$$

Where [I] is an $a \times a$ identity matrix. It is easily verifiable that equation (4-9) can be expressed as:

$$[C_G] = [T_G]^T[C][T_G], \qquad \{b_G\} = [T_G]^T\{b\} \tag{4-14}$$

Note that the static condensation is so called because we ignored the inertia effect on the deleted DoFs. Also note that to obtain the expression for the transformation matrix in equation (4-13), an assumption of zero body force density acting on the deleted DoFs was made. However, the fact that the expansion of equation (4-14) exactly gives the expression in equation (4-9) shows that this assumption does not affect the reduced stiffness matrix and the reduced force density vector. The condensed PD equilibrium equations as represented by equation (4-8) yields the exact solution of the PD model at the retained material points as would be obtained if we used the detailed model.

4.3 Reduced dynamic models

To reduce the order of a dynamic PD model, the equation of motion given in equation (2-112) may be written in partitioned form:

$$\begin{bmatrix} [M_{aa}] & [M_{ad}] \\ [M_{da}] & [M_{dd}] \end{bmatrix} \begin{Bmatrix} \{\ddot{u}_a\} \\ \{\ddot{u}_d\} \end{Bmatrix} + \begin{bmatrix} [C_{aa}] & [C_{ad}] \\ [C_{da}] & [C_{dd}] \end{bmatrix} \begin{Bmatrix} \{u_a\} \\ \{u_d\} \end{Bmatrix} = \begin{Bmatrix} \{b_a\} \\ \{b_d\} \end{Bmatrix} \tag{4-15}$$

If we assume the micromodulus function $[C]$ to be time invariant, then $[T_G]$ is independent of time and hence the second derivative of equation (4-12) with respect to time yields:

$$\{\ddot{u}\} = [T_G]\{\ddot{u}_a\} \tag{4-16}$$

Introducing equations (4-12) and (4-16) into equation (2-112) and pre-multiplying both sides by the transpose of the transformation matrix $[T_G]$ gives the equation of equilibrium of the reduced model:

$$[M_G]\{\ddot{u}_a\} + [C_G]\{u_a\} = \{b_G\} \tag{4-17}$$

where the matrices $[M_G]$ and $[C_G]$ and the vector $\{b_G\}$ are the condensed mass matrix, condensed micromodulus matrix and condensed body force vector respectively associated with the reduced model, defined as:

$$[M_G] = [T_G]^T[M][T_G], \qquad [C_G] = [T_G]^T[C][T_G], \qquad \{b_G\} = [T_G]^T\{b\} \tag{4-18}$$

If we neglect dynamic effects in the reduced model, equation (4-17) specialises to the reduced model for static problem defined in equation (4-8). Since the majority of storage requirement and computational effort required to implement this condensation technique is used in the computation of $[C_{dd}]^{-1}$, a computationally more efficient way to achieve the condensation of the PD static model is to employ the standard Gauss-Jordan elimination procedure [92].

4.4 Reduced eigenvalue models

Assume that the solution u to equation (2-77) is given by the general form of a plane wave:

$$u(x,t) = Ae^{i(kx-\omega t)} \tag{4-19}$$

where u is the displacement of a point x, A is the constant amplitude vector, k is the wave number, ω is the wave frequency and t is time. Substituting equation (4-19) into equation (2-77) and assuming no body force applied will yield:

$$-\omega^2\rho(x)A = \int_{\mathcal{H}_x} C(x,q)\left(e^{ik(q-x)} - 1\right)dV_k \cdot A \tag{4-20}$$

Taking Euler's transformation of equation (4-20) gives

$$-\omega^2\rho(x)u(x,t)$$

$$= \int_{\mathcal{H}_x} C(x,q)\big(\cos\big(k(q-x)\big) + i\sin\big(k(q-x)\big) - 1\big)dV_k \tag{4-21}$$

$$\cdot\, u(x,t)$$

Since the micromodulus function is an even function and $\sin\big(k(q-x)\big)$ is an odd function, equation (4-21) reduces to

$$\omega^2\rho(x)A = \int_{\mathcal{H}_x} C(x,q)\big(1 - \cos\big(k(q-x)\big)\big)dV_k \cdot A \tag{4-22}$$

It can be inferred from equation (2-73) that the integral in equation (4-22) can be written in a matrix form. Using the simplified notation

$$\mathcal{D}(k,\xi) = \int_{\mathcal{H}_x} C(x,q)\big(1 - \cos\big(k(q-x)\big)\big)dV_k \tag{4-23}$$

with the definition that $\xi = q - x$, then equation (4-23) can be written as

$$\omega^2\rho(x)A = \mathcal{D}(k,\xi)\cdot A \tag{4-24}$$

which gives us a classical eigenvalue problem with the following characteristic equation.

$$|\mathcal{D}(k,\xi) - \omega^2\rho(x)| = 0 \tag{4-25}$$

The dispersion matrix $\mathcal{D}(k,\xi)$ first appeared in [10]. The eigenvalues and eigenvectors resulting from equation (4-25) gives the natural frequencies and natural modes of the peridynamic system. Equation (4-25) may be written in matrix form as

$$|[\mathcal{D}] - \omega^2[M]| = 0 \tag{4-26}$$

In equation (4-26), $[M] = \rho[\mathrm{I}]$ is the mass-density matrix and $[\mathrm{I}]$ is the identity matrix. The reduced order eigenvalue problem may be stated as

$$|[\mathcal{D}_G] - \omega^2[M_G]| = 0 \tag{4-27}$$

where $[\mathcal{D}_G]$ is the statically condensed dispersion matrix, and is defined as

$$[\mathcal{D}_G] = [T_G]^T[\mathcal{D}][T_G] \tag{4-28}$$

4.5 Condensation of the micromodulus function

This section will illustrate the typical form of a condensed micromodulus function. Consider a one-dimensional homogeneous bar of length 1.0 with a micromodulus function of the form:

$$\mathbf{C}(\xi) = \begin{cases} 1.0\left(1 - \dfrac{|\xi|}{\delta}\right), & \text{if } |\xi| \leq \delta \\ 0, & \text{if } |\xi| > \delta \end{cases} \tag{4-29}$$

The bar is discretised into 100 nodes with interaction distance of $3dx$, where dx represents the distance between successive nodes. The reduced model consists of every fourth node in the detailed model as shown in Figure 4-1 in which retained nodes are designated with letter 'a' and deleted nodes are designated with letter 'd'.

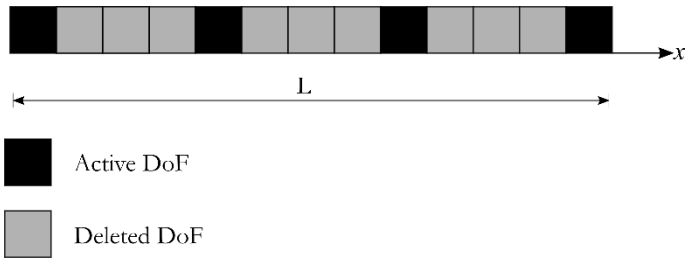

Figure 4-1: Schematic representation of 1D reduction process

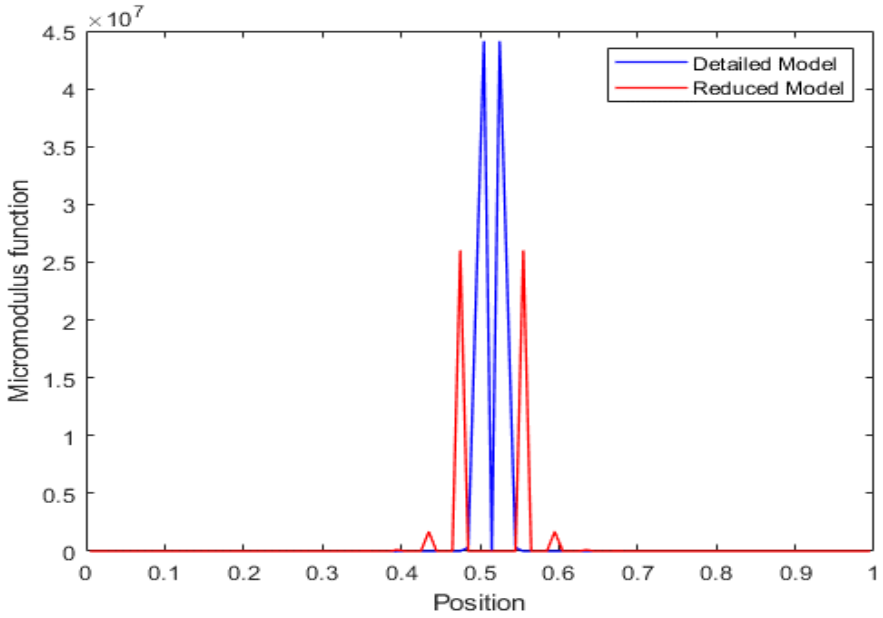

Figure 4-2: Coarsening of 1D Micromodulus function.

The micromodulus of the detailed model and that of the reduced model is shown in Figure 4-2. The micromodulus function of the reduced model as can be seen from Figure 4-2 is defined only at the retained DoFs.

4.6 Numerical results

4.6.1 Reduction of static problems

In this section, a series of numerical experiments will be undertaken to illustrate the application of this model reduction technique in coarsening one and two-dimensional PD models.

4.6.1.1 A bar with periodic microstructure

Consider a composite bar with length 1.0 and a periodic microstructure consisting of alternate strips S_{hard} and S_{soft} of hard and soft materials respectively as shown in Figure 4-3. Each strip is 0.05 in length. The interaction distance in both hard and soft materials is $3dx$. The micromodulus of the composite system is:

$$\mathbf{C}(\xi) = \begin{cases} 10.0\left(1-\dfrac{|\xi|}{\delta}\right), & \text{if } |\boldsymbol{q}-\boldsymbol{x}| \le \delta \text{ and } (\boldsymbol{x} \in S_{\text{hard}} \text{ and } \boldsymbol{q} \in S_{\text{hard}}) \\ 1.0\left(1-\dfrac{|\xi|}{\delta}\right), & \text{if } |\boldsymbol{q}-\boldsymbol{x}| \le \delta \text{ and } (\boldsymbol{x} \in S_{\text{soft}} \text{ or } \boldsymbol{q} \in S_{\text{soft}}) \\ 0, & \text{otherwise} \end{cases} \tag{4-30}$$

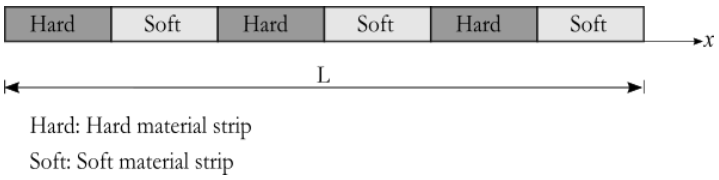

Figure 4-3: A schematic representation of the composite bar showing hard and soft material strips.

Bonds with both ends in a hard strip are assigned hard properties, otherwise, they are given soft material properties. Coarsening the detailed model is schematical represented by Figure 4-1. Every fourth material point in the detailed model is retained as an active point in the coarsened model. In the detailed model, a force density of $b = 0.002$ is applied to the rightmost material point while the leftmost material point is constrained from movement. Figure 4-4 shows the displacement fields of the detailed as well as coarsened model.

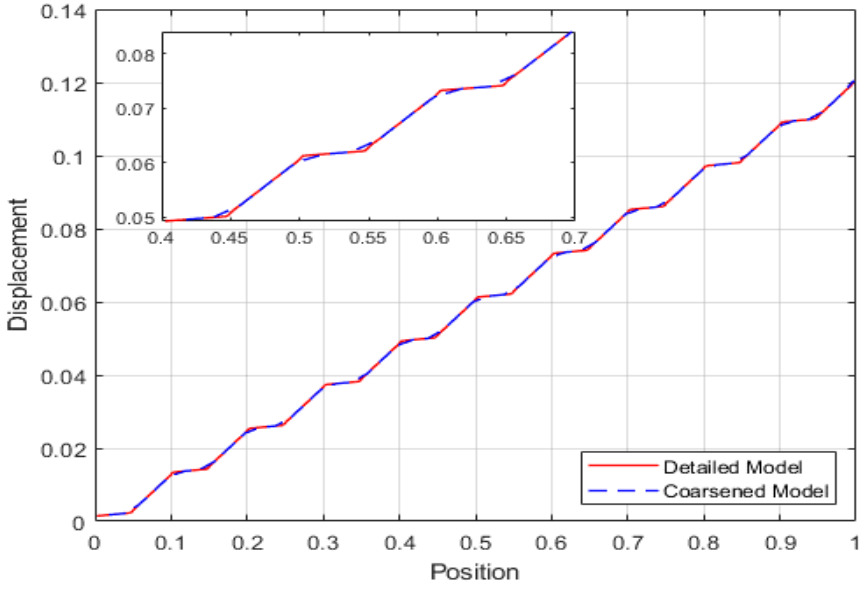

Figure 4-4: Displacement fields for detailed and reduced models

Results of displacement fields from simulation of both the detailed and reduced models shows exact matches for all shared material points between the two models and hence both have the same global stretch. However, as expected, the reduced model reflects less resolution of microstructural information than the detailed model.

4.6.1.2 Reduction of a static plate model

The static condensation can be employed in the reduction of static models of PD plates. The motivation for this may arises from the need to analyse a very large PD model and if the key focus is in determining the global response of the system without the need for a very detailed model. The objective in this example is to employ static condensation to eliminate all PD except those corresponding to the nodes located at the vertices of the plate as shown in Figure 4-5. The bottom length of the plate is 1.0 while every other edge of the plate is of length 0.5. The micromodulus function of the plate material has the form.

$$\mathbf{C}(\xi) = 10.0\left(1 - \frac{|\xi|}{\delta}\right), \qquad \text{if } |\boldsymbol{q} - \boldsymbol{x}| \leq \delta \tag{4-31}$$

The maximum interaction distance $\delta = 3dx$, where dx is the horizontal distance between nodes. A body force density of 0.001 is applied to the boundary nodes at topmost edge of the plate as shown in Figure 4-5. The detailed model is discretized into 100 material points.

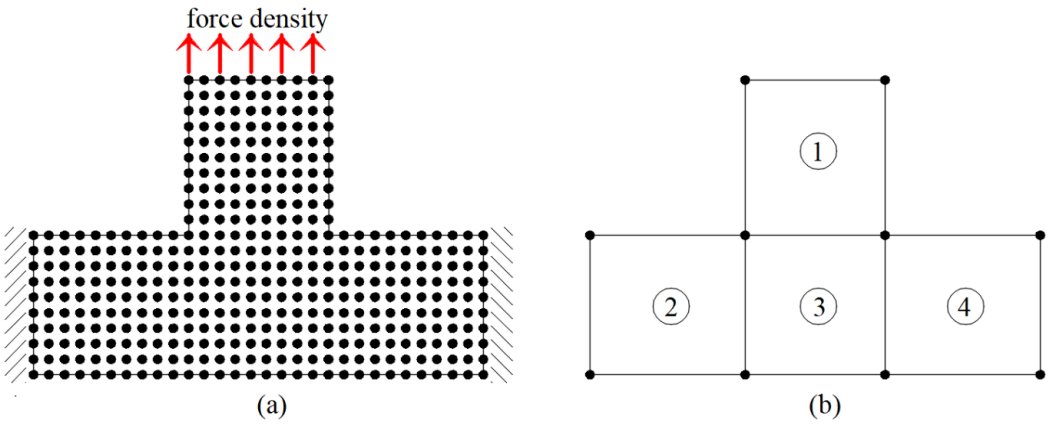

Figure 4-5: Schematic representation of the PD model of plate for static response analysis

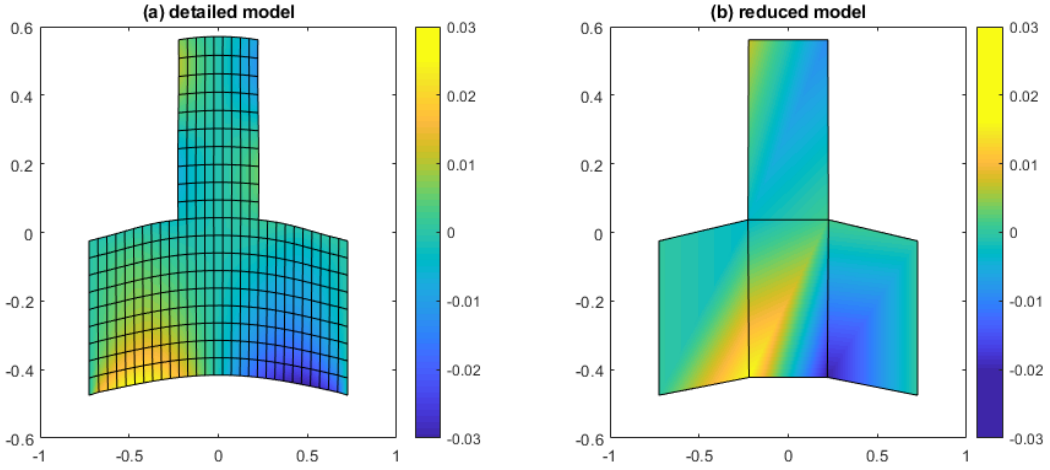

Figure 4-6: Displacement profile in x-direction (a) Detail model (b) Condensed mode

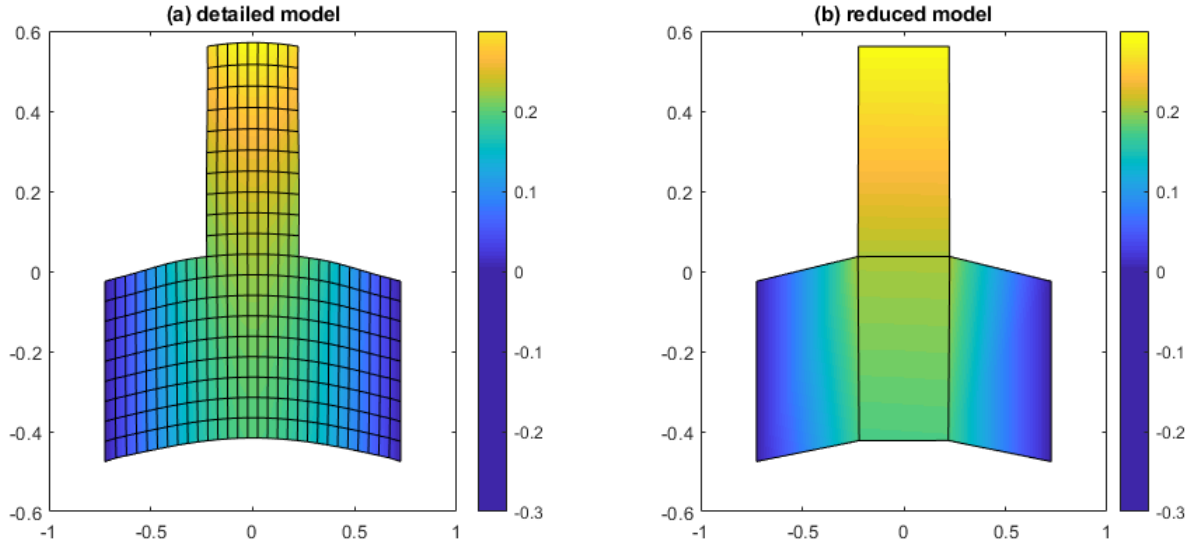

Figure 4-7: Displacement profile in y-direction (a) Detail model (b) Condensed model

The reduction procedure is achieved by condensing a group of nodes to form a substructure. At the end of the procedure, we are left with four (4) substructures bounded by ten (10) '*supernodes*' as shown in Figure 4-5(b). An examination of the displacement results obtained from the analysis of both the detailed and condensed models reveals that the solutions are exact.

This observation highlights the accuracy and effectiveness of the reduction procedure in capturing the essential behaviour of the system. By condensing multiple nodes into a smaller number of representative supernodes, the model order reduction technique successfully reduces the computational complexity of the analysis without sacrificing accuracy. This is particularly valuable in scenarios where computational efficiency is desired, allowing for the analysis of larger-scale systems or the exploration of extensive parametric studies.

4.6.2 Reduced Eigenproblems

4.6.2.1 A bar with one end fixed and the other free

Consider a bar of length $L = 1$ and uniform cross-sectional area $A = 1$ with the following material properties: Young Modulus $E = 1$, density $\rho = 1$. Let the bar be fixed at one end and free at the other end as shown in Figure 4-8.

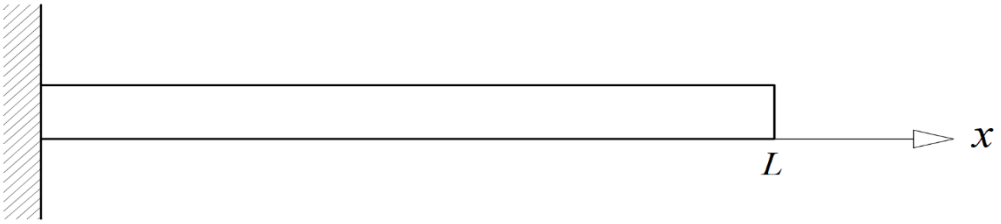

Figure 4-8: A bar with one end fixed and one end free.

To numerically compute the natural frequencies and mode shapes arising from (4-27), the given bar is discretized into 1000 nodes. The interaction distance characteristic of the bar material is assumed to be $3dx$, with dx being the distance between nodes. The material is assumed to have a micromodulus function of the form:

$$\boldsymbol{C}(\xi) = \frac{2E}{A\delta^2|\xi|} \tag{4-32}$$

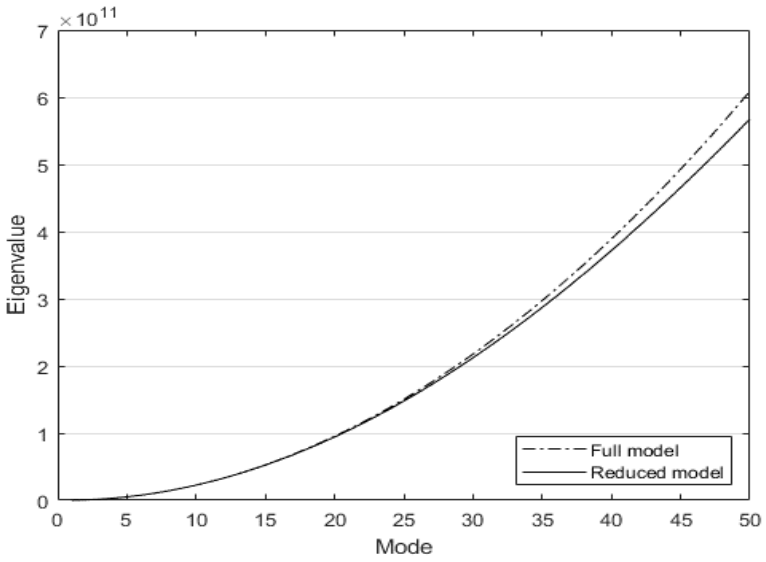

Figure 4-9: Comparison of eigenvalues from the full PD model and reduced model

The first five lowest frequencies of the bar as computed from (4-25) are shown in Table 4-1. These frequencies are then validated against frequencies obtained from the characteristic equation of a corresponding Finite Element (FE) model of the bar. The eigen values of the first 50 modes are presented in Figure 4-9

Table 4-1: Natural frequencies of the first five modes computed using the full PD model, reduced PD model and FE analysis.

Mode	FEM	Peridynamics		Difference between full and reduced model (%)
		Full model	Reduced model	
1	1.571	1.569	1.569	0.0006
2	4.712	4.708	4.708	0.0156
3	7.854	7.846	7.845	0.0724
4	10.996	10.984	10.982	0.1987
5	14.137	14.123	14.118	0.4223

Percentage difference between the natural frequencies computed from modal analysis of the full PD model and the reduced order PD model as presented in Table 4-1 shows a difference that ranges from 0.0006% to 0.4223%. This error margin coupled with the result presented in Figure

4-9 shows that the reduced model can accurately reproduce the lower eigenproperties of the full model.

4.6.3 Reduction of dynamic problems

In this section, the static condensation technique will be applied to reduce the order of a PD model and determine its time-history response. The objective is to determine the effectiveness of the model reduction technique in predicting the dynamic response of a given model despite the use of fewer DoFs. To illustrate the capabilities and limitation of the dynamic condensation technique, the bar shown in Figure 4-8 will be subjected to various excitation to determine the accuracy of the dynamic response predicted from the reduced order model. The bar will be assumed to have a Young's modulus of 200 GPa and a density of 7850 KG/m^3. The numerical integration method used to integrate the discretised peridynamic equation of motion for the transient analysis is the forward Euler method.

4.6.3.1 Free vibration of a bar using peridynamics

The transient response of the PD bar will be studied. Three initial condition cases will be studied.

4.6.3.1.1 Case 1: Displacement induced initial excitation

In this scenario, the bar is given an initial constant strain of 1×10^{-4}. The excitation is immediately removed to allow for free vibration of the bar. A transient analysis of the full PD model of the bar was conducted. The condensation process proceeded by retaining every forth node of the full PD model as shown in Figure 4-10.

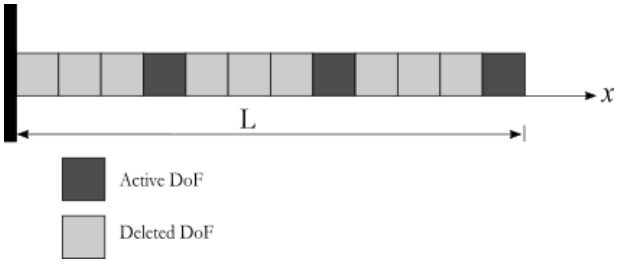

Figure 4-10: Discretization and condensation of the full PD model.

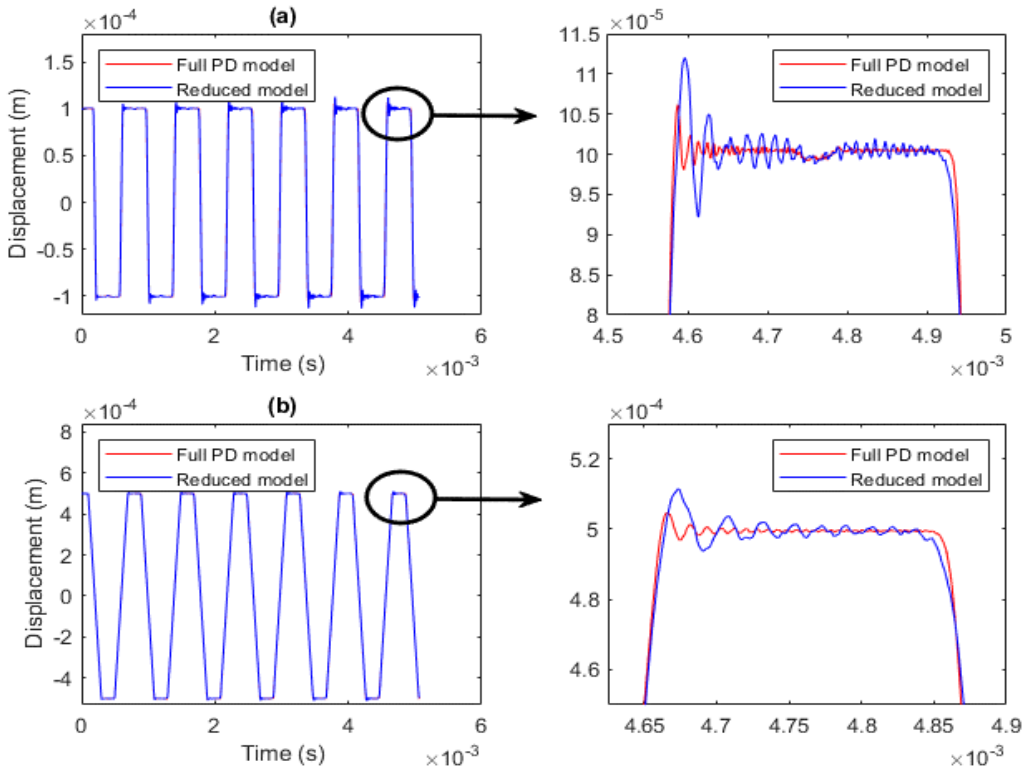

Figure 4-11: Time-history response of material points located at (a) $x = 0.0995$, and (b) $x = 0.4995$, for both full and reduced models.

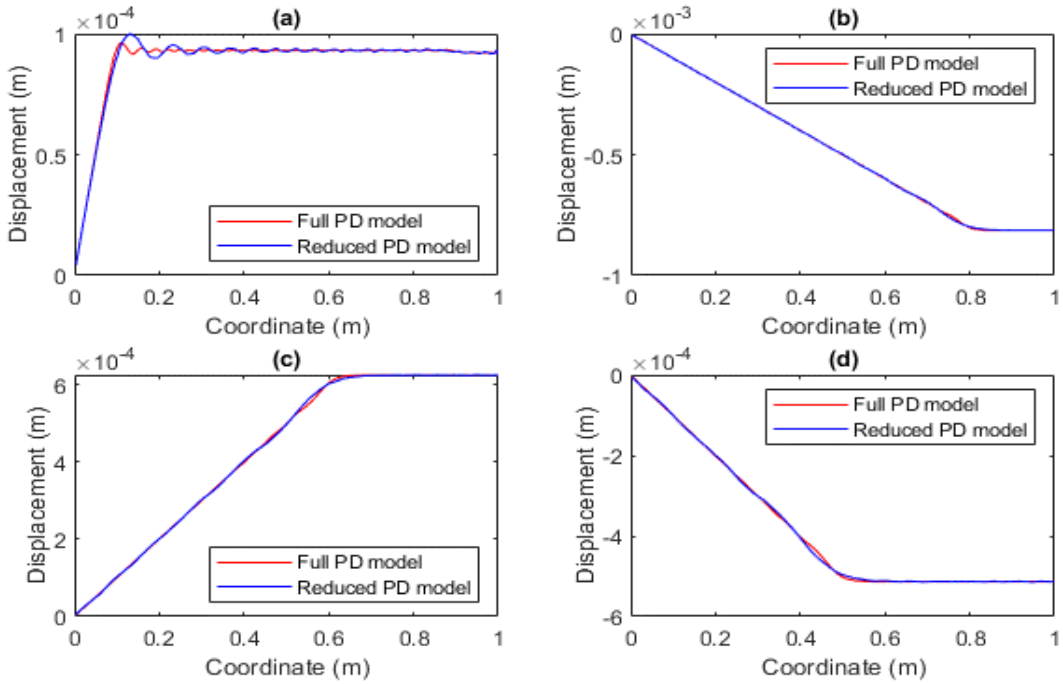

Figure 4-12: Displacement values at all nodes at (a) 5000th time step, (b) 10000th time step, (c) 20000th time step, and (d) 26000th time step.

The results of the time-history response of material points located at $x = 0.0995$ and $x = 0.4995$ arising from both the full PD model and the reduced model are shown in Figure 4-11(a and b) respectively. Figure 4-12 shows the displacement values of all nodes at the 5000th, 10000th, 20000th and 26000th time steps. These results show that the reduced model closely reproduces the dynamic response of the original PD model. However, as can be seen from Figure 4-11, there are some errors which arises because of our ignorance of inertia effects at the deleted DoF.

4.6.3.1.2 Case 2: Force induced initial excitation.

In this case study, initial constant body force density of 1×10^4 kN$/m^3$ is applied to every second node of the discretised PD bar and the force is immediately removed to allow for a free vibration of the bar. Equation (4-18) is used to condense the mass matrix, stiffness matrix and the force vector. The time-history response of points located at $x = 0.0995$, $x = 0.2995$, $x = 0.4995$ and $x = 0.7995$ for both the full and reduced models are shown in Figure 4-13 while Figure 4-14 shows the displacement values for all nodes at time steps 5000, 10000, 20000 and 26000. The results of the time-history analysis of the both the full PD model and the reduced model shows that the condensation technique can accurately reproduce the dynamic response of the full PD model of the bar.

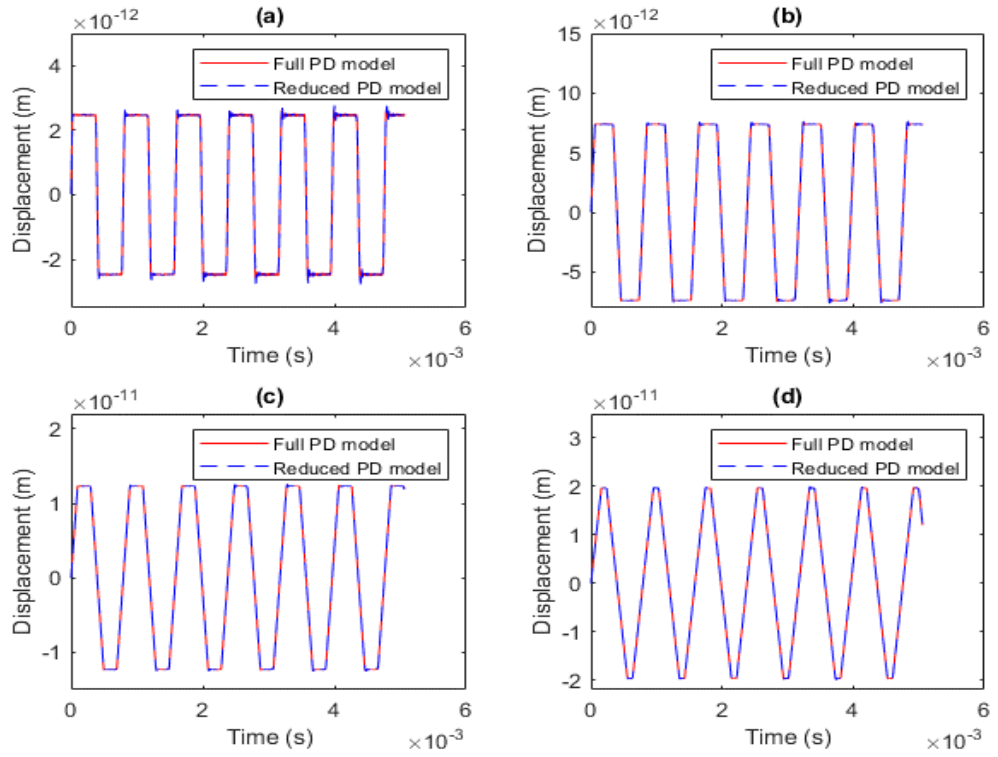

Figure 4-13: Time-history response of material points located at (a) $x = 0.0995$ (b) $x = 0.2995$ (c) $x = 0.4995$ and (d) $x = 0.7995$ for both the Full PD model and Condensed model.

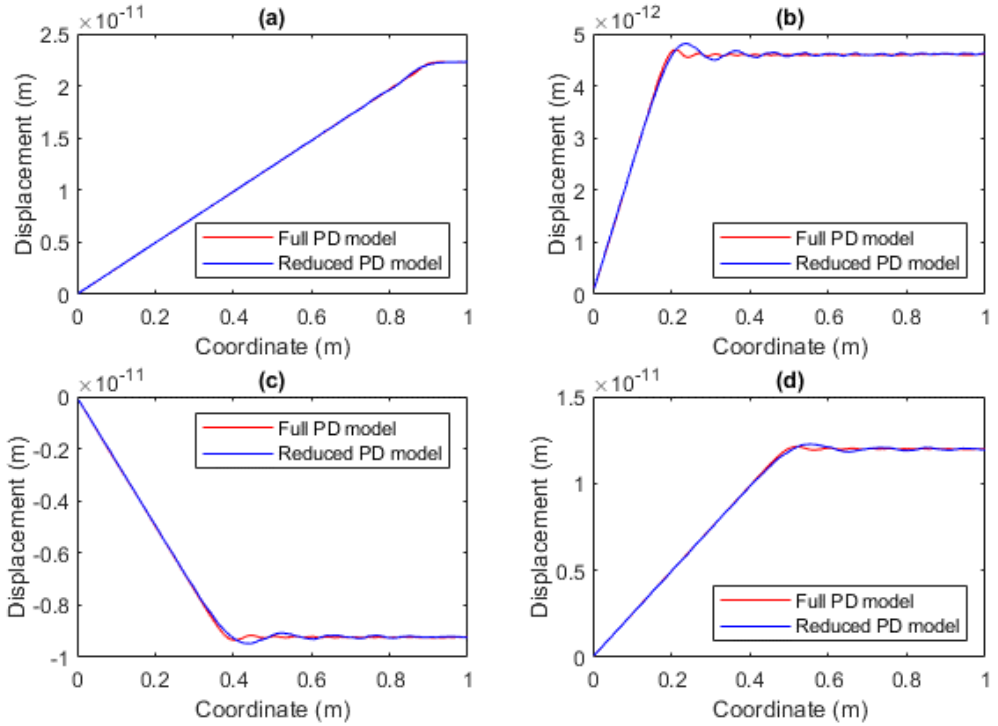

Figure 4-14: Displacement values at all nodes at (a) 5000th time step, (b) 10000th time step, (c) 20000th time step, and (d) 26000th time step.

4.6.3.2 Forced vibration.

The bar in this case is assumed to be subjected to a time-dependent body force density of the form $\{b(t)\} = \{b_o\}\sin(\omega t)$ such that b_o is the amplitude of excitation, ω is the frequency of excitation. The force is applied at the rightmost node of the bar.

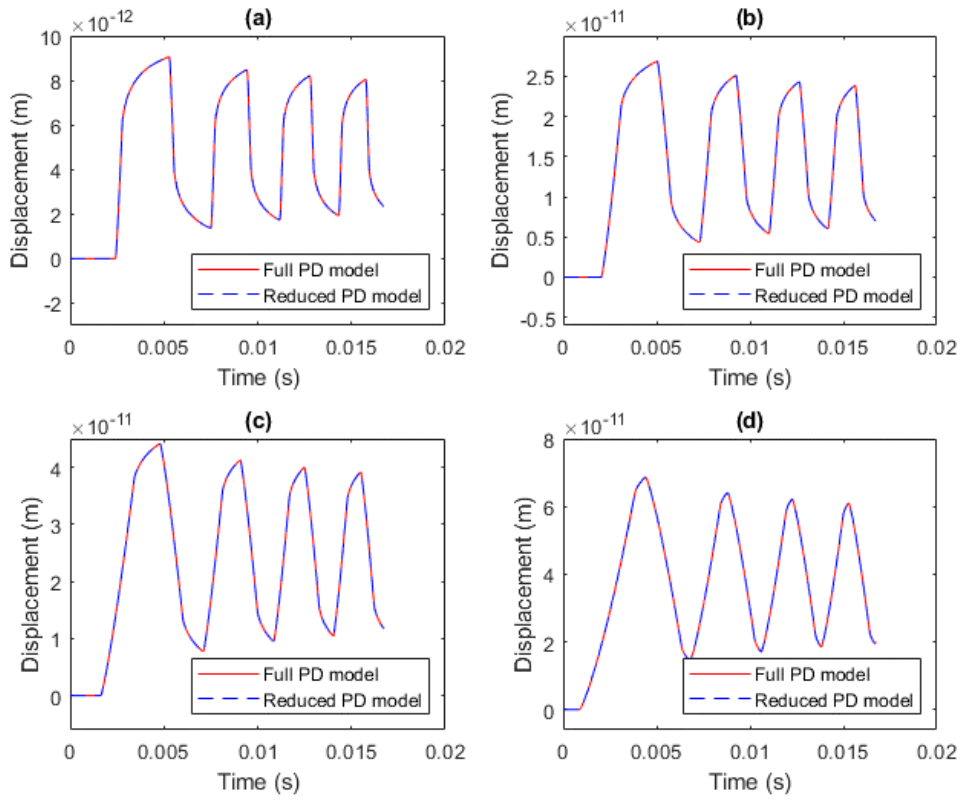

Figure 4-15: Time-history response of material points located at $x = 0.0995$, 0.2995, 0.4995 and 0.7995 for both the Full PD model and Condensed model.

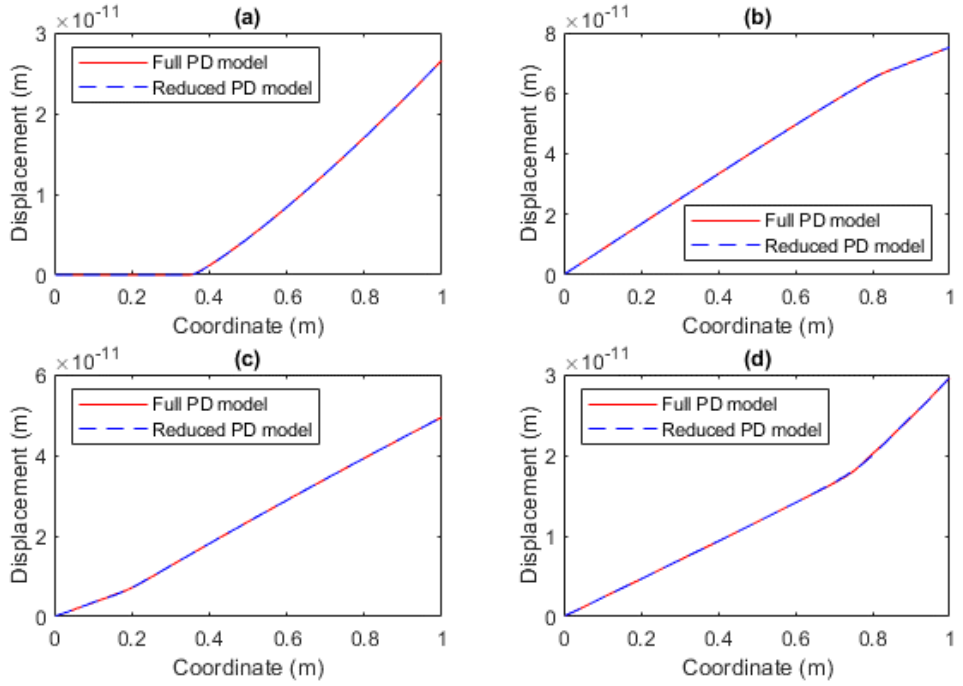

Figure 4-16: Displacement values at all nodes at (a) 10000th time step, (b) 20000th time step, (c) 50000th time step, and (d) 86000th time step

Results from a transient analysis of the full and reduced models for $b_o = 1 \times 10^4$ kN$/m^3$ and $\omega = 5$ rad/sec for a total of 86,00 time steps are shown in Figure 4-15 and Figure 4-16. The dynamic response of the full PD model was accurately predicted using the reduced model.

4.7 Conclusion

A model reduction procedure for PD systems based on static condensation has been developed and investigated in this study. The results of numerical experiments presented shows that the reduction algorithm based on static condensation technique can closely preserve the characteristics and response of the original model. In the static regime, the algorithm has proved to yield identical results compared to those obtained from the original model. Although the results of the eigenresponse prediction of the reduced model shows some errors as shown in the eigenresponse and transient analysis, however, the results show that the proposed algorithm has capabilities of accurate prediction of dynamic response at low frequencies.

Chapter 5

5.0 Static condensation of peridynamic heat transport model

The efficient simulation of heat transport phenomena using PD for practical applications is a good motivation for employing model order reduction techniques. This will enable PD to be utilized in modelling larger and more complex problems, thus facilitating its broader applications in industrial contexts. Using high-fidelity models in certain applications poses challenges due to their size and computational complexity. This is particularly evident when verifying the design and performance of large and complex systems. The need for reduced models becomes even more apparent in the repetitive usage of such systems in a design mode, such as control systems. Notably, control systems for manufacturing processes (e.g., brazing, and annealing furnaces) and thermal management of optical systems require efficient and responsive control [93].

Model order reduction provides a solution by offering simplified models that retain essential features. These reduced models enhance computational efficiency without sacrificing crucial insights or accuracy. This enables efficient and responsive control in applications like manufacturing process control and thermal management of optical systems.

In this chapter, these motivations are addressed by extending and tailoring the model order reduction framework based on static condensation protocol developed in 4.1 for peridynamic heat transport models. The proposed reduction framework is expected to significantly decrease the computational cost associated with PD transport model, allowing for the simulation of larger and more complex heat transport problems while maintaining fidelity to the underlying physics. The end goal is to expand the scope of applicability and effectiveness of PD in simulating large-scale industrial problems.

5.1 The nonlocal peridynamic heat transport model

The groundwork for this extension will begin with the derivation of the peridynamic heat equation by restating the peridynamic balance law (2-40). Let the region occupied by a body $\mathcal{B}$ be given by the open domain $\Omega \subseteq \mathbb{R}^n$. Let $\widetilde{\Omega} \subseteq \Omega$ be an open subregion, then a quantitative statement of a balance law for Ω can be stated in terms of a scalar intensive quantity q as:

$$\mathcal{A}(\widetilde{\Omega}, q) = \mathcal{P}(\widetilde{\Omega}) - \mathcal{F}(\widetilde{\Omega}, \mathbb{R}^n \backslash \widetilde{\Omega}; q) \tag{5-1}$$

where (5-1) postulate that $\mathcal{A}(\widetilde{\Omega}, q)$ (the time rate of change of the intensive quantity q) is equal to $\mathcal{P}(\widetilde{\Omega})$ (the rate at which the quantity is produced within the subdomain by sources, minus

$\mathcal{F}\left(\widetilde{\Omega}, \mathbb{R}^n \backslash \widetilde{\Omega}; q\right)$ (the rate at which the intensive quantity exits the subdomain). The rate of change and production of q within $\widetilde{\Omega}$ can be written as

$$\mathcal{A}\left(\tilde{\Omega}; q\right) = \frac{\partial}{\partial t}\int_{\tilde{\Omega}} q(\boldsymbol{x}, t)\, d\boldsymbol{x} \quad \text{and} \quad \mathcal{P}\left(\tilde{\Omega}\right) = \int_{\tilde{\Omega}} b(\boldsymbol{x}, t)\, d\boldsymbol{x} \tag{5-2}$$

If $\widetilde{\Omega} \subset \Omega$ is assumed to interact only with the open subregion $\widetilde{\Omega}_I \subset \Omega_I$, then (5-1) can be written as:

$$\mathcal{A}\left(\tilde{\Omega}; q\right) = \mathcal{P}\left(\tilde{\Omega}\right) - \mathcal{F}\left(\tilde{\Omega}, \tilde{\Omega}_I; q\right) \tag{5-3}$$

From the statement of the divergence theorem which can be stated as the flux of a vector $\boldsymbol{v} \in \mathbb{R}^n$ out of a region $\Omega_1 \subset \mathbb{R}^n$ is equal to the volume integral of the divergence of $\boldsymbol{v}$ over Ω_1. Thus from (2-1) and (2-4):

$$\mathcal{F}(\Omega_1, \Omega_2; q) = \int_{\Omega_1} \mathcal{D}(\boldsymbol{v})(\boldsymbol{x})\, d\boldsymbol{x} = \int_{\Omega_1}\int_{\Omega_2} \left(\boldsymbol{v}(\boldsymbol{x}, \boldsymbol{y}) + \boldsymbol{v}(\boldsymbol{y}, \boldsymbol{x}) \cdot \boldsymbol{\alpha}(\boldsymbol{x}, \boldsymbol{y})\right) d\boldsymbol{y}\, d\boldsymbol{x} \tag{5-4}$$

If one writes $\Omega_1 = \widetilde{\Omega}$ and $\Omega_2 = \widetilde{\Omega}_I$, then (5-4) becomes:

$$\begin{aligned}
\mathcal{F}\left(\widetilde{\Omega}, \widetilde{\Omega}_I; q\right) &= \int_{\widetilde{\Omega}}\int_{\widetilde{\Omega}_I} \left(\boldsymbol{v}(\boldsymbol{x}, \boldsymbol{y}) + \boldsymbol{v}(\boldsymbol{y}, \boldsymbol{x}) \cdot \boldsymbol{\alpha}(\boldsymbol{x}, \boldsymbol{y})\right) d\boldsymbol{y}\, d\boldsymbol{x} \\
&= -\int_{\widetilde{\Omega}_I}\int_{\widetilde{\Omega}} \left(\boldsymbol{v}(\boldsymbol{x}, \boldsymbol{y}) + \boldsymbol{v}(\boldsymbol{y}, \boldsymbol{x}) \cdot \boldsymbol{\alpha}(\boldsymbol{x}, \boldsymbol{y})\right) d\boldsymbol{y}\, d\boldsymbol{x} \\
&= -\int_{\widetilde{\Omega}_I}\int_{\widetilde{\Omega}\cup\widetilde{\Omega}_I} \left(\boldsymbol{v}(\boldsymbol{x}, \boldsymbol{y}) + \boldsymbol{v}(\boldsymbol{y}, \boldsymbol{x}) \cdot \boldsymbol{\alpha}(\boldsymbol{x}, \boldsymbol{y})\right) d\boldsymbol{y}\, d\boldsymbol{x} \\
\mathcal{F}\left(\widetilde{\Omega}, \widetilde{\Omega}_I; q\right) &= \int_{\widetilde{\Omega}_I} \mathcal{N}(\boldsymbol{v})(\boldsymbol{x})\, d\boldsymbol{x} \quad \forall \widetilde{\Omega} \subset \Omega
\end{aligned} \tag{5-5}$$

where the third equality follows from consideration of (2-2) and the fourth is due to (2-14). The balance law (5-1) can now be written as:

$$\frac{\partial}{\partial t}\int_{\tilde{\Omega}} q(\boldsymbol{x}, t)\, d\boldsymbol{x} + \int_{\widetilde{\Omega}_I} \mathcal{N}(\boldsymbol{v})(\boldsymbol{x})\, d\boldsymbol{x} = \int_{\tilde{\Omega}} b(\boldsymbol{x}, t)\, d\boldsymbol{x} \quad \forall\, \tilde{\Omega} \subset \Omega \tag{5-6}$$

Applying the nonlocal divergence theorem (2-17) yields:

$$\int_{\tilde{\Omega}} \left(\frac{\partial q(\boldsymbol{x}, t)}{\partial t} + \mathcal{D}(\boldsymbol{v}) - b(\boldsymbol{x}, t)\right) d\boldsymbol{x} = 0 \quad \forall\, \tilde{\Omega} \subset \Omega \tag{5-7}$$

which owing to the arbitrariness of $\tilde{\Omega}$, (5-7) localizes to the field equation:

$$\frac{\partial q(\boldsymbol{x},t)}{\partial t} + \mathcal{D}(\boldsymbol{v}) - b(\boldsymbol{x},t) = 0 \quad \forall \boldsymbol{x} \in \Omega \tag{5-8}$$

To uniquely determine $\boldsymbol{q}$, (5-8) is required to satisfy some constraint conditions. Let the interaction domain Ω_I be split into two disjoint subdomains Ω_{Id} and Ω_{In} such that $\Omega_{Id} \cap \Omega_{In} = \emptyset$ and either of Ω_{Id} and Ω_{In} could be an empty set. Ω_{Id} is the subdomain where Dirichlet boundary condition is applied and Ω_{In} is the subdomain where Neumann boundary condition is applied. Analogous to the boundary value problem of the classical local theory, constraints on the solution $\boldsymbol{q}$ of (5-8) over Ω is applied as follows: a given function value $\boldsymbol{g}_d$ is prescribed on the solution over Ω_{Id} such that:

$$q(\boldsymbol{x}) = g_d \qquad \forall \boldsymbol{x} \in \Omega_{Id} \tag{5-9}$$

To prescribe the Neumann type constraint, recall that in the classical boundary value problem, this involves prescribing a flux density $\boldsymbol{q} \cdot \boldsymbol{n}$ over the flux boundary. From (2-18) and the discussion that follows, the nonlocal flux density over Ω_{In} is given by $\int_{\Omega_I} \mathcal{N}(q)(\boldsymbol{x})\, d\boldsymbol{x}$. Let g_n be a given function value of the flux density over Ω_{In}. The Neumann constraint can be stated as

$$\int_{\Omega_{In}} \mathcal{N}(q)(\boldsymbol{x})\, d\boldsymbol{x} = g_{\boldsymbol{n}} \qquad \forall \boldsymbol{x} \in \Omega_{In} \tag{5-10}$$

The presence of the first order time derivative of the solution $\boldsymbol{q}$ in (5-8) means in addition to the boundary constraints (5-9), (5-10), initial conditions also need to be specified. The initial condition involves prescribing the initial values of the solution and its first derivative. Let $\boldsymbol{q}_I$ and $\dot{\boldsymbol{q}}_I$ be the initial values of $\boldsymbol{q}(\boldsymbol{x})$ and $\dot{\boldsymbol{q}}(\boldsymbol{x})$ respectively, then:

$$q(\boldsymbol{x},0) = q_I \quad \forall \boldsymbol{x} \in \Omega, for\ t = 0 \tag{5-11}$$

and

$$\dot{q}(\boldsymbol{x},0) = \dot{q}_I \quad \forall \boldsymbol{x} \in \Omega, for\ t = 0 \tag{5-12}$$

are the initial conditions. So that (5-8)-(5-12) give the complete definition of the nonlocal problem which can be stated as

$$\begin{cases} \rho\dot{q} = -\mathcal{D}(q)\,(\boldsymbol{x}) + b(\boldsymbol{x},t) & \forall \boldsymbol{x} \in \Omega_s \\ q(\boldsymbol{x}) = g_d & \forall \boldsymbol{x} \in \Omega_{Id} \\ \int_{\Omega_{In}} \mathcal{N}(q)(\boldsymbol{x})\, d\boldsymbol{x} = g_{\boldsymbol{n}} & \forall \boldsymbol{x} \in \Omega_{Id} \\ q(\boldsymbol{x},0) = q_I & \forall \boldsymbol{x} \in \Omega, for\ t = 0 \\ \dot{q}(\boldsymbol{x},0) = \dot{q}_I & \forall \boldsymbol{x} \in \Omega, for\ t = 0 \end{cases} \tag{5-13}$$

For the specific case of heat conduction, q is the stored internal energy density expressed as:

$$q = \rho C_v\big(\tau(\boldsymbol{x},t) - \tau^*(\boldsymbol{x})\big) \tag{5-14}$$

where ρ and C_v are the density and specific heat capacity of the material of the body, respectively. τ is the temperature of the current state and τ^* is the temperature of a reference state. Then the rate of stored energy is given by:

$$\frac{\partial q(\boldsymbol{x},t)}{\partial t} = \rho C_v \frac{\partial \tau(\boldsymbol{x},t)}{\partial t} \tag{5-15}$$

The stored internal energy density q is related to the interaction vector $\boldsymbol{v}$ through a constitutive law. Let the constitutive law be such that:

$$\boldsymbol{v} = \frac{1}{2}\big(\boldsymbol{\Theta} \cdot \mathcal{D}^*(\tau)\big) \tag{5-16}$$

where $\mathcal{D}^*(T) = \mathcal{G}(T)$ is the nonlocal gradient of the temperature field (see 2.2.1). $\boldsymbol{\Theta}$ is a second order tensor given by $\boldsymbol{\Theta} = k\mathbf{I}$, where k is a constant and $\mathbf{I}$ is the identity tensor. Substituting (5-15) and (5-16) into (5-8) and dropping the time and spatial dependence of variables for the sake of brevity and write $\tau(\boldsymbol{y},t) = \tau'$ and $\tau(\boldsymbol{x},t) = \tau$, we obtain

$$\begin{aligned} \frac{\partial T}{\partial t} &= -\frac{1}{2\rho C_v}\mathcal{D}\big(\boldsymbol{\Theta} \cdot \mathcal{D}^*(\tau)\big) + \frac{k}{\rho C_v} b \quad \forall \boldsymbol{x} \in \Omega \\ &= \int_{\Omega} \frac{k}{\rho C_v}\big((\tau' - \tau)\boldsymbol{\alpha} \cdot \boldsymbol{\alpha} - (\tau' - \tau)\boldsymbol{\alpha} \cdot \boldsymbol{\alpha}'\big)dx + \frac{k}{\rho C_v} b \\ &= \int_{\Omega} \frac{k}{\rho C_v}\big((\tau' - \tau)\boldsymbol{\alpha} \cdot \boldsymbol{\alpha} + (\tau' - \tau)\boldsymbol{\alpha} \cdot \boldsymbol{\alpha}\big)dx + \frac{k}{\rho C_v} b \end{aligned}$$

$$\frac{\partial T}{\partial t} = \int_{\Omega} \frac{k}{\rho C_v} \boldsymbol{\alpha} \cdot \boldsymbol{\alpha} (\tau' - \tau)\, d\boldsymbol{x} + \frac{k}{\rho C_v} b \qquad \forall \boldsymbol{x} \in \Omega \tag{5-17}$$

If we write $\gamma = \boldsymbol{\alpha} \cdot \boldsymbol{\alpha}$, we obtain:

$$\frac{\partial T}{\partial t} = \int_{\Omega} \frac{k}{\rho C_v} \gamma (\tau' - \tau)\, d\boldsymbol{x} + \frac{k}{\rho C_v} b \qquad \forall \boldsymbol{x} \in \Omega \tag{5-18}$$

The integrand of the integral in (5-17) and (5-18) without the factor $1/(\rho C_v)$ is the *thermal response function*, and k is a peridynamic parameter called the micro-conductivity of bonds. The general form [94] of the micro-conductivity is given by.

$$k(\xi, \delta) = k(0, \delta) g(\xi, \delta) \tag{5-19}$$

where $k(0, \delta) = k_0$ is a constant and $g(\xi, \delta)$ is the kernel and gives the spatial distribution of the intensity of long-range thermal interaction between material points in a material. The explicit form of the micro-conductivity will be given in section 5.2. Analogous to thermal diffusivity of the classical heat conduction model, we define a micro-diffusivity function as.

$$K = \frac{k}{\rho C_v} \gamma \tag{5-20}$$

Just like the micro-conductivity parameter, the micro-diffusivity function is also a parameter intrinsic to the material. Thus (5-18) can be written as

$$\frac{\partial T}{\partial t} = \int_{\Omega} K(\tau' - \tau)\, d\boldsymbol{x} + h \qquad \forall \boldsymbol{x} \in \Omega \tag{5-21}$$

where $h = \frac{b}{\rho C_v}$ is a heat source density. The explicit form of the micro-diffusivity function and hence the thermal response function depends on the choice of the kernel function. In what follows, some candidate kernel functions will be utilized to derive the explicit forms of the thermal response functions that appeared in the literature. It is important to state that the analysis and classification or systematic justification of the interaction kernels is not an objective of this thesis, rather, the objective is to demonstrate the robustness of the nonlocal operators by showing how for appropriate choice of the interaction kernel, the nonlocal operators are able to yield specific form of the Peridynamic heat equation. The approach here is to a posteriori select those kernels that will result in the form of thermal response functions that are of interest to this study. If we define the kernel function as $\boldsymbol{\alpha}(\boldsymbol{x}, \boldsymbol{y}) = \frac{\xi}{|\xi|^2}$, then diffusivity modulus (5-19) becomes:

$$K = \frac{k}{\rho C_v |\boldsymbol{\xi}|^2} \tag{5-22}$$

which leads to a form of the response function that appeared in [95] herein denoted as f_1 given by:

$$f_1 = \frac{k}{|\boldsymbol{\xi}|^2}(\tau' - \tau) \tag{5-23}$$

If we, however, define $\boldsymbol{\alpha}(\boldsymbol{x}, \boldsymbol{y}) = \frac{\boldsymbol{\xi}}{|\boldsymbol{\xi}|}$, then from (5-18) and (5-21), (5-20) becomes:

$$K = \frac{k}{\rho C_v} \tag{5-24}$$

resulting in a response function that was proposed in [96] herein denoted as f_2 and is expressed as:

$$f_2 = k(\tau' - \tau) \tag{5-25}$$

On the other hand, if we define the kernel in (5-18) as $\gamma = \frac{1}{|y-x|}$, we obtain from (5-20):

$$K = \frac{k}{\rho C_v |\boldsymbol{\xi}|} \tag{5-26}$$

which corresponds to the form of the response function in [97, 98] given as:

$$f_3 = \frac{k}{|\boldsymbol{\xi}|}(\tau' - \tau) \tag{5-27}$$

5.2 Relationship between micro-conductivity and thermal conductivity

The peridynamic micro-conductivity k is related to the thermal conductivity κ from the classical heat conduction model using the principle of constitutive correspondence [95, 97]. In [97] this relationship is established by assuming equivalence of thermal potential between the peridynamic and classical continuum models. To show the explicit form of this relationship, the following definitions are made based on [98]: The peridynamic thermal potential is given as

$$Z(\boldsymbol{x}, t) = \frac{1}{2}\int_{\mathcal{H}} z(\boldsymbol{y}, \boldsymbol{x}, t)\, dV_{\boldsymbol{y}} \tag{5-28}$$

where z is the microthermal potential. The microthermal potential is related to the normalized response function through:

$$f = \frac{\partial z}{\partial \theta} \tag{5-29}$$

where $\theta = \tau' - \tau$. The form of the microthermal potential corresponding to different form of the response functions are obtained by substituting either of equations (5-23), (2-25) or (2-27) into (2-29) to respectively obtain:

$$z_1 = k\frac{\tau^2}{2|\boldsymbol{\xi}|^2}, \quad z_2 = k\frac{\tau^2}{2}, \quad z_3 = k\frac{\tau^2}{2|\boldsymbol{\xi}|} \tag{5-30}$$

The thermal potential from the classical model is given as:

$$\hat{Z} = \frac{1}{2}(\nabla\tau \cdot \kappa\nabla\tau) \tag{5-31}$$

where κ is the thermal conductivity of the medium.

5.2.1 One-dimensional micro-conductivity

If a linear temperature field of the form $T(\boldsymbol{x}) = c|\boldsymbol{x}|$ is applied such that c is a constant and $|\boldsymbol{x}|$ is the length of the coordinate vector $\boldsymbol{x}$, then (5-30) becomes:

$$z_1 = k\frac{\boldsymbol{\xi}^2}{2|\boldsymbol{\xi}|^2}, \quad z_2 = k\frac{\boldsymbol{\xi}^2}{2}, \quad z_3 = k\frac{\boldsymbol{\xi}^2}{2|\boldsymbol{\xi}|} \tag{5-32}$$

and (5-31) becomes:

$$\hat{Z} = \frac{1}{2}\kappa c^2 \tag{5-33}$$

Let δ be the horizon of material points in the medium, substituting (5-32) into (5-28) assuming one-dimensional problem, yields:

$$Z_1(\boldsymbol{x},t) = \frac{1}{2}\int_{-\delta}^{\delta} k\frac{c^2\boldsymbol{\xi}^2}{2|\boldsymbol{\xi}|^2}A\,d\xi, \qquad Z_2(\boldsymbol{x},t) = \frac{1}{2}\int_{-\delta}^{\delta} k\frac{c^2\boldsymbol{\xi}^2}{2}A\,d\xi,$$
$$Z_3(\boldsymbol{x},t) = \frac{1}{2}\int_{-\delta}^{\delta} k\frac{c^2\boldsymbol{\xi}^2}{2|\boldsymbol{\xi}|}A\,d\xi \tag{5-34}$$

where A is the cross-sectional area associated with the point $\boldsymbol{x}$. If we neglect the effect of distance between material points on their interaction and assume a micro-conductivity function of the form $k(x,y) = k_0$, then (5-34) respectively evaluates to:

$$Z_1(\boldsymbol{x},t)=\frac{1}{2}\int_{-\delta}^{\delta}k_0\frac{c^2\boldsymbol{\xi}^2}{2|\boldsymbol{\xi}|^2}A\,d\xi=\frac{k_0c^2\delta A}{2}$$
$$Z_2(\boldsymbol{x},t)=\frac{1}{2}\int_{-\delta}^{\delta}k_0\frac{c^2\boldsymbol{\xi}^2}{2}A\,d\xi=\frac{k_0c^2\delta^3 A}{6} \tag{5-35}$$
$$Z_3(\boldsymbol{x},t)=\frac{1}{2}\int_{-\delta}^{\delta}k_0\frac{c^2\boldsymbol{\xi}^2}{2|\boldsymbol{\xi}|}A\,d\xi=\frac{k_0c^2\delta^2 A}{4}$$

Equating (5-33) and (5-35) respectively yields:

$$k_1=\frac{\kappa}{A\delta},\quad k_2=\frac{3\kappa}{A\delta^3},\quad k_3=\frac{2\kappa}{A\delta^2} \tag{5-36}$$

In the case where the distance between points is assumed to have considerable effect on the long-range thermal interaction between them, then the kernel function chosen for the micro-conductivity function must be able to capture the distribution of intensity of interaction. Typical kernel functions used in this case are the linear and quadratic kernel functions given respectively as $g(|\boldsymbol{\xi}|,\delta)=\left(1-\frac{|\xi|}{\delta}\right)$ and $g(|\boldsymbol{\xi}|,\delta)=\left(1-\left(\frac{\xi}{\delta}\right)^2\right)^2$ so that the micro-conductivity functions takes the form $k(\boldsymbol{x},\boldsymbol{y})=k_0\left(1-\frac{|\xi|}{\delta}\right)$ and $k(\boldsymbol{x},\boldsymbol{y})=k_0\left(1-\left(\frac{\xi}{\delta}\right)^2\right)^2$ respectively. For example, substituting these into the first of (1.50), working out the resulting integral and equating thermal potentials from peridynamics with that from the classical theory allow us to obtain expressions for the micro-conductivity corresponding to the different forms of the kernel functions respectively as

$$k=\frac{2\kappa}{A\delta}\left(1-\frac{|\xi|}{\delta}\right) \tag{5-37}$$

and

$$k=\frac{15\kappa}{8A\delta}\left(1-\left(\frac{\xi}{\delta}\right)^2\right)^2 \tag{5-38}$$

The micro-conductivity functions (5-37) and (5-38) all have compact support within the horizon. In other words, the interaction between a given point and any other point in a body cease if the distance between them is greater than the horizon (δ). The typical forms of different micro-conductivity functions are presented in Figure 5-1 which represents the graph of k_3 in (5-36) as well as (5-37) and (5-38).

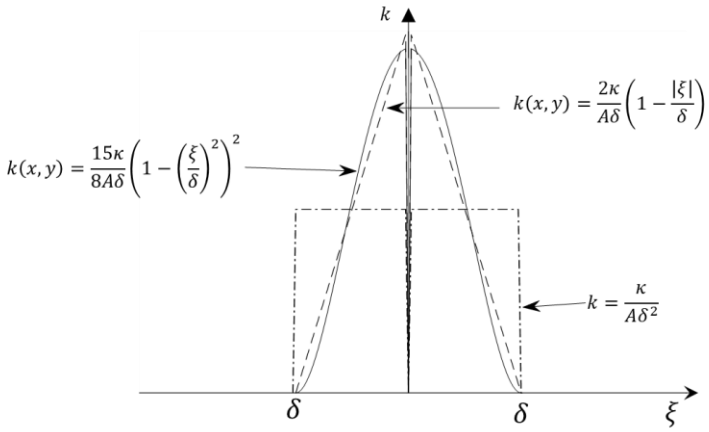

Figure 5-1 : Comparison of micro-conductivity functions.

Although the different forms of the thermal response functions and their associated micro conductivity functions have been established in the literature as cited, results of numerical experiments [67] have shown that the response function (1.43) provide the best approximation to the classical solution and would henceforth be used in the development of the proposed model reduction methodology. Also, the three different forms of the micro-conductivity functions presented in this section will be statically condensed in section 2.2. However, the choice of the micro-conductivity used in section 3.0 is limited to the constant function because of its simplicity of implementation and because the condensation of the peridynamic heat model with the other linear and quadratic micro-conductivity functions follows the same procedure.

5.2.2 Two-dimensional micro conductivity function

Following the same procedure laid out in section 5.2.1, the explicit form of the constant and triangular micro-conductivity as well as the corresponding diffusivity modulus function can be obtained. A constant micro modulus function with its corresponding diffusivity function is given as:

$$k = \frac{6\kappa}{\pi h\delta^3}, \qquad K = \frac{6\kappa}{\pi h\delta^3|\boldsymbol{\xi}|} \tag{5-39}$$

Interested readers are referred to [98] for discussion on the various forms of the response functions and their corresponding micro-conductivity functions.

5.3 The discrete heat conduction equation

Different discretization schemes have been proposed for the numerical approximation of balance laws arising from the peridynamic theory, such as the meshfree method [82, 86], the collocation methods [87, 88] and methods based on finite elements mesh [89, 90]. Due to its simple

implementation algorithm and relatively low computational cost, the meshfree method suggested in [82] is the most widely used [91] and is the preferred method in this work for these same reasons. In this approximation method, the discrete form of (5-21) is:

$$\dot{\tau}_i = \sum_{i}^{N} K(\tau_j - \tau_i)V_j + h_i \tag{5-40}$$

where $\rho_i = \rho(\boldsymbol{x}_i)$, $\dot{\tau} = \frac{\partial \tau_i}{\partial t}$ and N is the number of nodes in the neighbourhood of node i.

5.4 Static condensation of the peridynamic head conduction model

The assembled peridynamic transient heat conduction equations for the body in matrix form is given by:

$$\boldsymbol{I}\dot{\tau} + \boldsymbol{K}\tau = h \tag{5-41}$$

where $\boldsymbol{I}, \boldsymbol{K} \in \mathbb{R}^{n\times n}$ are the identity and diffusivity modulus matrices respectively and n is the total number of degrees of freedom in the system. In this context, (5-41) is referred to as the *full order model* of the system or simply *full model*. The objective of the model reduction is to replace the full model having n degree of freedom with a reduced order system having m degree of freedom, such that $m \ll n$. The reduced model is expected to preserve the heat conduction characteristics of the full model. To proceed with the model condensation, the degree of freedom of the system are separated into retained and truncated degrees of freedom. The retained degrees of freedom are those to be preserved while truncated degrees of freedom are those to be condensed out in the reduced model. Let r denote the retained degrees of freedom and let t denote the truncated degrees of freedom, then (5-41) can be partitioned as follows:

$$\begin{bmatrix} \boldsymbol{I}_{rr} & \boldsymbol{I}_{rt} \\ \boldsymbol{I}_{tr} & \boldsymbol{I}_{tt} \end{bmatrix} \begin{Bmatrix} \dot{\tau}_r \\ \dot{\tau}_t \end{Bmatrix} + \begin{bmatrix} \boldsymbol{K}_{rr} & \boldsymbol{K}_{rt} \\ \boldsymbol{K}_{tr} & \boldsymbol{K}_{tt} \end{bmatrix} \begin{Bmatrix} \tau_r \\ \tau_t \end{Bmatrix} = \begin{Bmatrix} h_r \\ h_t \end{Bmatrix} \tag{5-42}$$

Neglecting the transient term and assuming there is no heat source at the truncated degrees of freedom, then the solution of the second submatrix equation for τ_t yields

$$\tau_t = \boldsymbol{R}_G \tau_r \tag{5-43}$$

where $\boldsymbol{R}_G \in \mathbb{R}^{t\times r}$ is the condensation matrix, defined as

$$\boldsymbol{R}_G = -\boldsymbol{K}_{tt}^{-1}\boldsymbol{K}_{tr} \tag{5-44}$$

The condensation matrix relates the retained degrees of freedom and truncated degrees of freedom and is load independent because it is assumed there is no heat source at the truncated degrees of

freedom. Also note that in arriving at (5-43), the transient term in (5-42) have been neglected, hence this method is called static condensation method. The temperature state of the full model may be expressed as

$$\tau = \begin{Bmatrix} \tau_r \\ \tau_t \end{Bmatrix} = \boldsymbol{T}_G \tau_r \tag{5-45}$$

where $\boldsymbol{T}_G \in \mathbb{R}^{n \times r}$ is a transformation matrix given by:

$$\boldsymbol{T}_G = \begin{bmatrix} \boldsymbol{I} \\ \boldsymbol{R}_G \end{bmatrix} \tag{5-46}$$

where $\boldsymbol{I}$ is $r \times r$ identity matrix. If the transformation matrix is assumed to be independent of time, differentiating (5-45) with respect to time gives:

$$\dot{\tau} = \boldsymbol{T}_G \dot{\tau}_r \tag{5-47}$$

Substituting (5-46) and (5-47) into (5-41) and pre-multiplying by $\boldsymbol{T}_G^T$ yields

$$\boldsymbol{I}_G \dot{\tau}_r + \boldsymbol{K}_G \tau_r = h_G \tag{5-48}$$

where $\boldsymbol{I}_G$, $\boldsymbol{K}_G$ and h_G are the *reduced identity matrix*, *reduced diffusivity matrix* and *reduced load vector* respectively associated with the reduced model, defined as

$$\boldsymbol{I}_G = \boldsymbol{T}_G^T \boldsymbol{I} \boldsymbol{T}_G, \quad \boldsymbol{K}_G = \boldsymbol{T}_G^T \boldsymbol{K} \boldsymbol{T}_G, \quad h_G = \boldsymbol{T}_G^T h \tag{5-49}$$

5.4.1 Handling boundary conditions

It is necessary to provide some notes on how the Dirichlet and Neumann boundary conditions are handled in this model order reduction scheme. Dirichlet boundary condition is applied when a specified value of the temperature is imposed on the boundary volume. In the reduction process using static condensation, any region with Dirichlet boundary conditions must be retained in the reduced model. This is because, as indicated by equation (5-48), there is no transformation applied to the temperature field. To maintain the dynamic behaviour of the system, boundaries with Dirichlet conditions must be included in the reduced model.

On the other hand, Neumann boundary condition is applied when a specified value of heat is applied to the boundary volume, rather than temperature. In going from the full model to the reduced model, there is a transformation relationship between the heat source term in the full model and its counterpart in the reduced model, as defined in equation (5-49). This means that regardless of which regions are retained in the reduced model, the characteristics of the full model

are preserved. This provides greater flexibility in configuring the reduced model compared to the scenario with Dirichlet boundary conditions.

5.4.2 Condensation of parameters of peridynamic heat conduction model

The condensation of the micro-conductivity and micro-diffusivity functions will be illustrated using an example of a bar as shown in Figure 5-2. The goal is to demonstrate the behavior of the peridynamic parameters when subject to static condensation. Let the bar be of length 1unit. Three micro-conductivity functions and their corresponding micro-diffusivity functions will be studied: the constant (k_3 in (5-36)), linear (5-37) and quadratic (5-38) micro conductivity functions.

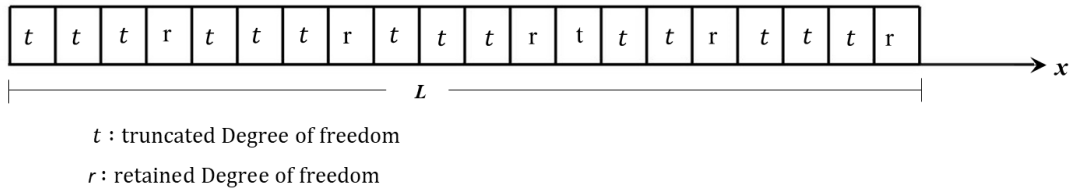

Figure 5-2 : A discretized bar to illustrate condensation of the micro-conductivity functions.

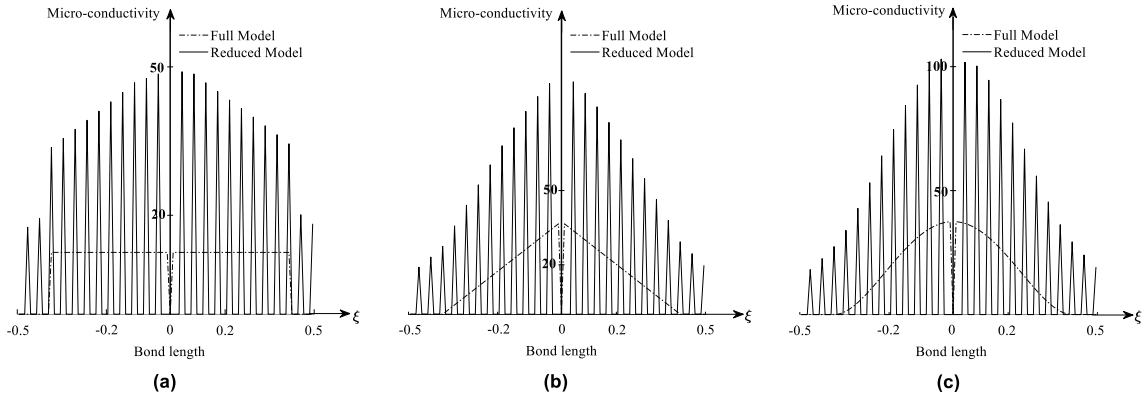

Figure 5-3 : Static condensation of micro-conductivity functions of a homogeneous bar: (a) Constant micro-conductivity, (b) Linear micro-conductivity and (c) Quadratic micro-conductivity

The horizon is $\delta = 0.4$ and $\rho, C_v = 1$. The bar is discretized into nodes with spacing $dx = 0.01$. Condensation is carried out by retaining every fourth node in the full model as shown in Figure 5-2. To proceed with the condensation, matrices of the micro-conductivity $\boldsymbol{k}$ and the diffusivity $\boldsymbol{K}$ of the bar is computed. These matrices are computed using the expression for k_3 in (5-36) as well as (5-37) and (5-38) in the case of micro-conductivity while the diffusivity matrices corresponding to these micro-conductivity functions are obtained by substituting the micro-conductivity functions into (5-27). Condensation is achieved by introducing $\boldsymbol{k}$ or $\boldsymbol{K}$ into the second

expression of (5-49) to obtain the condensed micro-conductivity matrix $\boldsymbol{k}_G$ or the condensed diffusivity matrix $\boldsymbol{K}_G$.

The condensed curves of both the micro-conductivity functions and the micro-diffusivity functions are characterised by sharp spikes as can be seen from Figure 5-3 and Figure 5-4, respectively. This behaviour is expected since the condensed model is defined only at the retained degrees of freedom.

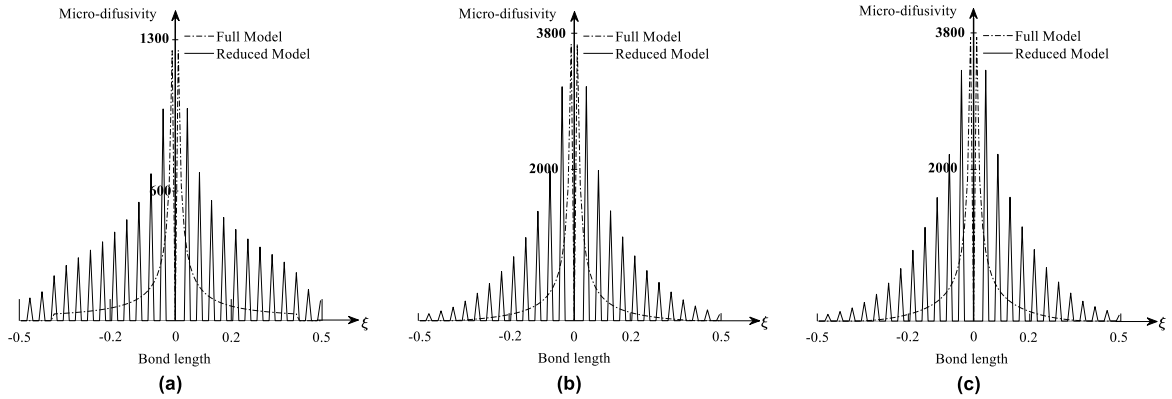

Figure 5-4 : Static condensation of micro-diffusivity functions of a homogeneous bar: (a) corresponding to constant micro-conductivity, (b) corresponding to linear micro-conductivity and (c) corresponding to quadratic micro-conductivity.

5.5 Numerical verification

The static condensation scheme described in section 5.4 will be tested on numerical problems to verify and demonstrate it capabilities in reducing the order of a peridynamic transient heat conduction model. To achieve this goal, the temperature field in a one-dimensional bar and two-dimensional plate is predicted using the proposed static condensation scheme and the result is compared with prediction using the full model.

5.5.1 A homogenous bar with constant temperature applied at both ends.

A homogeneous bar initially at zero temperature is subjected to boundary temperature of 1^oC at both ends as shown in Figure 5-5 . The bar has a length and thickness of 1 m and 0.01 m respectively. The specific heat capacity, thermal conductivity and density of the bar are specified as C_v=64 J/kgK, κ=233 W/mK and $\rho = 260\ kg/m^3$ respectively. The material of the bar is assumed to have a micro-conductivity function of the form given in (5-36).

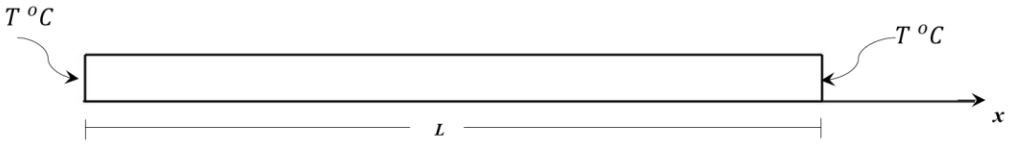

Figure 5-5 : A homogeneous bar subjected to constant temperature at both ends.

The bar is discretized into 100 nodes thus the spacing between nodes is $\Delta x = 0.01$. Three instances of the model reduction algorithm would be considered in this example. In the first instance, model order reduction of the bar is achieved by retaining every 2nd node of the full model. In the second instance, reduction is achieved by retaining every 5th node in the full model, and lastly in the third instance reduction is achieved by retaining every 10th node in the full model. A time step size of $\Delta t = 10^{-2}\ s$ is used and the simulation was run for 3000-time steps.

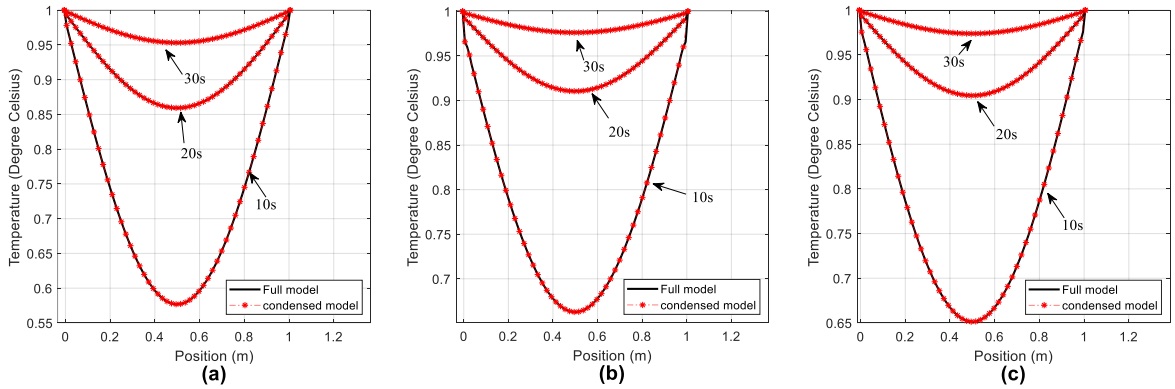

Figure 5-6 : Temperature distribution in a homogeneous bar subjected to constant temperature at both ends corresponding to retaining every 2nd node of the full model and response function (a) f_1 (b) f_2 and (c) f_3.

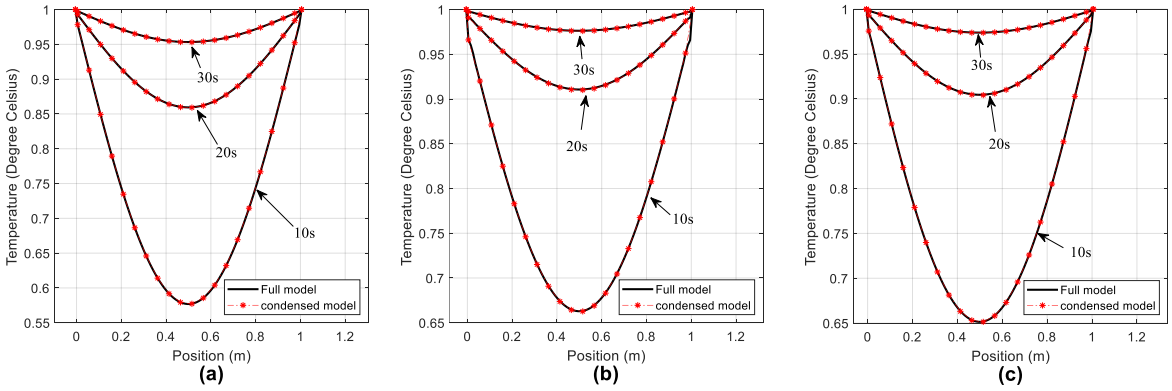

Figure 5-7: Temperature distribution in a homogeneous bar subjected to constant temperature at both ends corresponding to retaining every 5th node of the full model and response function (a) f_1 (b) f_2 and (c) f_3.

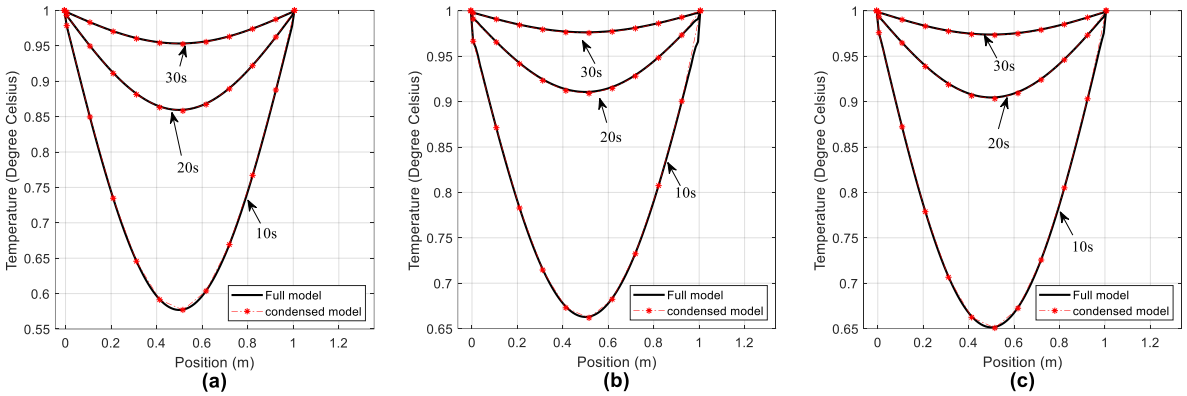

Figure 5-8: Temperature distribution in a homogeneous bar subjected to constant temperature at both ends corresponding to retaining every 10^{th} node of the full model and response function (a) f_1 (b) f_2 and (c) f_3.

Temperature prediction for both full model and reduced model are presented in Figure 5-6, Figure 5-7, and Figure 5-8. The reported results are temperature distribution across the bar corresponding to time steps $t = 10\,s$, $20\,s$ and $30\,s$. These results show a good correlation between the full model and reduce model irrespective of the reduction algorithm employed thus demonstrating the capability of the model order reduction scheme in preserving the dynamics of a one-dimensional transient peridynamic heat conduction model in-spite of using fewer degrees of freedom.

5.5.2 Numerical study of heat conduction in plate with a pre-existing crack

The static condensation scheme will be used to study temperature distribution in a plate with a pre-existing crack. The geometry of the plate is specified as length $L = 0.1\,m$, width $W = 0.1\,m$, thickness $H = 3.3 \times 10^{-4}\,m$ and the crack length $a = 1.6 \times 10^{-3}\,m$ as shown in Figure 5-9. The thermal conductivity, specific heat capacity and density are specified respectively as: $\kappa = 233\,W/mK$, $C_v = 64\,J/kgK$ and $\rho = 260\,kg/m^3$.

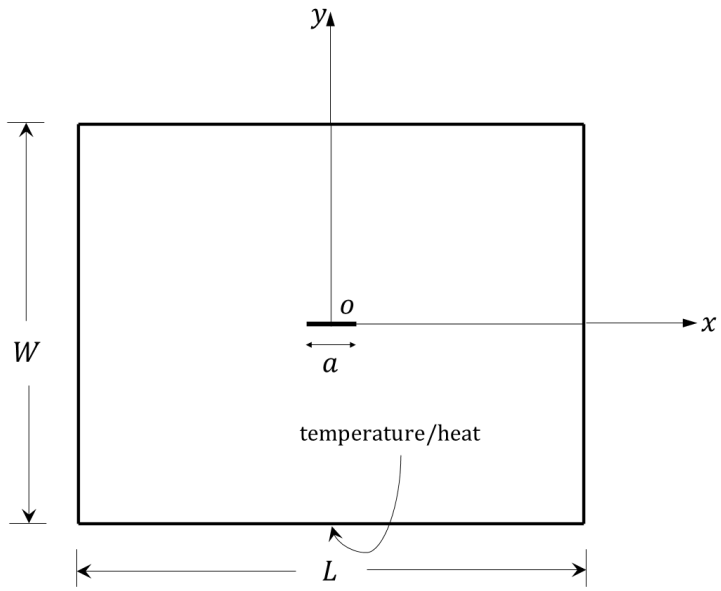

Figure 5-9 : Example 2 problem setup: A plate with pre-existing crack

The numerical implementation of the peridynamic transient heat conduction model proceed by discretizing the plate into 90 nodes along each edge, so that we have 8100 nodes. The distance between nodes is $\Delta x = \Delta y = 1.1\times10^{-4}$ m. The horizon of the full model is $\delta = 3.015\Delta x$. Model order reduction on the plate is carried out as shown schematically in Figure 5-10. The condensation algorithm adopted is to retain every second node of every second row. The total simulation time is $t = 10^{-3}$ s with a time step of $\Delta t = 10^{-6}$ s. The plate would be studied for two case scenarios: Dirichlet and Neumann boundary conditions.

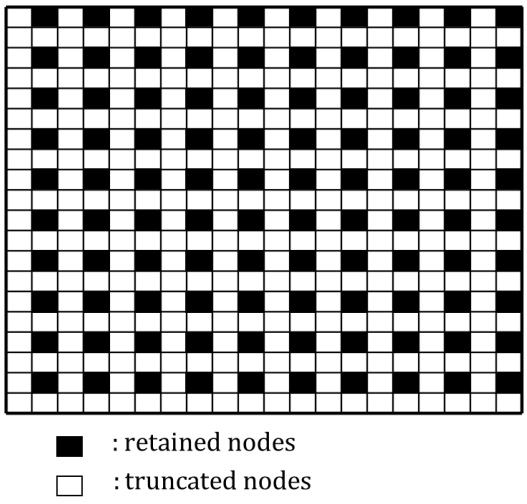

Figure 5-10 : Schematic representation of static condensation

5.5.3 Example 1. Case I: Dirichlet boundary condition

In this case, the plate is subjected to the following initial and boundary volume conditions respectively:

$$T\big((x,y),0\big) = 0^{o}C\,, \quad -L/2 \le x \le \frac{L}{2}, \quad -W/2 \le y \le W/2 \tag{5-50}$$

and

$$T\big((x,y),t\big) = 1^{o}C\,, \quad -\frac{L}{2} \le x \le \frac{L}{2}, \quad y = -W/2 \tag{5-51}$$

Note that in this case, although the condensation algorithm may exclude the boundary nodes, we are constrained to still retain them. Temperature distribution in time across the plate for both full model and the reduced model are shown Figure 5-11. A profile of the temperature along a grid of nodes parallel to the vertical axis of the plate at $x = -5.5\times10^{-5}$ m is also shown in Figure 5-12.

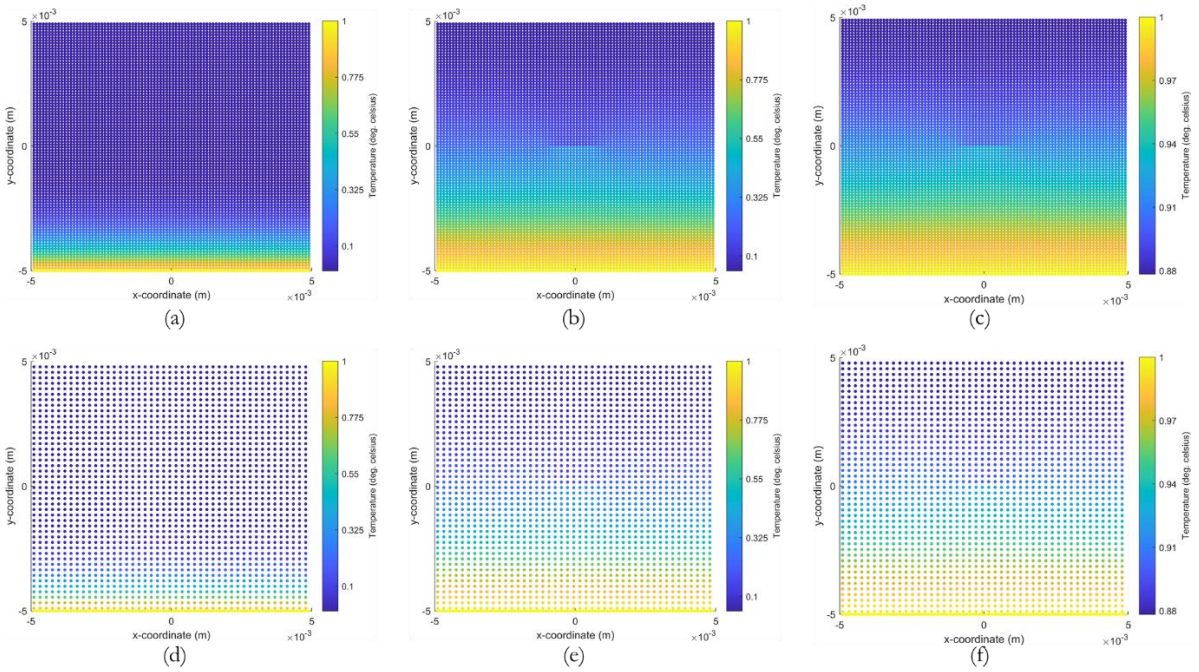

Figure 5-11 : Dirichlet boundary condition: Temperature distribution across the plate: (a) Full model corresponding to $t = 7\times10^{-5}$ s (b) Full model corresponding to $t = 7\times10^{-4}$ s (c) Full model corresponding to $t = 7\times10^{-3}$ s (d) Reduced model corresponding to $t = 7\times10^{-5}$ s (e) Reduced model corresponding to $t = 7\times10^{-4}$ s, (f) Reduced model corresponding to $t = 7\times10^{-3}$ s

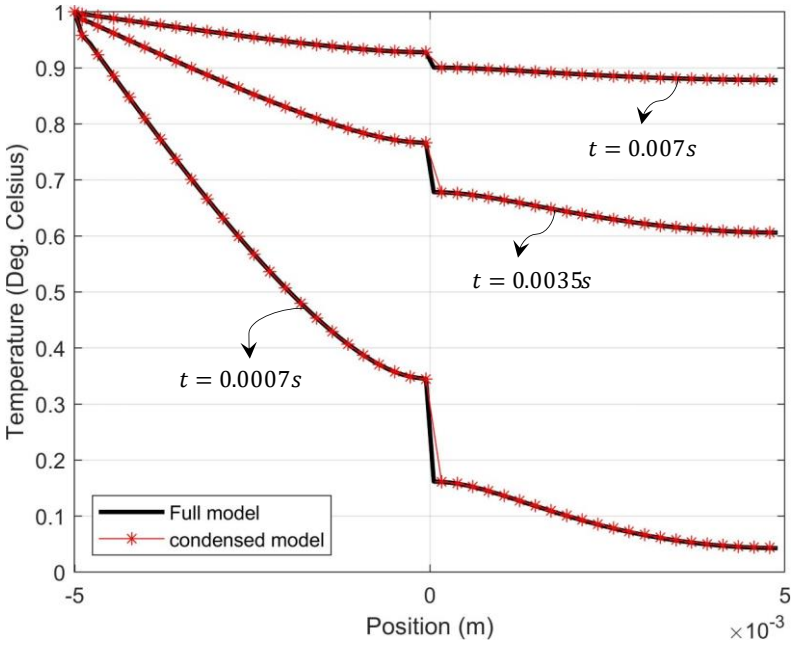

Figure 5-12 : Temperature profile along the grid at $x = -5.5\times10^{-5}\ m$ parallel to the $y-$axis of the plate with Dirichlet boundary condition.

The results presented in Figure 5-11 and Figure 5-12 show a very good match between predictions from the full model and those from the reduced model. The difference between the full model and reduce model curves close to the crack location in Figure 5-12 reflects wider spacing between nodes in the reduced model due to fewer nodes. Note that all boundary nodes subjected to the Dirichlet boundary condition were retained in the reduced model.

5.5.4 Example 2. Case II: Neumann boundary condition

The goal in this example is to demonstrate the performance of the model order reduction in reducing a 2D model with a Neumann type boundary condition. In this case, in addition to (5-50), the plate is subjected to the following conditions:

$$h\big((x,y),t\big) = 10^7, \qquad 0 \le x \le L, \quad y = 0 \tag{5-52}$$

Figure 5-13((a), (b), (c)) illustrate the full model prediction of the distribution of temperature over the plate, while Figure 5-13((d), (e), (f)) are the predicted temperature distribution in the plate from the reduced model corresponding to simulation times $t = 7\times10^{-5}$ s, $t = 7\times10^{-4}$ s and $t = 7\times10^{-3}$ s, respectively. Figure 5-14 present the curves of temperature profile along a grid parallel to the vertical axis of the plate for both full and reduced model corresponding to simulation times $t = 7\times10^{-4}$ s, $t = 3.5\times10^{-3}$ s and $t = 7\times10^{-3}$ s respectively.

The results presented show a near identical match between predictions from the full model and those from the reduced model. It is worthy to note that in the case of the Neumann type boundary condition, there was no constraint to the choice of nodes to retain and those to be condensed out. This potentially allows for the use of fewer degrees of freedom than in the scenario where a Dirichlet type boundary condition is imposed.

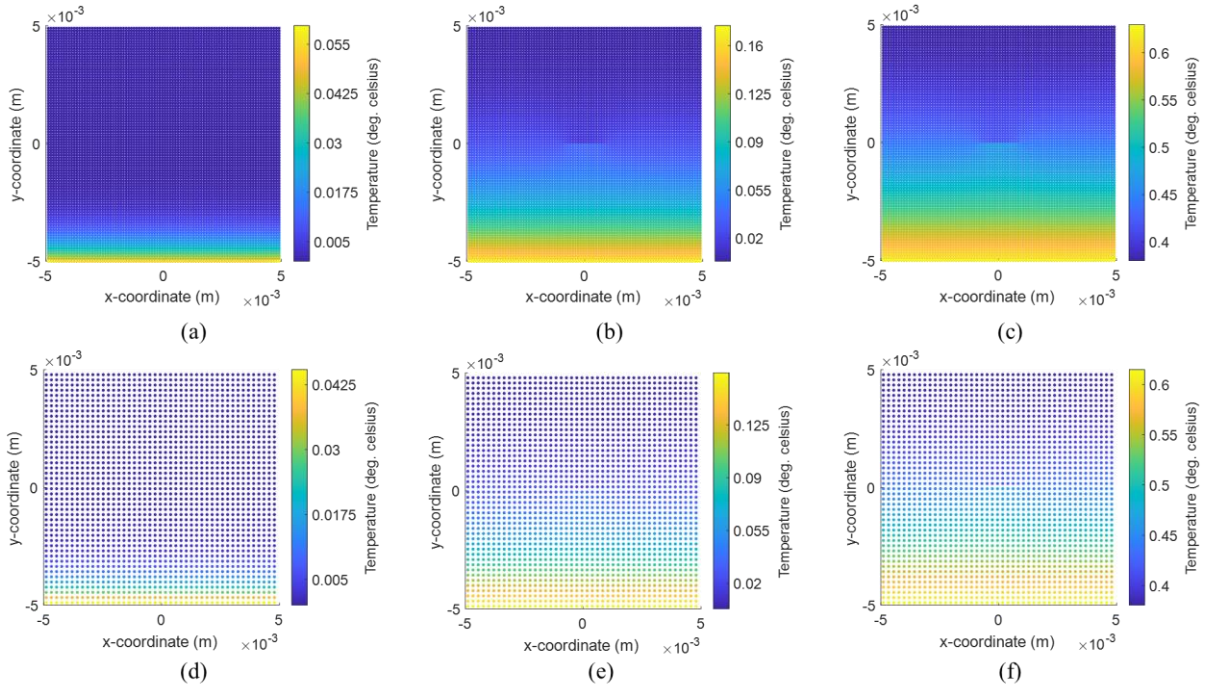

Figure 5-13 : Neumann boundary condition: Temperature distribution across the plate: (a) Full model corresponding to $t = 7\times10^{-5}$ s (b) Full model corresponding to $t = 7\times10^{-4}$ s (c) Full model corresponding to $t = 7\times10^{-3}$ s (d) Reduced model corresponding to $t = 7\times10^{-5}$ s (e) Reduced model corresponding to $t = 7\times10^{-4}$ s, (f) Reduced model corresponding to $t = 7\times10^{-3}$ s.

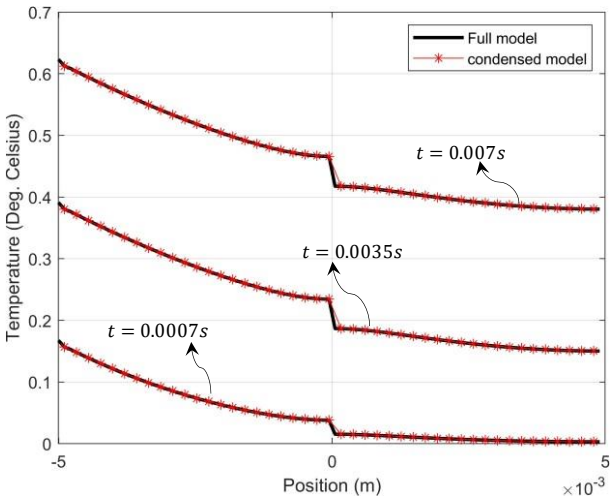

Figure 5-14 : Temperature profile along the grid at $x = -5.5\times10^{-5}$ m parallel to the $y-$axis of the plate with Neumann boundary condition.

5.5.5 Example 3. Neumann boundary condition with retained nodes selected randomly.

In this example, the plate of example 2 will be analysed using the same boundary conditions and plate properties. However, in coarsening the plate, instead of following a predetermined pattern as done in the previous examples, the retained nodes in this case will be selected randomly. The goal is to demonstrate the robustness of the condensation methodology in handling any kind of selection pattern during model reduction. In this condensation scheme, 2,025 nodes were randomly selected from a total of 8,190 nodes. Result of the temperature distribution over the surface of the plate is shown in Figure 5-15 while the temperature profile of nodes that falls along a grid located at $x = -5.5\times10^{-5}$ m is presented in Figure 5-16.

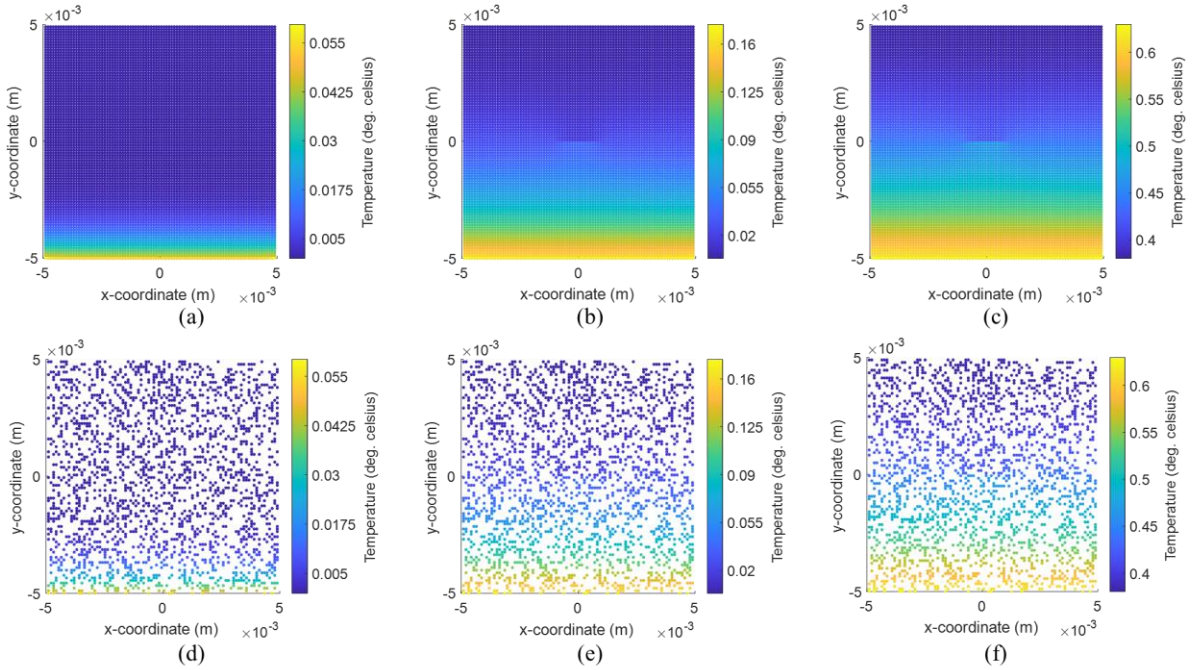

Figure 5-15: Neumann boundary condition: Temperature distribution across the plate: (a) Full model corresponding to $t = 7\times10^{-5}$ s, (b) Full model corresponding to $t = 7\times10^{-4}$ s (c) Full model corresponding to $t = 7\times10^{-3}$ s (d) Reduced model corresponding.

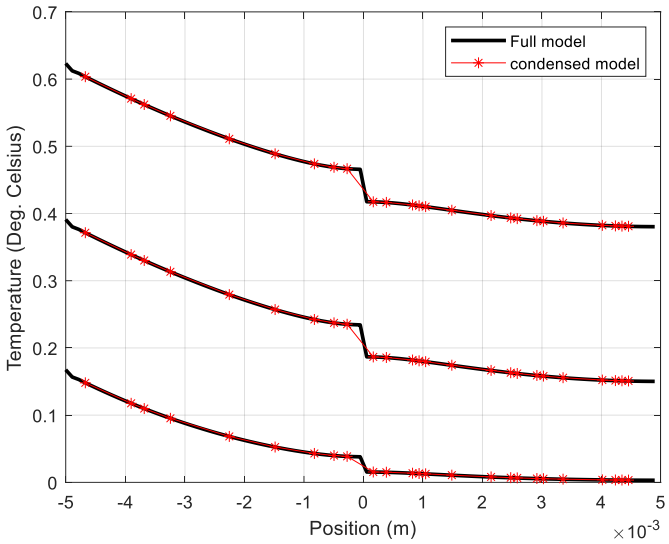

Figure 5-16: Temperature profile along a grid of the plate with Neumann boundary condition and condensation achieved through random selection of nodes.

The results presented in Figure 5-15 and Figure 5-16, show good agreement between prediction from the full model and the condensed model. This is a demonstration of the robustness of the condensation methodology in predicting accurate result irrespective of the algorithm or pattern employed in the condensation process.

5.5.6 Example 3. Nonuniform condensation

It is sometimes necessary to have high resolution at certain region of the model while such level of detail may not be required in other regions. This model order reduction can be selectively applied to accommodate this different resolution requirement. For example, high resolution may be required around regions close to the crack in the plate in section 5.5.4 to allow for more detailed information than is required in regions further away from the cracks. To achieve this, a nonuniform condensation algorithm will be implemented in this example where all nodes around the crack are retained and regions further away from the crack will be condensed. The region around the crack is defined by a square of dimension 0.0033 m×0.0033 m centred around the crack. Model reduction of regions away from the crack is achieved by retaining every second node of every second row.

Prediction of temperature distribution in time using the adaptive condensation scheme is presented alongside prediction from the full model in Figure 5-17. Temperature profile along a grid of nodes parallel to the vertical axis is also presented in Figure 5-18. In addition to the near identical prediction from both models as can be seen from Figure 5-17 and Figure 5-18, the temperature profile near the crack for both curves are also near identical. This contrasts with the case in sections

5.5.3 and 5.5.4 where there is a slight difference between the curves from the full and reduced models.

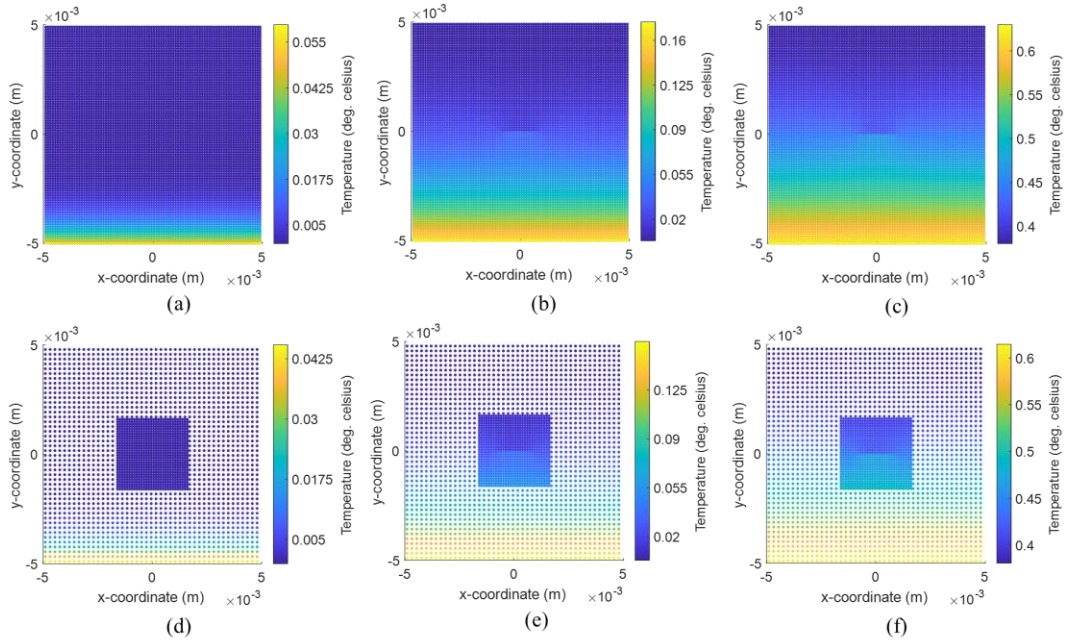

Figure 5-17 : Adaptive condensation: Temperature distribution across the plate: (a) Full model corresponding to $t = 10$ s (b) Full model corresponding to $t = 20$ s, (c) Full model corresponding to $t = 30$ s, (d) Reduced model corresponding to $t = 10$ s, (e) Reduced model corresponding to $t = 20$ s, (f) Reduced model corresponding to $t = 30$ s,

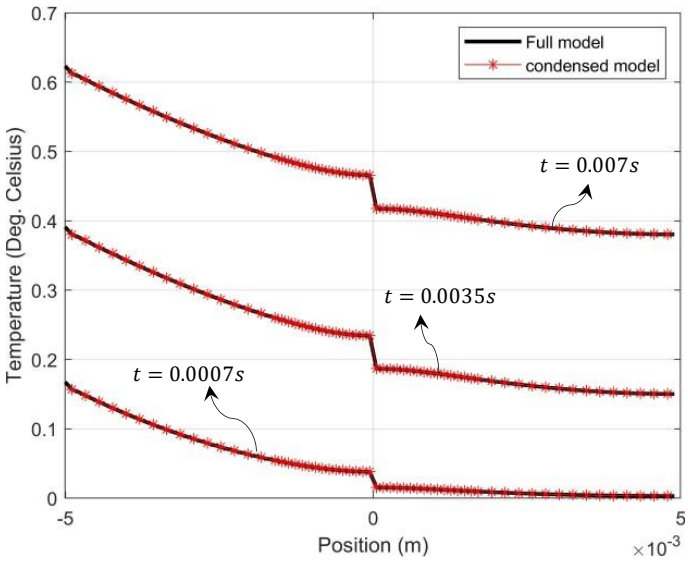

Figure 5-18 : Adaptive condensation. Temperature profile along a grid of the plate with Neumann boundary condition.

5.6 Conclusion

In this chapter, a nonlocal vector calculus was utilized to derive the general form of the nonlocal peridynamic transient heat conduction equation. It was demonstrated how the different explicit forms of the peridynamic heat transport equation developed in the literature can be recovered from the general form by using specific kernel functions.

A model order reduction of the nonlocal peridynamic transient heat conduction model based on static condensation algorithm was implemented. The results from predictions based on the full order model and reduced order model show a near perfect match thus demonstrating the capability of the model reduction scheme in preserving the characteristics of the system. The model reduction scheme also allows for adaptive implementation of the condensation algorithm so that a more detailed model is implemented in regions where higher resolution results are needed for greater insight into the numerical predictions.

The development in this thesis only treats systems with time invariant physical and geometrical characteristics. For example, model parameters such as the thermal conductivity or peridynamic bonds existing between material points must be time invariant. Because of this constraint, treatment of thermal conduction problems in the presence of propagating cracks is beyond the capabilities of the present scheme. In a future endeavour, the author would like to extend the capabilities of this model order reduction scheme to problems with time dependent properties.

Chapter 6

6.0 Introduction

This chapter focuses on the development of a multiscale constitutive theory for NOSBPD, within the framework of computational homogenization. The objective is to establish a homogenization framework that is anchored on a rigorous mathematical foundation that accounts for the nonlocal nature of PD. By developing such a computational homogenization framework, this chapter aims to provide a platform that bridges the gap between microscopic and the macroscopic behaviour of materials. The chapter layout the theoretical foundations, mathematical derivations, and computational implementation aspects of the proposed theory. Numerical examples and comparative analyses demonstrating the efficacy of the approach in accurately predicting the behaviour of materials with complex microstructures will be provided. The developed peridynamic computational homogenization theory contributes to the advancement of multiscale modelling in PD, enabling improved understanding and predictive capabilities for engineering applications.

6.1 A Computational Homogenization Framework for Peridynamics

The homogenization procedure developed in this chapter is a two-scale scheme: a microscopic scale represented by an RVE, and a macroscopic scale represented by a homogeneous effective medium. The constitutive law of the microscale model is assumed to be explicitly known at every point of the micro-domain while the constitutive law of the macromodel is not known everywhere. The objective is to retrieve a constitutive law of the macroscale substitute medium from a numerical solution of an initial volume constraint problem (IVCP) at the level of the underlying microstructure. In this multiscale framework, an RVE is assigned to each integration point of the macro continuum. A peridynamic equilibrium solution of the RVE is sought using boundary condition generated by the macroscale deformation gradient. The solution of the RVE IVCP yields the microscale stress field which is then homogenized to produce macroscale stresses and associated material tangent tensor. The coupling of the micro and macro scale is achieved through averaging relationships and the energetic equivalence statement of the Hill-Mandel micro-homogeneity condition.

6.1.1 Effective material constants

Consider a heterogeneous medium $\mathfrak{B}^o$ with characteristic size of heterogeneities to be l_{hetro}. Momentarily, let this medium be replaced by a homogeneous 'effective' medium $\mathfrak{B}^h$. The original heterogeneous medium is the microscale, and the geometrical arrangement and material characteristics of the heterogeneities constitute the microstructure while the effective medium is

the macroscale. Define a grid on $\mathfrak{B}^h$ and let each point $\bar{\boldsymbol{x}}$ on this grid be associated with a neighbourhood Ω_s. Let Ω_s be bounded by a region Ω_c of positive volume in $\mathbb{R}^n$. Let a sample of $\mathfrak{B}^h$occupying the regions Ω_s and Ω_c be denoted as Ω_s^h and Ω_c^h respectively. Also, let a sample of $\mathfrak{B}^o$ occupying Ω_s be denoted as Ω_s^o as shown in Figure 6-1.

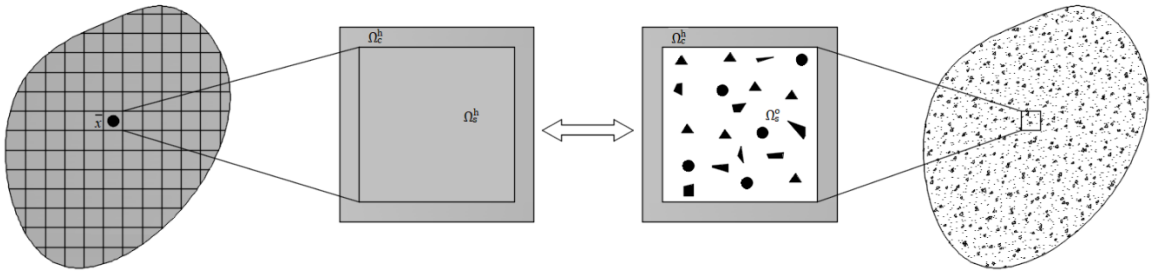

Figure 6-1: Schematic Representation of Homogenization Process: Defining Representative Volume Element (RVE) in a Heterogeneous Material

Now, define a grid on Ω_s and let the position of points on this grid in the reference configuration be denoted as $\boldsymbol{x}$. The grid associated with $\bar{\boldsymbol{x}}$ is called the macroscale and the grid associated with $\boldsymbol{x}$ is the microscale. Let the characteristic lengths associated with the macroscale and the microscale be l_{macro} and l_{micro} respectively. The morphology and material properties of the constituents of $\mathfrak{B}^o$ in the microscale is called the microstructure of $\mathfrak{B}^h$. If Ω_s^o exist such that

$$l_{hetro} \ll l_{micro} \ll l_{macro} \tag{6-1}$$

then Ω_s^o is referred to as a Representative Volume Element (RVE) associated with the macro point $\bar{\boldsymbol{x}}$ where (6-1) is the statement of the principle of separation of scale. This principle requires that the scale of the microstructure (or fluctuation of micro field such as stress and strain) should be much smaller than the size of the RVE considered which in turn should be much smaller than the characteristic length scale of the macro domain (or fluctuation of macro field variables).

Let $\mathfrak{B}^h$ be subjected to an affine deformation at its boundary. This will produce a homogeneous strain $\bar{\boldsymbol{\varepsilon}}$ (for small deformation). This homogeneous strain will in turn generate a homogeneous stress field $\bar{\boldsymbol{\sigma}}$ everywhere in $\mathfrak{B}^h$. For simplicity, we will assume linear elastic material response in both scales, then the material model that relates $\bar{\boldsymbol{\sigma}}$ and $\bar{\boldsymbol{\varepsilon}}$ given by the generalised Hooke's law:

$$\bar{\boldsymbol{\sigma}} = \mathbb{C}^* \bar{\boldsymbol{\varepsilon}} \qquad \text{or} \qquad \bar{\boldsymbol{\varepsilon}} = \mathbb{S}^* \bar{\boldsymbol{\sigma}} \tag{6-2}$$

is the effective or homogenised constitutive law, where $\mathbb{C}^*$ and $\mathbb{S}^*$ are the effective stiffness and compliance tensors, respectively. At the microscale, the constitutive relation in each phase of the microscale is given by:

$$\boldsymbol{\sigma}(\boldsymbol{x}) = \mathbb{C}(\boldsymbol{x})\boldsymbol{\varepsilon}(\boldsymbol{x}) \qquad \text{or} \qquad \boldsymbol{\varepsilon}(\boldsymbol{x}) = \mathbb{S}(\boldsymbol{x})\boldsymbol{\sigma}(\boldsymbol{x}) \tag{6-3}$$

If the condition for the existence of the RVE is satisfied (henceforth, this condition will be assumed to be satisfied), then the microscopic deformation will be assumed to admit the following decomposition:

$$\boldsymbol{u}(\boldsymbol{x}) = \bar{\boldsymbol{\varepsilon}}\boldsymbol{x} + \boldsymbol{u}^*(\boldsymbol{x}) \quad \text{and} \quad \boldsymbol{\varepsilon}(\boldsymbol{x}) = \bar{\boldsymbol{\varepsilon}} + \boldsymbol{\varepsilon}^* \tag{6-4}$$

where $\boldsymbol{u}^*(\boldsymbol{x})$ is the displacement fluctuation due to the presence of the microstructure and $\boldsymbol{\varepsilon}^* = \mathcal{G}_{\boldsymbol{x}}\boldsymbol{u}^*(\boldsymbol{x})$.

6.1.2 Micro-macro scale transition

6.1.2.1 Average theorems

The transition of mechanical properties from the microscale to the macroscale is achieved using volume average relations. Let ψ be a quantity defined over a domain Ω. We denote the volume average of ψ over Ω as:

$$\langle\psi\rangle = \frac{1}{V_\Omega}\int_\Omega \psi dV_\Omega \tag{6-5}$$

where V_Ω is the volume associated with Ω.

Theorem 4.1: *Nonlocal average stress theorem.* Let $\mathfrak{B}$ be a heterogeneous body occupying the region $\overline{\Omega} = \Omega_s \cup \Omega_c$ where Ω_s is the region where solution is sought and Ω_c is the boundary volume. we denote the average stress and average strain over Ω_s as $\langle\boldsymbol{\sigma}\rangle$ and $\langle\boldsymbol{\varepsilon}\rangle$ respectively. Let $\mathfrak{B}$ be in a state of static equilibrium when a constant stress tensor $\overline{\boldsymbol{\sigma}}$ is applied on the boundary volume Ω_c, then the volume average of the stress field in Ω_s is equal to $\overline{\boldsymbol{\sigma}}$, that is:

$$\langle\boldsymbol{\sigma}\rangle = \overline{\boldsymbol{\sigma}} \tag{6-6}$$

Proof: from (2-104), static equilibrium of the RVE in the absence of body forces requires the divergence of the Cauchy stress tensor in the case of small deformation to vanish, that is

$$\mathcal{D}_\omega(\boldsymbol{\sigma})(\boldsymbol{x}) = \boldsymbol{0} \tag{6-7}$$

The Cauchy stress field in Ω_s can be written as

$$\boldsymbol{\sigma}(\boldsymbol{x}) = \boldsymbol{\sigma}\mathcal{G}_{\omega_{\boldsymbol{x}}}(\boldsymbol{x}) \tag{6-8}$$

Taking the volume average of (6-8) and utilizing (2-20), yields

$$\langle\boldsymbol{\sigma}\rangle = \frac{1}{V_{\Omega_\mathrm{s}}}\int_{\Omega_\mathrm{s}} \boldsymbol{\sigma}\mathcal{G}_{\omega_{\boldsymbol{x}}}(\boldsymbol{x})dV_{\Omega_\mathrm{s}} = \frac{1}{V_{\Omega_\mathrm{s}}}\int_{\Omega_c} \boldsymbol{\sigma}\mathcal{S}_{\omega_{\boldsymbol{x}}}(\boldsymbol{x})dV_{\Omega_\mathrm{s}} + \frac{1}{V_{\Omega_\mathrm{s}}}\int_{\bar{\Omega}}\int_{\bar{\Omega}} \boldsymbol{x}\mathcal{G}^{*}_{\omega_{\boldsymbol{x}}}(\boldsymbol{\sigma})dV_{\bar{\Omega}}\,dV_{\bar{\Omega}} \tag{6-9}$$

Considering the relationship $\mathcal{D}_\omega = -\mathcal{G}^{*}_{\omega}$ and utilizing (6-7), then (6-9) reduces to

$$\begin{aligned}
\langle\boldsymbol{\sigma}\rangle &= \frac{1}{V_{\Omega_\mathrm{s}}}\int_{\Omega_c} \boldsymbol{\sigma}\mathcal{S}_{\omega_{\boldsymbol{x}}}(\boldsymbol{x})dV_{\Omega_\mathrm{s}} \\
&= \frac{1}{V_{\Omega_\mathrm{s}}}\int_{\Omega_c} \overline{\boldsymbol{\sigma}}\mathcal{S}_{\omega_{\boldsymbol{x}}}(\boldsymbol{x})dV_{\Omega_\mathrm{c}} \\
&= \frac{\overline{\boldsymbol{\sigma}}}{V_{\Omega_\mathrm{s}}}\int_{\Omega_c} \mathcal{S}_{\omega_{\boldsymbol{x}}}(\boldsymbol{x})dV_{\Omega_\mathrm{c}} \\
&= \frac{\overline{\boldsymbol{\sigma}}}{V_{\Omega_\mathrm{s}}}\int_{\Omega_\mathrm{s}} \mathcal{G}_{\omega_{\boldsymbol{x}}}(\boldsymbol{x})dV_{\Omega_\mathrm{s}} \\
&= \overline{\boldsymbol{\sigma}}
\end{aligned} \tag{6-10}$$

Theorem 4.2: *Nonlocal average strain theorem*. Let $\mathfrak{B}$ be as defined in theorem 4.1. If $\mathfrak{B}$ is subjected to applied displacement on the boundary volume Ω_c generated by a constant strain tensor $\bar{\boldsymbol{\varepsilon}}$ such that $\boldsymbol{u}^0 = \bar{\boldsymbol{\varepsilon}}\boldsymbol{x}$ for all $\boldsymbol{x} \in \Omega_c$, then the average of the infinitesimal strain field $\boldsymbol{\varepsilon}(\boldsymbol{x})$ (for all $\boldsymbol{x} \in \Omega_\mathrm{s}$) is equal to $\bar{\boldsymbol{\varepsilon}}$, that is:

$$\langle\boldsymbol{\varepsilon}\rangle = \bar{\boldsymbol{\varepsilon}} \tag{6-11}$$

Proof: from (6-5), the volume average of the strain field over Ω is given by:

$$\begin{aligned}
\langle\varepsilon_{ij}\rangle &= \frac{1}{V_{\Omega_\mathrm{s}}}\int_{\Omega_\mathrm{s}} \varepsilon_{ij}dV_{\Omega} = \frac{1}{2V_{\Omega_\mathrm{s}}}\int_{\Omega_\mathrm{s}} \left(\mathcal{G}_{x_j}(u_i) + \mathcal{G}_{x_i}(u_j)\right)dV_{\Omega_\mathrm{s}} \\
&= \frac{1}{2V_{\Omega_\mathrm{s}}}\int_{\Omega_c} \left(\mathcal{S}_{x_j}(u_i) + \mathcal{S}_{x_i}(u_j)\right)dV_{\Omega_\mathrm{c}} = \frac{1}{2V_{\Omega_\mathrm{s}}}\int_{\Omega_c} \left(\mathcal{S}_{x_j}(\bar{\varepsilon}_{ik}x_k) + \mathcal{S}_{x_i}(\bar{\varepsilon}_{jk}x_k)\right)dV_{\Omega_\mathrm{c}} \\
&= -\frac{1}{2V_{\Omega_\mathrm{s}}}\int_{\Omega_c} \left[\int_{\bar{\Omega}} (\bar{\varepsilon}_{ik}(x_k + x'_k)\otimes\beta_j dV_{\boldsymbol{x}'} + \int_{\bar{\Omega}} \left(\bar{\varepsilon}_{jk}(x_k + x'_k)\otimes\beta_i dV_{\boldsymbol{x}'}\right]dV_{\Omega_\mathrm{c}}\right. \\
&= \frac{1}{2V_{\Omega_\mathrm{s}}}\int_{\Omega_\mathrm{s}} \left(\bar{\varepsilon}_{ik}\mathcal{G}_{x_k}(x_j) + \bar{\varepsilon}_{jk}\mathcal{G}_{x_k}(x_i)\right)dV_{\Omega_\mathrm{s}}
\end{aligned}$$

$$= \frac{1}{2V_{\Omega_s}} \int_{\Omega_s} \left(\bar{\varepsilon}_{ik}\delta_{kj} + \bar{\varepsilon}_{jk}\delta_{ki}\right) dV_{\Omega_s}$$

$$= \frac{1}{2V_{\Omega_s}} \int_{\Omega_s} \left(\bar{\varepsilon}_{ij} + \bar{\varepsilon}_{ji}\right) dV_{\Omega_s}$$

$$= \bar{\varepsilon}_{ij}$$

This implies that the volume average of the strain field is completely defined in terms of the strain at the boundary volume.

6.1.2.2 Macrohomogeneity condition

In order for the averaged fields $\langle \boldsymbol{\sigma} \rangle$ and $\langle \boldsymbol{\varepsilon} \rangle$ to be admissible variables in the macroscale constitutive relation, the so-called Hill-Mandel macrohomogeneity condition [99] must be satisfied. The macrohomogeneity condition provide the basis for the substitution of an initially heterogeneous medium with a homogeneous one. This is achieved by prescribing an energetic equivalence between the heterogenous medium and the homogeneous substitution medium. Let the strain energy density of the underlying classical continuum material be:

$$U = \frac{1}{2}\sigma_{ij}\varepsilon_{ij} \tag{6-12}$$

then invoking the principle of constitutive correspondence allows us to write the strain energy of the peridynamic model as (6-12). The macrohomogeneity condition is stated as

$$\langle \sigma_{ij}\varepsilon_{ij} \rangle = \bar{\sigma}_{ij}\bar{\varepsilon}_{ij} \tag{6-13}$$

In other words, the condition requires that the average strain energy of the heterogeneous medium be equal to the strain energy density of the homogeneous medium. The condition under which (6-13) is satisfied for a peridynamic continuum material under constitutive correspondence will be established through a nonlocal analogue of the Hill's lemma.

Theorem 4.3: *Nonlocal Hill's lemma*: Consider the body defined in theorem 4.1. Let σ_{ij} and ε_{ij} be the stress and strain field in $\mathfrak{B}$ under prescribed boundary traction or boundary displacement, then

$$\langle \sigma_{ij}\varepsilon_{ij} \rangle - \bar{\sigma}_{ij}\bar{\varepsilon}_{ij} = \frac{1}{V_{\Omega_s}} \int_{\Omega_c} \left((\sigma_{ik} - \bar{\sigma}_{ik}) \mathcal{S}^{s}_{\omega_{x_k}} \left(u_i - x_j \bar{\varepsilon}_{ij}\right) \right) dV_{\Omega_c} \tag{6-14}$$

is the nonlocal Hill's lemma.

Proof: We can write the scalar product of the average of the stress and strain tensor as

$$\bar{\sigma}_{ij}\bar{\varepsilon}_{ij} = \frac{1}{V_{\Omega_s}}\int_{\Omega_s}\sigma_{ij}\bar{\varepsilon}_{ij}dV_{\Omega_s} = \frac{1}{V_{\Omega_s}}\int_{\Omega_s}\bar{\sigma}_{ij}\varepsilon_{ij}dV_{\Omega_s} = \frac{1}{V_{\Omega_s}}\int_{\Omega_s}\bar{\sigma}_{ij}\mathcal{G}^{s}_{\omega\,x_j}(u_i)dV_{\Omega_s} \tag{6-15}$$

Thus, we can rewrite (6-13) as:

$$\langle\sigma_{ij}\varepsilon_{ij}\rangle - \bar{\sigma}_{ij}\bar{\varepsilon}_{ij} = \frac{1}{V_{\Omega_s}}\int_{\Omega_s}\left(\sigma_{ij}\varepsilon_{ij} - \bar{\sigma}_{ij}\varepsilon_{ij} - \sigma_{ij}\bar{\varepsilon}_{ij} + \bar{\sigma}_{ij}\bar{\varepsilon}_{ij}\right)dV_{\Omega_s}$$

$$= \frac{1}{V_{\Omega_s}}\int_{\Omega_s}\left(\sigma_{ik}\mathcal{G}^{s}_{\omega\,x_k}(u_i) - \bar{\sigma}_{ik}\mathcal{G}^{s}_{\omega\,x_k}(u_i) - \sigma_{ik}\mathcal{G}^{s}_{\omega\,x_k}(x_j)\bar{\varepsilon}_{ij} + \bar{\sigma}_{ik}\mathcal{G}^{s}_{\omega\,x_k}(x_j)\bar{\varepsilon}_{ij}\right)dV_{\Omega_s}$$

$$= \frac{1}{V_{\Omega_s}}\int_{\Omega_c}\left(\sigma_{ik}\mathcal{S}^{s}_{\omega\,x_k}(u_i) - \sigma_{ik}\mathcal{S}^{s}_{\omega\,x_k}(x_j)\bar{\varepsilon}_{ij} - \bar{\sigma}_{ik}\mathcal{S}^{s}_{\omega\,x_k}(u_i) + \bar{\sigma}_{ik}\mathcal{S}^{s}_{\omega\,x_k}(x_j)\bar{\varepsilon}_{ij}\right)dV_{\Omega_c}$$

$$= \frac{1}{V_{\Omega_s}}\int_{\Omega_c}\left((\sigma_{ik} - \bar{\sigma}_{ik})\left(\mathcal{S}^{s}_{\omega\,x_k}(u_i) - \mathcal{S}^{s}_{\omega\,x_k}(x_j)\bar{\varepsilon}_{ij}\right)\right)dV_{\Omega_c}$$

$$= \frac{1}{V_{\Omega_s}}\int_{\Omega_c}\left((\sigma_{ik} - \bar{\sigma}_{ik})\mathcal{S}^{s}_{\omega\,x_k}\left(u_i - x_j\bar{\varepsilon}_{ij}\right)\right)dV_{\Omega_c}$$

which proves (6-14). It is obvious from (6-14) that for the Hill-Mandel condition (6-13) to be satisfied will require that:

$$\frac{1}{V_{\Omega_s}}\int_{\Omega_c}\left((\sigma_{ik} - \bar{\sigma}_{ik})\mathcal{S}^{s}_{\omega\,x_k}\left(u_i - x_j\bar{\varepsilon}_{ij}\right)\right)dV_{\Omega_c} = 0 \tag{6-16}$$

Thus, the satisfaction of the Hill-Mandel macrohomogeneity condition requires the integral in (6-16) to vanish.

6.1.3 RVE boundary volume constraints

In the classical continuum framework, the satisfaction of (6-16) is traditionally achieved in one of the following ways: (1) Voigt (or Taylor) assumption, (2) Reuss (or Sachs) assumption, (3) Homogeneous displacement (3) Prescribed periodicity in displacement (5) Homogeneous stress, and (6) Prescribed periodicity in traction. Methods 1-3 are categorised as deformation driven approaches while methods 4-6 are categorised as stress driven approaches. The task now is to establish the boundary requirements that will make the lemma (6-14) satisfy the Hill-Mandel condition in the nonlocal framework using the methods 1-6.

6.1.3.1 Voigt (Taylor) model

In this method [100], (6-16) is satisfied by assuming a homogeneous deformation of the form $u_i = x_j\bar{\varepsilon}_{ij}$ in $\overline{\Omega}$. This implies a constant strain field $\boldsymbol{\varepsilon}(\boldsymbol{x}) = \bar{\boldsymbol{\varepsilon}}$ in the RVE. Inserting this assumption into (6-2) yields

$$\bar{\sigma}_{ij} = \langle\sigma_{ij}\rangle = \langle\mathbb{C}_{ijkl}\bar{\varepsilon}_{kl}\rangle = \langle\mathbb{C}_{ijkl}\rangle\bar{\varepsilon}_{kl} = \mathbb{C}^*_{ijkl}\bar{\varepsilon}_{kl} \quad \Longrightarrow \mathbb{C}^*_{ijkl} = \langle\mathbb{C}_{ijkl}\rangle \tag{6-17}$$

From (6-17), the implication of the Taylor (Reuss) assumption is that the homogenized or effective stiffness tensor is simply the volume average of the stiffness tensor of the constituents. It will also be noticed that utilizing the Taylor assumption means we can obtain the effective material properties without the need to solve the microscale peridynamic (RVE) problem.

6.1.3.2 Reuss model

In this model [101], (6-16) is verified by assuming a constant stress $\boldsymbol{\sigma}(\boldsymbol{x}) = \bar{\boldsymbol{\sigma}}$ in $\overline{\Omega}$. If this assumption is inserted into (6-2) yields

$$\bar{\varepsilon}_{ij} = \langle\bar{\varepsilon}_{ij}\rangle = \langle\mathbb{S}_{ijkl}\bar{\sigma}_{kl}\rangle = \langle\mathbb{S}_{ijkl}\rangle\bar{\sigma}_{kl} = \mathbb{S}^*_{ijkl}\bar{\sigma}_{kl} \quad \Longrightarrow \mathbb{S}^*_{ijkl} = \langle\mathbb{S}_{ijkl}\rangle \tag{6-18}$$

thus, meaning that the effective compliance tensor is simply the volume average of the compliance tensor of the constituents. As with the Voigt model, the utilization of the Reuss assumption allow the determination of the effective properties without recourse to solving the microscopic peridynamic (RVE) model.

6.1.3.3 Constant Traction Boundary Volume Constraint (CTVBC)

One way of satisfying (6-16) is to prescribe appropriate traction on the boundary volume Ω_c. A traditional way of achieving this in the classical continuum framework is by applying the so-called constant traction boundary condition. In this nonlocal framework, this is achieved by imposing on the boundary volume Ω_c, a constant traction generated by constant stress field:

$$\boldsymbol{\sigma}(x) = \bar{\boldsymbol{\sigma}} \qquad \forall\, \boldsymbol{x} \in \Omega_c \tag{6-19}$$

Substituting (6-19) into (6-16) will vanish the boundary volume integral and therefore satisfying the Hill-Mandel condition (6-13).

6.1.3.4 Linear Displacement Boundary Volume Constraint (LDBVC)

This boundary condition is also referred to as homogeneous boundary condition in the literature. This boundary condition is achieved by applying appropriate displacement field to the boundary of the RVE that will varnish the gradient of the displacement terms of the integrand of the

boundary volume integral (6-16). A traditional way of achieving this is to apply a linear displacement of the form:

$$\boldsymbol{u}(\boldsymbol{x}) = \bar{\boldsymbol{\varepsilon}}\boldsymbol{x} \qquad \forall \boldsymbol{x} \in \Omega_c \tag{6-20}$$

Inserting (6-20) into (6-16) yields:

$$\begin{aligned}
&\frac{1}{V_{\Omega_s}} \int_{\Omega_c} \left((\sigma_{ik} - \bar{\sigma}_{ik}) \mathcal{S}^s_{\omega_{x_k}} \left(x_j \bar{\varepsilon}_{ij} - x_j \bar{\varepsilon}_{ij} \right) \right) dV_{\Omega_c} \\
&\qquad = \frac{1}{V_{\Omega_s}} \int_{\Omega_c} \left((\sigma_{ik} - \bar{\sigma}_{ik}) \mathcal{S}^s_{\omega_{x_k}} \left(x_j - x_j \right) \bar{\varepsilon}_{ij} \right) dV_{\Omega_c} \\
&\qquad = \frac{1}{V_{\Omega_s}} \int_{\Omega_c} \left((\sigma_{ik} - \bar{\sigma}_{ik}) \left(\delta_{jk} - \delta_{jk} \right) \bar{\varepsilon}_{ij} \right) dV_{\Omega_c} \\
&\qquad = \frac{1}{V_{\Omega_s}} \int_{\Omega_c} \left((\sigma_{ik} - \bar{\sigma}_{ik}) (\bar{\varepsilon}_{ik} - \bar{\varepsilon}_{ik}) \right) dV_{\Omega_c} \\
&\qquad = 0
\end{aligned}$$

Thus, proving (6-20) satisfies the Hill-Mandel condition (6-13).

6.1.3.5 Periodic Boundary Volume Constraint (PBVC)

This model is appropriate to model materials with periodic microstructure. The reference configuration of the RVE is assumed to be a geometric shape with even number of sides or faces for two- and three-dimensional problems, respectively. A square RVE is shown in Figure 6-1 for two-dimensional problems, with each pair i of the RVE boundary region assumed to be equally sized subsets, that is, there should be a one-to-one correspondence between points in Ω_i^+ and Ω_i^-.

Ω_3^-	Ω_2^+	Ω_4^+
Ω_1^-		Ω_1^+
Ω_4^-	Ω_2^-	Ω_3^+

Figure 6-2: Example square RVE showing corresponding boundary regions.

In this method, a displacement field of the form (6-4) is applied on the boundary region such that for each pair of boundary points $(\boldsymbol{x}^+ \in \Omega_i^+, \boldsymbol{x}^- \in \Omega_i^-)$:

$$\boldsymbol{u}^*(\boldsymbol{x}^+) = \boldsymbol{u}^*(\boldsymbol{x}^-) \tag{6-21}$$

The difference in displacement between two corresponding boundary points $\boldsymbol{x}^+, \boldsymbol{x}^-$ is then given by:

$$\boldsymbol{u}(\boldsymbol{x}^+) - \boldsymbol{u}(\boldsymbol{x}^-) = \bar{\boldsymbol{\varepsilon}}(\boldsymbol{x}^+ - \boldsymbol{x}^-) \tag{6-22}$$

To achieve static equilibrium of the RVE, an anti-periodic stress field is applied in the boundary domain such that:

$$\boldsymbol{\sigma}(\boldsymbol{x}^-) = -\boldsymbol{\sigma}(\boldsymbol{x}^+) \tag{6-23}$$

for each pair of points in Ω_i^+ and Ω_i^-.

Utilizing (6-22) and (6-23) the Hill-Mandel condition is satisfied as follows:

$$\frac{1}{V_{\Omega_s}} \int_{\Omega_c} \left((\sigma_{ik} - \bar{\sigma}_{ik}) \mathcal{S}^s_{\omega_{x_k}} \left(u_i - x_j \bar{\varepsilon}_{ij} \right) \right) dV_{\Omega_c}$$

$$= \frac{1}{V_{\Omega_s}} \sum_{i=1}^{n} \left[\int_{\Omega_{c\,i}^+} \left((\sigma_{ik}^+ - \bar{\sigma}^+{}_{ik}) \mathcal{S}^s_{\omega_{x_k}} \left(u_i^+ - x_j^+ \bar{\varepsilon}_{ij} \right) \right) dV_{\Omega_{c\,i}^+} \right.$$

$$\left. + \int_{\Omega_{c\,i}^-} \left((\sigma_{ik}^- - \bar{\sigma}^-{}_{ik}) \mathcal{S}^s_{\omega_{x_k}} \left(u_i^- - x_j^- \bar{\varepsilon}_{ij} \right) \right) dV_{\Omega_{c\,i}^-} \right]$$

$$= \frac{1}{V_{\Omega_s}} \sum_{i=1}^{n} \left[\int_{\Omega_{c\,i}^+} \left((\sigma_{ik}^+ - \bar{\sigma}^+{}_{ik}) \mathcal{S}^s_{\omega_{x_k}} \left(u_i^+ - x_j^+ \bar{\varepsilon}_{ij} \right) \right) dV_{\Omega_{c\,i}^+} \right.$$

$$\left. - \int_{\Omega_{c\,i}^-} \left((\sigma_{ik}^+ - \bar{\sigma}^+{}_{ik}) \mathcal{S}^s_{\omega_{x_k}} \left(u_i^- - x_j^- \bar{\varepsilon}_{ij} \right) \right) dV_{\Omega_{c\,i}^-} \right]$$

$$= \frac{1}{V_{\Omega_s}} \sum_{i=1}^{n} \left[\int_{\Omega_{c\,i}^+} \left((\sigma_{ik}^+ - \bar{\sigma}^+{}_{ik}) \mathcal{S}^s_{\omega_{x_k}} \underbrace{\left(u_i^+ - u_i^- - \bar{\varepsilon}_{ij} \left(x_j^+ - x_j^- \right) \right)}_{=0 \text{ from (6-22)}} \right) dV_{\Omega_{c_i}} \right]$$

$$= 0$$

6.1.4 Bounds for effective properties.

Predictions from the Voigt and Reuss assumptions were shown in [102] to provide the upper and lower bounds to the effective material properties. Effective stiffness and hence the effective elastic modulus obtained using any method should lie between this bound. That is,

$$\mathbb{C}^{*R} \leq \mathbb{C}^{*} \leq \mathbb{C}^{*V} \tag{6-24}$$

where $\mathbb{C}^{*R}$, $\mathbb{C}^{*V}$ are the effective stiffness tensors due to Reuss and Voigt assumptions respectively and $\mathbb{C}^{*}$ is the effective stiffness due to any other method. As emphasised in [103], the corresponding entries of $\mathbb{C}^{*R}$, $\mathbb{C}^{*}$ and $\mathbb{C}^{*V}$ do not necessarily satisfy (6-24), however, the corresponding diagonal terms and eigenvalues are shown to satisfy (6-24). It can also be shown that the inequality (6-24) hold true in terms of elastic constants such as bulk and shear moduli. Consider a given strain tensor ε_{kl} at a point, the stress σ_{ij} acting at the point for a linear 2D isotropic media undergoing small deformation is given by (6-23) and the fourth order isotropic tensor $\mathbb{C}_{ijkl}$ can be written as:

$$\mathbb{C}_{ijkl} = \kappa\delta_{ij}\delta_{kl} + \mu\left(\delta_{ik}\delta_{jl} + \delta_{il}\delta_{jk} - \delta_{ij}\delta_{kl}\right) \tag{6-25}$$

where κ and μ are the bulk and shear moduli respectively. If we define two fourth order isotropic tensors I_1 and I_2 as:

$$I_1 = \frac{1}{2}\delta_{ij}\delta_{kl} \quad \text{and} \quad \frac{1}{2}\left(\delta_{ik}\delta_{jl} + \delta_{il}\delta_{jk} - \delta_{ij}\delta_{kl}\right) \tag{6-26}$$

Then (6-25) can be written as

$$\mathbb{C} = 2\kappa I_1 + 2\mu I_2 \tag{6-27}$$

It can be shown from (6-27) that the compliance tensor can be written as:

$$\mathbb{S} = \frac{1}{2\kappa} I_1 + \frac{1}{2\mu} I_2 \tag{6-28}$$

For the sake of brevity, we will adopt a symbolic notation that will allow us write (6-27) and (6-28) as:

$$\mathbb{C} = (2\kappa, 2\mu), \qquad \mathbb{S} = \left(\frac{1}{2\kappa}, \frac{1}{2\mu}\right) \tag{6-29}$$

Given a two-phase composite having constituent material constants $\kappa_0, \kappa_1, \mu_0$ and μ_1 and volume fractions c_0 and $c_1$such that $\kappa_1 > \kappa_0$ and $\mu_1 > \mu_0$, then the volume average of the stiffness and compliance tensor can be written as:

$$[c_0\mathbb{C}_0 + c_1\mathbb{C}_1], \qquad [c_0\mathbb{S}_0 + c_1\mathbb{S}_1] \tag{6-30}$$

Utilizing (6-38) and (6-39) in (6-24), it can easily be shown that:

$$\left[\frac{2\kappa_0\kappa_1}{c_0\kappa_1 + c_1\kappa_0}, \frac{2\mu_0\mu_1}{c_0\mu_1 + c_1\mu_0}\right] \leq (2\kappa^*, 2\mu^*) \leq [2(c_0\kappa_0 + c_1\kappa_1), 2(c_0\mu_0 + c_1\mu_1)] \tag{6-31}$$

It follows from (6-31) that:

$$\frac{\kappa_0\kappa_1}{c_0\kappa_1 + c_1\kappa_0} \leq \kappa^* \leq c_0\kappa_0 + c_1\kappa_1 \tag{6-32}$$

and

$$\frac{\mu_0\mu_1}{c_0\mu_1 + c_1\mu_0} \leq \mu^* \leq c_0\mu_0 + c_1\mu_1 \tag{6-33}$$

where the left-hand sides of (6-32) and (6-33) give the Reuss lower bound while the right-hand sides give the Voigt upper bound, and κ^* and μ^* and the 2D effective bulk and shear moduli. It is noted that the distance between the Reuss lower bound and the Voigt upper bound is large and often does not give much information, a tighter bound is achieved using the Hashin-Shtrikman bounds [104].

$$\kappa_0 + \frac{c_1}{\frac{1}{\kappa_1 - \kappa_0} + \frac{3c_0}{3\kappa_0 + 4\mu_0}} \leq \kappa^* \leq \kappa_1 + \frac{c_0}{\frac{1}{\kappa_0 - \kappa_1} + \frac{3c_1}{3\kappa_1 + 4\mu_1}} \tag{6-34}$$

and

$$\mu_0 + \frac{c_1}{\frac{1}{\mu_1 - \mu_0} + \frac{6c_0(\kappa_0 + 2\mu_0)}{5\mu_0(3\kappa_0 + 4\mu_0)}} \leq \mu^* \leq \mu_1 + \frac{c_0}{\frac{1}{\mu_0 - \mu_1} + \frac{6c_1(\kappa_1 + 2\mu_1)}{5\mu_1(3\kappa_1 + 4\mu_1)}} \tag{6-35}$$

6.1.5 Computational implementation of the PDCHT

To obtain the numerical solution of the RVE in the PDCHT framework, the RVE is discretised following the procedure outlined in section 2.4. Being a nonlocal problem, the RVE is subjected to appropriate volume constraints. In the numerical validation that follows in section 6.2, the RVEs will be subjected to LDBVC and PBVC. Although computational algorithm to implement these

boundary conditions in the framework of finite element analysis is well established and discussed by many authors [105-108], however, implementing them in a nonlocal boundary value constraint problem such as the RVE in the PDCHT framework require special treatment. This is particularly the case with the PBVC. To implement the PBVC in the PDCHT framework, The displacement driven approach to homogenization is utilised in this work and thus, to determine the effective elasticity tensor, the first of (6-2) is employed. Combining this with (6-6) and (6-11) allow us to write the expression for the effective elasticity tensor as

$$\mathbb{C}^*_{ijkl} = \frac{1}{V_{\Omega_s}\bar{\varepsilon}_{kl}} \int_{\Omega_s} \sigma_{ij} dV_{\Omega_s} \tag{6-36}$$

where the stress field σ_{ij} in Ω_s is obtained using discretised peridynamic equation of motion (2-110) and $\bar{\varepsilon}_{kl}$ is the prescribed strain tensor on the boundary volume. for a two-dimensional problem, $\mathbb{C}^*_{ijkl}$ has six components. However, owing to its symmetric property, only three components are independent. Thus, to determine the components of $\mathbb{C}^*_{ijkl}$ for a two-dimensional problem require the application of three loading conditions that result in deformation modes which render all but one of the three independent components of the strain tensor to zero. For the purpose of this implementation, the applied strain tensors are given as

$$\bar{\varepsilon}_{11} = \begin{bmatrix} c & 0 \\ 0 & 0 \end{bmatrix}, \qquad \bar{\varepsilon}_{22} = \begin{bmatrix} 0 & 0 \\ 0 & c \end{bmatrix}, \qquad \bar{\varepsilon}_{12} = \begin{bmatrix} 0 & 1/2c \\ 1/2c & 0 \end{bmatrix} \tag{6-37}$$

where c is the magnitude of the prescribed strain tensor. These strains are then used to generate displacement in the boundary volume depending on the boundary condition used. In the case of LDBC, the displacement, $\boldsymbol{u}$ generated at every node $\boldsymbol{x}_i$ in the boundary volume after discretization of the RVE follows from (6-20) as

$$\boldsymbol{u}_i^{(1)} = \begin{Bmatrix} c\alpha_i \\ 0 \end{Bmatrix}, \qquad \boldsymbol{u}_i^{(2)} = \begin{Bmatrix} 0 \\ c\beta_i \end{Bmatrix}, \qquad \boldsymbol{u}_i^{(3)} = \begin{Bmatrix} c\beta_i \\ c\alpha_i \end{Bmatrix} \tag{6-38}$$

where α_i and β_i are the components of the coordinates of $\boldsymbol{x}_i$ in the first and second reference direction respectively. To implement the PBVC, nodes in the boundary volume are broadly grouped and categorised as 'facial' nodes and 'corner' nodes. Thus, from Figure 6-2, all nodes in boundary sub-volumes Ω_1^-, Ω_1^+, Ω_2^- and Ω_2^+ are facial nodes while those in Ω_3^-, Ω_3^+, Ω_4^- and Ω_4^+ are corner nodes. If we write (6-22) in expanded form for two-dimensional space, we have:

$$\begin{Bmatrix} u^{i+} \\ v^{i+} \end{Bmatrix} - \begin{Bmatrix} u^{i-} \\ v^{i-} \end{Bmatrix} = \begin{bmatrix} \bar{\varepsilon}_{11} & \bar{\varepsilon}_{12} \\ \bar{\varepsilon}_{12} & \bar{\varepsilon}_{22} \end{bmatrix} \begin{Bmatrix} \alpha^{i+} - \alpha^{i-} \\ \beta^{i+} - \beta^{i-} \end{Bmatrix} \tag{6-39}$$

for every pair of points in the *i*-th pair of two opposite parallel faces. Applying (6-39) to facial pairs $\Omega_1^-, \Omega_1^+, \Omega_2^-$ and Ω_2^+ result in the following relative displacement boundary constraints.

$$\left.\begin{aligned} u^{1+} - u^{1-} &= \bar{\varepsilon}_{11}(\alpha^{1+} - \alpha^{1-}) \\ v^{1+} - v^{1-} &= \bar{\varepsilon}_{12}(\alpha^{1+} - \alpha^{1-}) \end{aligned}\right\} \quad (a)$$
$$\left.\begin{aligned} u^{2+} - u^{2-} &= \bar{\varepsilon}_{12}(\beta^{2+} - \beta^{2-}) \\ v^{2+} - v^{2-} &= \bar{\varepsilon}_{22}(\beta^{2+} - \beta^{2-}) \end{aligned}\right\} \quad (b) \tag{6-40}$$

With the group of equations in (6-40)-(a) associated with the pair Ω_1^-, Ω_1^+ and the group (6-40)-(b) associated with the pair Ω_2^- and Ω_2^+ respectively. It will be noticed that each corner volume is shared by two facial volumes and applying (6-40) to nodes within these boundary volumes will lead to over constrained boundary. In order to eliminate this problem, the following translational periodicity is imposed at the corner boundary volumes: if we write $\Omega_3^- = \Omega_1^c, \Omega_3^+ = \Omega_2^c, \Omega_4^- = \Omega_3^c$ and $\Omega_4^+ = \Omega_4^c$, then volumes Ω_1^c and Ω_2^c are assumed to be images of Ω_3^c under horizontal and vertical translational symmetry respectively while Ω_4^c is the image of Ω_3^c under combined horizontal and vertical symmetry so that the following relative displacement constraints are imposed between nodes in the corner boundary volumes

$$\begin{aligned} u^{c_1} - u^{c_3} &= \bar{\varepsilon}_{12}(\beta^{c_1} - \beta^{c_3}) \\ v^{c_1} - v^{c_3} &= \bar{\varepsilon}_{22}(\beta^{c_1} - \beta^{c_3}) \end{aligned} \tag{6-41}$$

$$\begin{aligned} u^{c_2} - u^{c_3} &= \bar{\varepsilon}_{11}(\alpha^{c_2} - \alpha^{c_3}) \\ v^{c_2} - v^{c_3} &= \bar{\varepsilon}_{22}(\alpha^{c_2} - \alpha^{c_3}) \end{aligned} \tag{6-42}$$

and

$$\begin{aligned} u^{c_4} - u^{c_3} &= \bar{\varepsilon}_{11}(\alpha^{c_4} - \alpha^{c_3}) + \bar{\varepsilon}_{12}(\beta^{c_4} - \beta^{c_3}) \\ v^{c_4} - v^{c_3} &= \bar{\varepsilon}_{12}(\alpha^{c_4} - \alpha^{c_3}) + \bar{\varepsilon}_{22}(\beta^{c_4} - \beta^{c_3}) \end{aligned} \tag{6-43}$$

To eliminate translational rigid body motion of the RVE, nodes within the corner volume Ω_3^c are constrained. The determination of the effective elastic tensor in both problems proceeds under the assumption of small deformation and plane stress. This allows the use of infinitesimal strain tensor and Cauchy stress tensor directly in (2-101). Once the Cauchy stress field in the RVE is obtained, (6-36) is used to recover the effective elasticity tensor.

6.2 Validation of the homogenization scheme

Having established and justified the peridynamic correspondence homogenization theory (PDCHT) in section 6.1, numerical examples are presented in this section to benchmark the scheme against the Reus-Voigt and Hashin-Shtrikman bounds discussed in section 6.1.3. Prediction from the PDCHT would also be compared against predictions from other classical

mean field homogenization methods such as the Eshelby dilute estimate [109] and the Mori-Tanaka method [110]. Also, the result from the PDCHT will be compared to result obtained from computational homogenization based on the Finite Element Analysis. After validation of the PDCHT strategy, the framework will be used to predict the effective properties given elliptical inclusion in order to observe the influence of inclusion shape on the effective properties predicted by the method. All materials considered throughout this section are assumed to be two-phased consisting of a matrix phase and a stiffer fibre phase (inclusion). Properties associated with matrix will be denoted with the superscript (m) while those associated with the fibre phase will be denoted with superscript (f). Both matrix and fibre phases are assumed to be isotropic under isothermal linear elasticity.

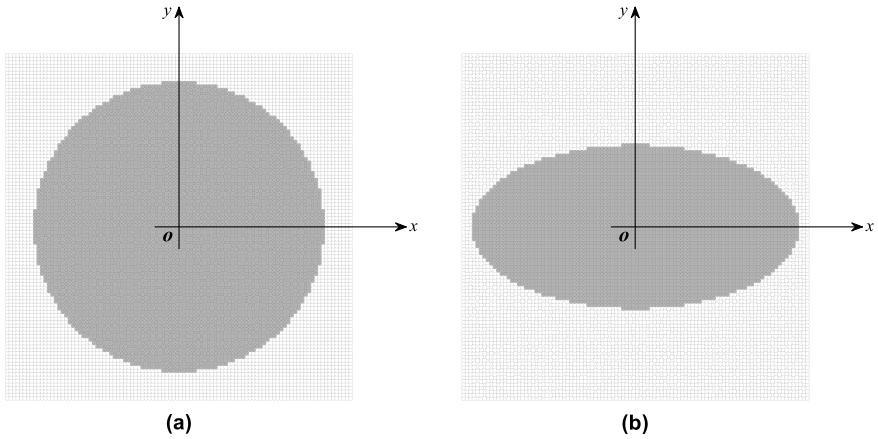

Figure 6-3: RVE geometry showing various configuration.

To pursue the objectives of validating the proposed method, three numerical examples will be considered. Figure 6-3 shows the RVE configurations to be considered in this section, and the properties of the constituent materials for the RVEs to be considered in the numerical examples are given in table 1.

Table 6-1: Material properties of the constituents of RVEs

Material	$\boldsymbol{E_1 = E_1(GPa)}$	$\boldsymbol{\nu_{12}}$	$\boldsymbol{\mu_{12}(GPa)}$	$\boldsymbol{\kappa_{12}(GPa)}$
Boron	379.30	0.10	172.41	158.04
Graphite	235.00	0.20	97.92	130.56
Glass	73.10	0.22	29.96	43.51
Aluminium	68.30	0.30	26.27	56.92
Epoxy	3.45	0.35	1.28	3.83

6.2.1 Comparing the PDCHT results with bounding theorems and other established methods.

In this example, effective properties predicted from the PDCHT will be compared against computational result from the bounding theorems of Reuss, Voigt and Hashin-Shtrikman, the mean field methods of Eshelby and Mori-Tanaka as well as the full-field method based on the finite element analysis as implemented by the authors. The material is assumed to be a glass in epoxy-matrix composite with properties given in Table 6-1 under a plane strain condition. The RVE geometry is assumed to consist of epoxy matrix with a circular glass fibre centrally placed as shown in Figure 6-3(a). The problem is solved over the range of all admissible fibre volume fractions $0 - 100\%$. Solutions will be sought considering LDBVC and PBVC. Results from the computations are presented below.

The predicted evolution of the effective elastic stiffness tensor and corresponding effective elastic constants from PDCHT, the bounding theorems and other established methods are presented in Figure 6-4 and Figure 6-5 respectively for the case of LDBVC. Similar analysis with the same RVE subjected to PBVC is conducted and the results are presented in Figure 6-6 and Figure 6-7 representing the evolution of the effective stiffness tensor and elastic constants respectively.

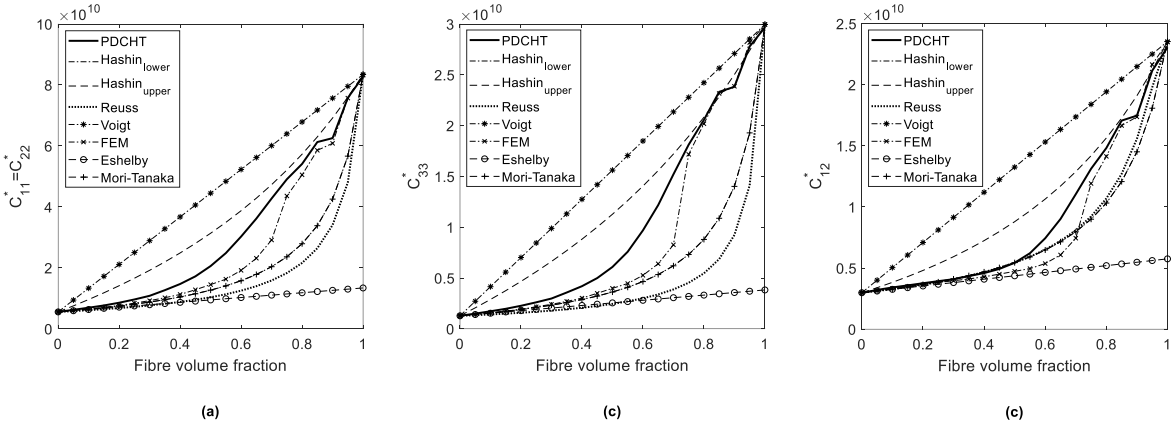

Figure 6-4: Evolution of the effective stiffness tensor of glass in epoxy-matrix composite – LDBVC (a) $C_{11}^* = C_{22}^*$ (b) C_{22}^* (c) C_{33}^* and (d) C_{12}^*

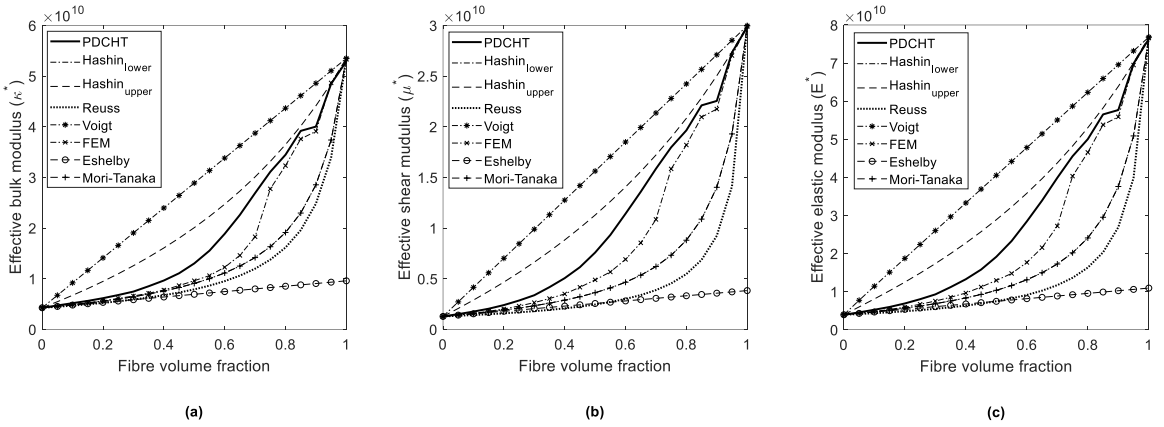

Figure 6-5: Evolution of the effective elastic constants – LDBVC (a) Effective bulk modulus, (b) Effective shear modulus and (c) Effective Elastic modulus

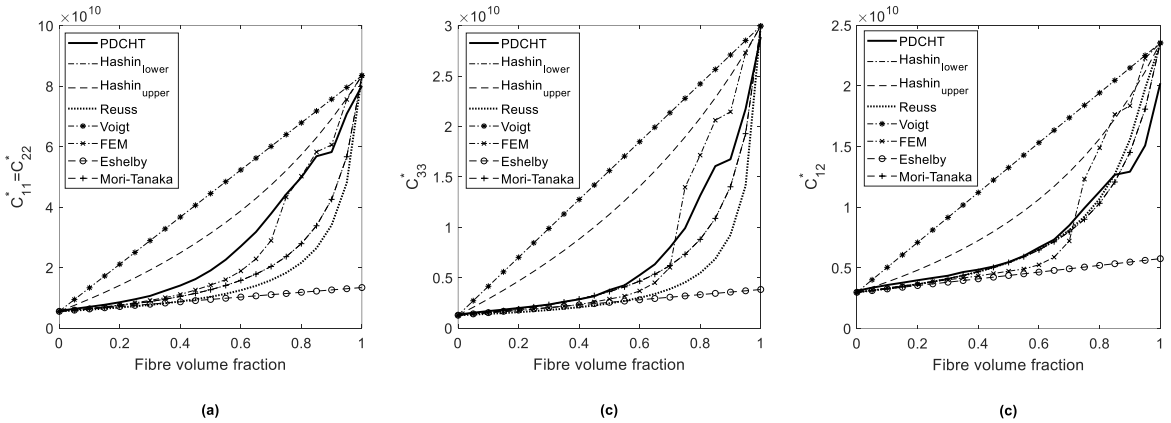

Figure 6-6: Evolution of the effective stiffness tensor of glass in epoxy-matrix composite – PBVC (a) $C_{11}^{*} = C_{22}^{*}$ (b) C_{22}^{*} (c) C_{33}^{*} and (d) C_{12}^{*}

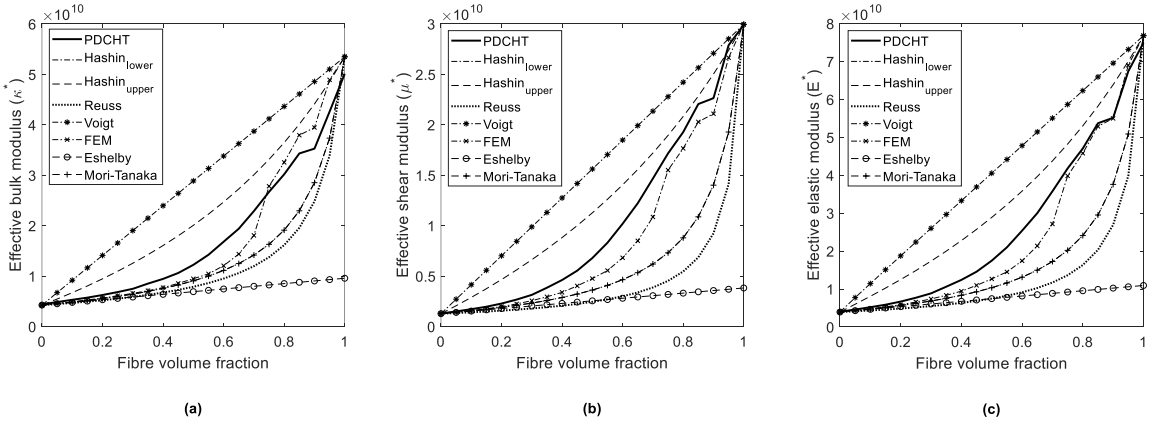

Figure 6-7: Evolution of the effective elastic constants – PBVC (a) Effective bulk modulus, (b) Effective shear modulus and (c) Effective Elastic modulus

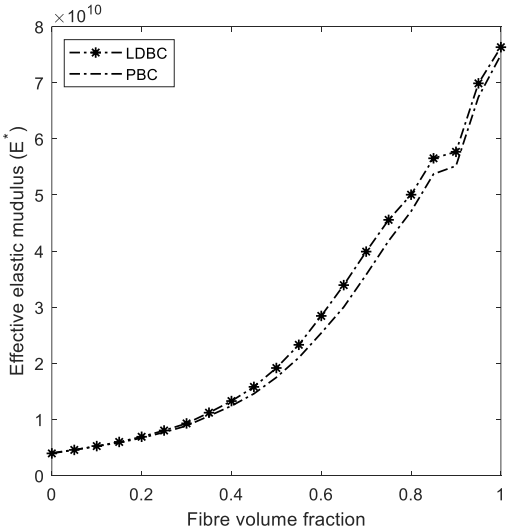

Figure 6-8: Evolution of effective elastic constant obtained using the LDBVC and PBVC

Prediction from PDCHT of the effective stiffness tensors presented in Figure 6-4 and Figure 6-6 lie within the Reuss-Voigt bound as well as the tighter Hashin-Shtrikman bound thus satisfying (6-24). Similar agreement with the bounding theorems is observed with prediction of the effective bulk and shear moduli as presented in Figure 6-5 and Figure 6-7 thus satisfying (6-32) and (6-33) for the Reuss-Voigt bounds and (6-34) and (6-35) for the Hashin-Shtrikman bounds. This is true for both the predictions under LDBVC and PBVC. Another consequence of the bounding equations (6-24), and (6-32)-(6-35) is that the elastic modulus from any proposed homogenization theory is predicted to lie within the Reuss-Voigt and Hashin-Shtrikman bound. The evolution of the effective elastic modulus obtained from the proposed theory indeed lies within these bounds as shown in Figure 6-5(c) and Figure 6-7(c) for LDBVC and PBVC, respectively.

The result of prediction from the PDCHT is also compared to predictions from the mean field homogenization methods of Eshelby and Mori-Tanaka as well as a full field computational method based on FEM solution of the RVE. The results from these methods are also presented in Figure 6-4 to Figure 6-7. The predictions from both the PDCHT and FEM comply with the bounding theorems and compared to predictions from the Mori-Tanaka method, the PDCHT prediction gives an upper estimate of the effective properties. It is worthy to note that the prediction in this example from the Mori-Tanaka method coincide with those from the Hasin-Shtrikman lower bound. This is the case in some situations and has been reported in the literature [111]. Predictions from the Eshelby dilute method agrees with results from the PDCHT only for very low fibre volume fraction. This is an expected trend as the dilute method is expected to give reasonable predictions only for very low (dilute) fibre volume fraction.

Since the fibre is assumed to be of circular cross-section, it can be shown that the maximum volume fraction that can be achieved with a perfectly circular fibre cross-section is 78.54%. Beyond this volume fraction, the circular geometry of the fibre cross-section degenerates and thereby causes a change in the morphology of the RVE. This change in morphology is reflected in the results predicted from the PDCHT and FEM solutions of the RVE and expectedly not the bounding theorems as shown in Figure 6-4 to Figure 6-7. A comparison of the predicted effective elastic modulus obtained using both LDBVC and PBVC as shown in Figure 6-8 shows that the prediction using the LDBVC provides an upper estimate of the two boundary conditions at least within the small deformation regime. This is a tested and proven result from the literature [103, 112, 113].

6.2.2 Comparing the PDCHT results with results from published works

The objective in this example is to compare predictions from the proposed PDCHT with experimental results from [114] and computational predictions from the following references: [72, 115-118]. The RVE is assumed to be a square array of circular shaped boron fibre placed in the centre of aluminium matrix as shown in Figure 6-3(a). The properties of boron and aluminium are given in Table 6-1. The RVE volume constrained problem is solved under the assumption of plane stress and PBVC.

Table 6-2: Effective material properties for boron/aluminium composite ($c_1 = 0.47$)

Models	$E_{11} = E_{22}$	ν_{12}	μ_{12}
PDHCT	140	0.185	52.5
Experiment [114]	140	0.29	52.0
OSBPDHT [117]	150	0.18	53.4
PD UC [72]	144.4	0.251	54.3
FEM [116]	144	0.19	57.2
LTEHOT [115]	144	0.195	54.34
VAMUCH [118]	144.1	0.195	54.39

**OSBPDHT=Ordinary State-based Peridynamic Homogenization Theory; PD UC=Peridynamic Unit Cell; FEM=Finite Element Method; LTEHOT=Linear Thermoelastic Higher-Order Theory; VAMUCH=Variational Asymptotic Method for Unit Cell Homogenization

Prediction of effective elastic properties of the composite system from the PDCHT is presented in Table 6-2 alongside results from some published references. Analysis of the results shows that the prediction from PDCHT provide the closest correlation to the experimental result from [114] in the estimate of the effective elastic and shear moduli. Compared to other computational methods, prediction of these moduli from the PDCHT gives the lower estimates. However, the

effective Poisson's ratio $\nu_{12} = 0.185$ predicted by the PDCHT is markedly different from the experimental result but agree well with predictions from the FEM, OSBPDHT, FEM, PD UC and LTEHOT.

6.2.3 Effective properties of RVE with elliptical fibre inclusion

In this example, two RVEs, the first with circular and the second with elliptical fibre inclusions as shown in Figure 6-3 (a) and Figure 6-3 (b) respectively will be considered. Two composites will be considered. The first is a glass in aluminium-matrix composite and the second is a graphite in aluminium-matrix composite with material properties as given in Table 6-1. The stiffness ratio (or phase contrast) φ ($\varphi \coloneqq E_{(f)}/E_{(m)}$) of the first material is 1.07 while that of the second material is 3.44. The objective in this example is to briefly demonstrate the capability of the PDCHT in capturing the effect of inclusion shape and phase contrast on the effective behaviour of materials using the LDBVC.

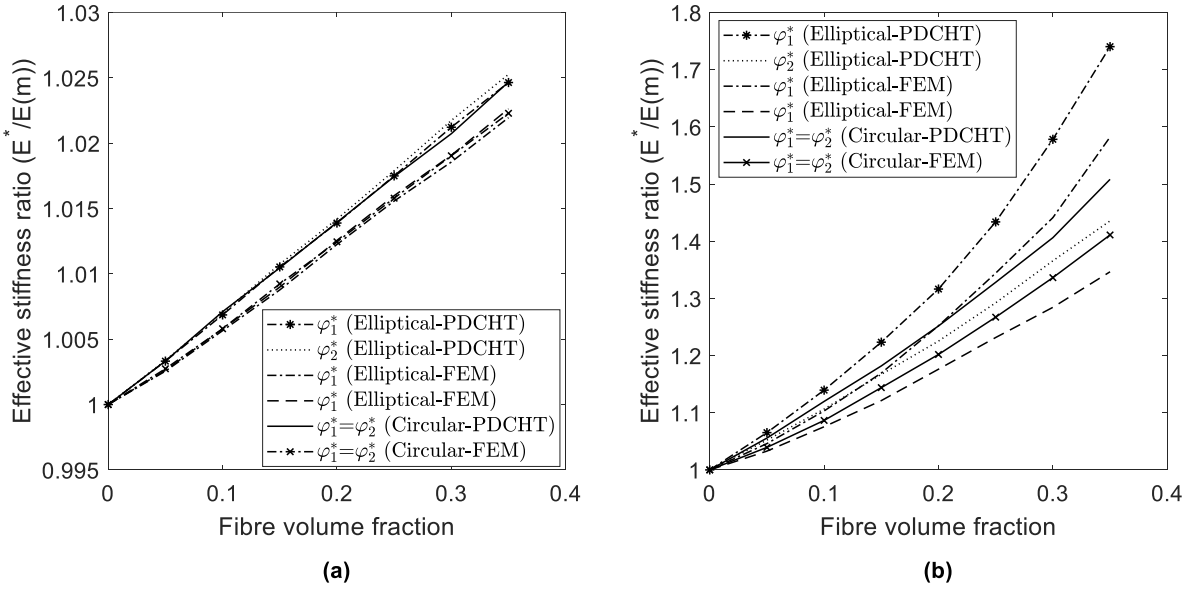

Figure 6-9: Evolution of effective stiffness ratio under LDBVC (a) $\varphi = 1.07$ (b) $\varphi = 3.44$

Table 6-3: Evolution of the elastic modulus in directions 1 and 2 (Glass in aluminium: circular inclusion)

Glass in aluminium: Circular inclusion, $\varphi = 1.07$						
	PD		FEM		Percentage difference	
$c_{(f)}$	$E1$	$E2$	$E1$	$E2$	$\%\,\Delta\,E1$	$\%\,\Delta\,E2$
0	6.84E+10	6.84E+10	6.83E+10	6.83E+10	1.88E-01	1.88E-01
0.05	6.87E+10	6.87E+10	6.85E+10	6.85E+10	2.47E-01	2.47E-01
0.1	6.89E+10	6.89E+10	6.87E+10	6.87E+10	3.17E-01	3.17E-01
0.15	6.91E+10	6.91E+10	6.89E+10	6.89E+10	3.09E-01	3.09E-01
0.2	6.94E+10	6.94E+10	6.92E+10	6.92E+10	3.34E-01	3.34E-01
0.25	6.96E+10	6.96E+10	6.94E+10	6.94E+10	3.50E-01	3.50E-01
0.3	6.98E+10	6.98E+10	6.96E+10	6.96E+10	3.53E-01	3.53E-01
0.35	7.01E+10	7.01E+10	6.98E+10	6.98E+10	4.21E-01	4.21E-01

Table 6-4: Evolution of the elastic modulus in directions 1 and 2 (Graphite in aluminium: circular inclusion)

Graphite in aluminium: Circular inclusion, $\varphi = 3.44$						
	PD		FEM		Percentage difference	
$c_{(f)}$	$E1$	$E2$	$E1$	$E2$	$\%\,\Delta\,E1$	$\%\,\Delta\,E2$
0	6.84E+10	6.84E+10	6.83E+10	6.83E+10	1.09E-01	1.09E-01
0.05	7.22E+10	7.22E+10	7.10E+10	7.10E+10	1.65E+00	1.65E+00
0.1	7.66E+10	7.66E+10	7.42E+10	7.42E+10	3.08E+00	3.08E+00
0.15	8.08E+10	8.08E+10	7.81E+10	7.81E+10	3.32E+00	3.32E+00
0.2	8.56E+10	8.56E+10	8.21E+10	8.21E+10	4.08E+00	4.08E+00
0.25	9.08E+10	9.08E+10	8.65E+10	8.65E+10	4.69E+00	4.69E+00
0.3	9.61E+10	9.61E+10	9.13E+10	9.13E+10	5.07E+00	5.07E+00
0.35	1.03E+11	1.03E+11	9.64E+10	9.64E+10	6.55E+00	6.55E+00

Table 6-5: Evolution of the elastic modulus in directions 1 and 2 (Glass in aluminium: elliptical inclusion)

Glass in aluminium: Elliptical inclusion, $\varphi = 1.07$						
	PD		FEM		Percentage difference	
$c_{(f)}$	$E1$	$E2$	$E1$	$E2$	$\%\,\Delta\,E1$	$\%\,\Delta\,E2$
0	6.84E+10	6.84E+10	6.83E+10	6.83E+10	1.88E-01	1.88E-01
0.05	6.87E+10	6.87E+10	6.85E+10	6.85E+10	2.65E-01	2.64E-01
0.1	6.89E+10	6.89E+10	6.87E+10	6.87E+10	3.08E-01	3.08E-01
0.15	6.91E+10	6.92E+10	6.89E+10	6.89E+10	3.62E-01	3.61E-01
0.2	6.94E+10	6.94E+10	6.91E+10	6.92E+10	3.49E-01	3.48E-01
0.25	6.96E+10	6.97E+10	6.94E+10	6.94E+10	3.77E-01	3.76E-01
0.3	6.99E+10	6.99E+10	6.96E+10	6.96E+10	4.48E-01	4.48E-01
0.35	7.01E+10	7.02E+10	6.98E+10	6.98E+10	4.50E-01	4.45E-01

Table 6-6: Evolution of the elastic modulus in directions 1 and 2 (Graphite in aluminium: elliptical inclusion)

Graphite in aluminium: Elliptical inclusion, $\varphi = 3.44$						
	PD		FEM		Percentage difference	
$c_{(f)}$	$E1$	$E2$	$E1$	$E2$	$\%\,\Delta\,E1$	$\%\,\Delta\,E2$
0	6.84E+10	6.84E+10	6.83E+10	6.83E+10	1.09E-01	1.09E-01
0.05	7.28E+10	7.19E+10	7.14E+10	7.05E+10	1.91E+00	1.94E+00
0.1	7.79E+10	7.56E+10	7.53E+10	7.35E+10	3.30E+00	2.90E+00
0.15	8.36E+10	7.98E+10	7.99E+10	7.66E+10	4.52E+00	4.04E+00
0.2	9.00E+10	8.38E+10	8.55E+10	8.03E+10	4.98E+00	4.12E+00
0.25	9.80E+10	8.84E+10	9.18E+10	8.41E+10	6.35E+00	4.80E+00
0.3	1.08E+11	9.34E+10	9.84E+10	8.77E+10	8.78E+00	6.06E+00
0.35	1.19E+11	9.82E+10	1.08E+11	9.20E+10	9.18E+00	6.30E+00

The evolution of the normalised effective elasticity modulus (effective stiffness ratio) $\varphi_i^* = E_i^*/E_{i(m)}$ with respect to fibre volume fraction $c_{(f)}$ for RVEs with both circular and elliptical inclusion for the two materials alongside results from FEM simulation of the same problems are presented in Figure 6-9. In Table 6-3 to Table 6-6, the evolution of the elastic modulus in directions 1 and 2 as well as the percentage difference between predictions from PDCHT and FEM are presented.

From the result presented for predictions from both PDCHT and FEM, the effective material behaviour as represented by the evolution of the effective elastic modulus for the RVE with circular inclusion shows linear behaviour for low material phase contrast $(\varphi = 1.07)$ and weak nonlinear behaviour for higher material phase contrast $(\varphi = 3.44)$. In the case of RVE with elliptical inclusion, the result for lower material phase contrast shows linear behaviour while the effective material behaviour at higher material phase contrast shows strong nonlinear behaviour. The amplified nonlinearity is because the elliptical inclusion introduces an anisotropy in the microgeometry of the composite. Also, the prediction of effective material properties for RVEs with circular inclusion from Table 6-3 and Table 6-4 shows an isotropic effective material response while predictions for RVEs with elliptical inclusion shows an orthotropic effective material behaviour.

Comparing the results from the PDCHT and FEM, it is noted that at lower material phase contrast, the predicted effective behaviour from the two methods shows good agreement for both inclusion shapes especially at low material phase contrast. The maximum percentage difference in the estimated results from these methods is 0.421% for circular inclusion and 0.45% for elliptical inclusion. However, at higher material phase contrast $(\varphi = 3.44)$, the maximum percentage

difference raises to 6.55% for circular inclusion and 9.2% in the case of elliptical inclusion, with the predictions from the PDCHT yielding more nonlinear behaviour with increasing material phase contrast. This nonlinear effective material behaviour is an expected prediction and has been reported in literature [119]. Also, the difference in result between the PDCHT and FEM predictions at high material phase contrast also did not come as a surprise because it has been reported in the literature [120, 121] that marked difference between different homogenization approaches at high stiffness ratio have been observed.

6.3 Conclusion

This chapter presented a first order homogenization theory in the framework of the NOSBPD correspondence model. The development of the theory is set on a rigorous mathematical framework consistent with the nonlocal nature of the peridynamic theory. Using this homogenization theory, it is now possible to obtain microstructure informed properties of materials for use at the macroscale within the framework of peridynamic modelling. The proposed nonlocal homogenization theory is validated by solving benchmark problems and comparing the results with those obtained using the Reuss, Voigt and Hashin-shtrikman bounding theorems, the mean field methods of Ehelby and Mori-Tanaka as well as the finite element method. These results are shown to comply with the bounding theorems as well as agree with results from the mean-field and full-field methods mentioned above.

Comparison of predictions from the proposed homogenization framework with results from the literature shows good agreement. Lastly, the PDCHT has been shown to be capable of capturing interesting material behaviour some of which have been reported in the literature such as the effect of change in the effective material property when the morphology of the RVE changes as illustrated in the first example. This effect was demonstrated more elaborately in the third example by comparing the prediction for RVEs with circular and elliptical shaped inclusion. The proposed method was also shown to be able to capture the effect of material phase contrast on the effective behaviour of the composite system.

The advantage of PDCHT theory over homogenization frameworks based on the classical continuum theory, derives from the strengths of the peridynamic theory. This framework is therefore especially useful in circumstances involving evolution of the microstructure or problems in which nonlocal interaction plays important role in the overall response of the heterogenous media. Another advantage that can be leveraged with this development is that because the peridynamic correspondence model uses familiar quantities from the classical continuum theory, Once the effective material tangent is obtained, we are free to use either of peridynamic theory or

the classical continuum theory to characterise the macroscopic response of the medium. Where the peridynamic theory is utilised at the macroscale, this result in a standard multigrid method we will call the PD^2 method. In the case where the classical theory is utilised, this result in what is referred to in the literature as Heterogenous Multiscale Method (HMM) [122]. In this case, numerical schemes such as the finite element method or the finite difference method can be utilised to solve the macro model.

Since one of the greatest strengths of the peridynamic theory lies in its capability in handling strong discontinuity in the response field of a system, this homogenization theory will be applied to problems with evolving microstructure such as micro-crack coalescing and propagation in a future work.

Chapter 7

7.0 Homogenization of Materials with Evolving Microstructure and Damage

7.1 Introduction

Motivated by the development of the peridynamic computational homogenization theory (PDCHT) in chapter 6.1, the objective in this chapter is to extend the application of the PDCHT to a class of materials with evolving microstructure. In other words, the focus in this chapter is in examining the influence of evolving microstructure on the effective response of materials at the macroscale. The effective behaviour represents the mechanical state of a point at the macroscale and is defined to be the average behaviour of the microstructure over a finite micro-subregion. The material properties arising from this state then gives the effective material properties at that point. Because the microstructure informs the mechanical condition of the macro-continuum point, an evolving microstructure will thus result in changes in material characteristics at the macroscale. Evolution of the microstructure refers to energy dissipating processes occurring at the microscale such as nucleation, propagation, and coalescing of crack. The irreversible changes brought about in a material by these microscale processes that result in degradation of the material is referred to as damage.

To achieve the aim of this contribution, section 7.2 presents a summary of implementation strategy of the homogenization framework in the context of evolving microstructure. Benchmark problems are then solved in section 7.3, with the results compared to those from [83] and the OSBPDHT proposed in [74]. It is noteworthy that the method proposed in this contribution differs from the OSBPDHT in that the former is based on the NOSBPD framework, which allows for a more generalized material model than the OSBPD. Furthermore, the NOSBPD uses classical continuum theory's stress and strain concepts, making hierarchical coupling of PD and CCM models across scales a more seamless process.

7.2 Summary of implementation strategy for PDCHT

The numerical implementation of the PDCHT involves several steps. In 6.1, the mathematical framework of the PDCHT was developed and was utilised to characterise the effective properties of composite materials. This chapter extends the PDCHT to characterize materials with evolving microstructure. The steps involved in the numerical implementation of the PDCHT are summarized below for the purpose of completeness of presentation in this chapter.

1. The originally heterogeneous peridynamic body is assumed to be macroscopically homogeneous and discretised using for example the meshless method [82] into nodes

which when taken together forms a grid. The nodes and grid in this scale are denoted respectively as the macroscopic nodes and macroscopic grid.

2. An RVE(P) is assigned to each node P on the macroscopic grid. The RVE is chosen to adequately describe all relevant microstructural morphology of the original heterogeneous material.

3. For each macroscopic node P, compute the evolution of the local macroscopic strain $\boldsymbol{\varepsilon}^*$. This macroscopic strain is then used to impose appropriate constraint to the boundary volume of the assigned RVE. Since the microscale RVE boundary constraint depends only on the first-order gradient of the macroscopic displacement field, this method is also called first-order homogenization.

4. The microscale volume constraint problem is solved using (2-88) to yield deformation $\boldsymbol{u}(\boldsymbol{x})$, strain $\boldsymbol{\varepsilon}(\boldsymbol{x})$ and consequently the stress $\boldsymbol{\sigma}(\boldsymbol{x})$ field within the RVE(P).

5. The stress field $\boldsymbol{\sigma}(\boldsymbol{x})$ is used in (6-6) via (6-5) to compute the average stress, $\boldsymbol{\sigma}^*$ over the RVE(P).

6. For each macroscopic node P, substitute $\boldsymbol{\varepsilon}^*$(P) and $\boldsymbol{\sigma}^*$(P) into (6-2) to compute the macroscopic stiffness tensor $\mathbb{C}^*$(P).

7.3 Numerical implementation of the first order homogenization

We present two numerical problems involving crack growth and accumulation in this section to demonstrate the validity of the proposed homogenization framework. The effective elastic tensor is determined in both problems based on the assumptions of small deformation and plane stress condition, thus justifying the utilisation of the infinitesimal strain tensor and the Cauchy stress tensor in (2-103). To accomplish this objective, the benchmark results from [117, 123] are used.

Since damage accumulation due to nucleation and propagation of cracks is known to induce anisotropy in the elastic properties of materials, we provide a brief remark on a suitable measure to quantify the crack induced anisotropy on the effective properties of the example material. Different measures [124-126] exist that seek to quantify elastic anisotropy of materials. However, the method proposed in [127] is preferred in this contribution due to its simplicity and most importantly its suitability for two dimensional problems. In this method, the elastic anisotropy index A for a two-dimensional crystal is given by:

$$A = \left(\left[\frac{1}{4}(C_{11} + C_{22} + 2C_{12})\,(S_{11} + S_{22} + 2S_{12}) - 1 \right]^2 \right.$$
$$\left. + 2\left[\frac{1}{6}(C_{11} + C_{22} - 2C_{12} + 4C_{66})(S_{11} + S_{22} - 2S_{12} + S_{66}) - 1 \right]^2 \right)^{\frac{1}{2}} \quad (7\text{-}1)$$

where C_{ij} and S_{ij} are the components of the elastic stiffness and compliance tensors respectively. In (7-1), A yields a value of zero for the limiting case of perfect isotropy while deviation from zero defines the degree of elastic anisotropy.

7.3.1 Material softening due to crack propagation.

In this example, the proposed homogenization scheme will be utilised to study the phenomenon of material softening due to the presence and interaction of cracks at the microscale. To this end, two scenarios are investigated and the RVEs considered are shown in Figure 7-1. Each RVE is taken to be a square of side length $W = 1$ m and comprise of a matrix material with an elastic modulus $E = 2{\times}10^9$ Pa and a Poisson ratio $\nu = 0.3$. In the first scenario, the RVE in Figure 7-1(a) is utilised, which consists of a single horizontally propagating crack whose origin is at the centre of the RVE. The RVE for the second scenario is given in Figure 7-1(b) and consists of two coalescing cracks. In the first case, the length of the crack at any given instant of time is L, while in the second scenario, the length of each crack is $L/2$. In both scenarios, the initial length of the crack is taken to be $L = 0$ and the final total length is $L = 1$ m.

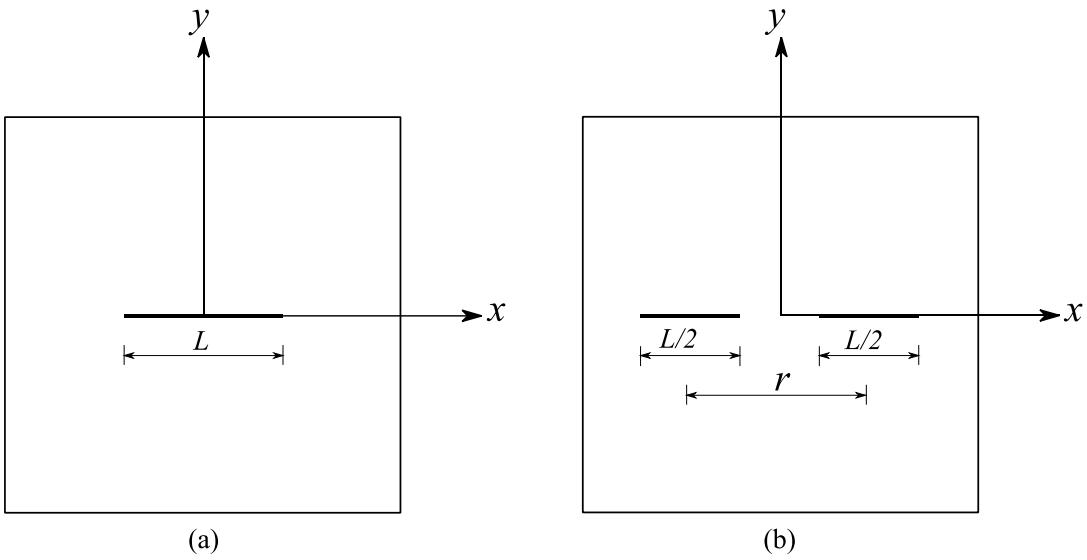

Figure 7-1: RVEs with (a) Single subscale crack (b) Two interacting subscale cracks

Note that although one of the key advantages offered by peridynamics is in the modelling of autonomous crack propagation. However, in this contribution, the propagation of the crack is controlled to be consistent with the propagation in the referenced contributions [117, 123]. To achieve the desired crack length consistent with crack propagation in the referenced works, the analyses in this example are conducted under a quasi-static loading assumption through multiple load steps. The realisation of each load step is represented by a specific length of crack.

The simulation is done over crack propagation processes spanning twenty-one discrete crack lengths in the interval [0-1] and [0-0.5] for the first and second scenarios respectively, which translate to a crack growth of 0.05 m for each load step. The distance r between the origin of the two cracks in Figure 7-1(b) is given as 0.25 m, thus allowing the cracks to coalesce at $L = 0.5$ m.

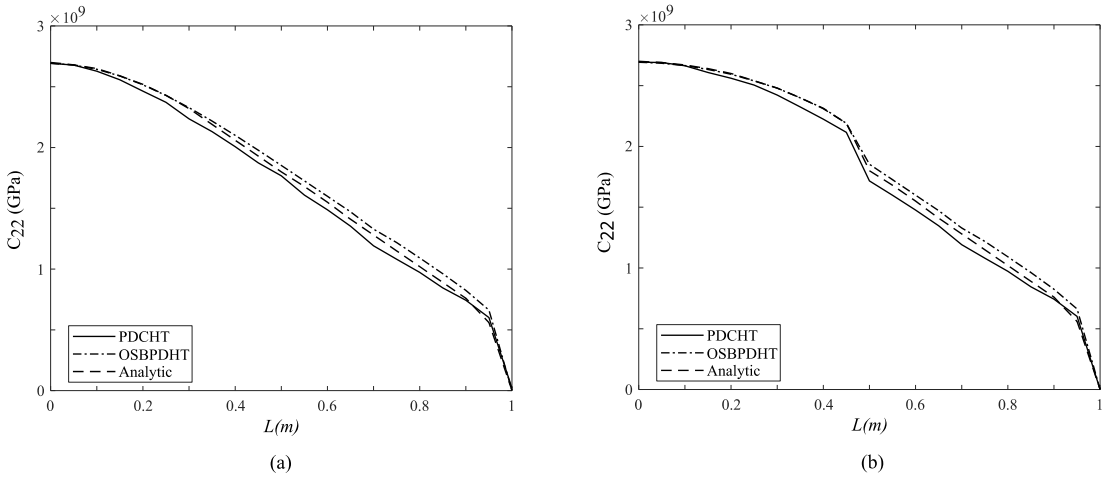

Figure 7-2: Evolution of the component $\mathbf{C_{22}}$ of the effective stiffness tensor (a) RVE with a single propagating crack, (b) RVE with two coalescing cracks

The effective tangent matrices of the material were evaluated as its microstructure evolved due to the single propagating crack and two coalescing cracks, respectively, following the technique outlined in section 7.2. Evolution of the C_{22} component of the effective tangent stiffness matrices for the case of a single propagating crack is presented as Figure 7-2(a) and for the case of two coalescing cracks is presented as Figure 7-2(b). These results are compared with results from [117, 123]. Results from the single propagating crack scenario indicate a smooth relationship between material softening and crack growth. However, in the case of the two cracks, an abrupt change in the relationship is observed as the two cracks coalesce. This phenomenon is attributed to interaction between the coalescing cracks. It was noted in [123] that when multiple crack coalesce, this lead to significant increase in a damage energy release rate which lead to amplification of damage which in this case is characterized by the sudden change in material softening as observed.

In both cases, it is observed from Figure 7-2 (a) and (b) that the results obtained from the proposed first order peridynamic homogenization theory correlate well with results from [117, 123].

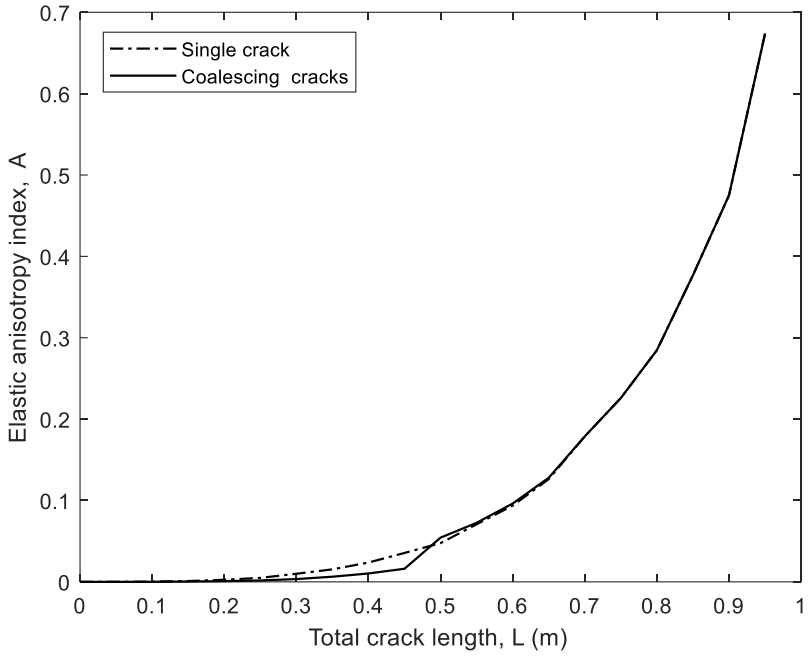

Figure 7-3: Elastic anisotropy index for the single crack and coalescing cracks

To quantitatively measure the degree of anisotropy that may be induced on the elastic property of material due to crack growth, (7-1) is utilized to compute the elastic anisotropy index A of the effective material tensor. Figure 7-3 shows the evolution of the elastic anisotropic indices for the case of a single crack and two coalescing cracks. As can be seen from the figure, the propagation of cracks results in increasing anisotropy. Comparison of anisotropic indices from the two cases shows an almost identical growth trend except for the jump corresponding to crack length close to when the two coalescing cracks were about to merge. This jump in elastic anisotropy index correlates well with the jump captured in the evolution of the C_{22} component of the effective material stiffness tensor as shown in Figure 7-2(b).

7.3.2 Damage evolution due to randomly distributed microcracks

In this second example, we study the evolution of damage due to randomly distributed microcracks of equal length L. Two case studies would be investigated. In the first case, the RVE consists of microcracks that are aligned horizontally Figure 7-4 (a) while in the second case, the microcracks in the RVE are randomly aligned Figure 7-4 (b). In both case studies, the material of the RVE is taken to consist of an isotropic matrix having an elastic modulus $E = 2\times10^9$Pa and Poisson ratio $v = 0.3$.

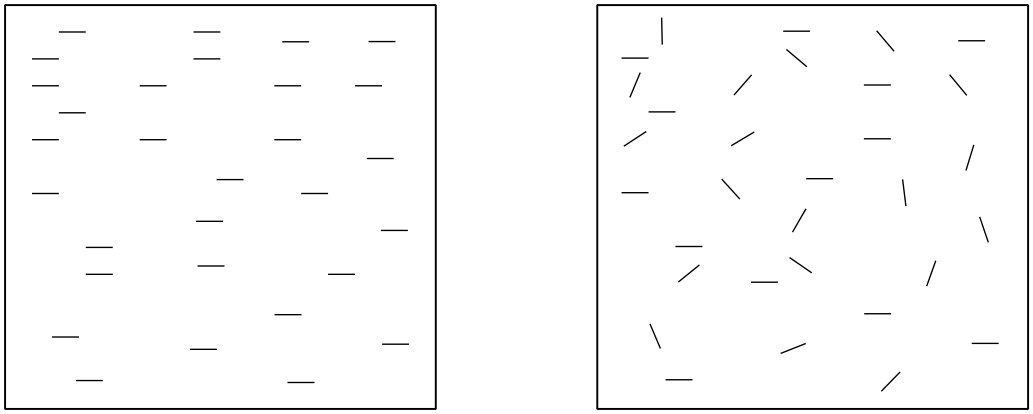

(a) (b)

Figure 7-4: Arrangement of randomly distributed microcracks (a) Horizontally aligned (b) Randomly aligned.

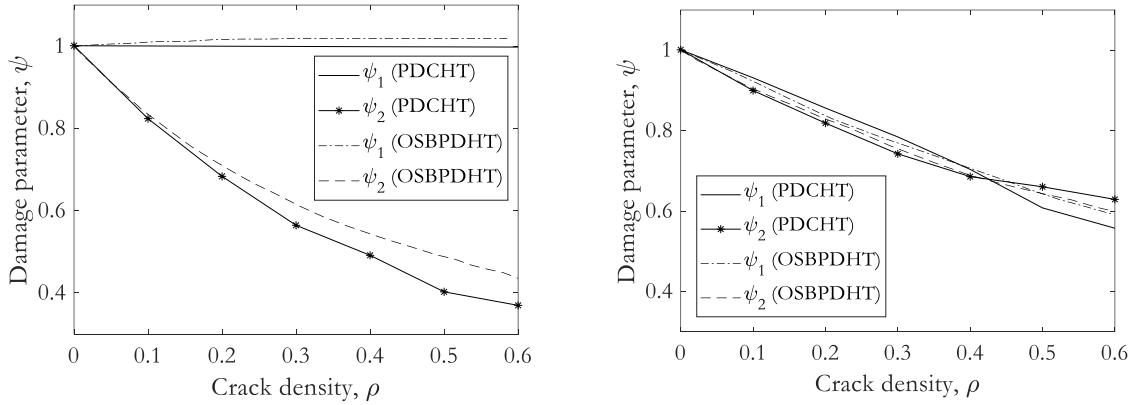

Figure 7-5: Evolution of damage due to random cracks (a) Horizontally aligned, (b) Randomly aligned.

To obtain the effective properties of the material with evolving microstructure as characterised by crack growth, the implementation strategy highlighted in section 7.2 was executed. The evolution of damage due to randomly distributed cracks is presented in Figure 7-5(a) for cracks that are horizontally aligned and in Figure 7-5(b) for cracks that are randomly oriented as a function of crack density ρ. Each curve represents the evolution of a normalised damage parameter ψ_n which measures the softening of the elastic modulus and is given as

$$\psi_n = \frac{E_n^*}{E} \tag{7-2}$$

where E_n^* is the effective elastic modulus in the coordinate direction $n = 1,2$, such that $n = 1$ corresponds with the horizontal coordinate axis and $n = 2$ corresponds to the vertical coordinate axis. E is the elastic modulus of the undamaged matrix material.

In the case of horizontally aligned cracks, the damage parameter ψ_1 remained largely unchanged as the damage process progresses as seen in Figure 7-5(a), which suggests that the material essentially retained its mechanical properties in the $n = 1$ direction. However, in the $n = 2$ coordinate direction, the evolution of the damage parameter ψ_2 shows progressive softening of the material as the damage process progresses.

In the second scenario where the randomly distributed microcracks are given random orientations, the results of the computational homogenization as presented in Figure 7-5(b) indicate that while the damage due to increasing prevalence of microcracks caused the material to soften, the effective material behaviour did not however deviate much from its original isotropic state.

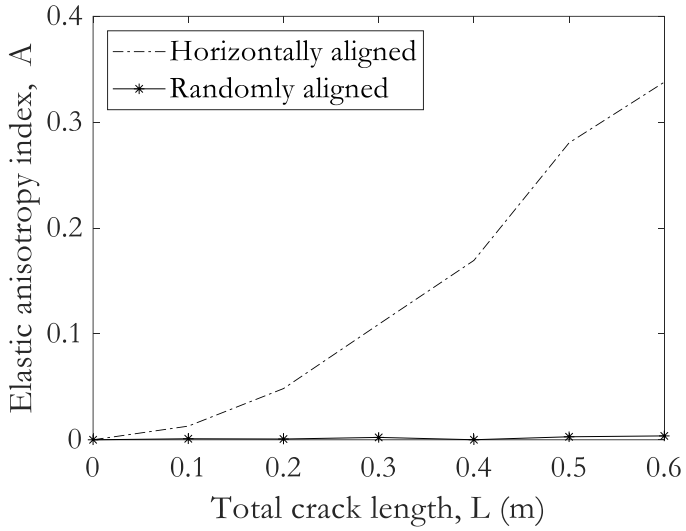

Figure 7-6: Elastic anisotropy index for cracks aligned horizontally and randomly.

It is inferred from Figure 7-5(a) that the prevalence of horizontally oriented, randomly distributed microcracks transformed a hitherto isotropic material into an effective anisotropic material. To quantitatively measure the degree of anisotropy induced, (7-1) is employed to evaluate the elastic anisotropy index A. Figure 7-6 show the elastic anisotropy indices for the two cases of horizontally aligned and randomly aligned cracks as the cracks accumulate. Figure 7-6 indicate that while the accumulation of horizontal cracks has the effect of increasing the anisotropy of the material, the accumulation of randomly aligned cracks essentially did not induce much anisotropy in comparison.

For the purpose of model validation, the evolution of effective damage obtained using the PDCHT was compared with previous results from OSBPDHT [117]. Results shown in Figure 7-5(a) and Figure 7-5(b) show agreement in the overall trend of the results from both methods. However, there are noticeable differences in the details of the results because although the same crack

densities were used in both studies, the randomness in the distribution and orientation of microcracks in both studies made it impossible to exactly reproduce the distribution of the microcracks and their orientations as in [117]. Microcracks have been shown to interact with one another when their distance apart is less than some minimum value as demonstrated in the results presented in Figure 7-2(b). Since each instance of randomly generated microcracks give rise to different arrangement and hence different interaction between microcracks, it is expected that analysis of two different distribution will yield different results. It has also been demonstrated in the results presented in Figure 7-5 that the orientation of the microcracks has significant influence on the effective response. Since two instances of randomly generated cracks with arbitrary orientation give rise essentially to two different microstructures, it follows that the variation in the result of analysis from these instances of the microstructure is an expected consequence.

7.4 Conclusion

In this chapter, the PDCHT developed in chapter 6.1 was utilised to study the evolution of effective material response of damaged media. The PDCHT is an energy-based homogenization procedure which ensures constitutive equivalence between two structurally dissimilar materials by enforcing a strain energy equivalence between them. This computational homogenization was performed in a quasi-static analysis framework in which different loading conditions are assumed to yield progressive damage either in the form of propagating crack or increasing incidence of microcracks.

Two numerical examples were solved. The first example allows us to study the effect of propagating crack and crack interaction on the effective material coefficients. It was demonstrated that the presence of crack changes material behaviour in this case from isotropic to mild and strongly anisotropic. As cracks propagate, the material exhibits softening in one or both directions.

In the second example, we studied the damage evolution of a material due to proliferation of microcracks. Two case studies were investigated. The first case is when the microcracks are randomly distributed but horizontally aligned while the second case is where the randomly distributed microcracks are given arbitrary orientations. Effective material coefficients obtained from the first scenario shows a strongly anisotropic effective behaviour while in the second case, the effective behaviour essentially remained isotropic. However, in both cases, the material exhibited softening with increasing damage accumulation.

A further development of these studies is expected. The foundation laid here can be utilised to study phenomena that occur out of interaction of microcracks with macro-cracks. Example of

such phenomena is crack shielding and amplification of macrocracks due to interaction with microcracks. In this framework, the damage due to microcracks can be homogenised so that their interaction with the macrocrack would be applied in an average sense.

Chapter 8

8.0 Computational homogenization of viscoelastic composites

8.1 Introduction

The design and optimization of viscoelastic composite materials is an important and growing area of research in materials science and engineering. The increasing acceptability of viscoelastic composite materials in industries such as civil, aerospace, automotive, and biomedical engineering is partly due to the advantage it offers designers and engineers to tailor its microstructure to achieve optimal overall or 'effective' performance. This is achieved not only through choosing the optimal parameters of the constituent materials but also choosing the optimal layout and arrangement of the constituent materials.

Computational homogenization schemes are a popular method for characterizing the properties of viscoelastic composite materials. These schemes are numerical frameworks that are used to predict the effective properties of a composite material by simulating the behaviour of the individual constituent materials and their interactions at the subscale. Traditionally, most computational homogenization schemes for analysis of composite systems [128-130] in general and viscoelastic composite systems [131, 132] in particular, have been developed based on classical continuum mechanics, which is built upon the assumption of local action as well as smooth and continuous deformation. However, there are many mechanisms that give rise to processes in composite materials which invalidate these fundamental assumptions of the classical theory.

Discontinuous material behaviour, such as fracture, presents a significant challenge for modelling within the framework of classical continuum mechanics. This is because the theory relies on spatial derivatives to describe physical system which necessarily impose the conditions of smooth and continuous deformation on the material. This mathematical framework is not suitable for modelling fracture processes such as brittle fracture and fragmentation [10].

Strain localization in materials that exhibit strain softening due to damage is another problem that is difficult to model using the classical continuum theory. Using the classical framework to model such phenomenon presents two problems. The first is the non-uniqueness of the result due to the loss of ellipticity of the governing differential equations of the classical theory and the second is a numerical problem that typically manifest as the spurious localization of strain into a narrow band that is dependent on grid size of the numerical scheme, e.g. element size in finite element model [5]. As a result, it is deemed inappropriate to utilise models based on the classical continuum framework to characterise materials that exhibit strain-softening behaviour [5, 133].

Crazing is a key mechanism of deformation in polymers, which is characterized by the nucleation and propagation of small cracks at the surface of the material. The size of the specimen plays a crucial role in the behaviour of crazed polymers. This is because as the specimen size decreases, the probability of craze nucleation at the surface increases, leading to more deformation. Thus, the larger the ratio of surface to volume in the specimen, the more likely it is for crazes to nucleate and propagate, leading to a decrease in the mechanical strength of the material. This is a manifestation of a more general phenomenon known as size effect. Size effect is known to be notoriously difficult to model in the framework of the classical theory. This is because the resolution of this effect require a length scale parameter to be present in the constitutive model [134]. Unfortunately, such a parameter does not exist in the constitutive model of the classical theory.

Considering these challenges and motivated by the capability of PD to alleviate challenges such as the capability to capture the size-scale effects and nonlocal spatial interactions in composites [135], quasi-brittle materials [11] and bilayered systems [136], this chapter presents a numerical modelling method that utilizes the PDCHT proposed in chapter 6.1 to assess the influence of microscopic variations on the macroscopic response of viscoelastic composites. This method involves solving boundary value problems in a microscopic domain to calculate a homogenized stiffness based on the microstructure of the composite. The PD model represents the material as a network of bonds that interact via a nonlocal interaction kernel, allowing for the capture of nonlocal effects and the prediction of the effective properties of the composite.

The remainder of this chapter is organized as follows. In the next section, a brief overview of the of viscoelastic constitutive model is provided. Then the proposed homogenization framework is described in detail, including the mathematical formulation and the numerical algorithms used to solve the resulting equations. Finally, some numerical examples to demonstrate the effectiveness of the proposed method will be solved and the results compared with those obtained using other approaches.

8.2 Linear viscoelastic constitutive model

The constituents of the composites studied in this thesis will be assumed to be isotropic and linear in behaviour. From (2-101), it is clear that the NOSBPD can admit a wide range of constitutive models from CCM, and the response function adopted will depend on the type of material behaviour anticipated. Since the goal in this chapter is to extend the PDCHT to encompass viscoelastic materials, this section will introduce the concept of viscoelastic constitutive model from the CCM and derive a form of the constitutive model that can be easily and efficiently

implemented within the NOSBPD computational framework. There are two main approaches to developing viscoelastic models in CCM: the integral approach and the differential approach. Only the integral approach will be pursued in this contribution. The response function in the integral form for a linear non-ageing viscoelastic material takes the form:

$$\sigma_{ij}(t) = \int_0^t C_{ijkl}(t-\tau)\frac{d}{d\tau}\varepsilon_{kl}(\tau)d\tau \tag{8-1}$$

where $C_{ijkl}(t-\tau)$ is the fourth order stress relaxation stiffness tensor. The relaxation stiffness tensor is typically approximated by a series of decaying exponents also called Prony series such that:

$$C_{ijkl}(t) = C_{ijkl_\infty} + \sum_{m=1}^{n} C_{ijkl_m}\exp\left(-\frac{t}{\tau_m}\right) \tag{8-2}$$

where the first term, C_{ijkl_∞} is the equilibrium or elastic modulus of the material while each subsequent term in the series represent a relaxation mode of the material. Introducing (8-2) into (8-1) yields

$$\begin{aligned}\sigma_{ij}(t) &= \int_0^t C_{ijkl_\infty}\frac{d}{d\tau}\varepsilon_{kl}(\tau)d\tau + \sum_{m=1}^{n}\int_0^t C_{ijkl_m}\exp\left(-\frac{t-\tau}{\tau_m}\right)\frac{d}{d\tau}\varepsilon_{kl}(\tau)d\tau \\ &= C_{ijkl_\infty}\varepsilon_{kl}(t) + \sum_{m=1}^{n}\int_{-\infty}^t C_{ijkl_m}\exp\left(-\frac{t-\tau}{\tau_m}\right)\frac{d}{d\tau}\varepsilon_{kl}(\tau)d\tau \\ &= \sigma_{ij_\infty}(t) + \sum_{m=1}^{n} h_{ij_m}(t)\end{aligned} \tag{8-3}$$

where $\sigma_{ij_\infty}(t) = C_{ij_\infty}\varepsilon_{kl}(t)$ represents the elastic component of the material response, and

$$h_{ij_m}(t) = \int_0^t C_{ijkl_m}\exp\left(-\frac{t-\tau}{\tau_m}\right)\frac{d\varepsilon_{kl}(\tau)}{d\tau}d\tau \tag{8-4}$$

commonly referred to as *state variable* is the viscous response of the material. Notice that to obtain the stress at a particular time, the constitutive relationship given by (8-3) leads to the requirement of computing the integral in (8-4). This is not suitable for implementation in a numerical scheme as this will require the entire history of the deformation to be stored. This is obviously not a computationally efficient strategy. To obtain a computationally more efficient form of (8-3), numerical incremental procedure is normally utilised. To achieve this, the loading time t is divided

into discrete interval Δt such that $t_{n+1} = t_n + \Delta t$. Now, considering the time interval $[t_n, t_{n+1}]$, the deformation history can be split into two periods of $0 \le \tau \le t_n$ of known deformation and $t_n \le \tau \le t_{n+1}$ of unknown deformation. The integral in (8-4) can then be additively split into

$$
\begin{aligned}
h_{ij}^{n+1}{}_m &= \int_0^{t_n} C_{ijkl}{}_m \exp\left(-\frac{t_{n+1}-\tau}{\tau_m}\right)\frac{d\varepsilon_{kl}(\tau)}{d\tau}\,d\tau \\
&\quad + \int_{t_n}^{t_{n+1}} C_{ijkl}{}_m \exp\left(-\frac{t_{n+1}-\tau}{\tau_m}\right)\frac{d\varepsilon_{kl}(\tau)}{d\tau}\,d\tau \\
&= \int_0^{t_n} C_{ijkl}{}_m \exp\left(-\frac{t_n+\Delta t-\tau}{\tau_m}\right)\frac{d\varepsilon_{kl}(\tau)}{d\tau}\,d\tau \\
&\quad + \int_{t_n}^{t_{n+1}} C_{ijkl}{}_m \exp\left(-\frac{t_{n+1}-\tau}{\tau_m}\right)\frac{d\varepsilon_{kl}(\tau)}{d\tau}\,d\tau \\
&= \int_0^{t_n} C_{ijkl}{}_m \exp\left(-\frac{\Delta t}{\tau_m}\right)\exp\left(-\frac{t_n-\tau}{\tau_m}\right)\frac{d\varepsilon_{kl}(\tau)}{d\tau}\,d\tau \\
&\quad + \int_{t_n}^{t_{n+1}} C_{ijkl}{}_m \exp\left(-\frac{t_{n+1}-\tau}{\tau_m}\right)\frac{d\varepsilon_{kl}(\tau)}{d\tau}\,d\tau \\
&= \exp\left(-\frac{\Delta t}{\tau_m}\right)\int_0^{t_n} C_{ijkl}{}_m \exp\left(-\frac{t_n-\tau}{\tau_m}\right)\frac{d\varepsilon_{kl}(\tau)}{d\tau}\,d\tau \\
&\quad + \int_{t_n}^{t_{n+1}} C_{ijkl}{}_m \exp\left(-\frac{t_{n+1}-\tau}{\tau_m}\right)\frac{d\varepsilon_{kl}(\tau)}{d\tau}\,d\tau \\
&= \exp\left(-\frac{\Delta t}{\tau_m}\right) h_{ij}^{n}{}_m + \int_{t_n}^{t_{n+1}} C_{ijkl}{}_m \exp\left(-\frac{t_{n+1}-\tau}{\tau_m}\right)\frac{d\varepsilon_{kl}(\tau)}{d\tau}\,d\tau
\end{aligned}
\tag{8-5}
$$

If the change in strain in each time interval is assumed to be constant, then we can write:

$$
\frac{d\varepsilon_{kl}}{dt} = \frac{\Delta\varepsilon_{kl}}{\Delta t} = \frac{\varepsilon_{kl}^{n+1} - \varepsilon_{kl}^{n}}{\Delta t} \tag{8-6}
$$

Substitution of (8-6)into (8-5) yields:

$$
\begin{aligned}
h_{ij}^{n+1}{}_m &= \exp\left(-\frac{\Delta t}{\tau_m}\right) h_{ij}^{n}{}_m + \int_{t_n}^{t_{n+1}} C_{ijkl}{}_m \exp\left(-\frac{t_{n+1}-\tau}{\tau_m}\right)\frac{\varepsilon_{kl}^{n+1}-\varepsilon_{kl}^{n}}{\Delta t}\,d\tau \\
&= \exp\left(-\frac{\Delta t}{\tau_m}\right) h_{ij}^{n}{}_m + C_{ijkl}{}_m \tau_m \left(1 - \exp\left(-\frac{\Delta t}{\tau_m}\right)\right)\frac{\varepsilon_{kl}^{n+1}-\varepsilon_{kl}^{n}}{\Delta t}
\end{aligned}
$$

$$= \exp\left(-\frac{\Delta t}{\tau_m}\right) h^n_{ij}{}_m(t_n) + C_{ijkl}{}_m \frac{\tau_m}{\Delta t}\left(1 - \exp\left(-\frac{\Delta t}{\tau_m}\right)\right)[\varepsilon^{n+1}_{kl} - \varepsilon^n_{kl}] \quad (8\text{-}7)$$

If we write $A_m = \frac{\tau_m}{\Delta t}\left(1 - \exp\left(-\frac{\Delta t}{\tau_m}\right)\right)$, then (8-7) can be written as:

$$h^{n+1}_{ij}{}_m = \exp\left(-\frac{\Delta t}{\tau_m}\right) h^n_{ij}{}_m + A_m C_{ijkl}{}_m[\varepsilon^{n+1}_{kl} - \varepsilon^n_{kl}] \quad (8\text{-}8)$$

Note that equation (8-8) is a recursive function that depends only on the values $h^n_{ij}{}_m$ and ε^n_{kl} from the previous time step to calculate the stress state at the current time step, thus eliminating the requirement to store the entire history of deformation. The components of the stress relaxation stiffness tensor can be expressed in terms of relaxation modulus $E(t)$, shear relaxation modulus $G(t)$ and bulk relaxation modulus $K(t)$ which are the viscoelastic analogues of elastic Young's modulus, shear modulus and bulk modulus, respectively. These viscoelastic moduli are normally obtained via experimentation. To utilise these experimental data in mathematical modelling, the discrete data are usually approximated using Prony series. In this representation, $E(t)$, $G(t)$, and $K(t)$ are typically approximated respectively as

$$E(t) = E_\infty + \sum_{m=1}^{n} E_m \mathrm{e}^{-\frac{t}{\tau^E_m}}, \quad G(t) = G_\infty + \sum_{m=1}^{n} G_m \mathrm{e}^{-\frac{t}{\tau^G_m}}, \quad K(t) = K_\infty + \sum_{m=1}^{n} K_m \mathrm{e}^{-\frac{t}{\tau^K_m}} \quad (8\text{-}9)$$

where the subscript ∞ designate the equilibrium or elastic response of the viscoelastic material, so that the stiffness relaxation tensors $\mathbf{C}_\infty$ and $\mathbf{C}_m$ in (8-3) for plane stress condition are respectively given as

$$\mathbf{C}_\infty = \frac{E_\infty}{1-\nu^2}\begin{bmatrix} 1 & \nu & 0 \\ \nu & 1 & 0 \\ 0 & 0 & \frac{1-\nu}{2} \end{bmatrix}, \qquad \mathbf{C}_m = \frac{E_m}{1-\nu^2}\begin{bmatrix} 1 & \nu & 0 \\ \nu & 1 & 0 \\ 0 & 0 & \frac{1-\nu}{2} \end{bmatrix} \quad (8\text{-}10)$$

8.3 Dynamic properties

Although material properties such as the relaxation modulus arising from the result of static measurement are sufficient to produce useful characteristics of viscoelastic materials, however, to gain deeper insight into certain rheological characteristics of viscoelastic materials sometimes require expressing the mechanical properties in an alternative form. A very popular alternative is the representation of viscoelastic properties in the frequency domain, often termed as dynamic

properties. This can be achieved through dynamic mechanical tests or by converting the result of static measurements. In this communication, the robustness of the proposed methodology will be demonstrated by recovering the effective dynamic properties of viscoelastic composites from the effective static properties. Important dynamic parameters of interest in the characterisation of viscoelastic materials are the storage modulus E' and loss modulus E''. The vector sum of the storage and loss moduli is called the complex modulus, and is typically represented as

$$E^*(t) = E'(t) + E''(t) \tag{8-11}$$

where E' represents the elastic component of the material response while E'' represents the viscous component. The tangent of the loss angle or phase lag between stress and strain given by

$$\delta = \tan(\phi) = \frac{E''}{E'} \tag{8-12}$$

is called the tangent modulus or loss tangent/damping factor and provides information on the proportion of energy lost during a deformation cycle, thus providing a quantitative means to measure the degree of viscous response in the total response of a material. The storage and loss moduli are respectively given [137] as

$$E' = E_0\left(\sum_{m=1}^{n}\bar{E}_m + \sum_{m=1}^{n}\bar{E}_m\frac{\tau_m^2\omega^2}{1+\tau_m^2\omega^2}\right) \tag{8-13}$$

and

$$E'' = E_0\left(\sum_{m=1}^{n}\bar{E}_m\frac{\tau_m\omega}{1+\tau_m^2\omega^2}\right) \tag{8-14}$$

where $\bar{E}_m = E_m/E_0$ and $E_0 = E(t=0)$ is the instantaneous relaxation modulus.

8.4 Computational homogenization

In this contribution, a first-order computational homogenization procedure is proposed for a composite made partly or wholly of viscoelastic constituents. The objective is to determine the overall mechanical properties of the composite material. This objective is born out of the need to understand how the microstructure of the composite material influences its overall behaviour at the macroscale. This information is useful in predicting and optimizing the performance of composite materials. By understanding the relationship between the microstructure and the macroscopic behaviour of composite material, it is possible to design composite materials with specific properties and performance characteristics for a particular application.

This proposed nonlocal homogenization scheme just like most computational homogenization schemes is composed of three main components. The first is the identification of relevant scales in the problem which are usually denoted as microscale and macroscale. Secondly, a localization procedure that involves finding the stress solution of a mechanical model at the microscale given a macrostrain. Lastly, the development of a homogenization rule that yields macroscopic stress based on the micro fields of the stress tensor.

8.4.1 Definition of scales and homogenization rule

Given a heterogeneous material M composed of more than one constituent phase (at least one of which is viscoelastic), the objective in this nonlocal first-order computational homogenization scheme is to find an equivalent or substitute material $\overline{M}$ that will have the same overall behaviour as M. The approximation of M with $\overline{M}$ is based on two key assumptions. The first is that if the constituent phases in M exhibit linear behaviour, then the response of the effective (substitute) material $\overline{M}$ will likewise be linear [138, 139]. Thus, in this regard, the constitutive function that relates stress and strain fields in M^* takes the linear form:

$$\bar{\sigma}_{ij}(t) = \bar{C}_{ijkl}\bar{\varepsilon}_{kl}(t) \tag{8-15}$$

where $\bar{C}_{ijkl}$ is the time dependent effective stiffness relaxation tensor, and overbar in (8-15) and elsewhere in this chapter indicates field variables associated with the substitute homogeneous material. The substitute homogeneous material $\overline{M}$ will henceforth be designated as the macroscale. The second assumption is that of statistical homogeneity of the composite system M. This means that M exhibits the same average behaviour over any randomly selected subregion that is sufficiently large in comparison with the size of individual microstructural elements or phase such as the size of inclusions [138]. Any such subregion is called a representative volume element (RVE) and represents the microscale for the purpose of this homogenization scheme. Since the average properties of the composite material are the same within the RVE as they are for the entire material, this allows the use of volume average of field over the RVE instead of volume average of fields over the entire material.

Once the implication of linear effective behaviour and statistical homogeneity is granted, the next task is to find the relationship between the microscopic field of stress and strain with their macroscopic counterparts. This is achieved through the application of nonlocal stress and strain average theorems. Consider a heterogeneous body $\mathfrak{B}$ which occupies a region $\overline{\Omega} = \Omega_s \cup \Omega_c$ such that Ω_s represents the region where solution is sought and Ω_c represents the boundary region. The

average stress and average strain over Ω_s are denoted as $\langle \boldsymbol{\sigma} \rangle$ and $\langle \boldsymbol{\varepsilon} \rangle$, respectively. The nonlocal average stress theorem states that if $\mathfrak{B}$ attains static equilibrium when a constant stress tensor $\overline{\boldsymbol{\sigma}}$ is applied on the boundary domain Ω_c, then the volume average of the stress field in Ω_s is equal to $\overline{\boldsymbol{\sigma}}$, that is

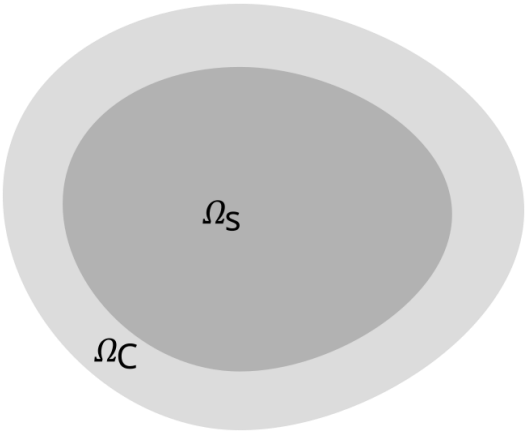

Figure 8-1: Micro computational domain showing solution and boundary domains.

$$\langle \boldsymbol{\sigma} \rangle = \overline{\boldsymbol{\sigma}} \tag{8-16}$$

On the other hand, the nonlocal average strain theorem states that if $\mathfrak{B}$ is subjected to displacement on the boundary domain Ω_c which is produced by a constant strain tensor $\bar{\boldsymbol{\varepsilon}}$ such that $\boldsymbol{u}^0 = \bar{\boldsymbol{\varepsilon}}\boldsymbol{x}$ for all $\boldsymbol{x} \in \Omega_c$, then:

$$\langle \boldsymbol{\varepsilon} \rangle = \bar{\boldsymbol{\varepsilon}} \tag{8-17}$$

where the quantities $\langle \boldsymbol{\sigma} \rangle$ and $\langle \boldsymbol{\varepsilon} \rangle$ are respectively given by:

$$\langle \boldsymbol{\sigma} \rangle = \frac{1}{V_{\Omega_s}} \int_{\Omega_s} \boldsymbol{\sigma}(\mathbf{x}_\mu) dV_{\Omega_s} \tag{8-18}$$

and

$$\langle \boldsymbol{\varepsilon} \rangle = \frac{1}{V_{\Omega_s}} \int_{\Omega_s} \boldsymbol{\varepsilon}(\mathbf{x}_\mu) dV_{\Omega_s} \tag{8-19}$$

8.4.2 Localization and solution of the microscale RVE problem

To ensure that the macroscale homogeneous material $\bar{M}$ can reproduce the behaviour of the original microscale heterogeneous material M, energy equivalence is prescribed between the two materials. This energetic equivalence requires the two material systems to have the same internal

energy despite possessing different microstructure. This is achieved by satisfying the nonlocal macrohomogeneity condition:

$$\langle \sigma_{ij}\varepsilon_{ij} \rangle = \bar{\sigma}_{ij}\bar{\varepsilon}_{ij} \tag{8-20}$$

It was shown in 6.1.2.2 that the macrohomogeneity condition is satisfied by the following statement of nonlocal Hill's lemma:

$$\langle \sigma_{ij}\varepsilon_{ij} \rangle - \bar{\sigma}_{ij}\bar{\varepsilon}_{ij} = \frac{1}{V_{\Omega_s}} \int_{\Omega_c} \left((\sigma_{ik} - \bar{\sigma}_{ik}) \mathcal{S}^{S}_{\omega_{x_k}} \left(u_i - x_j \bar{\varepsilon}_{ij} \right) \right) dV_{\Omega_c} \tag{8-21}$$

where $\mathcal{S}^{S}_{\omega}$ denotes a weighted nonlocal gradient operator, $\omega(\boldsymbol{x}, \boldsymbol{x}'): \mathbb{R}^n \times \mathbb{R}^n \longrightarrow \mathbb{R}^+$ is a weight function and the superscript S implies that $\mathcal{S}$ is a symmetric gradient operator (please see [42] for detailed explanation on nonlocal gradient operator and general element of nonlocal vector calculus). The Hill's lemma (8-21) is satisfied by prescribing appropriate boundary conditions (see 6.1.2 and 6.1.3). These include application of homogeneous displacement, homogeneous stress, and periodic boundary conditions. In this chapter, only the homogenous displacement boundary condition will receive attention notably because it is the most compatible of the boundary conditions with the peridynamic framework and the easiest to implement. An appropriate displacement field is applied to the boundary of the RVE so that the gradient of the displacement terms of the integrand of the boundary volume integral (8-21) is vanished. A typical way to achieve this is to apply linear displacement of the form:

$$\boldsymbol{u}(\boldsymbol{x}) = \bar{\boldsymbol{\varepsilon}}\boldsymbol{x} \qquad \forall \boldsymbol{x} \in \Omega_c \tag{8-22}$$

which has been shown in 6.1.3 to vanish the right-hand side of (8-21). Equation (8-22) provides the boundary volume constraint of the microscale problem in terms of field of macro strain. To complete the definition of the computational homogenization scheme, it is necessary to define the microscale volume constraint problem.

8.4.3 RVE volume constraint problem

Consider the composite material M. Let Ω represents the region occupied by an RVE of M. Let Ω be assumed to be in a state of static equilibrium. To formulate a well-posed microscale VCP, Ω is split into two sub volumes as shown in Figure 8-1. The first is Ω_S where solution is sought and the second Ω_C where boundary constraints are imposed. Let $\boldsymbol{\sigma}_\mu$ and $\boldsymbol{\varepsilon}_\mu$ be the micro fields stress and strain in Ω obtained as solution to the following initial volume constraint problem (IVCP):

$$\begin{cases} \int_{\mathcal{B}_\delta(\boldsymbol{x})} \left[\underline{\mathbf{T}}[\boldsymbol{x}_\mu]\langle \boldsymbol{x}'_\mu - \boldsymbol{x}_\mu\rangle - \underline{\mathbf{T}}[\boldsymbol{x}']\langle \boldsymbol{x}_\mu - \boldsymbol{x}'_\mu\rangle\right] d\boldsymbol{x}'_\mu + \mathbf{b}(\boldsymbol{x}_\mu, t) = 0 & \forall \boldsymbol{x}_\mu \in \Omega_S \\ \boldsymbol{u}_\mu(\boldsymbol{x}_\mu) = \boldsymbol{g}_\mu & \forall \boldsymbol{x}_\mu \in \Omega_C \\ \boldsymbol{u}_\mu(\boldsymbol{x}_\mu, 0) = \boldsymbol{u}_{\mu(I)} & \forall \boldsymbol{x}_\mu \in \Omega, \text{for } t = 0 \\ \dot{\boldsymbol{u}}_\mu(\boldsymbol{x}_\mu, 0) = \dot{\boldsymbol{u}}_{\mu(I)} & \forall \boldsymbol{x}_\mu \in \Omega, \text{for } t = 0 \end{cases} \tag{8-23}$$

where the subscript μ in (8-23) and anywhere else in this communication designate field variables associated with the microscale. The force density vector $\underline{\mathbf{T}}[\cdot_\mu]\langle\cdot\cdot\rangle$ is given by (2-87) and the response function that relates the micro field stress $\boldsymbol{\sigma}_\mu$ and strain $\boldsymbol{\varepsilon}_\mu$ is given by (8-1) (for linear material behaviour).

8.5 Implementation strategy

The proposed homogenization scheme consists of the following steps:

1. This step consists of solving the viscoelastic volume constraint problem (8-23) at the microscale to obtain the micro fields of stress and strain within the RVE. To do this, a nested spatial and time numerical integration strategy is used. In spatial integration, the total force acting on a material point is evaluated at a given time, while in time integration, material points are tracked over time. Using a meshfree method [63], the spatial integration of the NOSBPD model is numerically implemented using a discrete form of the first of (8-23) given as

$$\sum_{q=1}^{N} \left[\underline{\mathbf{T}}[\boldsymbol{x}_p, t]\langle \boldsymbol{x}_q - \boldsymbol{x}_p\rangle - \underline{\mathbf{T}}[\boldsymbol{x}_q, t]\langle \boldsymbol{x}_p - \boldsymbol{x}_q\rangle\right] V_q + \mathbf{b}_p = 0 \tag{8-24}$$

where N denotes the total number of material points located within the horizon of the primary material point p. To compute the current accelerations, velocities, and positions of points, the time integration procedure uses the forward Euler method. The explicit time integration of (2-110) yields the following acceleration, velocity, and displacement at time $t = t^n$:

$$\begin{aligned} \ddot{\boldsymbol{u}}_p^n &= \frac{\boldsymbol{\mathcal{L}}_p^n + \mathbf{b}_p}{\rho_p} \\ \dot{\boldsymbol{u}}_p^{n+1} &= \dot{\boldsymbol{u}}_p^n + \ddot{\boldsymbol{u}}_p^n \Delta t \\ \boldsymbol{u}_p{}^{n+1} &= \boldsymbol{u}_p^n + \dot{\boldsymbol{u}}_p^{n+1} \Delta t \end{aligned} \tag{8-25}$$

where $\boldsymbol{\mathcal{L}}_p^n = \sum_{q=1}^{N}\left[\underline{\mathbf{T}}[\boldsymbol{x}_p, t]\langle \boldsymbol{x}_q - \boldsymbol{x}_p\rangle - \underline{\mathbf{T}}[\boldsymbol{x}_q, t]\langle \boldsymbol{x}_p - \boldsymbol{x}_q\rangle\right] V_q$. Since the RVE VCP is a quasi-static problem, implementing equation (8-23) using the forward Euler method will require solving the model as a dynamic problem and then extracting the steady-state solution from the dynamic solution. It is thus proposed in this study to utilize Adaptive Dynamic Relaxation (ADR) [83] to recover the steady state solution of equation (8-25). This strategy gives rise to two notions of time parameters: a numerical time t_{num} which defines the time necessary for the dynamic solution to converge to the steady-state solution and a material time t_{mat} which is the period over which the viscoelastic response is measured. For numerical implementation, the two times are respectively discretized into interval Δt_{num} and Δt_{mat}.

2. In the second step, macro field stress $\bar{\sigma}_{ij}$ and strain $\bar{\varepsilon}_{ij}$ are obtained as volume averages of the micro fields σ_{ij} and ε_{ij} using (8-18) and (8-19). The micro field variables are then utilised in (8-15) to extract the effective stiffness relaxation tensor $\bar{C}_{ijkl}$.

3. Once the effective stiffness relaxation tensor is obtained, effective viscoelastic material functions such as the effective relaxation modulus $\bar{E}(t)$ and hence $\bar{G}(t)$ and $\bar{K}(t)$ are easily computed. This is usually achieved by assuming constant Poisson's ratio.

4. Prony series (8-9) is then used to mathematically represent the discrete values of the effective relaxation moduli determined in step 3 above. To achieve this in the present contribution, a least squares curve fitting code was written in MATLAB to determine the coefficients E_∞, E_m and τ_m^E.

5. Dynamic properties such as the storage and loss moduli as well as tangent of phase lag are respectively obtained from (8-13), (8-14), and (8-12).

8.6 Numerical examples

In this section, the capability of the proposed homogenization scheme to predict the effective properties of composite materials made wholly or partly of viscoelastic materials. To achieve this aim, computational experiments are carried out to determine the effective material properties of two sets of composite materials. The first is a two-phase matrix-inclusion composite in which one of the phases is elastic and the other viscoelastic. The second is a two-phase matrix-inclusion composite material consisting of a viscoelastic inclusion in a viscoelastic matrix. All numerical experiments are conducted for an inclusion volume fraction of 50%. All computations are carried out under the assumption of plane stress state and that all constituent materials are isotropic and

nonaging and the response is measured in the linear regime. The RVE that is representative of the composite materials characterised in this study is shown in Figure 8-2.

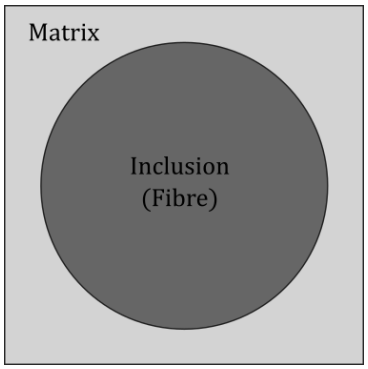

Figure 8-2: RVE showing microstructure topology of composites.

8.6.1 Two-phase composite with elastic inclusion and viscoelastic matrix

In this numerical example, the composite consists of an elastic inclusion and viscoelastic matrix as obtained from [132]. The elastic modulus and Poisson's ratio of the inclusion phase are respectively given as $E = 20$ and $\nu = 0.21$, while the relaxation modulus and Poisson's ratio of the inclusion phase are given respectively as $E(t) = 3 + 17\mathrm{e}^{-t}$ and $\nu = 0.38$.

To implement this problem, the RVE is discretised into 100×100 material points. The choice of a horizon size of $3\Delta x$, where Δx represents the length of a material point, was made to facilitate a comparison of the results obtained from peridynamic simulation with those obtained from classical continuum models. It has been previously demonstrated [82] that this horizon size effectively yields results that converge towards the classical solution. Simulation is done with time step $\Delta t_{mat} = 0.01$ s over a total period of 10^3 s. A numerical time step $\Delta t_{\text{num}} = 1$ s is used.

The results of the effective stress relaxation stiffness tensor and effective loss tangent computed using the proposed nonlocal computational homogenization scheme and those computed using an asymptotic homogenization framework [132] are presented in Figure 8-3 and Figure 8-5, respectively. Figure 8-3 shows the effective stress relaxation stiffness tensor computed by both the nonlocal computational homogenization scheme and the asymptotic homogenization scheme over the specified simulation period. It is clear from the figure that the results obtained by the nonlocal computational homogenization scheme closely match those obtained by the asymptotic homogenization framework. This agreement indicates that the proposed nonlocal computational homogenization scheme can accurately predict the time-domain properties of a heterogeneous material, as represented by the component of the effective stress relaxation stiffness tensor.

For further analysis, the effective relaxation modulus of the composite system is extracted from the effective stress relaxation stiffness tensor obtained from the simulation. The effective relaxation modulus obtained is presented in Figure 8-4. The data presented in Figure 8-4 is curve fitted using the curve fitting code developed in MATLAB to obtain the Prony series coefficients. This allows for the representation of the data in the form (8-9), which can be useful for further analysis and understanding of the underlying dynamics of the system. The Prony coefficients obtained are presented in Table 8-1. To compute the effective dynamic properties of the composite system, the coefficients of the effective relaxation modulus obtained above are used in (8-13) and (8-14) to compute the storage and loss moduli, respectively. These are then used in (8-12) to compute the tangent modulus.

Table 8-1: Prony coefficients for effective relaxation modulus data

Parameter	Fitted value
E_∞	5.4219
E_1	7.5459
E_2	7.1634
τ_1	2.6270
τ_2	0.9876

Figure 8-5 shows the effective loss tangent computed using this proposed framework and compared with results from [132]. Again, it can be observed that the nonlocal computational homogenization scheme shows good corelation with results obtained by the asymptotic homogenization framework. This agreement demonstrates that the proposed nonlocal computational homogenization scheme can accurately predict the frequency-domain properties of a composite material made of elastic inclusion and viscoelastic matrix, as represented by the effective loss tangent.

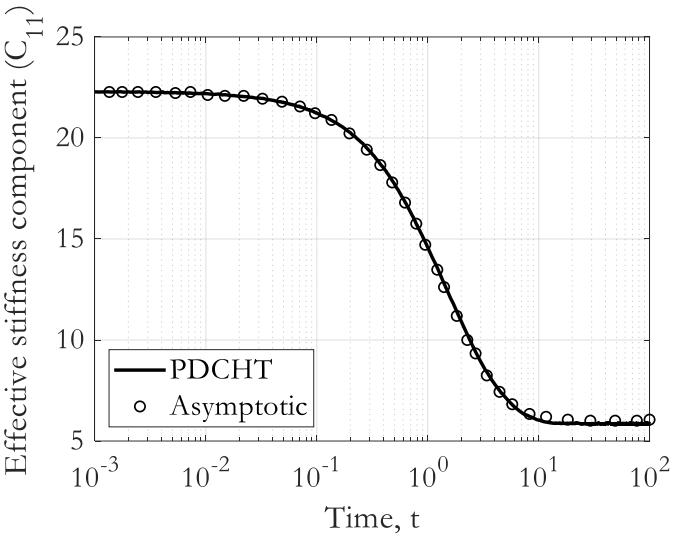

Figure 8-3: Effective stress relaxation stiffness tensor. Graph showing the C_{11} component.

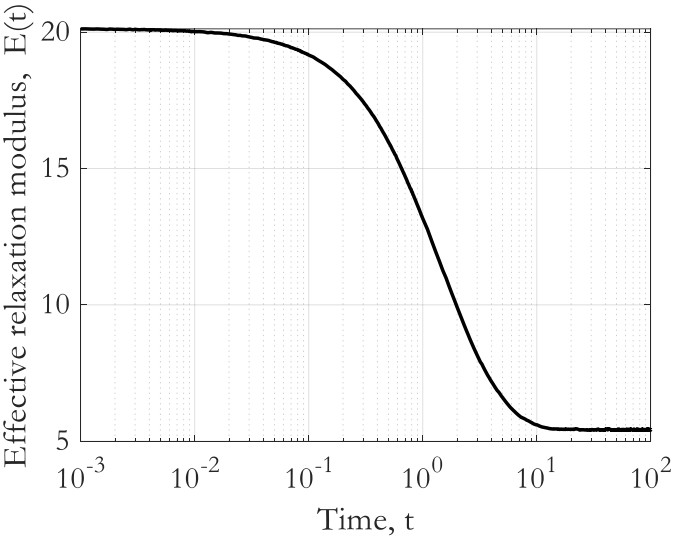

Figure 8-4: Effective relaxation modulus obtained from the effective stress relaxation stiffness tensor.

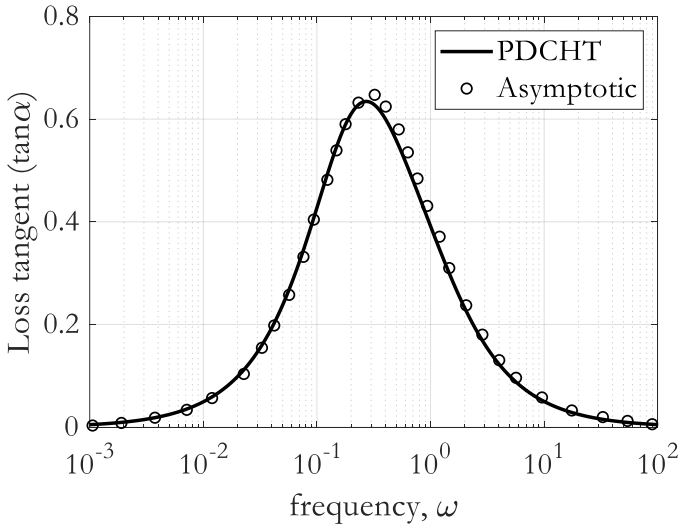

Figure 8-5: Effective loss tangent in frequency domain

8.6.2 Two-phase composite with viscoelastic inclusion and matrix phases.

This example considers a composite with both inclusion and matrix phases to be viscoelastic. The material properties are obtained from [132]. The relaxation modulus and Poisson's ratio for the inclusion phase are respectively given as $E(t) = 3 + 17\mathrm{e}^{-t/10}$ and $\nu = 0.38$ while those for the matrix phase are respectively given as $E(t) = 3 + 17\mathrm{e}^{-t}$ and $\nu = 0.38$. The RVE is discretised into 100×100 points, and a horizon size of $3\Delta x$ is used for the same reason stated in 8.6.1.

Table 8-2: Coefficients of Prony series representation of effective relaxation modulus

Parameter	Fitted value
E_∞	3.0
E_1	14.5
E_2	2.5
τ_1	1.7760
τ_2	27.1185

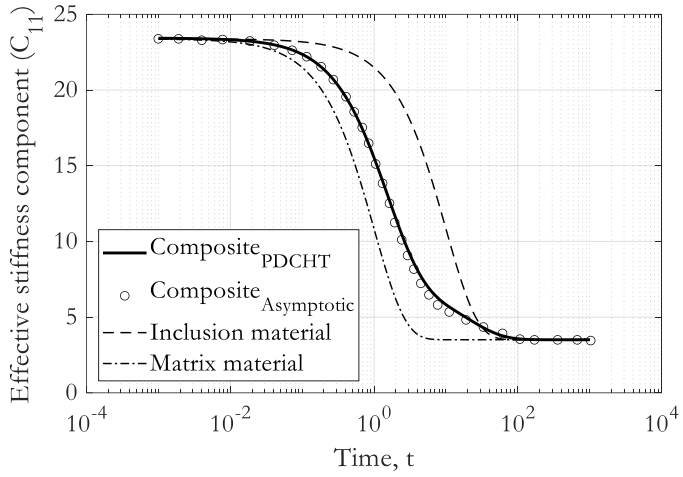

Figure 8-6: Component C_{11} of the effective stiffness tensor of a two-phase matrix-inclusion composite system with both matrix and inclusion made of viscoelastic materials.

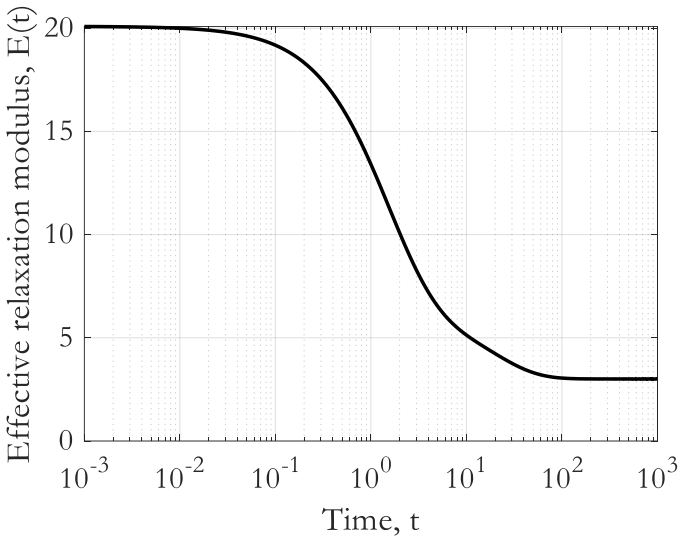

Figure 8-7: Effective relaxation modulus of the composite system obtained from the effective stiffness tensor.

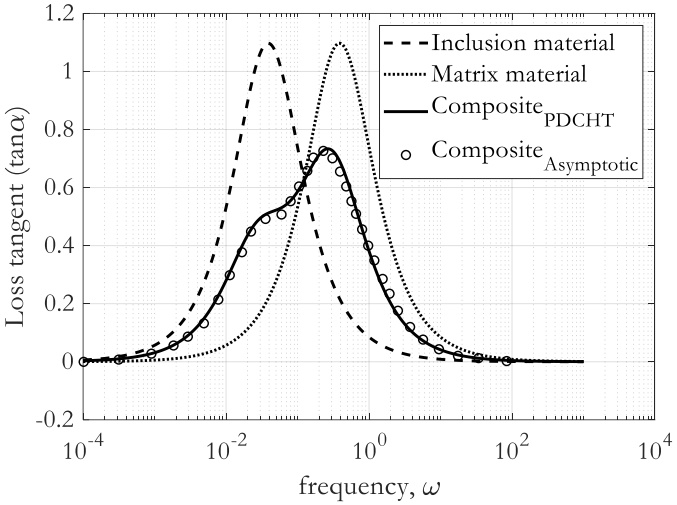

Figure 8-8: Effective loss tangent of a two-phase matrix-inclusion composite system made of viscoelastic inclusion and matrix.

The results of the effective stress relaxation stiffness tensor and effective loss tangent for the matrix-inclusion composite made wholly of viscoelastic materials are presented in Figure 8-6 and Figure 8-8, respectively. These figures compare the results obtained using this proposed nonlocal computational homogenization scheme to those obtained using an asymptotic homogenization framework [132]. Figure 8-6 shows a strong corelation between the effective stress relaxation stiffness tensor for the composite material computed using both the nonlocal computational homogenization scheme and the asymptotic homogenization framework over the entire simulation period.

To enable the determination of the effective dynamic properties of this composite system, its effective relaxation modulus is extracted using the procedure stated in 8.6.1. The effective relaxation modulus is presented as Figure 8-7 and the coefficients of the Prony series representation of the effective relaxation modulus as obtained by curve fitting process are presented in Table 8-2. The Prony series coefficients in Table 8-2 are utilised to determine the effective loss tangent of the composite system and the result presented in Figure 8-8. The effective loss tangent presented in Figure 8-8 shows good agreement with result of computation using the asymptotic homogenization in [132]. This demonstrates the capacity of the proposed nonlocal homogenization scheme to accurately predict both time and frequency domain effective characteristics of composites made wholly of viscoelastic constituents.

8.6.3 Effect of nonlocality on the effective mechanical properties of composites

To demonstrate the capacity of the proposed nonlocal homogenization scheme in capturing nonlocal interactions, a parametric study on the composite system presented in 8.6.1 will be

undertaken in this section. The purpose of this study is to investigate the effect of the nonlocal parameter, as represented by the peridynamic horizon δ, on the effective properties of composites in both the time and frequency domains.

The parametric study will involve varying the horizon size, which is the parameter that controls the degree of nonlocal interactions in PD, while keeping all other model parameters fixed. By doing so, it is possible to observe how the effective properties of the composite system change as the degree of nonlocality is varied. To quantify the effect of the horizon size on the effective properties of the viscoelastic composite, the effective stress relaxation modulus, the effective storage modulus, and the effective loss modulus will be calculated for a range of different horizon sizes.

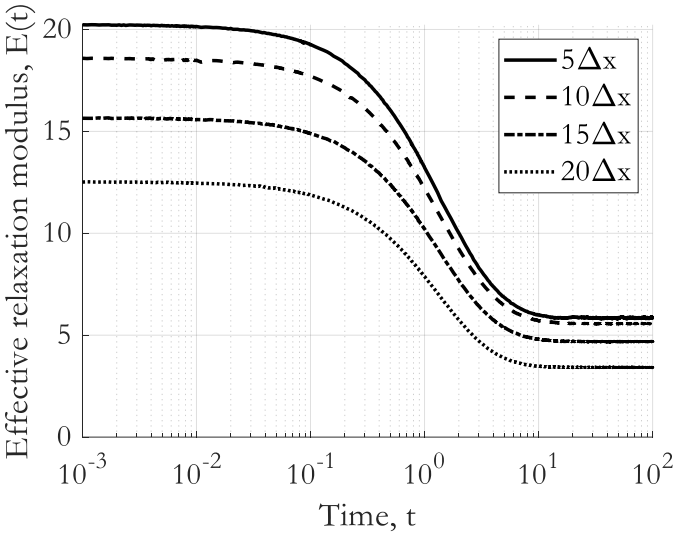

Figure 8-9: Effect of nonlocality on the effective relaxation modulus of a two-phase matrix-inclusion composite system

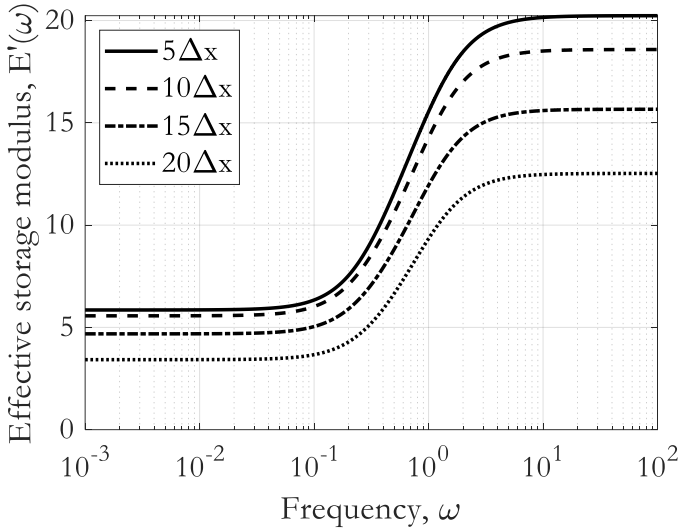

Figure 8-10: Effect of nonlocality on the effective loss modulus of a two-phase matrix-inclusion composite system

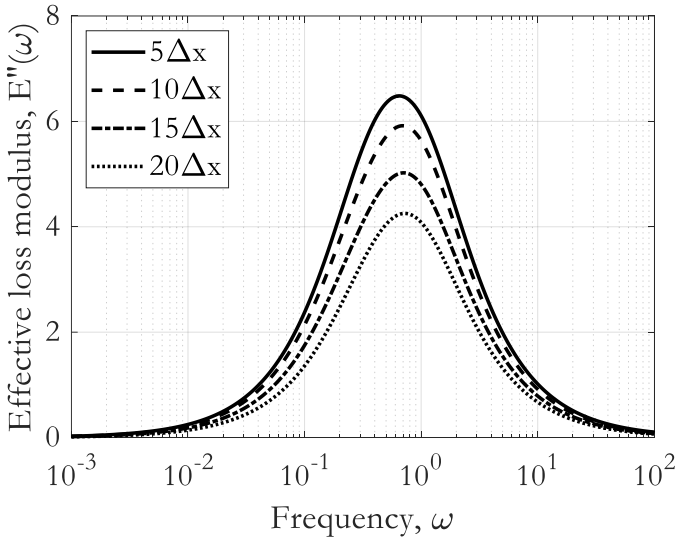

Figure 8-11: Effect of nonlocality on the effective storage modulus of a two-phase matrix-inclusion composite system

Results of the parametric study on the effect of nonlocal interaction on the effective properties of the viscoelastic composite are presented in Figure 8-9, Figure 8-10 and Figure 8-11. Figure 8-9 shows the effective relaxation modulus of the composite for different horizon sizes. The results of the parametric study indicate that as the horizon size, which represents the degree of nonlocal interaction, increases, the effective relaxation modulus decreases. This demonstrates that an increase in nonlocal interaction results in a reduction in the ability of the material to resist stress. This phenomenon can be attributed to the fact that increasing the degree of nonlocality leads to a more diffused stress distribution throughout the material, which results in a lower stress level

within the material. As a result, the average value of the stress field is also reduced, leading to a decrease in the effective stiffness of the composite system.

To study the effect of nonlocal interaction on the dynamic properties of the composite, the effective storage and loss moduli were computed over a range of horizon sizes, and the results are presented in Figure 8-10 and Figure 8-11, respectively. Analysis of these results shows that increasing the nonlocal interaction not only reduces the storage modulus, which is a measure of the resistance of the material to deformation under an applied load, but also the loss modulus, which is a measure of the material's dissipation of energy.

Since nonlocal behaviour is the basis for size effects observed in materials [140], attempts will be made in the following passage to correlate the results of the parametric studies undertaken and presented above with experimental results reported in the literature. When the sample size of a material decreases, the surface to volume ratio increases thus increasing the likelihood of occurrence and relevance of mechanisms occurring at the surface such as crazing in viscoelastic polymer which causes damage and energy dissipation [141] and is also an important mechanism of fracture [142]. In other words, the effect that the specimen size as described by the ratio of surface area to volume has on the behaviour of polymers manifest as size effect which is characterised as nonlocal behaviour. Thus, increasing the surface area to volume ratio can be interpreted as increasing the degree of nonlocal interaction in the material. To be able to compare the implications of results from the parametric studies with experimental observations, a numerical relaxation test to compute the creep strain in a rod of a unit cross-sectional area and unit length is undertaken. The creep strain is computed for material stress relaxation moduli corresponding to horizon sizes $10\Delta x$, $15\Delta x$ and $20\Delta x$ as presented in Figure 8-9. Results from these simulations are presented in Figure 8-12.

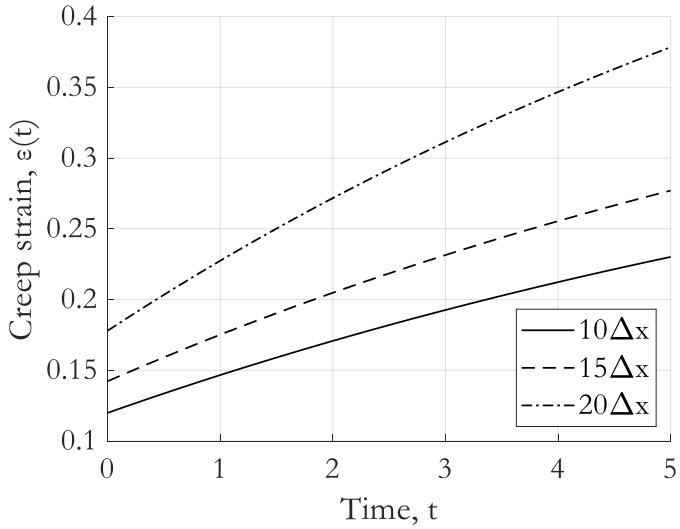

Figure 8-12: Creep strain during stress relaxation in a bar for effective relaxation moduli obtained from different degree of nonlocality.

Figure 8-12 shows that increasing the horizon size has the effect of increasing the rate of creep as indicated by the increasing steepness of the curve. This behaviour correlate well with result of experiment in [143] in which increasing the ratio of the surface area to volume of polymers was observed to increase the rate of creep for a given applied stress.

8.7 Conclusion

In this chapter, a nonlocal computational homogenization scheme, was proposed for determining the effective properties of viscoelastic composite materials using NOSBPD theory. The scheme builds on an earlier nonlocal homogenization scheme by introducing a further nonlocality in time through the integral viscoelastic constitutive model. Numerical experiments were carried out on two viscoelastic matrix-inclusion composite systems to demonstrate the capability of the scheme in reproducing results from asymptotic homogenization in the framework of classical continuum mechanics, and good agreement was found between the results from the proposed scheme and those from referenced literature.

In addition to the numerical experiments, a parametric study was conducted to study the influence of nonlocal interaction on the effective properties of the composite materials. The horizon size was varied while holding other model parameters constant to investigate the effect of varying the degree of nonlocality on the behaviour of the composite system. The results of this parametric study showed that as the degree of nonlocality was increased, the effective behaviour of the composite system became more ductile. This result highlights the importance of accounting for nonlocal interactions when determining the effective properties of viscoelastic composites.

This is especially important with the increasing application of viscoelastic materials in nanocomposites and nanotechnologies. At these small length scales, the significance of nonlocal interactions increases, and thus, it is important to account for these interactions to accurately predict the behaviour of the composite system. This proposed scheme provides a useful tool for understanding the effect of nonlocal interactions on the effective properties of viscoelastic composite materials and could be used as foundation for future studies in this area, especially in the context of nanocomposites and nanotechnologies.

Other potential areas for further research include the application of the proposed scheme to more complex geometries, multiphase systems, and other phenomena that lead to nonlocal interactions such as fracture. Since fracture is inherently a nonlocal process, as such, a nonlocal framework such as the one proposed in this paper is necessary to produce accurate results when analysing viscoelastic composite systems undergoing fracture.

Chapter 9

9.0 Conclusion and future work

9.1 Summary of contributions

This thesis aimed to advance the frontier of computational simulation of nonlocal and discontinuous material response in the framework of peridynamic theory by developing multiscale modelling frameworks that enables the exchange of information between multiple scales within the peridynamic theory. This aim is motivated by the need to increase the computational efficiency of peridynamics and the requirement for a framework that allows for computation of effective properties of heterogeneous materials. The thesis proposed two broad categories of multiscale modelling frameworks. Methods belonging to the first category are herein designated as model order reduction frameworks while the methodology of the second category is called computational homogenization framework.

9.1.1 Model order reduction methodologies

Two model order reduction schemes were proposed: the coarsening method and the model order reduction methodology based on static condensation algorithm. The contributions of this thesis in this regard are summarised below:

- Chapter 3.0 presents the development of the coarsening method for linear peridynamics. The contribution of this thesis in this regards was to extend the one-dimensional framework originally proposed in [34] to two dimensions. The extended framework was then applied to benchmark problems to demonstrate its effectiveness. Results from the benchmark numerical problems demonstrated the effectiveness of coarsening methodology in reducing the order of static linear peridynamic model without compromising on the essential features of the solution.
- Chapter 4.1 presents the development of a model order reduction methodology for linear peridynamics based on static condensation algorithm. To verify its effectiveness, the method was applied to reduce the order of one- and two-dimensional models. Results from these analyses showed the effectiveness of the proposed scheme in reducing the order of static, dynamic, and eigenproblems without compromising the essential characteristics of the system.
- Chapter 5.0 presents an extended application of the proposed model reduction method based on static condensation framework to reduce the order of peridynamic heat transport

model. Results from benchmark studies demonstrates the effectiveness of the reduction methodology in reducing the order of peridynamic heat transport models. Additionally, it was demonstrated that this model order reduction scheme allows for condensation to proceed by either selecting the degrees of freedom to be retained or eliminated from the analysis in a predetermined pattern or randomly selected. Equally, the methodology was demonstrated to also allow for adaptive condensation, that is, allowing for high resolution simulation to run in one region of the model and lower resolution simulation in other regions.

9.1.2 Computational homogenization framework

In response to the need for a framework for characterisation of heterogeneous material within the peridynamic framework, PDCHT was proposed for characterizing effective behaviour of heterogeneous materials at the macro-scale based on mechanisms of deformation and damage occurring at a subscale. Contributions made in this regard are summarised below:

- Chapter 6.1 presents the development of the proposed PDCHT. To set the development of the nonlocal homogenization theory on a consistent mathematical framework, a nonlocal vector calculus was used to derive expressions for essential nonlocal kinematic quantities, the nonlocal average theorems, and the nonlocal macrohomogeneity condition. These provided the foundation upon which the peridynamic computational homogenization framework rest. To validate the proposed nonlocal homogenization scheme, benchmark problems were solved, and the results compared with those obtained using the Reuss, Voigt and Hashin-Shtrikman bounding theorems, the mean-field methods of Ehelby and Mori-Tanaka, as well as the finite element method. The PDCHT was shown to be capable of capturing interesting material behaviour, some of which have been reported in the literature, such as the effect of change in the effective material property when the morphology of the RVE changes. The proposed method was also shown to be able to capture the effect of material phase contrast on the effective behaviour of the composite system.

- Chapter 7.0 presents the application of the PDCHT to characterize the effective response of materials with evolving microstructure, since one of the major advantages offered by the PDCHT theory over homogenization frameworks based on CCM which derives from the strengths of PD theory is in circumstances involving discontinuous material behaviour such as propagation of cracks. In this extended application of the PDCHT, two benchmark problems involving material softening due to crack propagation and damage evolution due

to randomly distributed microcracks was studied. Results from these benchmark studies demonstrated the capability of the PDCHT in characterising materials with evolving microstructure.

- Chapter 8.0 presents the development of a PDCHT for viscoelastic heterogeneous media. The motivation to develop this framework stems from the desire to develop a homogenization scheme that can account for processes and phenomena occurring in viscoelastic heterogenous media that are driven by nonlocal behaviour such as size effect and fracture for which frameworks based on the classical continuum theory lack the capability of modelling. The proposed framework was used to calculate the effective properties in both time and frequency domains of two viscoelastic matrix-inclusion composite systems. The results of calculations were found to compare well with results from the literature. A parametric study was also conducted to investigate the influence of nonlocal interaction on the effective properties by varying the horizon size. Results showed that increasing the degree of nonlocality reduces the stiffness of the composite system as well as increase its rate of creep. The capability to account for nonlocal interaction highlights the potential of this proposed scheme to provide a more comprehensive understanding of the behaviour of viscoelastic composite materials over a wide range of material behaviour.

9.2 Future work

This thesis is a key step in a research direction that promises to unlock the potential of peridynamics as a tool for the computational characterisation of large-scale systems as well as providing a framework for characterisation of the effective properties of systems with evolving microstructure or systems exhibiting complex nonlocal responses. The development of these multiscale frameworks for peridynamics presents opportunities for future work.

9.2.1 Future research direction in the model reduction schemes

An area for future work for the model order reduction schemes proposed in this thesis involve optimizing their computational efficiency. Although the developed frameworks have already been demonstrated to be capable of significantly reducing the computational resource requirement, there is still room for improvement. One potential approach to increasing efficiency could be to incorporate machine learning techniques into the model reduction process, allowing for faster and more accurate predictions of material behaviour at different scales.

Since the order reduction framework proposed in this thesis is based on the static condensation algorithm, it neglects the inertia terms completely and thus while yielding exact reduced static solution, it yields reduced results for eigenvalue problems that are exact only for zero frequency. To enhance the accuracy of prediction especially for eigenproblems, the dynamic reduction algorithm can be used instead of the static condensation algorithm used in this thesis. The dynamic reduction algorithm allows for arbitrary choice of the frequency at which the model reduction yields exact results.

9.2.2 Future research direction in computational homogenization

The foundation laid in this thesis for computational homogenization can be explored on many fronts. One avenue for further exploration could be to extend the framework to incorporate more complex material behaviours, such as plasticity of functionally graded materials, which are often observed in real-world engineering systems. This would require incorporating appropriate constitutive model into the framework and developing appropriate coupling strategies between different scales.

Another future research direction is in comparative analysis of computational results from the proposed homogenization theory which is a first-order nonlocal computational homogenization theory and the second-order computational homogenization theory from the local CCM. This promises to yield interesting results because while the first order PDCHT proposed in this thesis was demonstrated to be capable of capturing nonlocal material response as manifested in size effect, the classical first-order computational homogenization is known to yield inaccurate results in this regard and thus motivated the need to develop the so-called second order computational homogenization theory. This comparison will not only serve to further validate the results of the proposed PDCHT, but also demonstrate the superior capability of the nonlocal homogenization scheme compared to its local counterpart.

References

1. Oden, J.T., T. Belytschko, I. Babuska, and T.J.R. Hughes, *Research directions in computational mechanics*. Computer Methods in Applied Mechanics and Engineering, 2003. **192**(7): p. 913-922 DOI: https://doi.org/10.1016/S0045-7825(02)00616-3.
2. Okereke, M.I., A.I. Akpoyomare, and M.S. Bingley, *Virtual testing of advanced composites, cellular materials and biomaterials: A review*. Composites Part B: Engineering, 2014. **60**: p. 637-662 DOI: https://doi.org/10.1016/j.compositesb.2014.01.007.
3. Segev, R., *Locality and continuity in constitutive theory*. Archive for Rational Mechanics and Analysis, 1988. **101**(1): p. 29-39 DOI: https://doi.org/10.1007/BF00281781.
4. Jirásek, M., S. Rolshoven, and P. Grassl, *Size effect on fracture energy induced by non-locality*. International Journal for Numerical and Analytical Methods in Geomechanics, 2004. **28**(7-8): p. 653-670 DOI: https://doi.org/10.1002/nag.364.
5. Jirásek, M., *Nonlocal models for damage and fracture: Comparison of approaches*. International Journal of Solids and Structures, 1998. **35**(31): p. 4133-4145 DOI: https://doi.org/10.1016/S0020-7683(97)00306-5.
6. Belytschko, T., Y.Y. Lu, and L. Gu, *Crack propagation by element-free Galerkin methods*. Engineering Fracture Mechanics, 1995. **51**(2): p. 295-315 DOI: https://doi.org/10.1016/0013-7944(94)00153-9.
7. Jirásek, M., *Nonlocal Theories in Continuum Mechanics*. Acta Polytechnica, 2004. **44**(5-6) DOI: https://doi.org/10.14311/610.
8. Srinivasa, A.R. and J.N. Reddy, *An Overview of Theories of Continuum Mechanics With Nonlocal Elastic Response and a General Framework for Conservative and Dissipative Systems*. Applied Mechanics Reviews, 2017. **69**(3) DOI: 10.1115/1.4036723.
9. Bažant Zdeněk, P. and M. Jirásek, *Nonlocal Integral Formulations of Plasticity and Damage: Survey of Progress*. Journal of Engineering Mechanics, 2002. **128**(11): p. 1119-1149 DOI: 10.1061/(ASCE)0733-9399(2002)128:11(1119).
10. Silling, S.A., *Reformulation of elasticity theory for discontinuities and long-range forces*. Journal of the Mechanics and Physics of Solids, 2000. **48**(1): p. 175-209 DOI: https://doi.org/10.1016/S0022-5096(99)00029-0.
11. Hobbs, M., T. Dodwell, G. Hattori, and J. Orr, *An examination of the size effect in quasi-brittle materials using a bond-based peridynamic model*. Engineering Structures, 2022. **262**: p. 114207 DOI: https://doi.org/10.1016/j.engstruct.2022.114207.

12. Wang, C., J. Zhao, and W. Zheng, *Progressive Failure Analysis of Soil Slope with Strain Softening Behavior Based on Peridynamics.* Advances in Civil Engineering, 2023. **2023**: p. 6816673 DOI: https://doi.org/10.1155/2023/6816673.
13. Yang, Z., E. Oterkus, and S. Oterkus, *Analysis of Functionally Graded Timoshenko Beams by Using Peridynamics.* Journal of Peridynamics and Nonlocal Modeling, 2021. **3**(2): p. 148-166 DOI: 10.1007/s42102-020-00044-9.
14. Yang, Z., E. Oterkus, and S. Oterkus, *Peridynamic formulation for higher order functionally graded beams.* Thin-Walled Structures, 2021. **160**: p. 107343 DOI: https://doi.org/10.1016/j.tws.2020.107343.
15. Yang, Z., E. Oterkus, and S. Oterkus, *Peridynamic modelling of higher order functionally graded plates.* Mathematics and Mechanics of Solids, 2021. **26**(12): p. 1737-1759 DOI: 10.1177/10812865211004671.
16. Nguyen, C.T., S. Oterkus, and E. Oterkus, *An energy-based peridynamic model for fatigue cracking.* Engineering Fracture Mechanics, 2021. **241**: p. 107373 DOI: https://doi.org/10.1016/j.engfracmech.2020.107373.
17. Karpenko, O., S. Oterkus, and E. Oterkus, *Peridynamic investigation of the effect of porosity on fatigue nucleation for additively manufactured titanium alloy Ti6Al4V.* Theoretical and Applied Fracture Mechanics, 2021. **112**: p. 102925 DOI: https://doi.org/10.1016/j.tafmec.2021.102925.
18. Vazic, B., E. Oterkus, and S. Oterkus, *In-Plane and Out-of Plane Failure of an Ice Sheet using Peridynamics.* Journal of Mechanics, 2020. **36**(2): p. 265-271 DOI: 10.1017/jmech.2019.65.
19. Vazic, B., E. Oterkus, and S. Oterkus, *Peridynamic Model for a Mindlin Plate Resting on a Winkler Elastic Foundation.* 2020 DOI: 10.1007/s42102-019-00019-5.
20. Heo, J., Z. Yang, W. Xia, S. Oterkus, and E. Oterkus, *Free vibration analysis of cracked plates using peridynamics.* Ships and Offshore Structures, 2020. **15**(sup1): p. S220-S229 DOI: 10.1080/17445302.2020.1834266.
21. Candaş, A., E. Oterkus, and C.E. İmrak, *Dynamic Crack Propagation and Its Interaction With Micro-Cracks in an Impact Problem.* Journal of Engineering Materials and Technology, 2020. **143**(1) DOI: 10.1115/1.4047746.
22. Yang, Z., B. Vazic, C. Diyaroglu, E. Oterkus, and S. Oterkus, *A Kirchhoff plate formulation in a state-based peridynamic framework.* Mathematics and Mechanics of Solids, 2019: p. 108128651988752 DOI: 10.1177/1081286519887523.

23. Kefal, A., A. Sohouli, E. Oterkus, M. Yildiz, and A. Suleman, *Topology optimization of cracked structures using peridynamics.* Continuum Mechanics and Thermodynamics, 2019 DOI: 10.1007/s00161-019-00830-x.
24. Huang, Y., S. Oterkus, H. Hou, E. Oterkus, Z. Wei, and S. Zhang, *Peridynamic model for visco-hyperelastic material deformation in different strain rates.* Continuum Mechanics and Thermodynamics, 2019 DOI: 10.1007/s00161-019-00849-0.
25. Vazic, B., H. Wang, C. Diyaroglu, S. Oterkus, and E. Oterkus, *Dynamic propagation of a macrocrack interacting with parallel small cracks.* AIMS Material Science, 2017. **4**(1): p. 118-136 DOI: http://dx.doi.org/10.3934/matersci.2017.1.118.
26. De Meo, D., L. Russo, and E. Oterkus, *Modeling of the Onset, Propagation, and Interaction of Multiple Cracks Generated From Corrosion Pits by Using Peridynamics.* Journal of Engineering Materials and Technology, 2017. **139** DOI: https://doi.org/10.1115/1.4036443.
27. Kefal, A. and E. Oterkus, *Displacement and stress monitoring of a chemical tanker based on inverse finite element method.* Ocean Engineering, 2016. **112**: p. 33-46 DOI: https://doi.org/10.1016/j.oceaneng.2015.11.032.
28. Oterkus, E., E. Madenci, O. Weckner, S. Silling, P. Bogert, and A. Tessler, *Combined finite element and peridynamic analyses for predicting failure in a stiffened composite curved panel with a central slot.* Composite Structures, 2012. **94**(3): p. 839-850 DOI: https://doi.org/10.1016/j.compstruct.2011.07.019.
29. Oterkus, E. and E. Madenci, *Peridynamic Theory for Damage Initiation and Growth in Composite Laminate.* Key Engineering Materials, 2012. **488-489**: p. 355-358 DOI: 10.4028/www.scientific.net/KEM.488-489.355.
30. E, W., *Principles of Multiscale Modeling.* 2011: Cambridge University Press. Available from: https://books.google.co.uk/books?id=9uTjKO2Ix-YC.
31. Weinan, E. and B. Engquist, *The heterognous multiscale methods.* Communications in Mathematical Sciences, 2003. **1**(1): p. 87-132.
32. Ongaro, G., P. Seleson, U. Galvanetto, T. Ni, and M. Zaccariotto, *Overall equilibrium in the coupling of peridynamics and classical continuum mechanics.* Computer Methods in Applied Mechanics and Engineering, 2021. **381**: p. 113515 DOI: https://doi.org/10.1016/j.cma.2020.113515.
33. D'Elia, M., Q. Du, and M. Gunzburger, *Recent Progress in Mathematical and Computational Aspects of Peridynamics*, in *Handbook of Nonlocal Continuum Mechanics for Materials and Structures*, G.Z. Voyiadjis, Editor. 2017, Springer International Publishing: Cham. p. 1-26 DOI: 10.1007/978-3-319-22977-5_30-1.

34. Silling, S.A., *A Coarsening Method for Linear Peridynamics*. 2011. **9**(6): p. 609-622 DOI: http://dx.doi.org/10.1615/IntJMultCompEng.2011002674.
35. Eom, K., S.-C. Baek, J.-H. Ahn, and S. Na, *Coarse-graining of protein structures for the normal mode studies*. Journal of Computational Chemistry, 2007. **28**(8): p. 1400-1410 DOI: https://doi.org/10.1002/jcc.20672.
36. Guyan, R.J., *Reduction of stiffness and mass matrices*. AIAA Journal, 1965. **3**(2): p. 380-380 DOI: https://doi.org/10.2514/3.2874.
37. Pearson, K., *LIII. On lines and planes of closest fit to systems of points in space*. The London, Edinburgh, and Dublin Philosophical Magazine and Journal of Science, 1901. **2**(11): p. 559-572 DOI: https://doi.org/10.1080/14786440109462720.
38. Pinnau, R., *Model Reduction via Proper Orthogonal Decomposition*, in *Model Order Reduction: Theory, Research Aspects and Applications*, W.H.A. Schilders, H.A. van der Vorst, and J. Rommes, Editors. 2008, Springer Berlin Heidelberg: Berlin, Heidelberg. p. 95-109 DOI: https://doi.org/10.1007/978-3-540-78841-6_5.
39. FOX, R.L. and H. MlURA, *An approximate analysis technique for design calculations*. AIAA Journal, 1971. **9**(1): p. 177-179 DOI: https://doi.org/10.2514/3.6141.
40. Noor, A.K. and J.M. Peters, *Reduced Basis Technique for Nonlinear Analysis of Structures*. AIAA Journal, 1980. **18**(4): p. 455-462 DOI: https://doi.org/10.2514/3.50778.
41. Almroth, B.O., P. Stern, and F.A. Brogan, *Automatic choice of global shape functions in structural analysis*. AIAA Journal, 1978. **16**(5): p. 525-528 DOI: https://doi.org/10.2514/3.7539.
42. Du, Q., M. Gunzburger, R.B. Lehoucq, and K. Zhou, *A Nonlocal Vector Calculus, Nonlocal Volume-Constrained Problems, and Nonlocal Balance Laws*. Mathematical Models and Methods in Applied Sciences, 2013. **23**(03): p. 493-540 DOI: https://doi.org/10.1142/S0218202512500546.
43. Gunzburger, M. and R.B. Lehoucq, *A Nonlocal Vector Calculus with Application to Nonlocal Boundary Value Problems*. Multiscale Modeling & Simulation, 2010. **8**(5): p. 1581-1598 DOI: https://doi.org/10.1137/09076660.
44. Bobaru, F., M. Yang, L.F. Alves, S.A. Silling, E. Askari, and J. Xu, *Convergence, adaptive refinement, and scaling in 1D peridynamics*. International Journal for Numerical Methods in Engineering, 2009. **77**(6): p. 852-877 DOI: https://doi.org/10.1002/nme.2439.
45. Bobaru, F. and Y.D. Ha, *Adaptive refinement and multiscale modeling in 2D peridynamics*. 2011. **9**(6): p. 635-660 DOI: http://dx.doi.org/10.1615/IntJMultCompEng.2011002793.

46. Dipasquale, D., M. Zaccariotto, and U. Galvanetto, *Crack propagation with adaptive grid refinement in 2D peridynamics*. International Journal of Fracture, 2014. **190**(1): p. 1-22 DOI: https://doi.org/10.1007/s10704-014-9970-4.

47. Silling, S., D. Littlewood, and P. Seleson, *Variable horizon in a peridynamic medium*. Journal of Mechanics of Materials and Structures, 2015. **10**(5): p. 591-612 DOI: http://dx.doi.org/10.2140/jomms.2015.10.591.

48. Ren, H., X. Zhuang, Y. Cai, and T. Rabczuk, *Dual-horizon peridynamics*. International Journal for Numerical Methods in Engineering, 2016. **108**(12): p. 1451-1476 DOI: https://doi.org/10.1002/nme.5257.

49. Gu, X., Q. Zhang, and X. Xia, *Voronoi-based peridynamics and cracking analysis with adaptive refinement*. International Journal for Numerical Methods in Engineering, 2017. **112**(13): p. 2087-2109 DOI: https://doi.org/10.1002/nme.5596.

50. Macek, R.W. and S.A. Silling, *Peridynamics via finite element analysis*. Finite Elements in Analysis and Design, 2007. **43**(15): p. 1169-1178 DOI: https://doi.org/10.1016/j.finel.2007.08.012.

51. Littlewood, D.J. *Simulation of Dynamic Fracture Using Peridynamics, Finite Element Modeling, and Contact*. in *ASME 2010 International Mechanical Engineering Congress and Exposition*. 2010. DOI: https://doi.org/10.1115/IMECE2010-40621.

52. Agwai, A., I. Guven, and E. Madenci, *Drop-Shock Failure Prediction in Electronic Packages by Using Peridynamic Theory*. IEEE Transactions on Components, Packaging and Manufacturing Technology, 2012. **2**(3): p. 439-447 DOI: https://doi.org/10.1109/TCPMT.2011.2175924.

53. Badia, S., P. Bochev, J. Fish, M. Gunzburger, R. Lehoucq, M. Nuggehally, and M. Parks, *A Force-Based Blending Model for Atomistic-to-Continuum Coupling*. International Journal for Multiscale Computational Engineering - INT J MULTISCALE COMPUT ENG, 2007. **5** DOI: http://dx.doi.org/10.1615/IntJMultCompEng.v5.i5.30.

54. Fish, J., M. Nuggehally, M. Shephard, C. Picu, S. Badia, M. Parks, and M. Gunzburger, *Concurrent ATC coupling based on a blend of the continuum stress and the atomistic force*. Computer Methods in Applied Mechanics and Engineering, 2007. **196**: p. 4548-4560 DOI: https://doi.org/10.1016/j.cma.2007.05.020.

55. Kilic, B. and E. Madenci, *Coupling of peridynamic theory and the finite element method*. Journal of Mechanics of Materials and Structures, 2010. **5**: p. 707-733 DOI: http://dx.doi.org/10.2514/6.2009-2395.

56. Liu, W. and J.-W. Hong, *A coupling approach of discretized peridynamics with finite element method.* Computer Methods in Applied Mechanics and Engineering, 2012. **245-246**: p. 163-175 DOI: https://doi.org/10.1016/j.cma.2012.07.006.

57. Seleson, P., S. Beneddine, and S. Prudhomme, *A force-based coupling scheme for peridynamics and classical elasticity.* Computational Materials Science, 2013. **66**: p. 34-49 DOI: https://doi.org/10.1016/j.commatsci.2012.05.016.

58. Shojaei, A., T. Mudric, M. Zaccariotto, and U. Galvanetto, *A coupled meshless finite point/Peridynamic method for 2D dynamic fracture analysis.* International Journal of Mechanical Sciences, 2016. **119**: p. 419-431 DOI: https://doi.org/10.1016/j.ijmecsci.2016.11.003.

59. Shojaei, A., M. Zaccariotto, and U. Galvanetto, *Coupling of 2D discretized Peridynamics with a meshless method based on classical elasticity using switching of nodal behaviour.* Engineering Computations, 2017. **34**: p. 00-00 DOI: https://doi.org/10.1108/EC-03-2016-0078.

60. Lubineau, G., Y. Azdoud, F. Han, C. Rey, and A. Askari, *A morphing strategy to couple non-local to local continuum mechanics.* Journal of the Mechanics and Physics of Solids, 2012. **60**(6): p. 1088-1102 DOI: https://doi.org/10.1016/j.jmps.2012.02.009.

61. Azdoud, Y., F. Han, and G. Lubineau, *A Morphing framework to couple non-local and local anisotropic continua.* International Journal of Solids and Structures, 2013. **50**(9): p. 1332-1341 DOI: https://doi.org/10.1016/j.ijsolstr.2013.01.016.

62. Azdoud, Y., F. Han, and G. Lubineau, *The morphing method as a flexible tool for adaptive local/non-local simulation of static fracture.* Computational Mechanics, 2014. **54**(3): p. 711-722 DOI: https://doi.org/10.1007/s00466-014-1023-3.

63. Han, F., G. Lubineau, Y. Azdoud, and A. Askari, *A morphing approach to couple state-based peridynamics with classical continuum mechanics.* Computer Methods in Applied Mechanics and Engineering, 2016. **301**: p. 336-358 DOI: https://doi.org/10.1016/j.cma.2015.12.024.

64. Galvanetto, U., T. Mudric, A. Shojaei, and M. Zaccariotto, *An effective way to couple FEM meshes and Peridynamics grids for the solution of static equilibrium problems.* Mechanics Research Communications, 2016. **76**: p. 41-47 DOI: https://doi.org/10.1016/j.mechrescom.2016.06.006.

65. Han, F., G. Lubineau, and Y. Azdoud, *Adaptive coupling between damage mechanics and peridynamics: A route for objective simulation of material degradation up to complete failure.* Journal of the Mechanics and Physics of Solids, 2016. **94**: p. 453-472 DOI: https://doi.org/10.1016/j.jmps.2016.05.017.

66. Han, F. and G. Lubineau, *Coupling of nonlocal and local continuum models by the Arlequin approach.* International Journal for Numerical Methods in Engineering, 2012. **89**(6): p. 671-685 DOI: https://doi.org/10.1002/nme.3255.

67. Alali, B. and R.P. Lipton, *Multiscale Analysis of Heterogeneous Media in the Peridynamic Formulation.* arXiv: Analysis of PDEs, 2010 DOI: https://doi.org/10.48550/arXiv.1004.4621.

68. Alali, B. and R. Lipton, *Multiscale Dynamics of Heterogeneous Media in the Peridynamic Formulation.* Journal of Elasticity, 2012. **106**(1): p. 71-103 DOI: https://doi.org/10.1007/s10659-010-9291-4.

69. Buryachenko, V.A., *Effective elastic modulus of heterogeneous peristatic bar of random structure.* International Journal of Solids and Structures, 2014. **51**(17): p. 2940-2948 DOI: https://doi.org/10.1016/j.ijsolstr.2014.04.020.

70. Buryachenko, V.A., *Effective properties of thermoperistatic random structure composites: Some background principles.* Mathematics and Mechanics of Solids, 2017. **22**(6): p. 1366-1386 DOI: https://doi.org/10.1177/1081286516632581.

71. Buryachenko, V.A., *Generalized Mori–Tanaka Approach in Micromechanics of Peristatic Random Structure Composites.* Journal of Peridynamics and Nonlocal Modeling, 2020. **2**(1): p. 26-49 DOI: https://doi.org/10.1007/s42102-019-00023-9.

72. Madenci, E., A. Barut, and N. Phan, *Peridynamic unit cell homogenization for thermoelastic properties of heterogenous microstructures with defects.* Composite Structures, 2018. **188**: p. 104-115 DOI: https://doi.org/10.1016/j.compstruct.2018.01.009.

73. Buryachenko, V.A., *Computational homogenization in linear elasticity of peristatic periodic structure composites.* Mathematics and Mechanics of Solids, 2019. **24**(8): p. 2497-2525 DOI: https://doi.org/10.1177/1081286518768039.

74. Fatim Zahra, A.B., M. El Rhabi, A. Hakim, and A. Laghrib, *Analysis of the nonlocal wave propagation problem with volume constraints.* Mathematical Modeling and Computing, 2020. **7** DOI: https://doi.org/10.23939/mmc2020.02.334.

75. Zhang, S. and Y. Nie, *A well-posed parameter identification for nonlocal diffusion problems.* Mathematical Methods in the Applied Sciences, 2022. **45**(16): p. 9194-9217 DOI: https://doi.org/10.1002/mma.8298.

76. Alzahrani, H., G. Turkiyyah, O. Knio, and D. Keyes, *Space-Fractional Diffusion with Variable Order and Diffusivity: Discretization and Direct Solution Strategies.* Communications on Applied Mathematics and Computation, 2022. **4**(4): p. 1416-1440 DOI: https://doi.org/10.1007/s42967-021-00184-9.

77. Lehoucq, R.B., P.L. Reu, and D.Z. Turner, *A Novel Class of Strain Measures for Digital Image Correlation*. Strain, 2015. **51**(4): p. 265-275 DOI: https://doi.org/10.1111/str.12138.

78. Vollmann, C., P.D.V. Schulz, P.D.L. Frerick, P.D.M. Gunzburger, and J.P.D.M. Siebenborn, *Nonlocal Models with Truncated Interaction Kernels - Analysis, Finite Element Methods and Shape Optimization*. 2019: Universität Trier. Available from: https://books.google.co.uk/books?id=eZZizQEACAAJ.

79. D'Elia, M. and P. Bochev, *Formulation, analysis and computation of an optimization-based local-to-nonlocal coupling method*. Results in Applied Mathematics, 2021. **9**: p. 100129 DOI: https://doi.org/10.1016/j.rinam.2020.100129.

80. Silling, S.A., M. Epton, O. Weckner, J. Xu, and E. Askari, *Peridynamic States and Constitutive Modeling*. Journal of Elasticity, 2007. **88**(2): p. 151-184 DOI: https://doi.org/10.1007/s10659-007-9125-1.

81. Bergel, G.L. and S. Li, *The total and updated lagrangian formulations of state-based peridynamics*. Computational Mechanics, 2016. **58**(2): p. 351-370 DOI: https://doi.org/10.1007/s00466-016-1297-8.

82. Silling, S.A. and E. Askari, *A meshfree method based on the peridynamic model of solid mechanics*. Computers & Structures, 2005. **83**(17): p. 1526-1535 DOI: https://doi.org/10.1016/j.compstruc.2004.11.026.

83. Madenci, E. and E. Oterkus, *Peridynamic Theory and Its Applications*. 2014, New York, United States: Springer, New York DOI: https://doi.org/10.1007/978-1-4614-8465-3.

84. Silling, S.A., M. Zimmermann, and R. Abeyaratne, *Deformation of a Peridynamic Bar*. Journal of Elasticity, 2003. **73**(1): p. 173-190 DOI: https://doi.org/10.1023/B:ELAS.0000029931.03844.4f.

85. Silling, S.A., *Chapter 1 - Introduction*, in *Peridynamic Modeling, Numerical Techniques, and Applications*, E. Oterkus, S. Oterkus, and E. Madenci, Editors. 2021, Elsevier. p. 1-31 DOI: https://doi.org/10.1016/B978-0-12-820069-8.00008-1.

86. Parks, M.L., R.B. Lehoucq, S.J. Plimpton, and S.A. Silling, *Implementing peridynamics within a molecular dynamics code*. Computer Physics Communications, 2008. **179**(11): p. 777-783 DOI: https://doi.org/10.1016/j.cpc.2008.06.011.

87. Wang, H. and H. Tian, *A fast and faithful collocation method with efficient matrix assembly for a two-dimensional nonlocal diffusion model*. Computer Methods in Applied Mechanics and Engineering, 2014. **273**: p. 19-36 DOI: https://doi.org/10.1016/j.cma.2014.01.026.

88. Evangelatos, G.I. and P.D. Spanos, *A collocation approach for spatial discretization of stochastic peridynamic modeling of fracture.* 2011. **6**(7-8): p. 1171-1195 DOI: http://dx.doi.org/10.2140/jomms.2011.6.1171.

89. Chen, X. and M. Gunzburger, *Continuous and discontinuous finite element methods for a peridynamics model of mechanics.* Computer Methods in Applied Mechanics and Engineering, 2011. **200**(9): p. 1237-1250 DOI: https://doi.org/10.1016/j.cma.2010.10.014.

90. Wang, H. and H. Tian, *A fast Galerkin method with efficient matrix assembly and storage for a peridynamic model.* Journal of Computational Physics, 2012. **231**(23): p. 7730-7738 DOI: https://doi.org/10.1016/j.jcp.2012.06.009.

91. Seleson, P. and D.J. Littlewood, *Convergence studies in meshfree peridynamic simulations.* Computers & Mathematics with Applications, 2016. **71**(11): p. 2432-2448 DOI: https://doi.org/10.1016/j.camwa.2015.12.021.

92. Paz, M., *Practical Reduction of Structural Eigenproblems.* American Society Of Civil Engineers ASCE Journals, 1983. **109**(11): p. 2591-2599 DOI: https://doi.org/10.1061/(ASCE)0733-9445(1983)109:11(2591).

93. Hogan, J., Roy E and D.K. Gartling, *Reduced order models for thermal analysis : final report : LDRD Project No. 137807.* 2010: United States. p. Medium: ED; Size: 18 p. DOI: https://doi.org/10.2172/991534.

94. Huang, D., G. Lu, C. Wang, and P. Qiao, *An extended peridynamic approach for deformation and fracture analysis.* Engineering Fracture Mechanics, 2015. **141**: p. 196-211 DOI: https://doi.org/10.1016/j.engfracmech.2015.04.036.

95. Bobaru, F. and M. Duangpanya, *The peridynamic formulation for transient heat conduction.* International Journal of Heat and Mass Transfer, 2010. **53**(19): p. 4047-4059 DOI: https://doi.org/10.1016/j.ijheatmasstransfer.2010.05.024.

96. Gerstle, W., S. Silling, D. Read, V. Tewary, and R. Lehoucq, *Peridynamic Simulation of Electromigration.* Computers, Materials \& Continua, 2008. **8**(2) DOI: https://doi.org/10.3970/cmc.2008.008.075.

97. Oterkus, S., E. Madenci, and A. Agwai, *Peridynamic thermal diffusion.* Journal of Computational Physics, 2014. **265**: p. 71-96 DOI: https://doi.org/10.1016/j.jcp.2014.01.027.

98. Agwai, A.G., *A Peridynamic Approach for Coupled Fields.*2011,The University of Arizona.

99. Hill, R., *The essential structure of constitutive laws for metal composites and polycrystals.* Journal of the Mechanics and Physics of Solids, 1967. **15**(2): p. 79-95 DOI: https://doi.org/10.1016/0022-5096(67)90018-X.

100. Voigt, W., *Ueber die Beziehung zwischen den beiden Elasticitätsconstanten isotroper Körper.* Annalen der Physik, 1889. **274**(12): p. 573-587 DOI: http://dx.doi.org/10.1002/andp.18892741206.

101. Reuss, A., *Berechnung der Fließgrenze von Mischkristallen auf Grund der Plastizitätsbedingung für Einkristalle.* ZAMM - Journal of Applied Mathematics and Mechanics / Zeitschrift für Angewandte Mathematik und Mechanik, 1929. **9**(1): p. 49-58 DOI: https://doi.org/10.1002/zamm.19290090104.

102. Hill, R., *The Elastic Behaviour of a Crystalline Aggregate.* Proceedings of the Physical Society. Section A, 1952. **65**(5): p. 349-354 DOI: http://dx.doi.org/10.1088/0370-1298/65/5/307.

103. Yu, W., *An Introduction to Micromechanics.* Applied Mechanics and Materials, 2016. **828**: p. 3-24 DOI: https://doi.org/10.4028/www.scientific.net/amm.828.3.

104. Hashin, Z. and S. Shtrikman, *A variational approach to the theory of the elastic behaviour of multiphase materials.* Journal of the Mechanics and Physics of Solids, 1963. **11**(2): p. 127-140 DOI: https://doi.org/10.1016/0022-5096(63)90060-7.

105. Tian, W., L. Qi, X. Chao, J. Liang, and M. Fu, *Periodic boundary condition and its numerical implementation algorithm for the evaluation of effective mechanical properties of the composites with complicated micro-structures.* Composites Part B: Engineering, 2019. **162**: p. 1-10 DOI: https://doi.org/10.1016/j.compositesb.2018.10.053.

106. Otero, F., S. Oller, X. Martinez, and O. Salomón, *Numerical homogenization for composite materials analysis. Comparison with other micro mechanical formulations.* Composite Structures, 2015. **122**: p. 405-416 DOI: https://doi.org/10.1016/j.compstruct.2014.11.041.

107. Smit, R.J.M., W.A.M. Brekelmans, and H.E.H. Meijer, *Prediction of the mechanical behavior of nonlinear heterogeneous systems by multi-level finite element modeling.* Computer Methods in Applied Mechanics and Engineering, 1998. **155**(1): p. 181-192 DOI: https://doi.org/10.1016/S0045-7825(97)00139-4.

108. de Souza Neto, E.A. and R.A. Feijóo, *Variational Foundations of Large Strain Multiscale Solid Constitutive Models: Kinematical Formulation*, in *Advanced Computational Materials Modeling.* p. 341-378 DOI: https://doi.org/10.1002/9783527632312.ch9.

109. Eshelby, J.D. and R.E. Peierls, *The determination of the elastic field of an ellipsoidal inclusion, and related problems.* Proceedings of the Royal Society of London. Series A. Mathematical and Physical Sciences, 1957. **241**(1226): p. 376-396 DOI: https://doi.org/10.1098/rspa.1957.0133.

110. Mori, T. and K. Tanaka, *Average stress in matrix and average elastic energy of materials with misfitting inclusions.* Acta Metallurgica, 1973. **21**(5): p. 571-574 DOI: https://doi.org/10.1016/0001-6160(73)90064-3.

111. González, J.M.S., J.A.H. Ortega, and X.O. Olivella, *A comparative study on homogenization strategies for multi-scale analysis of materials.* Monograph CIMNE. 2013: International Centre for Numerical Methods in Engineering. Available from: https://www.scipedia.com/public/Ortolano_et_al_2013a.

112. Denisiewicz, A., M. Kuczma, K. Kula, and T. Socha, *Influence of Boundary Conditions on Numerical Homogenization of High Performance Concrete.* Materials, 2021. **14**: p. 1009 DOI: https://doi.org/10.3390/ma14041009.

113. Giesen Loo, E. and F.P. van der Meer, *Stress-controlled weakly periodic boundary conditions: Axial stress under varying orientations.* International Journal for Numerical Methods in Engineering, 2020. **121**(19): p. 4458-4470 DOI: https://doi.org/10.1002/nme.6441.

114. Kenaga, D., J.F. Doyle, and C.T. Sun, *The Characterization of Boron/Aluminum Composite in the Nonlinear Range as an Orthotropic Elastic-Plastic Material.* Journal of Composite Materials, 1987. **21**(6): p. 516-531 DOI: https://doi.org/10.1177/002199838702100603.

115. Aboudi, J., M.-J. Pindera, and S.M. Arnold, *Linear Thermoelastic Higher-Order Theory for Periodic Multiphase Materials.* Journal of Applied Mechanics, 2001. **68**(5): p. 697-707 DOI: https://doi.org/10.1115/1.1381005.

116. Sun, C.T. and R.S. Vaidya, *Prediction of composite properties from a representative volume element.* Composites Science and Technology, 1996. **56**(2): p. 171-179 DOI: https://doi.org/10.1016/0266-3538(95)00141-7.

117. Xia, W., E. Oterkus, and S. Oterkus, *Ordinary state-based peridynamic homogenization of periodic micro-structured materials.* Theoretical and Applied Fracture Mechanics, 2021. **113**: p. 102960 DOI: https://doi.org/10.1016/j.tafmec.2021.102960.

118. Yu, W. and T. Tang, *Variational asymptotic method for unit cell homogenization of periodically heterogeneous materials.* International Journal of Solids and Structures, 2007. **44**(11): p. 3738-3755 DOI: https://doi.org/10.1016/j.ijsolstr.2006.10.020.

119. Jöchen, K., *Homogenization of the Linear and Non-linear Mechanical Behavior of Polycrystals.*2013,Karlsruhe Institute of Technology DOI: https://doi.org/10.5445/ksp/1000032289.

120. Klusemann, B. and B. Svendsen, *Homogenization methods for multi-phase elastic composites: Comparisons and benchmarks.* Technische Mechanik - European Journal of Engineering Mechanics, 2010. **30**(4): p. 374-386.

121. Klusemann, B., H.J. Böhm, and B. Svendsen, *Homogenization methods for multi-phase elastic composites with non-elliptical reinforcements: Comparisons and benchmarks*. European Journal of Mechanics - A/Solids, 2012. **34**: p. 21-37 DOI: https://doi.org/10.1016/j.euromechsol.2011.12.002.

122. E, W., B. Engquist, X. Li, W. Ren, and E. Vanden-Eijnden, *Heterogeneous multiscale methods: A review*. Communications in Computational Physics, 2007. **2**(3): p. 367-450.

123. Markenscoff, X. and C. Dascalu, *Asymptotic homogenization analysis for damage amplification due to singular interaction of micro-cracks*. Journal of the Mechanics and Physics of Solids, 2012. **60**(8): p. 1478-1485 DOI: https://doi.org/10.1016/j.jmps.2012.04.004.

124. Kube, C.M., *Elastic anisotropy of crystals*. AIP Advances, 2016. **6**(9): p. 095209 DOI: http://dx.doi.org/10.1063/1.4962996.

125. Zener, C.M. and S. Siegel, *Elasticity and Anelasticity of Metals*. The Journal of Physical and Colloid Chemistry, 1949. **53**(9): p. 1468-1468 DOI: https://doi.org/10.1021/j150474a017.

126. Ranganathan, S.I. and M. Ostoja-Starzewski, *Universal Elastic Anisotropy Index*. Physical Review Letters, 2008. **101**(5): p. 055504 DOI: https://doi.org/10.1103/PhysRevLett.101.055504.

127. Li, R., Q. Shao, E. Gao, and Z. Liu, *Elastic anisotropy measure for two-dimensional crystals*. Extreme Mechanics Letters, 2020. **34**: p. 100615 DOI: https://doi.org/10.1016/j.eml.2019.100615.

128. Michel, J.C., H. Moulinec, and P. Suquet, *Effective properties of composite materials with periodic microstructure: a computational approach*. Computer Methods in Applied Mechanics and Engineering, 1999. **172**(1): p. 109-143 DOI: https://doi.org/10.1016/S0045-7825(98)00227-8.

129. Feyel, F. and J.-L. Chaboche, *FE2 multiscale approach for modelling the elastoviscoplastic behaviour of long fibre SiC/Ti composite materials*. Computer Methods in Applied Mechanics and Engineering, 2000. **183**(3): p. 309-330 DOI: https://doi.org/10.1016/S0045-7825(99)00224-8.

130. Petracca, M., L. Pelà, R. Rossi, S. Oller, G. Camata, and E. Spacone, *Multiscale computational first order homogenization of thick shells for the analysis of out-of-plane loaded masonry walls*. Computer Methods in Applied Mechanics and Engineering, 2017. **315**: p. 273-301 DOI: https://doi.org/10.1016/j.cma.2016.10.046.

131. Tran, A.B., J. Yvonnet, Q.C. He, C. Toulemonde, and J. Sanahuja, *A simple computational homogenization method for structures made of linear heterogeneous viscoelastic materials*. Computer

Methods in Applied Mechanics and Engineering, 2011. **200**(45): p. 2956-2970 DOI: https://doi.org/10.1016/j.cma.2011.06.012.

132. Yi, Y.-M., S.-H. Park, and S.-K. Youn, *Asymptotic homogenization of viscoelastic composites with periodic microstructures*. International Journal of Solids and Structures, 1998. **35**(17): p. 2039-2055 DOI: https://doi.org/10.1016/S0020-7683(97)00166-2.

133. Bažant, Z.P., *Instability, Ductility, and Size Effect in Strain-Softening Concrete*. Journal of the Engineering Mechanics Division, 1976. **102**(2): p. 331-344 DOI: https://doi.org/10.1061/JMCEA3.0002111.

134. Fleck, N.A., G.M. Muller, M.F. Ashby, and J.W. Hutchinson, *Strain gradient plasticity: Theory and experiment*. Acta Metallurgica et Materialia, 1994. **42**(2): p. 475-487 DOI: https://doi.org/10.1016/0956-7151(94)90502-9.

135. Laurien, M., A. Javili, and P. Steinmann, *Peridynamic modeling of nonlocal degrading interfaces in composites*. Forces in Mechanics, 2022: p. 100124 DOI: https://doi.org/10.1016/j.finmec.2022.100124.

136. Laurien, M., A. Javili, and P. Steinmann, *Nonlocal wrinkling instabilities in bilayered systems using peridynamics*. Computational Mechanics, 2021. **68**(5): p. 1023-1037 DOI: https://doi.org/10.1007/s00466-021-02057-7.

137. Kaliske, M. and H. Rothert, *Formulation and implementation of three-dimensional viscoelasticity at small and finite strains*. Computational Mechanics, 1997. **19**(3): p. 228-239 DOI: https://doi.org/10.1007/s004660050171.

138. Hashin, Z., *Viscoelastic Behavior of Heterogeneous Media*. Journal of Applied Mechanics, 1965. **32**(3): p. 630-636 DOI: https://doi.org/10.1115/1.3627270.

139. Christensen, R.M., *Viscoelastic properties of heterogeneous media*. Journal of the Mechanics and Physics of Solids, 1969. **17**(1): p. 23-41 DOI: https://doi.org/10.1016/0022-5096(69)90011-8.

140. Bažant, Z.P., *Size effect*. International Journal of Solids and Structures, 2000. **37**(1): p. 69-80 DOI: https://doi.org/10.1016/S0020-7683(99)00077-3.

141. Jie, M., C.Y. Tang, Y.P. Li, and C.C. Li, *Damage evolution and energy dissipation of polymers with crazes*. Theoretical and Applied Fracture Mechanics, 1998. **28**(3): p. 165-174 DOI: https://doi.org/10.1016/S0167-8442(98)00002-0.

142. Van Krevelen, D.W. and K. Te Nijenhuis, *Chapter 13 - Mechanical Properties of Solid Polymers*, in *Properties of Polymers (Fourth Edition)*, D.W. Van Krevelen and K. Te Nijenhuis, Editors. 2009, Elsevier: Amsterdam. p. 383-503 DOI: https://doi.org/10.1016/B978-0-08-054819-7.00013-3.

143. Wu, J.B.C. and N. Brown, *The effect of specimen size on the mechanical behaviour associated with crazing.* Journal of Materials Science, 1977. **12**(8): p. 1527-1534 DOI: https://doi.org/10.1007/BF00542803.